

**MANIPULATION OF CELL AND PARTICLE
TRAJECTORY IN MICROFLUIDIC DEVICES**

by

Collin David James Edington

Bachelor of Science, Carnegie Mellon University, 2010

Submitted to the Graduate Faculty of
the Swanson School of Engineering in partial fulfillment
of the requirements for the degree of

Doctor of Philosophy

University of Pittsburgh

2014

UNIVERSITY OF PITTSBURGH
SWANSON SCHOOL OF ENGINEERING

This dissertation was presented

by

Collin David James Edington

It was defended on

August 26th 2014

and approved by

William R. Wagner, PhD, Professor Departments of Surgery and Bioengineering

Anna C. Balazs, PhD, Professor Department of Chemical and Petroleum Engineering

Steven Little, PhD, Professor Department of Chemical and Petroleum Engineering

Satdarshan Monga, MD, Professor Department of Pathology

Alan Wells, MD, Professor Department of Pathology

Dissertation Advisors: William R. Wagner, PhD, Professor Departments of Surgery and
Bioengineering,

Alan J. Russell, PhD, Professor Disruptive Healthcare Technology Institute, Carnegie
Mellon University

Copyright © by Collin David James Edington

2014

MANIPULATION OF CELL AND PARTICLE TRAJECTORY IN MICROFLUIDIC DEVICES

Collin David James Edington, PhD

University of Pittsburgh, 2014

Microfluidics, the manipulation of fluid samples on the order of nanoliters and picoliters, is rapidly emerging as an important field of research. The ability to miniaturize existing scientific and medical tools, while also enabling entirely new ones, positions microfluidic technology at the forefront of a revolution in chemical and biological analysis. There remain, however, many hurdles to overcome before mainstream adoption of these devices is realized. One area of intense study is the control of cell motion within microfluidic channels. To perform sorting, purification, and analysis of single cells or rare populations, precise and consistent ways of directing cells through the microfluidic maze must be perfected. The aims of this study focused on developing novel and improved methods of controlling the motion of cells within microfluidic devices, while simultaneously probing their physical and chemical properties. To this end we developed protein-patterned smart surfaces capable of inducing changes in cell motion through interaction with membrane-bound ligands. By linking chemical properties to physical behavior, protein expression could then be visually identified without the need for traditional fluorescent staining. Tracking and understanding motion on cytotactic surfaces guided our development of new software tools for analyzing this motion. To enhance these cell-surface interactions, we then explored methods to adjust and measure the proximity of cells to the channel walls using electrokinetic forces and 3D printed microstructures. Combining our work with patterned substrates and 3-dimensional microfabrication, we created micro-robots capable of rapid and precise movements via magnetic actuation. The micro-robots were shown to be effective tools for mixing laminar flows,

capturing or transporting individual cells, and selectively isolating cells on the basis of size. In the course of development of these microfluidic tools we gained valuable new insights into the differences and limitations of planar vs. 3D lithography, especially for fabrication of magnetic micro-machines. This work as a whole enables new mechanisms of control within microfluidics, improving our ability to detect, sort, and analyze cells in both a high throughput and high resolution manner.

TABLE OF CONTENTS

PREFACE	xxv
1.0 INTRODUCTION	1
1.1 CELL ROLLING AND RELATED BIOLOGY	3
1.1.1 The selectin family of adhesion molecules	4
1.1.2 Leukocyte rolling	7
1.1.3 Parallel plate flow is commonly used to study cell rolling	8
1.2 MICROFLUIDICS AND MEMS DEVICES	9
1.2.1 Traditional photolithography	9
1.2.1.1 Soft lithography for microfluidics	9
1.2.2 Microfluidic methods of continuous separation	10
1.2.2.1 Mechanical forces	10
1.2.2.2 Acoustic forces	13
1.2.2.3 Electrical forces	13
1.2.2.4 Chemical forces	14
1.2.2.5 Optical forces	14
1.2.2.6 Magnetic forces	14
1.2.3 Two photon polymerization enables three-dimensional lithography	15
2.0 TAILORING THE TRAJECTORY OF CELL ROLLING WITH CY- TOTACTIC SURFACES	17
2.1 INTRODUCTION	17
2.2 MATERIALS AND METHODS	23

2.2.1 Investigation of P-selectin activity and immobilization techniques using surface plasmon resonance	23
2.2.1.1 Direct amine coupling	23
2.2.1.2 Streptavidin/Biotin coupling	23
2.2.1.3 Fc/Protein A coupling	24
2.2.1.4 Control surfaces	24
2.2.2 Kinetic assays	24
2.2.3 Synthesis and fabrication of a rationally designed cytotoxic surface	25
2.2.4 Tracking and analysis of HL-60 cell rolling on a patterned surface	28
2.3 RESULTS	29
2.3.1 Investigating methods of P-selectin immobilization using SPR	29
2.3.2 Synthesis and fabrication of a rationally designed cytotoxic surface	30
2.3.3 Tracking and analysis of HL-60 cell rolling on patterned surfaces	33
2.4 DISCUSSION	35
2.5 CONCLUSION	41
3.0 CELL TRACKING AND REGISTRATION	42
3.1 INTRODUCTION	42
3.1.1 Segmentation	43
3.1.2 Linking	44
3.1.3 Cell rolling	45
3.2 METHODS	46
3.2.1 Microfluidic channel fabrication	46
3.2.2 Equipment	47
3.2.3 Software overview	47
3.2.4 Background removal	47
3.2.5 Cell detection	49
3.2.6 Cell tracking	50
3.2.7 Analysis tools	52
3.3 RESULTS	53
3.3.1 Performance evaluation	53

3.3.2	Analysis tools	55
3.3.2.1	Plotting motion	55
3.3.2.2	Speed histogram	55
3.3.2.3	Speed analysis	58
3.3.2.4	Tracklets and editing	58
3.3.2.5	Average trajectory	58
3.4	DISCUSSION	60
3.4.1	Real-time tracking in brightfield images	60
3.4.2	Triphasic rolling behavior	60
3.4.3	Automated feature detection	62
3.4.4	Equipment limitations	64
3.4.5	Target areas for improvement	64
3.5	CONCLUSION	65
3.5.1	Software download	65
4.0	CELLULAR FOCUSING AND LOCALIZATION	66
4.1	INTRODUCTION	66
4.1.1	Existing methods of cell focusing	66
4.1.1.1	Electrophoresis	67
4.1.1.2	Dielectrophoresis	68
4.1.2	Two-photon polymerization	70
4.2	MATERIALS AND METHODS	71
4.2.1	Microfluidic channels within conductive parallel plates	71
4.2.2	Modeling	72
4.2.3	Testing the effect of uniform applied DC fields on cell velocity	73
4.2.4	3D printed filters	74
4.3	RESULTS	76
4.3.1	Modeling indicates uniform field generation throughout channel	76
4.3.2	Electrophoretic focusing results are inconsistent	78
4.3.3	3D printed filters	78
4.4	DISCUSSION	81

4.4.1 Promising new forms of electrokinetic manipulation	84
4.4.2 Printed filters enable easy interrogation of particle location	89
4.5 CONCLUSION	91
5.0 MAGNETIC MICRO-ROBOTS FOR NON-CONTACT MANIPULATION OF CELLS AND PARTICLES	93
5.1 INTRODUCTION	93
5.1.1 Magnetic micro-robots for control of micro-object motion	94
5.1.2 Two photon polymerization for micro-robot fabrication	95
5.2 MATERIALS AND METHODS	96
5.2.1 Electromagnetic-coil system	96
5.2.2 Magnetic microspheres	99
5.2.3 Magnetic nanoparticle composite resist	102
5.2.4 3D printing of MNP-composite resist	103
5.2.5 Sputtered nickel docks	104
5.2.6 Electroplated nickel docks	105
5.2.7 Microfluidic channels	106
5.2.7.1 Lateral migration of micro-particles between streamlines	106
5.2.7.2 Rotational flow induced by spinning spherical micro-robots inside a microfluidic channel	110
5.2.7.3 Magnetic docking	115
5.3 RESULTS	121
5.3.1 Composite resist characterization	121
5.3.2 3D printed microrobots	121
5.3.3 Magnetic docking substrates	124
5.3.4 Size-dependence of micro-particle trajectory in microfluidic channels	124
5.3.5 Manipulation in microfluidic channels with multiple micro-robots	126
5.4 DISCUSSION	129
5.4.1 IP-G composites exhibit superior patterning, adhesion, and consistency	129
5.4.2 Limitations imposed by the physics of TPP	130
5.4.3 3D printing magnetic micro-robots	131

5.4.4 Spinning microspheres can generate particle size gradients in laminar flow	134
5.5 CONCLUSION	135
6.0 SUMMARY AND FUTURE DIRECTIONS	136
6.1 FUTURE DIRECTIONS	139
APPENDIX A. CHAMBER BOTTOM FABRICATION WORKFLOW	141
APPENDIX B. PSGL-1 BIOTINYLATED MICROSPHERES	145
APPENDIX C. CALCULATION OF THE VELOCITY PROFILE IN A LAMINAR FLOW MICROFLUIDIC CHANNEL	149
APPENDIX D. TPP OF SU-8 MNP COMPOSITES	151
APPENDIX E. PARTICLE TRACKING AROUND SPINNING MICROSPHERES	152
BIBLIOGRAPHY	153

LIST OF TABLES

3.1	Cell tracking validation	56
4.1	Electric and dielectric properties of HL-60 cells	68
5.1	Electromagnetic-coil system	101
5.2	Magnetic properties of NdFeB Microspheres	101
5.3	Magnetic nanoparticle properties	102
5.4	Two photon polymerization laser properties	103

LIST OF FIGURES

1.1	PSGL-1 and P-selectin molecules. A, schematic diagram of PSGL-1. SH indicates the location of a cysteine that forms a disulfide bond with the corresponding cysteine on another PSGL-1 molecule to create the PSGL-1 homodimer. The epitopes for the anti-PSGL-1 mAbs PL1 and PL2 are marked. Not shown are the post-translationally added O-glycans, N-glycans, and tyrosine sulfates. B, schematic diagrams of native and recombinant P-selectin. mP-selectin contains an N-terminal C-type lectin domain, followed by an EGF-like domain, nine consensus repeats (CR), a transmembrane domain (TM), and a cytoplasmic domain (cyto). sP-selectin contains all of the extracellular domains. Lec-EGF contains only the lectin and EGF domains, plus a C-terminal extension that includes a factor Xa cleavage site and the epitope for the mAb HPC4. The epitopes for the anti-P-selectin mAbs G1 and S12 are shown. Reprinted with permission from ASBMB [1].	5
1.2	Illustrations of white blood cell rolling under shear flow. Rapid association and dissociation of bonds allow transient tethering as the cell rolls along activated endothelial cells. Selectins and their ligands exhibit both “catch” and “slip” type bond formation depending on applied force. Reprinted from [2], copyright 2000, with permission from Elsevier.	6

1.3	Illustrations by A. Waller (c. 1846). The tongue of a frog was spread thin to allow observation of blood capillaries via transmission microscopy. In these experiments he observed cell sticking, rolling, and extravasation, laying the groundwork for later studies on cell motility across the endothelium. Reprinted from [3], public domain.	8
1.4	The basic concept of soft lithography. A photo-mask is used to transfer a pattern to a layer of photoresist on a silicon wafer. After development, that resist can be used to form the microfluidic channels when PDMS is poured over the mold, or the wafer can be etched to create a negative impression of the pattern in the silicon. The cured PDMS can be peeled off of the mold, oxidized, and bonded to an additional piece of PDMS or glass to form closed channels. Reproduced with permission from [4]. Copyright 2001, American Institute of Physics.	11
1.5	Microfluidic technologies for cell sorting and separation take advantage of intrinsic differences in their biophysical properties. (a) Continuous kinetic methods depend on the rate of cell deflection perpendicular to the channel. (b) Continuous equilibrium methods involve migration to property-dependent equilibrium positions. (c) Elution methods depend on forces antiparallel to flow to create differential retention. Reprinted with permission from [5]. Copyright 2010, Analytical and Bioanalytical Chemistry.	12
1.6	General concept of 3D printing two-photon polymerization. The area in which the laser power is high enough to initiate polymerization is known as the voxel. Typically ellipsoid in shape, the height d_x and cross-section d_{xy} of the voxel depend on laser power and beam focus. Adapted from [6], open source license under Creative Commons 3.0.	15
1.7	Miniature of the Brandenburg Gate, written by means of Nanoscribe's <i>Photonic Professional GT</i> system. © Nanoscribe. Image reprinted with permission [7].	16

2.1	Modeling by Alexeev et al. indicates that chemically or mechanically patterned substrates (left and right respectively) with regions of sharply distinct adhesiveness can redirect rolling vesicles by generating asymmetrical strains that alter the energy landscape, leading to motion toward the centerline of the stripes and perpendicular to the direction of flow. Snapshots above show strain on a capsule and substrate as the capsule encounters sticky areas. Lines on the substrate indicate the boundary of an adhesive patch. Deformation of the capsule at the boundary enhance the contact area with the substrate. Adapted with permission from [8]. Copyright 2007 American Chemical Society.	20
2.2	Predicted trajectories of the centers of mass for capsules of differing compliancy on (a) chemically and (b) mechanically patterned substrates. Stripe angle is 45° and rolling direction is left to right. Adapted with permission from [8]. Copyright 2007 American Chemical Society.	21
2.3	Artistic rendition of the microfluidic device used in this study. The device was designed with the capability to sort cells using patterned stripes of P-selectin, although sorting effectiveness has not yet been studied. Angled stripes on either side of the channel direct rolling cells (blue) toward the center pathway where they are collected as they exit the device. Cells that do not interact with the surface or do not express P-selectin glycoprotein ligand-1 (red) follow the direction of flow and exit through the two side channels. Reprinted with permission from [9]. Copyright 2011 American Chemical Society.	22
2.4	An overview of the process for fabricating the microfluidic cell sorter shown in Figure 2.3. Striped patterns are achieved by depositing gold using sputtering and a negative photoresist lift-off technique. Oxygen plasma bonding is then used to seal a PDMS channel to the glass substrate. After applying a fluorinated agent to block non-specific interactions, P-selectin is covalently attached to the gold stripes [10]. Reprinted with permission from [9]. Copyright 2011 American Chemical Society.	26

2.5	The normalized binding response of PSGL-1 to P-selectin covalently bound to the gold surface of a surface plasmon resonance sensor. Binding was performed with EDC/NHS chemistry (direct amine coupling), and nonlinear curve fitting was used to calculate the predicted response based on a 334 nM K_D from literature [1]. Calculated K_D was 314.4 nM.	31
2.6	Characterization of the physical and chemical patterning of the cytotoxic surface. Scanning electron microscopy (a,b) shows that the stripes are patterned at a high resolution with well-defined edges. Control chambers (c) exhibit high amounts of nonspecific binding in the central channel. Chambers modified with blocking agent and P-selectin (d) demonstrated a significant reduction in nonspecific binding and visible patterning of the fluorescent microspheres, indicating that P-selectin was confined to the gold stripes. Reprinted with permission from [9]. Copyright 2011 American Chemical Society.	32
2.7	Percentage of cells exhibiting cytotoxic behavior, defined as a velocity below 50% of the hydrodynamic velocity. Because many of the interacting cells only appeared to interact with a single stripe before detaching and becoming free-flowing, we also classified the subset of cells that interacted multiple times. The percentage of total cells exhibiting behavior indicative of a single cytotoxic interaction (black) was higher in chambers modified with P-selectin. Chambers with blocking agent showed an increased likelihood of repeated interactions (gray). Almost no instances of multiple interactions were observed on chambers without P-selectin. (N = 3477 cells). Reprinted with permission from [9]. Copyright 2011 American Chemical Society.	34

2.8	Behaviors of interacting and noninteracting cells were visibly different. A representative path of an interacting cell (a) and a noninteracting cell (b) are magnified to demonstrate the rolling behavior and direction of fluid flow (left to right), respectively. By combining the paths of multiple cells from a single video file, the average path they take over a single stripe can be plotted. The mean of this path is shown in red, with black lines representing one standard deviation from the mean. Average paths for interacting (c) and noninteracting (d) cells are shown ((c) n = 6 cells, 92 data points; (d) n = 9 cells, 96 data points). Reprinted with permission from [9]. Copyright 2011 American Chemical Society.	36
2.9	Plots of displacement versus time for the five states of adhesion identified by Chang (left) and sample plots of similar behavior identified in our cell tracking videos (right). The five states are no adhesion (a), fast adhesion (b), transient adhesion (c), firm adhesion (d), and saltation (e). These behaviors represent different dynamic states of adhesion mediated by the biophysical and kinetic properties of the system. Left figure copyright (2000) National Academy of Sciences, U.S.A. [11]. Reprinted with permission from [9]. Copyright 2011 American Chemical Society.	38
2.10	Schematic of a channel used for sorting cells based on membrane stiffness. The stripes patterned in the PDMS ceiling of the channel forced cells through a gap of height h that was varied depending on stiffness. SEM images and experimental setup are also shown. (E) shows sorting of untreated K562 cells (green) and 2 μ M cytochalasin D softened K562 cells (blue). Adapted from [12], open access PLOS ONE.	40
3.1	Flowchart of the different components of the tracking program, with subroutines grouped by language. Arrows indicate the flow of information, and main processes are bolded.	48
3.2	Scoring region around a cell located at index $(x, y) = (0, 0)$, giving preference to cells moving from left to right with the direction of fluid flow. Units for both axes are in pixels.	51

3.3	Screenshot of the tracking and analysis interface, with cell number and path overlaid onto the video file, selection tools (right-hand column), and analysis tools (top menus). Cell tracks and labels have been enhanced for readability.	54
3.4	Overlay of a selection of cell trajectories on the background image. Inlay shows magnified portion of highlighted paths.	57
3.5	Sample data showing cell displacement from initial starting position. Plotting lateral displacement from a common origin makes it easier to rapidly identify unusual behavior (1), interacting (14), and non-interacting cells (6, 12, 13).	59
3.6	Automatic detection of gold/protein stripes is used to generate an averaged trajectory for one or more cells. Path in red shows the mean location of the cell on stripe and gap regions. Green lines show \pm SE.	61
3.7	Velocity of HL-60 cells rolling on variable density (striped) patterns of P-selectin. Response appears triphasic with increasing shear stress. P-selectin incubation concentration was 70 nM. Data points are mean velocity \pm SE. $N \geq 42$ cells for each data point.	63
4.1	EP and DEP. (a) Charged and neutral particle in a uniform electric field. The charged particle (left) feels an EP force, whereas the dipole induced in the uncharged particle (right) will not result in a net force ($F=F+$). (b) A neutral particle in a nonuniform electric field. The particle will experience a net force toward the electric-field maximum because the field magnitude is different at each end of the particle ($F < F+$). Reprinted with permission from [13]. Copyright 2006 Annual Reviews.	69
4.2	Mathematical modeling of the Claussius-Mossatti factor as a function of frequency for THP-1 cells and red blood cells. Unique CM-factor curves allow the two cell types to be separated in regions where the CM-factor is positive for THP-1 cells and negative for RBCs (white arrows). Reprinted from [14], with permission from Elsevier.	71

4.3	Three dimensional model of the simple microfluidic channel being modeled in IES COULOMB(left). Gray area represents PDMS (1.5 mm thick), light blue is pyrex glass (0.5 mm thick), and dark blue is fluid (30 μm channel height). The internal channel is visible in the translucent wireframe cross-section on the right. Automatic meshing of boundary elements in preparation for modeling (right).	72
4.4	Models of 3D printed filters designed to concentrate cells toward the substrate (left, vertical filter) or move cells horizontally in response to their height in the channel (right, horizontal filter). The interior of the vertical filter slopes downward to guide particles too large to fit through the 5x5 μm rectangular channels. The horizontal filter makes it easier to query the height of cells when viewing from overhead.	75
4.5	Isocontours of the z-component of electric field (V/cm) within the channel. Strong geometric effects occur in the corners of the channel, but the field remains highly uniform across the middle 90%.	76
4.6	The total E-field magnitude (black) and x-, y-, z-components (red, blue, green, respectively) along the length of the channel. Measured along a line equidistant between the channel walls, floor, and ceiling. The z-component is the primary contributor to the total field magnitude, and maintains a consistent strength of ~ 7 V/cm between $D = 2$ mm and $D = 10$ mm, which is the area beneath the plates, and encompasses most of the channel length.	77
4.7	Histogram of cell velocity distribution. Cell velocities without an applied field (blue) were distributed around the predicted maximum hydrodynamic velocity (B) that was calculated in APPENDIX C. Green and orange regions show the shift in predicted velocity in the event of $\pm 10\%$ error in flow rate or channel height (respectively). With an applied potential of 30 V, predicted to generate a field of ~ 7 V/cm inside the channel, cell velocities (red) were significantly slower and more tightly grouped, as would be expected for a focused distribution. They also centered nicely around the predicted hydrodynamic velocity 5 μm (or 1 cell radius) from the channel floor (A).	79

4.8	Smoothed histogram of average cell speed with (red dashed line) and without (black solid line) an electric field. Experiment was conducted with 10-fold diluted PBS, made isotonic with sucrose. Flow rate is 0.5 $\mu\text{L}/\text{min}$, plate potential 30 V. This data is representative of $\sim 90\%$ of results.	80
4.9	SEM image of the entry way of the particle filter designed to force cells closer to the substrate. Entrance is $\sim 28 \mu\text{m}$ in height, and exit is $\sim 12 \mu\text{m}$ tall, the average diameter of an HL-60 cell.	80
4.10	Time-lapse projection of 5 μm polystyrene beads flowing through printed filters. Fluid flow is left-to-right. Lower outlets show particles in the upper half of the channel (A). Some particles are small enough to exit prematurely through the printed channels (B). The majority of particles appear to exit through the upper outlets, indicating that they are in the bottom 50% of the channel (C).	82
4.11	Time-lapse projection of HL-60 cells flowing through printed filters. Fluid flow is left to right. The visible bubbles were trapped during gluing of the thin glass substrate to a microscope slide, and are not inside the fluid channel. Cells flowing through the horizontal filter are concentrated into discrete flow lines.	83
4.12	Microfluidic channel for contactless dielectrophoretic separation of cells. Fluidic electrodes are isolated from sample flow by 20 μm PDMS walls. Sawtooth geometry increases capacitively coupled electric field, thereby increasing cDEP forces on cells. Reprinted from [15], open access JOVE Creative Commons.	85
4.13	Fabrication and operation of the first long-range, low-voltage, contactless DEP device. Electrodes are not integrated into the channel layer, and operate with electrode spacing of more than 2 mm, using 1-3 V. Frequencies of 100 kHz to 1 MHz were used to successfully separate red blood cells from whole blood in a capillary driven flow channel. Adapted from figures 1 and 2 from [16] with permission of the Royal Society of Chemistry.	87

4.14	Microsieves printed in etched glass channels with pore diameters of 5.5 μm (a), 5 μm (b), 4 μm (c), and 3.5 μm (d) respectively. Results of microparticle sieving with the 4 μm pore size shown in (e), (f), and (g). Adapted from [17] with permission of the Royal Society of Chemistry (RSC).	90
4.15	Crossing manifold micromixers (CMMs) in microchannels, both fabricated from SU-8 resist. Adapted from [18] with permission of the Royal Society of Chemistry (RSC).	91
5.1	Tangential fluid velocity around a rotating microsphere. Adapted with permission from [19]. Copyright 2012, AIP Publishing LLC.	95
5.2	Free body diagram of a spherical micro-object in contact with the substrate, within the rotational flows induced by a spinning micro-robot. Viewed along the radial axis, ignoring radial and vertical fluidic drag forces. The microscopic roughness on the object and the substrate is enlarged. Adapted with permission from [19]. Copyright 2012, AIP Publishing LLC.	96
5.3	Calculated focal intensity distribution of a typical writing spot. (a) Iso-intensity surfaces. The profiles along the two black lines are depicted in b) and c). (b) Lateral profiles of E^2 (red) and E^4 (purple) correspond to one-photon exposure and two-photon exposure, respectively. (c) Axial profiles of E^2 (red) and E^4 (purple). The horizontal lines in b) and c) correspond to the iso-intensity values of the surfaces in a). Adapted with permission from [20]. Copyright 2013, John Wiley and Sons.	97
5.4	Schematic of TPP operation using ORMOCOMP photoresist to fabricate helical microstructures. Adapted from [21] with permission of the Royal Society of Chemistry.	98

5.5	(a) Four orthogonally oriented iron-core electromagnets are used to generate an in-plane uniform magnetic field. (b) A vertically placed solenoid is used to generate an out-of-plane uniform magnetic field. (c) The workspace in the center of the solenoid is 40 mm in diameter. (d) The coil current is controlled with an Arduino Uno microcontroller board. (e) The samples are imaged using a 20x or 32x objective in an inverted phase contrast microscope (Axio Observer, Carl Zeiss). (f) Images of the samples were captured at 19 frames per second with a CCD digital camera (QICAM 12-bit, QImaging). (g) A desktop computer with the custom user interface communicates with the microcontroller board for real-time adjustment of magnetic field parameters. Reproduced from [22] with permission of the Royal Society of Chemistry.	100
5.6	AutoCAD design of masks for microfluidic channel (blue outline) and magnetic docks (red circles). The narrow inlet (upper left inlet) concentrates particles along the top of the channel. The docks are arranged to allow spinning microrobots to hand off captured particles, moving them through the buffer flow (lower left inlet) and toward successively lower outlets (right).	107
5.7	Plot of the lateral location of the fluid interface between the wide and narrow inlets. The narrow inlet was designated the “top” of the channel, with the wide, buffer inlet at the “bottom”. A power fit shows good agreement with the experimental data, allowing us to predict the inlet flows needed to locate the interface at any given dock on the substrate.	108
5.8	Diagram of the different forces influencing the motion of a microparticle under laminar flow (U_f).	111
5.9	The microfluidic channel was modeled as a rectilinear block with dimensions of $1000\ \mu\text{m}$ (length) \times $100\ \mu\text{m}$ (width) \times $60\ \mu\text{m}$ (height) with three spheres each of a diameter of $20\ \mu\text{m}$ located at the center of its length.	112
5.10	Streamlines were taken on the equatorial plane of the spheres at $z = 10\ \mu\text{m}$. a) Gap size = 0.3 radius of sphere (R). b) Gap size = $0.5R$. b) Gap size = $0.7R$. b) Gap size = $0.9R$. b) Gap size = $1.1R$. b) Gap size = $1.3R$. The short blue solid dash indicates how much flow is compressed through the gap.	113

5.11 Profile of fluid velocity at $z = 10 \mu\text{m}$, with varying gap-to-wall ratios as a function of microsphere radius R	114
5.12 Streamlines were taken on the equatorial plane of the spheres at $z = 10 \mu\text{m}$. For a)–c), the vertical separation was fixed at $2.5R$ while horizontal separation varied from $1.5R$ for a), $2R$ for b) to $2.5R$ for c). For d)–f), the horizontal separation was fixed at $1R$ while vertical separation varied from $2.5R$ for d), $3R$ for e) to $3.5R$ for f).	116
5.13 The micro-robot was modeled as a $30 \mu\text{m}$ -in-diameter sphere placed on top of a dock with an outer diameter of $30 \mu\text{m}$ and a thickness of 500 nm	117
5.14 a) B_z varied while magnetization of the micro-robot and the relative permeability of dock were kept constant at 50 kA/m and 100 , respectively. b) The relative permeability of dock varied while B_z and magnetization of the micro-robot were kept constant at 4 mT and 50 kA/m , respectively. c) Magnetization of the micro-robot varied while B_z and relative permeability of the dock were kept constant at 4 mT and 100 , respectively.	119
5.15 B_z , relative permeability of the dock and magnetization of the micro-robot were kept constant at 4 mT , 100 and 50 kA/m , respectively. Lateral misalignments were normalized by radius of the robot. a) Influence on the interactive force in z -direction (F_z) b) Influence on the interactive force in radial direction (F_{ct}).	120
5.16 Sample SEM image of the line test used to characterize writing parameters. Sample is IP-G resist containing $1 \text{ vol.}\%$ magnetite MNPs. Lines are written with increasing power from left to right, bottom to top, in a snaking fashion, with power changing in 2% increments from $0\text{-}100\%$. On the left-hand side, lines are missing (A) or poorly polymerized (B) due to insufficient power and poor adhesion. On the right, excessive power caused localized heating, monomer degradation, and gas formation that destroyed the feature resolution (C).	122

5.17	Brightfield microscopy of 3D printed microrobots in water. Various structures were designed: (A) corkscrew, (B) spinning disk, (C) spinning bar, and (D) flagella/sputnik. Structures are printed in IP-G resist with 1 vol% Fe ₃ O ₄ MNPs. Structures were well formed but could only spin at ≤ 1 Hz. Structures with 2% MNPs were poorly formed and failed to adhere properly to the substrate.	123
5.18	AutoCAD model of subsection of magnetic docking arrays, showing donut shaped docks with 1 diameter spacing. Diameters are labeled on the substrate as inner/outer diameter in microns. Brightfield microscope inset of sputtered nickel dock with 30/90 μm dimensions (lower right).	125
5.19	Size-dependent vertical migration of particles in induced rotational flow. Flow rate is 4.5 $\mu\text{L}/\text{min}$ (channel height 76 μm). Field strength = 1.5 mT, rotation frequency = 15 Hz. Magnetic micro-robot size was 56 μm in diameter.	127
5.20	Freezeframe of high-speed footage of spinning microspheres (white dotted outline) on magnetic docks (black dotted outline) with polystyrene beads of various sizes. Vertical distribution (in 5 μm increments) of particle sizes are shown for bins around discrete microsphere diameters. Distributions are normalized to the total number of particles in each bin. Flow rate is 3.03 $\mu\text{L}/\text{min}$ (channel height 76 μm), number of frames combined = 3,654. Field strength 1.5 mT, rotation frequency = 20 Hz.	128
5.21	Polymerization threshold of IP-G magnetic nanoparticle composite. Colored regions highlight combinations of laser power and scan speed that create well-formed lines on the surface of glass substrates. Parameters above these contours result in localized heating, monomer degradation, and gas evolution. Parameters below the contours result in insufficient polymerization and/or weak adhesion. Increasing concentrations of magnetic nanoparticles (vol.%) are shown in successively darker shades.	132

6.1	A comparison of different methods of force application and cell/particle sorting across various metrics. These ratings are the author’s subjective opinion and serve more as a general guide to the relative strengths and weaknesses of each method. Properties such as efficiency, reliability, and cost can vary wildly within each technique, depending on the complexity of the fabrication process and the supporting equipment required.	138
B1	Flow cytometry of Alexa Fluor 488 anti-PSGL-1 labeled microspheres shows strong signal from PSGL-1 modified microspheres, indicating that the ligand is successfully bound to the beads in high concentrations.	145
C1	MATLAB plot of velocity profile within a laminar flow channel.	150
E1	Overlay of manually tracked particle paths on video frame of spinning microspheres under flow.	152

PREFACE

I am eternally grateful to the multitude of individuals who have supported and guided me during my journey. First I would like to thank the Department of Bioengineering at the University of Pittsburgh, and the current and former chairs Dr. Sanjeev Shroff and Dr. Harvey Borovetz, for welcoming me into the program and supporting my academic and personal development. I would also like to thank my dissertation committee for their valuable input that helped guide my research aims, especially Dr. William Wagner, my co-advisor and committee chair. Finally, I would like to extend my gratitude to Dr. Alan Russell, for mentoring me and giving me the opportunity to be a part of his amazing group. He taught me how to stand up to for my work while still being my own harshest critic.

I would especially like to thank all the members of the Russell lab: Rick Koepsel, Jill Andersen, Hironobu Murata, Chad Cummings, Alan Campbell, and Bill Clafshenkel. They have volunteered their time and energy on a daily basis to help me succeed. Special thanks to Rick, Jill, and Hiro, for four years of mentoring, technical brilliance, emotional support, and witty banter. Equal thanks are in order for Zvi Liron who inspired me with his energy and passion for science, even from half-way around the world.

My great appreciation also goes out to Carsen Kline, Matt Moneck, and Mats Forssell, who generously volunteered their time and expertise to help me overcome obstacles in the clean room and MEMS lab. Without them I am certain these experiments would not have been possible.

Most importantly I would like to thank my family and my girlfriend Katie. No significant undertaking is possible without the love, support, and encouragement of those closest to you. My parents are my greatest inspiration, and every day I strive to live up to the qualities that they exemplify in their own lives.

The following passage is taken from pages 279-280 of Robert M. Pirsig's *Zen and the Art of Motorcycle Maintenance*. It has resonated with my experiences on a number of levels, and I thought it important to include here as a reminder that roadblocks on the way from point A to point B are perhaps the most important part of science. I believe a PhD teaches you, among other things, the intangible skills needed to navigate those obstacles, and true discovery often occurs during the journey, not at the destination.

A screw sticks, for example on a side cover assembly. You check the manual to see if there might be any special cause for this screw to come off so hard, but all it says is 'Remove side cover plate' in that wonderful terse technical style that never tells you what you want to know. There's no earlier procedure left undone that might cause the cover screws to stick.

If you're experienced you'd probably apply a penetrating liquid and an impact driver at this point. But suppose you're inexperienced and you attach a self-locking plier wrench to the shank of your screwdriver and really twist it hard, a procedure you've had success with in the past, but which this time succeeds only in tearing the slot of the screw. Your mind was already thinking ahead to what you would do when the cover plate was off, and so it takes a little time to realize that this irritating minor annoyance of a torn screw slot isn't just irritating and minor. You're stuck. Stopped. Terminated. It's absolutely stopped you from fixing the motorcycle.

This isn't a rare scene in science or technology. This is the commonest scene of all. Just plain stuck. In traditional maintenance this is the worst of all moments, so bad that you have avoided even thinking about it before you come to it.

The book's no good to you now. Neither is scientific reason. You don't need any scientific experiments to find out what's wrong. It's obvious what's wrong. What you need is an hypothesis for how you're going to get that slotless screw out of there and scientific method doesn't provide any of these hypotheses. It operates only after they're around. This is the zero moment of consciousness. Stuck. No answer. Honked. Kaput. It's a miserable experience emotionally. You're losing time. You're incompetent. You don't know what you're doing. You should be ashamed of yourself. You should take the machine to a real mechanic who knows how to figure these things out.

It's normal at this point for the fear-anger syndrome to take over and make you want to hammer on that side plate with a chisel, to pound it off with a sledge if necessary. You think about it, and the more you think about it the more you're inclined to take the whole machine to a high bridge and drop it off. It's just outrageous that a tiny little slot of a screw can defeat you so totally. What you're up against is the great unknown, the void of all Western thought. You need some ideas, some hypotheses. Traditional scientific method, unfortunately, has never quite gotten around to say exactly where to pick up more of those hypotheses. Traditional scientific method has always been at the very best, 20-20 hindsight. It's good for seeing where you've been. It's good for testing the truth of what you think you now, but it can't tell you where you ought to go, unless where you ought to go is a continuation of where you were going in the past. Creativity, originality, inventiveness, intuition, imagination- 'unstuckness,' in other words- are completely outside its domain.

[...]

To put it in more concrete terms: If you want to build a factory, or fix a motorcycle, or set a nation right without getting stuck, then classical, structured, dualistic subject-object knowledge, although necessary, isn't enough. You have to have some feeling for the quality of the work. You have to have a sense of what's good. That is what carries you forward. This sense isn't just something you're born with, although you are born with it. It's also something you can develop. It's not just 'intuition,' not just unexplainable 'skill' or 'talent.' It's the direct result of contact with basic reality, Quality, which dualistic reason has in the past tended to conceal.

1.0 INTRODUCTION

The medical field has advanced at an increasingly rapid pace in recent centuries. This advancement is largely thanks to our ability to probe the inner workings of biology at increasingly smaller scales. In the past, physicians and scientists could only observe symptomatic relationships between diseases and treatments. Beginning with the invention of the microscope (disputably sometime around the late 1500s), and accelerating in the 19th and 20th centuries, new and increasingly high resolution methods have been developed to observe and understand the cellular and molecular mechanisms of the human body. This in turn has driven the development of new diagnostics and clinical treatments for disease and dysfunction that would not have been possible without the considerable insight that comes from direct observation.

Only in the past few decades has our ability to physically manipulate biology gradually approached the resolution of our imaging capabilities. Advances in chemistry, biology, engineering, and computation have enabled numerous new technologies such as high-throughput DNA sequencing, designer drugs, *in-vitro* fertilization, and single cell analysis. New materials and manufacturing methods have played a considerable role in this revolution. Thanks in large part to advances made in the semiconductor industry, we are now able to manufacture electrical, mechanical, chemical, and optical devices at the micrometer and nanometer size range. Collectively known as MEMS devices (Micro Electro-Mechanical Systems), these tiny machines are capable of performing tasks far too delicate for human hands.

A subclass of MEMS, known as microfluidic devices, are tiny fluid handling systems designed to operate on nanoliters and picoliters of liquid. Born from the convergence of molecular analysis, genomics, and microelectronics, the rapid growth of microfluidic R&D was stimulated by a series of DARPA and DoD programs in the 1990s aimed at developing

field-deployable sensors for chemical and biological threats in the wake of the cold war [23]. Thanks to those early developments, the manipulation of fluids in miniscule channels has emerged as a distinct new field. Channels, valves, reaction vessels, heaters, filters, mixers, pumps, and other integrated MEMS components can be used to recapitulate laboratory tests and medical assays on a single chip, dramatically reducing the necessary volumes (and thereby cost) of samples and reagents, as well as reducing the need for expensive laboratory equipment [23, 24, 25, 26, 27, 28, 29, 30]. The benefits of miniaturization are abundant: high surface area, rapid diffusion, reduced contamination, massively parallel testing, portability, low cost. Microfluidics have already found commercial application for screening protein crystallization conditions [31, 32], single cell [33, 34] and single molecule [35, 36, 37] analysis, and high-throughput screening for drug development [38, 39].

With all the great promise that microfluidics hold, routine commercial adoption has been slower than anticipated due to a number of limitations. One revolves around sample handling and preparation. Converting biological samples, such as blood, feces, or soil to a microfluidic-compatible format often requires preparation steps outside the device. Pumping, valving, and on-chip reagent storage also require improvement over existing solutions [23]. Cell handling, the act of controlling cell motion in channels by passive or active means, is also an important challenge for single and multi-cell analyses. To enable massively parallel study of cell-to-cell variations in phenotype, stiffness, protein expression, or metabolism, there must also be ways of moving and positioning cells with sub-micron accuracy. Doing so rapidly and efficiently, thousands of times per second, is a considerable and enticing challenge. With this challenge in mind, we were motivated to investigate a number of new techniques for manipulating cells within microfluidic devices. While the methods are varied, they are linked by the common goals of continuous operation under fluid flow and specificity toward cellular properties.

Specific Aim 1: Microfluidic cell manipulation by differential rolling adhesion on cytotactic surfaces. We hypothesized that an appropriately patterned surface containing the adhesion protein P-selectin would invoke a 2-dimensional rolling response in leukocytes expressing the membrane-bound P-selectin Glycoprotein Ligand-1 (PSGL-1). This behavior could then be quantified and ultimately used to isolate rolling cells from a

heterogeneous sample. To test this hypothesis, we designed and built microfluidic channels with chemically distinct regions. Immobilization of P-selectin to these regions allowed us to test a theoretical model of rolling behavior against observational results. Collection and analysis of large volumes of data were expedited by the development of custom tracking program.

Specific Aim 2: Control and measure the location of cells relative to the solid/liquid interface. We hypothesized that passive or active means of focusing cells would be beneficial to improving cell-surface interactions. Two approaches were explored. First, modeling was used to guide the design of external electrodes to induce an electric field within a microfluidic chamber. This field could then be used to impose electrokinetic forces on the negatively charged cell membrane. In addition, we also explored a newly available microfabrication technique, 3D laser lithography, to craft passive structures to move cells and query their location within the channel.

Specific Aim 3: Explore a non-contact method for size-specific cell manipulation using vortex capture. Capture of spherical particles in the rotational flow surrounding a spinning object has been demonstrated with magnetic micro-robots. We hypothesized that extending this technique to laminar flow conditions would result in size-specific sorting of particles in a continuous fashion. We fabricated multiple varieties of tethered micro-robots using 3D lithography and traditional lithography, comparing and contrasting the two methods. Successfully crafted devices were able to distribute mixtures of polystyrene beads into gradients of increasing size.

1.1 CELL ROLLING AND RELATED BIOLOGY

The first, and perhaps foremost way in which we study biology today is by dividing it at the cellular level into identifiable lineages. Nearly all cell phenotypes are identified by the complex matrix of proteins and carbohydrates decorating the cell membrane, primarily because they are easily accessible and appear in distinct combinations that can be identified with fluorescent staining. The biological function of many of these molecules is still poorly

understood. Adhesion receptors are of particular interest because they mediate the attachment of cells to other cells or the extracellular matrix, and often perform double duty as signal transducers. In the late 80s and early 90s, a new family of adhesion molecules was discovered when three vascular proteins were successfully cloned [40, 41, 42]. Known as the selectin family of adhesion molecules, they are responsible for adhesive interactions between hematopoietic cells and the vascular endothelium. Selectins govern a physical phenomenon known as cell rolling, wherein a free flowing cell tethers to the endothelium and begins to roll along the vascular wall.

1.1.1 The selectin family of adhesion molecules

Selectins are expressed on most leukocytes (L-selectin), activated endothelial cells, and platelets (E- and P-selectin). They share a common N-terminal C-type lectin domain, followed by an epidermal growth factor (EGF)-like domain, a series of short consensus repeats, a transmembrane domain, and a cytoplasmic tail [1]. A schematic of this arrangement for P-selectin and one of its ligands, PSGL-1, can be seen in Figure 1.1. Selectins have a particular affinity for sialylated, fucosylated oligosaccharides, such as sialyl-Lewis^x (sLe^x) and certain sulfated glycoproteins and proteoglycans [43, 44].

Selectin binding is calcium dependent, and rolling is a result of transient adhesion caused by rapid bond formation and dissociation with a high tensile strength [45]. Perhaps one of the most interesting properties of the selectin bond is its unique reaction kinetics. Up to a certain limit, the bond lifetime of the selectin-ligand system actually increases with applied force, resulting in stronger adhesion. Such systems are known as catch-bonds [46]. Both P- and L-selectin are also known to behave like traditional “slip” bonds above a critical force, resulting in a biphasic “catch-slip” response to increasing shear forces [47]. E-selectin has been shown to follow an even more complex “slip-catch-slip” motif, resulting in a triphasic rolling response to increasing flow rates [48].

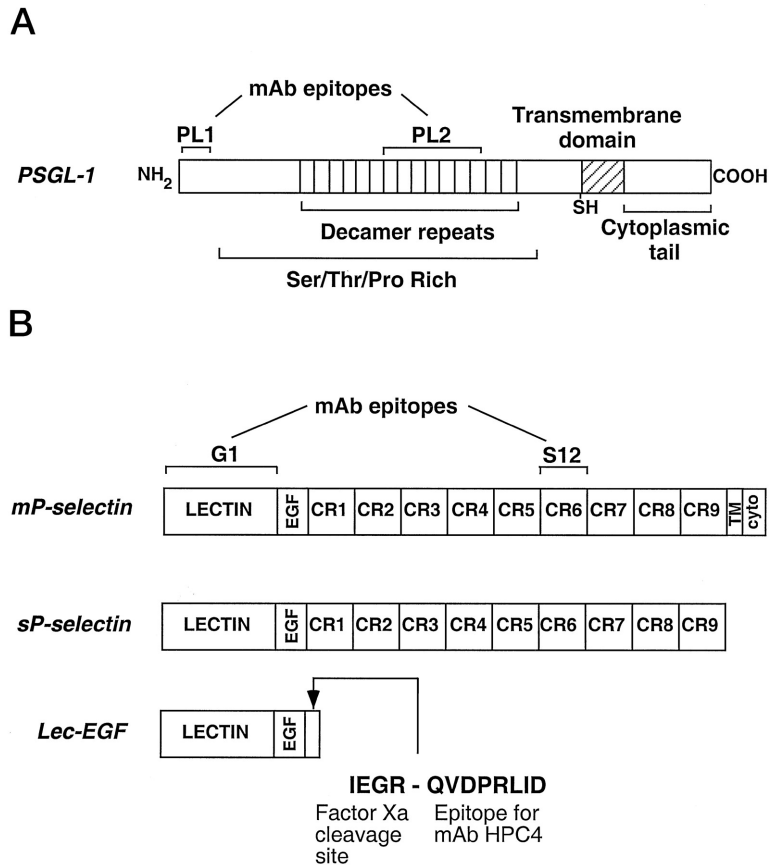


Figure 1.1: PSGL-1 and P-selectin molecules. A, schematic diagram of PSGL-1. SH indicates the location of a cysteine that forms a disulfide bond with the corresponding cysteine on another PSGL-1 molecule to create the PSGL-1 homodimer. The epitopes for the anti-PSGL-1 mAbs PL1 and PL2 are marked. Not shown are the post-translationally added O-glycans, N-glycans, and tyrosine sulfates. B, schematic diagrams of native and recombinant P-selectin. mP-selectin contains an N-terminal C-type lectin domain, followed by an EGF-like domain, nine consensus repeats (CR), a transmembrane domain (TM), and a cytoplasmic domain (cyto). sP-selectin contains all of the extracellular domains. Lec-EGF contains only the lectin and EGF domains, plus a C-terminal extension that includes a factor Xa cleavage site and the epitope for the mAb HPC4. The epitopes for the anti-P-selectin mAbs G1 and S12 are shown. Reprinted with permission from ASBMB [1].

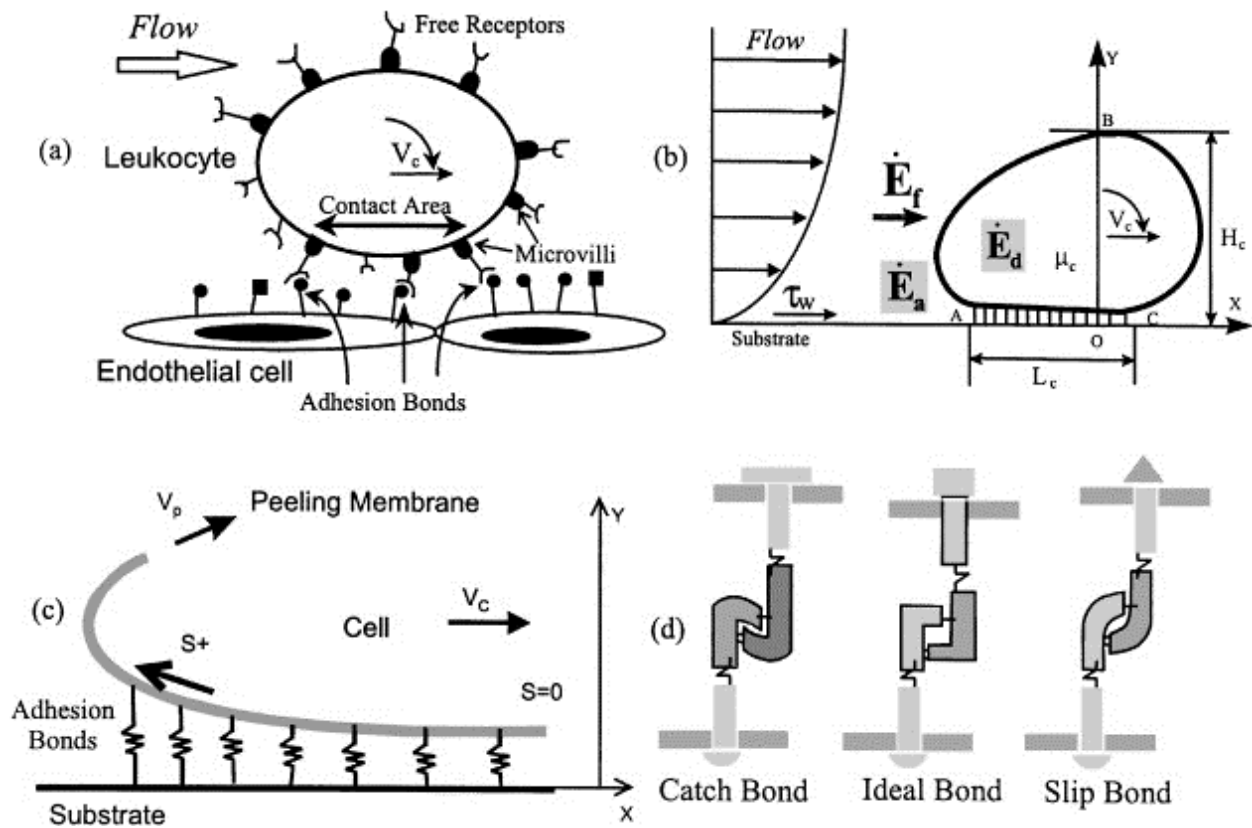


Figure 1.2: Illustrations of white blood cell rolling under shear flow. Rapid association and dissociation of bonds allow transient tethering as the cell rolls along activated endothelial cells. Selectins and their ligands exhibit both “catch” and “slip” type bond formation depending on applied force. Reprinted from [2], copyright 2000, with permission from Elsevier.

1.1.2 Leukocyte rolling

Cell rolling is a common and important physiological process in inflammation, wound healing, cell homing, and cancer metastasis [49, 50, 51, 52, 53]. During the course of normal inflammation, cytokines and histamine are released by damaged tissues and promote the rapid expression of the adhesion proteins E- and P-selectin on vascular endothelial cells. Selectin family molecules bind weakly to carbohydrate ligands on the surface of leukocytes, such as PSGL-1 [54]. These weak bonds rapidly form and dissociate, causing leukocytes to roll along the endothelium. Expression of immunoglobulin ligands, such as ICAM-1 and VCAM-1, on the endothelium eventually halts the motion of rolling leukocytes. Chemokine gradients then cause them to transmigrate through the endothelium, a process also known as extravasation [55]. By this mechanism, leukocytes are able to rapidly localize to the site of injury and exit the blood flow.

Rolling behavior was first observed more than 150 years ago by Henri marquis Du Trochet in 1824 [56], and later illustrated by Dr. Augustus Waller during his intravital microscopy observations of frogs and toads in 1846 (see Figure 1.3). Since then, leukocyte-endothelial interactions have been identified as a key component in the inflammatory response, with implications in a wide array of medical disorders such as adult respiratory distress syndrome (ARDS) [57], immune vasculitis, cancer metastasis [58], transplant rejection[59], and autoimmune disorders [60].

Since cell rolling precedes neutrophil infiltration, understanding and controlling it can have valuable applications in controlling the inflammatory response. One such application has been demonstrated in the ischemia/reperfusion model of kidney and liver transplantation in rats [61, 62]. In these studies, soluble PSGL-1 was used to inhibit neutrophil infiltration in response to ischemia/reperfusion, a common issue associated with organ transplantation. The treatment resulted in considerably reduced organ injury, increased blood flow, and improved organ function/survival. A better understanding of cell rolling is therefore valuable for developing new clinical treatments.

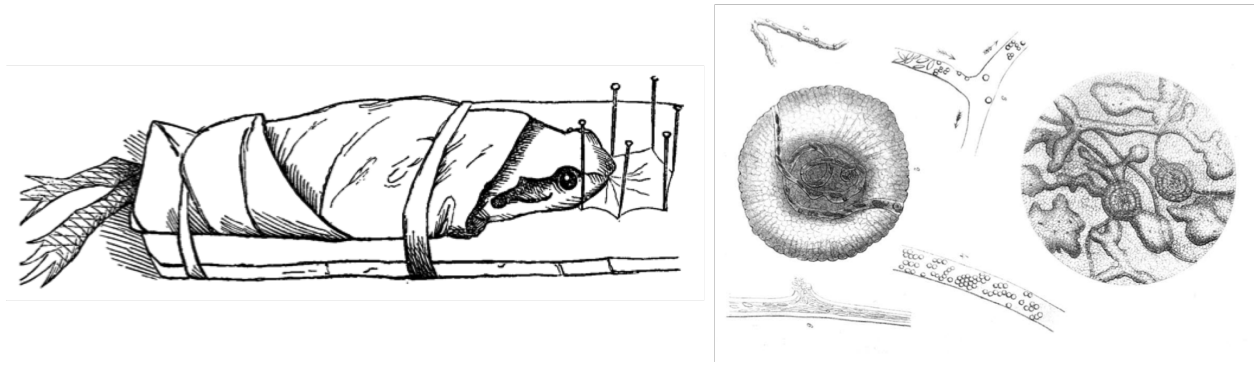


Figure 1.3: Illustrations by A. Waller (c. 1846). The tongue of a frog was spread thin to allow observation of blood capillaries via transmission microscopy. In these experiments he observed cell sticking, rolling, and extravasation, laying the groundwork for later studies on cell motility across the endothelium. Reprinted from [3], public domain.

1.1.3 Parallel plate flow is commonly used to study cell rolling

The study of cell rolling *in-vitro* has been conducted primarily in parallel plate flow chambers, a sort of macroscopic precursor to microfluidic devices [63]. Selectins are adsorbed or covalently bound to one or both of the plates, and cells expressing ligands are introduced into the chamber at a steady flow rate. Cell rolling can then be observed with traditional microscopy. These experiments have been used to identify new ligands for selectins, thereby identifying potential therapeutic targets for anti-inflammatory therapies. Aigner et al., for example, identified CD24 as a mediator of rolling of PSGL-1 negative breast carcinoma cells on P-selectin [64], subsequently leading to the use of CD24 as a new prognostic marker in breast cancer and its association with multiple properties linked to tumor growth and metastasis [65, 66].

Tumor infiltration by neutrophils is often necessary for the acquisition of a metastatic phenotype, and chronic inflammation has a strongly carcinogenic effect on tissues due to the development of reactive oxygen species [67]. Studies have also shown that some cancer cells have the ability to roll on activated endothelium [68], or piggyback on leukocytes and use them as a vehicle for extravasation [49, 50, 51]. Therefore, studying cell rolling and

leukocyte behavior in association with tumor cells is extremely important for developing improved treatments and limiting metastatic potential.

Rolling on activated endothelium is also being leveraged for improved cell therapy by engineering the cell membrane with small peptides that bind to selectins, mimicking the natural ligands expressed on leukocytes [52]. Attachment of these peptides to stem cells has been shown to induce rolling, and might enhance their delivery to areas of injury following systemic injection, hopefully increasing their engraftment, survival, and efficacy.

1.2 MICROFLUIDICS AND MEMS DEVICES

1.2.1 Traditional photolithography

As previously mentioned, microfluidics and MEMS devices are built using lithographic manufacturing methods borrowed from the semiconductor industry. Lithography typically involves the transfer of a pattern, called a mask, onto a wafer of silicon or glass coated in a thin layer of UV curable photoresist. The mask can either be written via laser ablation onto a chrome coated glass plate, or for low resolution applications, printed on a plastic sheet with a printer. The pattern is exposed using a controlled dosage of light, typically in the UV spectrum, and the resist is developed to reveal the pattern. The resist layer is then used to protect the underlying substrate in some areas, while exposing it in others. A wide variety of processes are then available to etch, oxidize, and coat the wafer with metals, oxides, and polymers. Using multiple masks and patterns, nearly any conceivable combination of disparate materials can be built up in a planar fashion to create solid structures, such as transistors, conductive traces, cantilevers for AFM tips, combs for gyroscopes and accelerometers, or molds for soft lithography.

1.2.1.1 Soft lithography for microfluidics Soft lithography borrows the high resolution patterning from regular lithography to create negative impression molds for soft polymers. By either etching the molds into silicon or embossing them on its surface with

raised photoresist, the shapes can then be transferred into the cured polymer. By far the most popular polymer used in soft lithography, especially in microfluidic applications, is poly(dimethylsiloxane) or PDMS. It is transparent, gas permeable, and reproduces molded patterns with a high degree of accuracy and minimal shrinkage. Figure 1.4 shows the basic process of creating microfluidic channels using soft lithography.

By combining hard and soft lithography, microfluidic devices can be crafted to perform a wide array of functions and apply differential forces on cells using fluidic, acoustic, electrical, magnetic, and optical means. These forces are most commonly applied to methods of separating cells based on differences in mechanical, chemical, or electrical properties.

1.2.2 Microfluidic methods of continuous separation

Traditional methods of sorting cells use fluorophores and antibodies to selectively label them. Fluorescent activated cell sorting (FACS) or its magnetic counterpart MACS are then used to isolate the cells of interest based on this labeling. These methods can have high startup costs (\$250,000 for FACS systems) and require milliliters of samples and reagents. Fluid shear stresses and the use of fluorophores and antibodies can also influence cell fate and function [69]. Other macroscale methods, like centrifugation, can also be incompatible with small sample volumes. Separation of leukocytes from whole blood, one of the most common uses of centrifugation, still introduces chemical agents such as Ficoll even though labeling is not used. Because leukocytes are highly sensitive to their environment, centrifugation or FACS sorting might alter their immunophenotype or change surface marker expression [70, 71, 72]. Consequently, microfluidic methods of cell sorting may allow reduced costs, lower sample volumes, and gentler methods of label free separation. Figure 1.5 shows generalizations of the three basic ways of performing separation using gradient force fields.

1.2.2.1 Mechanical forces Some of the earliest microfluidic devices performed functions that were intrinsic to the physical design of the channel, and therefore required no additional features to accomplish tasks such as size sorting, mixing, and particle concentration. Hydrodynamic forces induced by streamline manipulation have been used to arrange

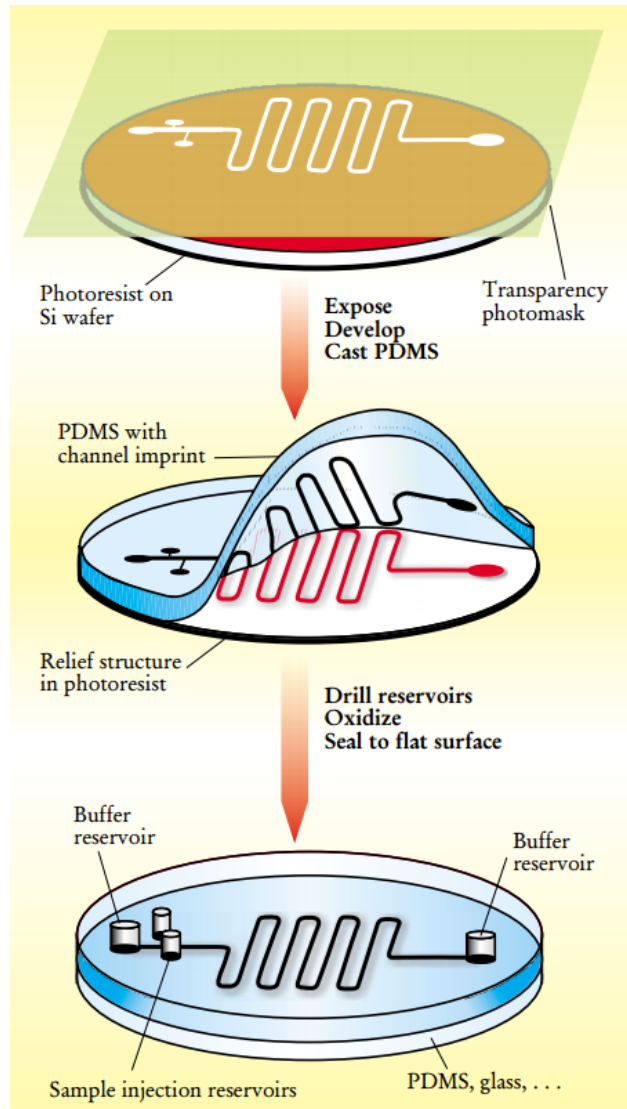


Figure 1.4: The basic concept of soft lithography. A photo-mask is used to transfer a pattern to a layer of photoresist on a silicon wafer. After development, that resist can be used to form the microfluidic channels when PDMS is poured over the mold, or the wafer can be etched to create a negative impression of the pattern in the silicon. The cured PDMS can be peeled off of the mold, oxidized, and bonded to an additional piece of PDMS or glass to form closed channels. Reproduced with permission from [4]. Copyright 2001, American Institute of Physics.

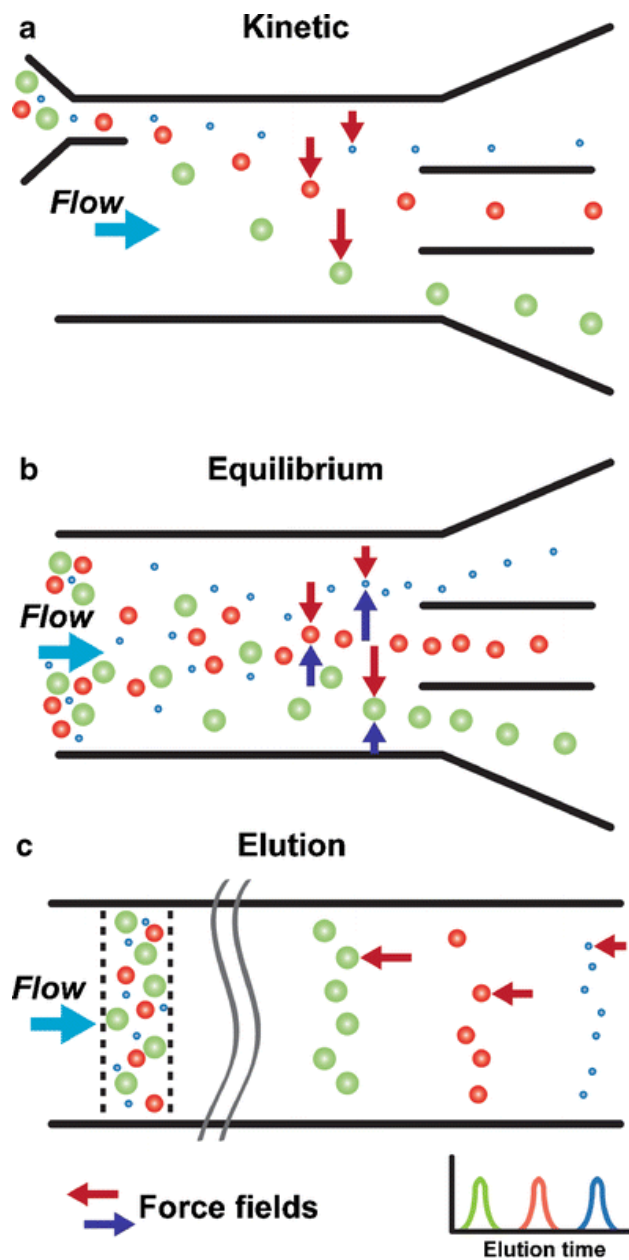


Figure 1.5: Microfluidic technologies for cell sorting and separation take advantage of intrinsic differences in their biophysical properties. (a) Continuous kinetic methods depend on the rate of cell deflection perpendicular to the channel. (b) Continuous equilibrium methods involve migration to property-dependent equilibrium positions. (c) Elution methods depend on forces antiparallel to flow to create differential retention. Reprinted with permission from [5]. Copyright 2010, Analytical and Bioanalytical Chemistry.

cells by size and shape [73, 74], while inertial lift forces and secondary flow have achieved 100-300 fold enrichment of cells and bacteria from dilute samples [75, 76, 77].

Other methods of flow disruption, such as micropost arrays, herringbone shapes, and other microstructures can be directly integrated into the channel using soft lithography [78, 79, 80]. For example, Huang et al. used migration of blood through a micropost array to isolate nucleated red blood cells [81]. Hsu et al. have used herringbone shapes to induce micro-vortices that improve capture of rare circulating tumor cells [80].

While flow forces are very efficient and simple to incorporate, they often cannot differentiate between important properties of different types of cells. More complex methods of force generation are needed to act on those cells not suited to hydrodynamic separation.

1.2.2.2 Acoustic forces Acoustic radiation forces, applied by a microfabricated ultrasonic transducer, can generate differential acoustic radiation forces that separate cells and particles by size, density, and compressibility [82]. Lenshof et al. have used this force to perform whole blood plasmapheresis [83], and Petersson et al. have performed continuous, size-based particle separation [84]. Like hydrodynamic forces, acoustic forces act on mechanical properties of cells and particles, and are therefore limited in many of the same ways.

1.2.2.3 Electrical forces Electrical forces are an attractive way to measure certain properties of cells and isolate them from one another. Almost all biological cells are charged or exhibit an electrical dipole thanks to the concentration of charged species in the glycocalyx surrounding the cell and the ion pumps incorporated into the membrane [85]. Electrophoresis, the application of a DC electrical field to cell-containing fluids, has been used to study cell surface charge for decades, and can be applied within microfluidics to perform similar functions [86].

The use of AC fields, especially in the kHz and MHz frequencies, can be used to induce a dipole moment in cells and generate force fields based on their dielectric properties. Dielectrophoresis (DEP) has several advantages over electrophoresis (EP): it reduces electrochemistry at the electrode surface, reduces Joule heating and gas formation in the fluid,

can be more gentle to cells, and can separate cells with no net charge, as long as they have differing dielectric properties [87, 88]. DEP has been used to for live/dead separations of cells of the same phenotype [89, 90], as well as for separating different phenotypes from one another [91].

1.2.2.4 Chemical forces Small samples can be probed for rare and specific types of cells by using high affinity species, such as antibodies and adhesion proteins, patterned into microfluidic chambers or contained in different flow streams [72]. These chemical methods are often combined with some of the mechanical methods mentioned earlier, such as micropost arrays and herrinbone shapes, to increase the rate of cell interaction with the surface-bound molecules [92]. New models of adhesive affinity kinetics indicate that adhesive patterns can be used not just for capture, but also in a continuous manner via transient adhesion [8].

1.2.2.5 Optical forces Optical forces are a relatively newer method of cell handling that use radiation pressure to perform optical trapping, force measurements, and single cell manipulation via optical tweezers [93]. Optical bars and lattices have been used to trap, manipulate, and continuously sort cells and colloids based on their optical polarizability [94, 95, 96]. The primary disadvantage of optical methods of manipulation is that they require an unobstructed path through the microfluidic channel, which can be difficult or impossible to achieve in combination with integrated MEMS and other handling methods.

1.2.2.6 Magnetic forces Magnetic forces for cell manipulation have emerged as particularly attractive options in recent years. Traditional microfluidic devices are transparent to magnetic fields, allowing long-distance application of forces with external electromagnetic coils. Magnetism has almost no physical effects on biological cells and proteins, and the forces that can be generated on magnetic particles and MEMS components within microfluidic channels are extremely large relative to the volume of material being used.

Attachment of magnetic particles to cells, similar to MACS, is still the most common way of magnetic sorting. Saliba et al. used biofunctionalized magnetic beads, in self-assembled columns within a microfluidic device, to capture B-lymphocyte subpopulations

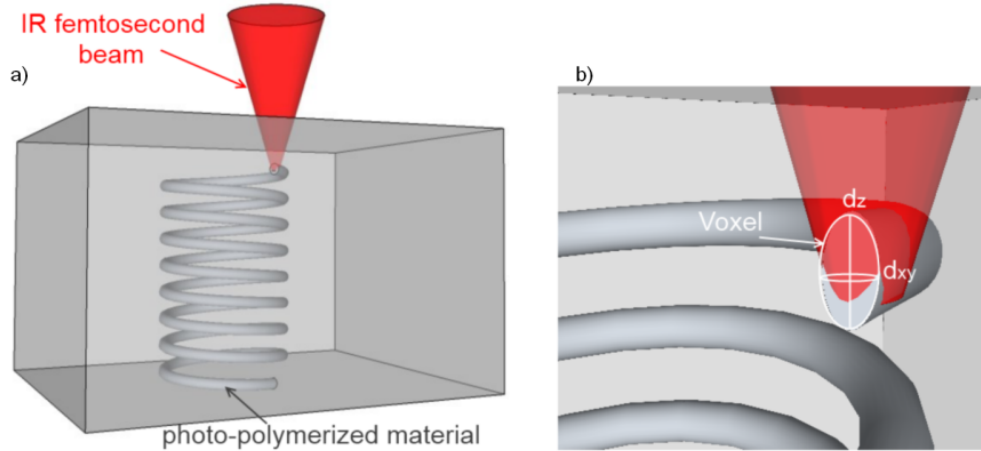


Figure 1.6: General concept of 3D printing two-photon polymerization. The area in which the laser power is high enough to initiate polymerization is known as the voxel. Typically ellipsoid in shape, the height d_z and cross-section d_{xy} of the voxel depend on laser power and beam focus. Adapted from [6], open source license under Creative Commons 3.0.

for immunophenotyping and in-situ culture [97]. Sitti et al. have proposed non-contact methods of magnetic manipulation using tiny, magnetic “robots” that can be moved at will with an external field [98, 99, 100, 19].

1.2.3 Two photon polymerization enables three-dimensional lithography

Two photon polymerization (TPP), also known as direct laser writing (DLW) is a recently commercialized tool for mask-free prototyping and fabrication of polymer structures [101, 102, 103]. In contrast to traditional, planar photolithography, TPP operates on the principle of two photon absorption to polymerize photoresist structures. Two photon polymerization uses a tightly focused, femtosecond pulsed laser spot that is scanned through a volume of unpolymerized thick film resist.

Within a small region at the focal point of the beam, the intensity is high enough for two photon absorption to occur. This phenomenon occurs in a non-linear fashion, with a specific energy threshold below which no polymerization occurs [20]. The non-linear nature



Figure 1.7: Miniature of the Brandenburg Gate, written by means of Nanoscribe's *Photonic Professional GT* system. © Nanoscribe. Image reprinted with permission [7].

of TPP makes it possible to write within a 3-dimensional volume without causing partial polymerization of the resist as the unfocused portion of the laser passes through the material.

Two-photon polymerization can achieve resolutions below 100 nm, and is rapidly being applied to overcome many of the limitations of traditional lithography. While the process is still less than a decade old, and widespread availability of TPP equipment remains a factor limiting its adoption, there are now commercially available options that allow researchers without extensive knowledge of optical physics to utilize TPP for their research. The future of lithography and microfluidics look extremely bright, and many exciting new technologies are just over the horizon.

2.0 TAILORING THE TRAJECTORY OF CELL ROLLING WITH CYTOTACTIC SURFACES

The work presented in this chapter is adapted from a peer reviewed publication from the journal *Langmuir* (Edington et al. 2011) [9].

2.1 INTRODUCTION

The ability to separate specific populations of cells from a heterogeneous sample is a fundamental requirement for studying cell biology. Medical diagnostics and cell-based therapies also rely on cell separation technologies to ensure safe and effective treatment. Since the 1970s, fluorescent activated cell sorting (FACS) has been the workhorse of cell separation techniques due to the high specificity, rapid separation, and wide range of commercially available fluorescent markers [104, 105]. While FACS has evolved considerably over the past 40 years to increase specificity, efficiency, and speed, it still remains an expensive and often timeconsuming process that relies on covalently bound or antibody conjugated markers to identify specific cell populations. As a result, the technique is not ideal for sensitive cell populations or applications where cell phenotype must be preserved. The additional cost and complexity of cell labeling also limits the use of FACS and similar techniques in point-of-care diagnostics. The limitations of label-based cell separation techniques have inspired the development of numerous label-free methods, many of which are based on microfluidic manipulation of cell solutions. These methods rely primarily on physical properties, such as dielectric charge, cell size, and autofluorescence to separate different populations [106, 107, 108, 109, 110, 111, 112]. However, many cell phenotypes are exclusively defined

by their expression of specific membrane proteins, rather than electrical or mechanical properties. There exists a need for a device capable of continuous, label-free separation of cells based on the expression of surface proteins.

By rationally tailoring the microenvironment of a cell, it may be possible to manipulate and characterize the cell without attaching ligands to its surface. As cells pass over surfaces, there is an opportunity to deliver signals to the cell from the surface that cause the cell to alter its behavior. Surfaces that can deliver a stimulus that directs cells toward or away from the surface are known as cytotactic surfaces. Indeed, in biology, such surfaces already exist. Following tissue injury, one of the earliest steps of the inflammatory response is the recruitment of white blood cells (leukocytes) from nearby vasculature. Leukocyte extravasation is initiated by the expression of cell adhesion molecules, including E- and P-selectin, on the surface of activated endothelial cells, which causes free floating leukocytes expressing P-selectin Glycoprotein Ligand-1 (PSGL-1) to adhere to the vessel walls and roll to the site of injury before escaping the blood vessel [113]. Selectin mediated rolling has been studied extensively,[113, 114, 115, 116, 117, 118, 119, 120, 121, 122, 123, 124, 125] and a number of attempts have been made to purify hematopoietic cells based on this unique interaction [126, 127, 128]. Some of these methods are based on differential rolling adhesion in one dimension or static adhesion, but they are not continuous and require careful collection of samples at specified time points.

A recent computational model reveals an improved method of adhesion-based separation by incorporating arrays of chemically and mechanically patterned surface features [129]. The model suggests that passive, label-free cell separation could be accomplished in a microfluidic package by utilizing smart surfaces to identify differences in cell surface ligands or cell membrane stiffness. The virtual surface utilizes angled stripes of variable stiffness or adhesiveness. As cells roll along the virtual surface under laminar flow, they can obtain a net displacement perpendicular to the direction of flow upon interacting with a diagonal stripe that has a higher adhesive interaction or lower modulus than the bulk material. This predicted displacement results from a change in shear forces as laminar flow pushes the capsule across each stripe, and is also a function of the capsules stiffness, meaning that two capsules with different compliances or adhesive properties will exhibit different amounts of

displacement, effectively sorting them. The capsule’s path is altered as it passes from the weakly adhesive bulk material to the “sticky” stripe, and after exposure to multiple stripes the compliant capsules gain displacement perpendicular to the direction of flow. The strain modeling and predicted paths of rolling cells are illustrated in Figures 2.1 and 2.2 [8].

Control of cell motion in two dimensions would allow for the physical segregation of interacting and noninteracting cells in a continuous manner, making such a sorting method attractive. Consequently, experimentally verifying and understanding this prediction is an important step toward the practical development of an adhesion based sorting device. Results from experimental manipulations of leukocytes appear to support the Balazs model, including the observation of lateral displacement on stripes of P-selectin and the absence of the effect in the case of rigid microspheres [130, 131]. Only the macroscopic behavior of cells in these systems has been investigated, and therefore, the data lack the necessary resolution to verify the model. In order to more fully understand cellular motion across patterned surfaces, we developed a system in which we could observe these interactions on a submicrometer scale. A mechanistic understanding of this effect would be important in the successful development of adhesion-based methods of cell sorting.

We designed a microfluidic device to study the directed rolling of cells using a cytotoxic surface of covalently immobilized P-selectin. We patterned this surface to the dimensions outlined in the Balazs model and observed the response of rolling HL-60 cells [132]. HL-60 cells are a human myeloid cell line expressing high levels of PSGL-1 that are commonly used in leukocyte rolling experiments [113, 115, 130, 132, 133]. The paths of the cells were recorded using a customized MATLAB tracking program and compared to the theoretical response predicted by the model. The device represents a foundation that can be adapted to any transiently binding cell/ligand combination. With improvements in micropatterning technology, cytotoxic microfluidic devices could be designed to screen for the presence of many different surface markers simultaneously, without the obligatory attachment of a potentially disruptive chemical tag to the cell. For the scope of this study, however, we are concerned primarily with characterizing the specific response of HL-60 cells to patterned stripes of P-selectin. The philosophy of this approach is outlined in Figure 2.3.

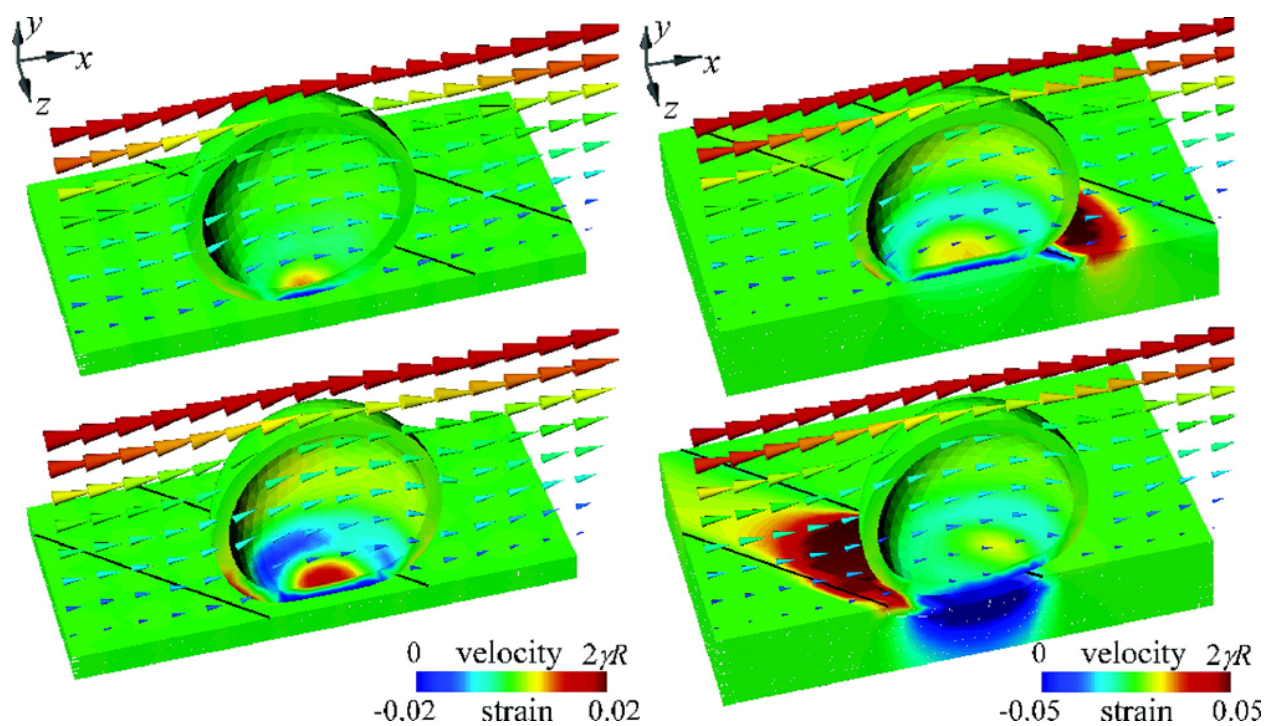


Figure 2.1: Modeling by Alexeev et al. indicates that chemically or mechanically patterned substrates (left and right respectively) with regions of sharply distinct adhesiveness can redirect rolling vesicles by generating asymmetrical strains that alter the energy landscape, leading to motion toward the centerline of the stripes and perpendicular to the direction of flow. Snapshots above show strain on a capsule and substrate as the capsule encounters sticky areas. Lines on the substrate indicate the boundary of an adhesive patch. Deformation of the capsule at the boundary enhance the contact area with the substrate. Adapted with permission from [8]. Copyright 2007 American Chemical Society.

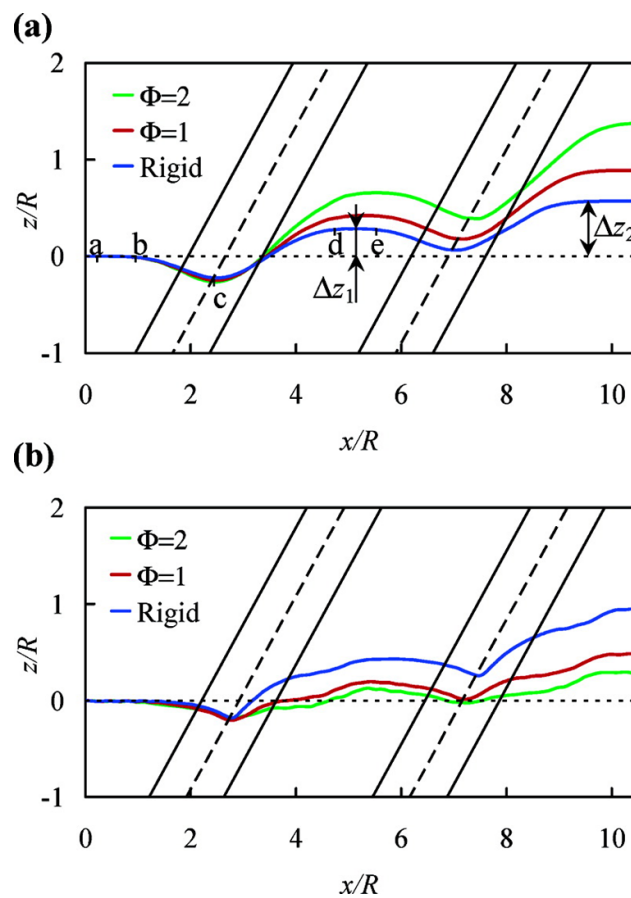


Figure 2.2: Predicted trajectories of the centers of mass for capsules of differing compliancy on (a) chemically and (b) mechanically patterned substrates. Stripe angle is 45° and rolling direction is left to right. Adapted with permission from [8]. Copyright 2007 American Chemical Society.

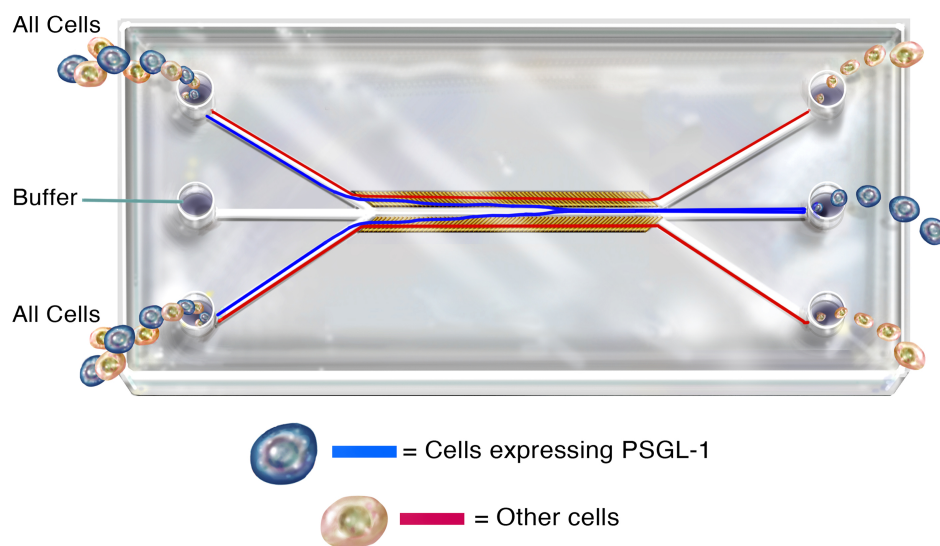


Figure 2.3: Artistic rendition of the microfluidic device used in this study. The device was designed with the capability to sort cells using patterned stripes of P-selectin, although sorting effectiveness has not yet been studied. Angled stripes on either side of the channel direct rolling cells (blue) toward the center pathway where they are collected as they exit the device. Cells that do not interact with the surface or do not express P-selectin glycoprotein ligand-1 (red) follow the direction of flow and exit through the two side channels. Reprinted with permission from [9]. Copyright 2011 American Chemical Society.

2.2 MATERIALS AND METHODS

2.2.1 Investigation of P-selectin activity and immobilization techniques using surface plasmon resonance

Direct observations of P-selectin immobilization and activity were performed using a Biacore T100 surface plasmon resonance (SPR) system, using methods partially adapted from Mehta et al. [1]. Protein immobilization experiments were performed on plain gold surfaces (Biacore SIA Au Kit, BR-1004-05). All immobilization steps were performed at flow rates of 5 $\mu\text{L}/\text{min}$ and kinetic assays were performed at 50 $\mu\text{L}/\text{min}$ unless otherwise noted. Gold sensor surfaces were modified with a carboxylic acid-functionalized thiol monolayer; 10 mM 11-mercaptoundecanoic acid (MUA, Sigma 674427) in ethanol, for 1 hour.

2.2.1.1 Direct amine coupling After assembling and loading the sensor chip into the SPR, 10 mM MES running buffer (2-(N-morpholino)ethanesulfonic acid) was used to stabilize the surface and establish a baseline. Freshly made activation solutions of 50 mM N-hydroxysuccinimide (NHS) and 200 mM N-ethyl-N'-(dimethylaminopropyl) carbodiimide (EDC) in DI water were then injected over the surface for 10 minutes to form NHS ester leaving groups. After a 60 second buffer rinse, 70 nM recombinant P-selectin Fc chimera (R&D Systems, 137-PS-050) in 10 mM pH 6 MES buffer was injected until a baseline shift of ~ 3500 RU was achieved (roughly 20 minutes). After rinsing, unreacted groups were capped with ethanolamine (1 M, pH 8 in water, 10 min reaction) to prevent non-specific binding to the analyte.

2.2.1.2 Streptavidin/Biotin coupling Sensor chips were prepared as described above, with 200 $\mu\text{g}/\text{mL}$ streptavidin (Sigma 4762) in 10 mM, pH 4.5 sodium acetate buffer used in place of P-selectin (6,00-8,000 RU). After capping with ethanolamine, the surface was reacted with biotinylated P-selectin (25 nM in PBS, 2 $\mu\text{L}/\text{min}$ flow rate). P-selectin was conjugated using a Pierce EZ-LinkTM Sulfo-NHS-LC-Biotinylation kit (Pierce 21435) according to the included instructions.

2.2.1.3 Fc/Protein A coupling Protein A (Pierce 21184) sensors were made in a similar fashion, with 2 μM protein A in 10 mM, pH 5 sodium acetate buffer. After rinsing and capping with ethanolamine, P-selectin (25 nM) was then injected, allowing the Fc-chimerized regions to bind to the protein A surface (3,500 RU).

2.2.1.4 Control surfaces In all three immobilization chemistries, control surfaces were run in parallel during kinetic tests to determine the background signal that should be subtracted from the experimental channel readings. Antibody control surfaces were immobilized with P-selectin in an identical fashion to the experimental regions, but were then blocked to saturation with 250 nM Human P-Selectin/CD62P Antibody (R&D Systems BBA30) to prevent PSGL-1 binding. Control data were adjusted for antibody drift by assuming equal signal gain for every RU of antibody lost. BSA control surfaces were also prepared by immobilizing BSA in place of P-selectin in the same manner as the experimental chamber, however direct amine coupling was also used for BSA controls in protein A experiments, as a BSA/Fc chimera was not readily available.

2.2.2 Kinetic assays

After P-selectin functionalization, surfaces were stabilized for 1 hour at flow rates of 50 $\mu\text{L}/\text{min}$, then overnight in standby mode to prevent signal drift. To evaluate the density and activity of surface-bound P-selectin, the binding response to PSGL-1 in solution was compared for each immobilization method. Serial dilutions of recombinant Human PSGL-1/CD162 Fc chimera (R&D Systems 3345-PS-050) in DPBS with calcium and magnesium (Sigma D8662) were prepared. Samples ranged from 32 nM to 3.2 μM in ten-fold increments, including a zero concentration control sample. PSGL-1 was perfused over experimental and control channels simultaneously at 50 $\mu\text{L}/\text{min}$ for 30 seconds, followed by running buffer. Bound PSGL-1 was removed by injection of 10 mM EDTA between samples.

2.2.3 Synthesis and fabrication of a rationally designed cytotactic surface

To generate a surface that could influence the direction in which cells rolled over it, we selected a foundation layer of glass upon which we could fabricate the necessary synthetic elements. Using the Balazs/Alexeev model to define the geometry, we designed a network of gold stripes on glass slides. Gold stripes were chosen in lieu of microcontact printing because they provided a substrate for the covalent immobilization of the P-selectin and provided greater visual contrast for image tracking purposes [131, 10]. The stripes were arranged in two rows along the sides of the fluid channel, with an unpatterned region in the middle. The individual stripes were 5 μm wide with a space of 10 μm between each stripe, and were angled at 45 with respect to the direction of flow in order to direct cells towards the center channel. A diagram of the fabrication procedure is shown in Figure 2.4.

A 4-inch polished glass wafer was patterned using image reversal of AZ5214-E photoresist (Microchemicals Inc.) and a bright field chrome photomask of the stripe pattern (Photo Sciences Inc). A sputtered titanium underlayer (5 nm) was subsequently coated with sputtered gold (20 nm) and the gold-striped glass wafer was then diced into individual units that would form the bottoms of the flow chambers. The quality of the patterned surface was characterized by scanning electron microscopy (SEM, FEI Sirion).

The sidewalls and ceiling of the fluid channels (1.2 mm wide by 10 mm long) were made from poly(dimethyl siloxane) (PDMS). A silicon mold for the PDMS top layer was prepared by traditional lithographic techniques and anisotropic reactive ion etching to a depth of 30 μm . After etching, the wafers were cleaned and treated with trichloro(1,1,2,2 perfluorooctyl)silane vapor to facilitate PDMS release from the mold. The polymer was made using a SYLGARD 184 silicone elastomer kit (Dow Corning Corporation). After combining the base and curing agent (10:1), the mixture was degassed under vacuum for 45 minutes. Degassed PDMS was poured evenly over the mold and allowed to cure overnight at room temperature, then baked at 70 C for 1 hour. After curing, the PDMS was cut into individual units and holes were punched at the inlets and outlets.

In order to achieve a strong mechanical seal and prevent leaks between the cytotactic surface and the chamber walls, the PDMS and glass were bonded using an oxygen plasma

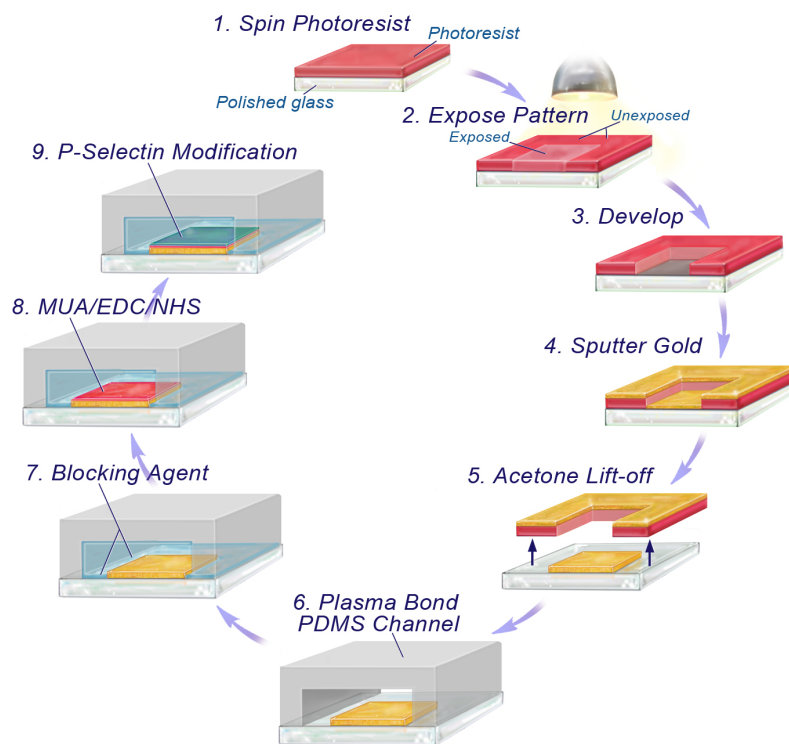


Figure 2.4: An overview of the process for fabricating the microfluidic cell sorter shown in Figure 2.3. Striped patterns are achieved by depositing gold using sputtering and a negative photoresist lift-off technique. Oxygen plasma bonding is then used to seal a PDMS channel to the glass substrate. After applying a fluorinated agent to block non-specific interactions, P-selectin is covalently attached to the gold stripes [10]. Reprinted with permission from [9]. Copyright 2011 American Chemical Society.

treatment.^{32,33} The layers were activated in a plasma barrel etcher (International Plasma Corporation, O₂ plasma, 18 sec, 50 W, 1 Torr). Following plasma activation, the layers were heated to 75 C for 5 minutes. They were then mounted in a Karl Sss MJB3 Contact Aligner and brought into light contact to initiate bonding.

A rational design of the cytotoxic surface requires that the non-biologically active part of the surface is inert. We therefore blocked the glass surface within one hour of plasma treatment using a 1% solution of (heptadecafluoro-1,1,2,2-tetrahydrodecyl)dimethyl-chlorosilane (Gelest, Inc.) in filtered acetonitrile. A micropipette was used to inject 10 μ L of blocking solution into the sealed chambers. After incubation at room temperature for 1 hour, chambers were rinsed repeatedly with acetonitrile and dried with nitrogen.

Our next step was to introduce the cytotoxic element onto the gold stripes by chemical modification.³¹ A 11-mercaptoundecanoic acid (MUA) solution was prepared by combining MUA (11 mg), pure ethanol (10 mL), and HCl (50 μ L). The solution was then filtered with a PTFE syringe filter and infused with argon gas for 10 minutes. MUA solution (10 μ L) was injected into the flow chambers and the tray holding the chambers was charged with argon and sealed. After incubation for 1 hour at room temperature the flow chambers were washed 3 times with ethanol and dried with nitrogen.

To prepare the MUA-modified gold stripes for attachment to a biomolecule, an EDC-NHS solution was prepared by combining N-(3-Dimethylaminopropyl)-N-ethylcarbodiimide hydrochloride (EDC, 20 mg) with N-Hydroxysuccinimide (NHS, 12 mg) in acetonitrile (10 mL). The EDC-NHS solution (10 μ L) was injected into the chambers using a micropipette. After incubating for 30 minutes at room temperature, the chambers were washed with acetonitrile and dried with nitrogen.

Finally a P-selectin solution was prepared by combining P-selectin stock solution (ADP3-200, R&D Systems, 10 μ L of 200 μ g/mL) with filtered Dulbeccos Phosphate Buffered Saline (DPBS, Fischer-Scientific BW17-512F, 90 μ L) for a final concentration of 20 μ g/mL of P-selectin. The chambers were injected with P-selectin (10 μ L) solution and incubated for 1 hour at room temperature. After incubation the chambers were rinsed repeatedly with DPBS and dried with nitrogen. After P-selectin modification, chambers were stored at 4 C until use.

P-selectin site density was determined using mouse anti-human P-selectin (R&D Systems, ADP3) followed by goat anti-mouse IgG-HRP (R&D Systems, HAF007) and a spectrophotometric assay. P-selectin density was determined to be 1300 molecules/ μm^2 . Additionally, the stability of P-selectin on gold-coated surfaces was tested in dry and wet (PBS) conditions. P-selectin activity decreased after 32 days of storage (4 °C) in dry and wet conditions by 25% and 70%, respectively.

P-selectin modification was verified by labeling with fluorescent polystyrene microbeads (0.5 μm diameter, Invitrogen F-8813) that were functionalized with human P-selectin mAb (R&D Systems, BBA30). Briefly, carboxylate modified polystyrene microspheres were incubated in a solution of EDCHCl (4 mg), NHS (2.2 mg) and DI water (1 mL) for 30 minutes. After rinsing with DI water, the microspheres were then incubated with human P-selectin mAb (100 $\mu\text{g}/\text{mL}$) reconstituted in phosphate buffer (10 mM, pH 8.5) for 1 hour before being washed with DPBS. A 1:9 solution of microspheres (15 mg/mL) and DPBS was injected into the flow chambers and incubated at room temperature for 1 hour, then rinsed with DPBS and dried with nitrogen. Fluorescence imaging was used to visualize the quality of the chemical modification.

2.2.4 Tracking and analysis of HL-60 cell rolling on a patterned surface

Human leukocyte cells (HL-60, ATCC #CCL-240) were cultured in polystyrene tissue culture flasks (DB Falcon, 75 cm²) under recommended ATCC conditions (37 °C, 5% CO₂) with a growth medium consisting of ATCC-formulated Isocoves Modified Dulbeccos Medium with 20% Fetal Bovine Serum. Cell concentration was maintained between 105-106 cells/mL.

Flow experiments were performed using a solution of PBS with 1 mM CaCl₂ and 1 mM MgCl₂. Consistent flow rates were achieved using a Harvard Apparatus PHD2000 infuser with 3 microsyringes (Hamilton Co. GASTIGHT #1802). In parallel with the microsyringes was a microinjector (Narishige, IM-9A) for manual infusion, flushing of the chambers, and introduction of cells. After priming the system with liquid, a small volume of cells (10-15 μL) was introduced to the lower inlet tube at a concentration of 1×10^5 cells/mL.

Images and videos were acquired using a Leica DM-IRB inverted microscope with a 40x objective, a Leica DFC480 C-mount 5 megapixel camera, and the Leica Application Suite (Ver. 3.3.0). A range of flow rates from 0.03 $\mu\text{L}/\text{min}$ to 0.24 $\mu\text{L}/\text{min}$ were evaluated. Fluid velocities and shear stress were calculated for each flow rate [134].

Tracking data were acquired from the recorded video segments using a custom, GUI-based MATLAB tracking software. The software estimates the background and subtracts it from each frame. Then, ring shaped templates of different sizes (Laplacian filters of varying standard deviation) are applied to the subtracted image to identify cells. A one-to-one assignment algorithm is then used to connect the detected cells across multiple frames for continuous tracking.

Before tracking, the software located the edges of the stripes to allow analysis of cell motion at four different regions: within stripes, within gaps, in the gap-to-stripe transition region, and in the stripe-to-gap transition region. Measuring motion in each of these regions provided the necessary resolution to compare experimental data to the model predictions. The necessary factor to convert pixels to distance was determined to be 0.5 microns/pixel. The frame rate was 10.0 frames per second, and was verified with a recording of a timed LED circuit board.

A more comprehensive discussion of the tracking software and improvements made after this work are given in the next chapter.

2.3 RESULTS

2.3.1 Investigating methods of P-selectin immobilization using SPR

Increased baseline response values indicated that P-selectin immobilization was successful for all 3 chemistries tested. Kinetic analysis of the binding response to PSGL-1 yielded dissociation constants ranging from 67.9 nM to 314.4 nM, which agree well with reported values ranging from 46 nM by Ushiyama et al. [135] to 334 nM by Mehta et al. [1]. We found that direct amine coupling resulted in the most consistent responses in both immobilization

and kinetic activity; most likely a result of the reduced number of steps and reagents required. Test chambers constructed using streptavidin/biotin and protein A/Fc methods were found to cause cell rolling, but results were not significantly different from those using amine coupling. Therefore all experimental rolling data shown below was collected using amine coupling of P-selectin.

2.3.2 Synthesis and fabrication of a rationally designed cytotactic surface

The Balazs model predicts that a glass surface with an appropriate array of bioactive stripes would alter the trajectory of cells rolling over it. As described above, we used sputtered gold deposition and custom designed masks to deposit a foundation for the attachment of a bioactive molecule. The physical dimensions of the resultant stripes were measured using a mechanical stylus profilometer. Stripe width was $6.6 \pm 0.2 \mu\text{m}$, spacing between stripes was $8.0 \pm 0.1 \mu\text{m}$, and vertical thickness of the gold was approximately 29 nm. Scanning electron microscopy was used to visualize the profile of the stripes and verify the accuracy of the gold patterning.

The glass surfaces were then bonded to PDMS channels using oxygen plasma as described above. Plasma bonding was performed prior to chemical immobilization of P-selectin to avoid the harmful effects of high-energy plasma on the deposited protein, and to ensure a strong, continuous seal around the channels and inlets. Once the sealed chamber was established, the blocking agent was applied through the inlet ports, followed by the chemical species necessary to immobilize P-selectin to the gold stripes.

To examine the effectiveness of chemical patterning, fluorescent polystyrene microspheres conjugated with anti-P-selectin mAb were exposed in flow to the surface. The data reveal that P-selectin was immobilized almost exclusively on the striped regions, with minimal non-specific binding when the blocking agent had been applied (Figure 2.6). Flow chambers without blocking agent showed much less contrast between stripes and bulk material.

Normalized Binding Response of PSGL-1 to Surface Bound P-selectin

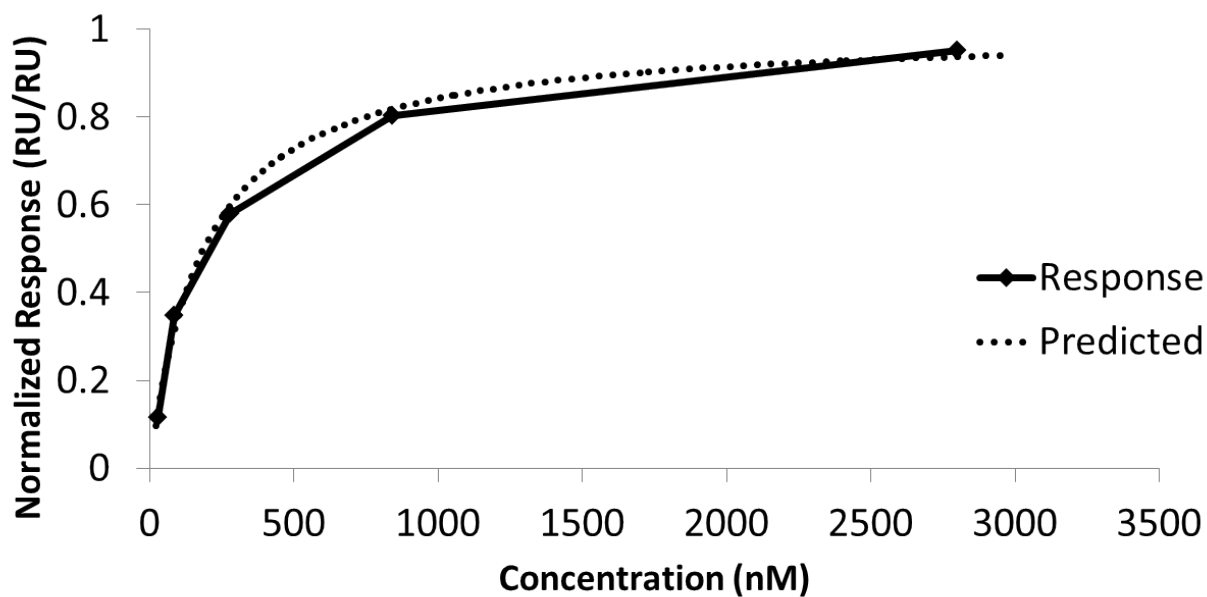


Figure 2.5: The normalized binding response of PSGL-1 to P-selectin covalently bound to the gold surface of a surface plasmon resonance sensor. Binding was performed with EDC/NHS chemistry (direct amine coupling), and nonlinear curve fitting was used to calculate the predicted response based on a 334 nM K_D from literature [1]. Calculated K_D was 314.4 nM.

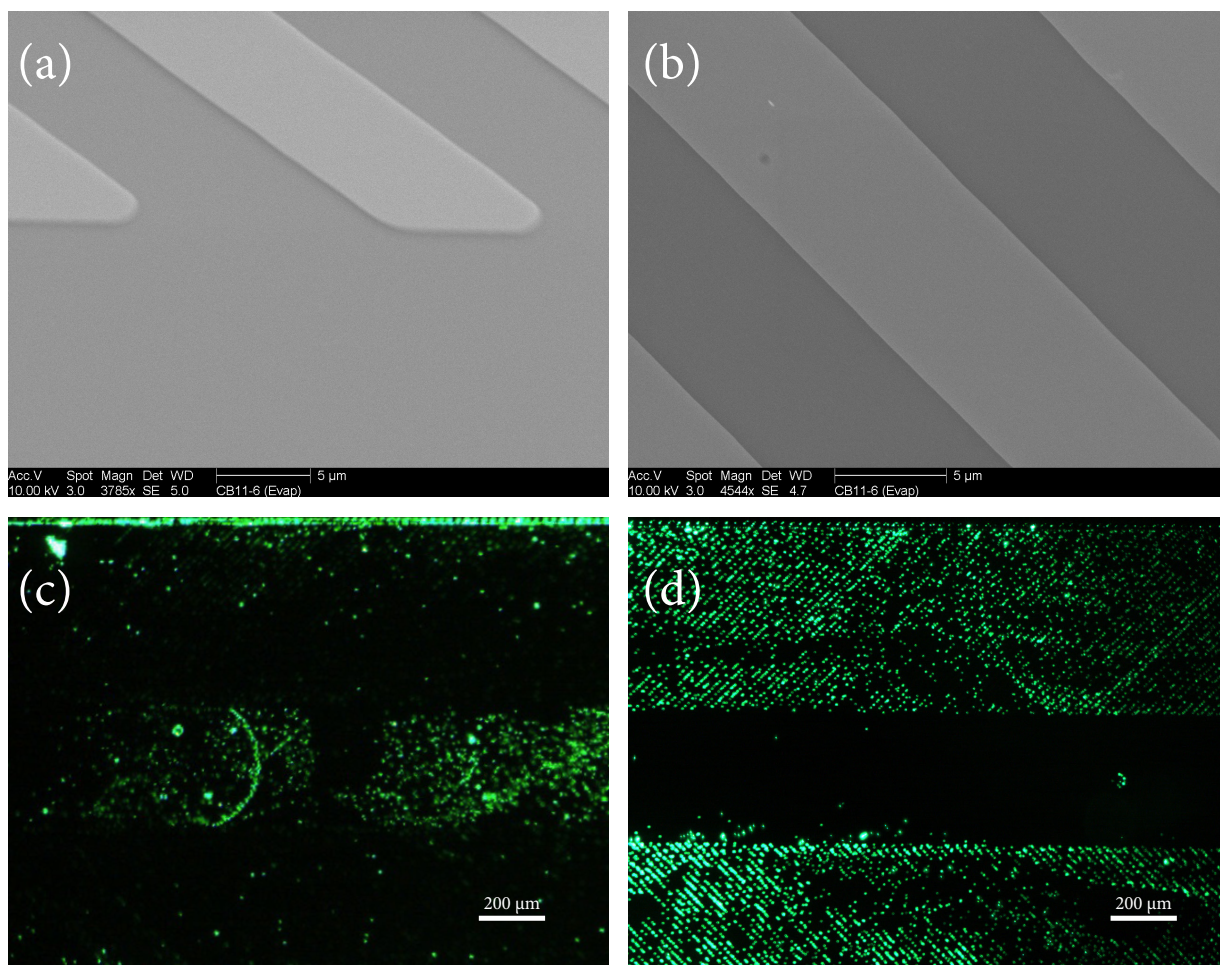


Figure 2.6: Characterization of the physical and chemical patterning of the cytotoxic surface. Scanning electron microscopy (a,b) shows that the stripes are patterned at a high resolution with well-defined edges. Control chambers (c) exhibit high amounts of nonspecific binding in the central channel. Chambers modified with blocking agent and P-selectin (d) demonstrated a significant reduction in nonspecific binding and visible patterning of the fluorescent microspheres, indicating that P-selectin was confined to the gold stripes. Reprinted with permission from [9]. Copyright 2011 American Chemical Society.

2.3.3 Tracking and analysis of HL-60 cell rolling on patterned surfaces

Previous studies in cell rolling have either normalized velocity for all cells or used velocity changes to differentiate between floating and rolling cells [122, 131]. In order to study individual interactions, however, a more precise approach was necessary. First, cells exhibiting velocities below 50% of the hydrodynamic velocity were identified using the tracking data. Cell paths were then manually examined for irregularities that might inhibit analysis. Any cells exhibiting permanent adhesion or paths perturbed by other cells were excluded. Cells exhibiting velocities consistent with the predicted hydrodynamic velocity were assumed to be non-interacting and were also excluded.

The fraction of all cells exhibiting cytotoxic interactions reaches a maximum when blocking agent and P-selectin are used concurrently (Figure 2.7). Cells interacting with multiple stripes were not observed in control chambers without P-selectin, and a higher frequency of stripe interactions was observed when blocking agent was used. Flow rate (within the range tested) did not have any significant effect on the frequency of interactions observed. The fraction of cells exhibiting permanent adhesion was about 23% in the blocking+P-selectin experiments. We found that incubation concentrations of P-selectin below 1-2 nM were insufficient to induce stable rolling of HL-60s. Concentrations above 36 nM no longer reduced the average rolling speed, indicating that all available sites on the substrate were populated, or that the surface concentration of P-selectin was dense enough to saturate all available PSGL-1 molecules at the cell/surface interface.

Detachment of HL-60 cells from P-selectin surfaces has been shown to be a random, history independent process that occurs when new adhesive bonds fail to form [131]. As a result, it can be difficult to determine precisely when and where a cell detaches from the surface, and behavior across any single stripe may not effectively capture the complete interaction. Therefore, we isolated paths in which cells interacted with at least 3 consecutive stripes, and averaged their motion over those specific stripes. An example of a cell exhibiting multiple interactions is shown in Figure 2.8 (a). An averaged path of multiple interacting cells is shown below exhibiting an average displacement of approximately 10% (Figure 2.8c, n=6 cells). The same form of analysis is shown for non-interacting cells from the same video file, demonstrating an absence of lateral displacement (Figure 2.8b/d, n=9 cells).

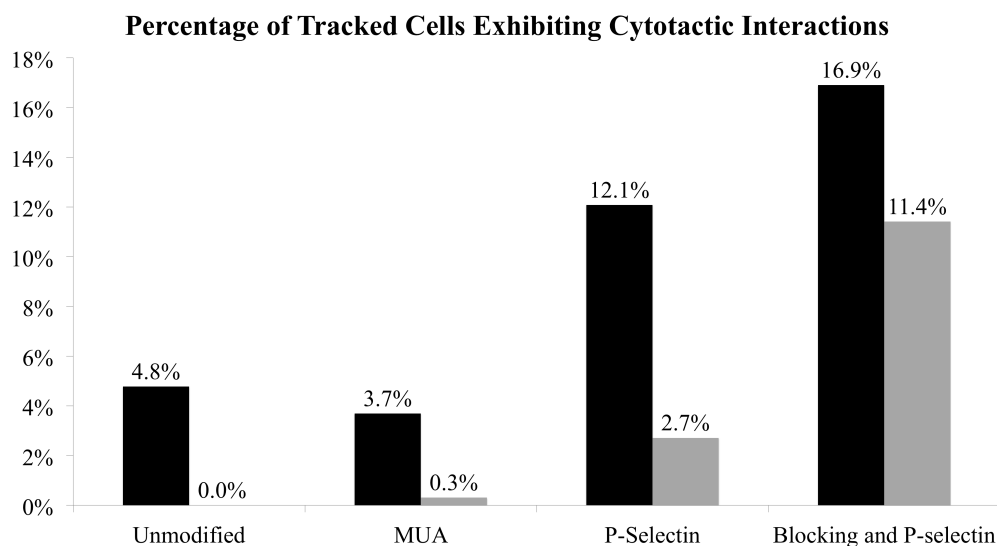


Figure 2.7: Percentage of cells exhibiting cytotactic behavior, defined as a velocity below 50% of the hydrodynamic velocity. Because many of the interacting cells only appeared to interact with a single stripe before detaching and becoming free-flowing, we also classified the subset of cells that interacted multiple times. The percentage of total cells exhibiting behavior indicative of a single cytotactic interaction (black) was higher in chambers modified with P-selectin. Chambers with blocking agent showed an increased likelihood of repeated interactions (gray). Almost no instances of multiple interactions were observed on chambers without P-selectin. (N = 3477 cells). Reprinted with permission from [9]. Copyright 2011 American Chemical Society.

For each cell included in Figure 2.8, the net vertical displacement was calculated as the difference between the starting and ending positions. An independent means t-test revealed that the average displacement of the interacting cells ($27.3 \pm 8.8 \mu\text{m}$) was significantly different ($p=0.001$) from that of the non-interacting cells ($2.7 \pm 2.8 \mu\text{m}$). The slight positive displacement of the interacting cells can easily be attributed to the marginal error of aligning the chambers manually under the microscope. Assuming that the slope of the chamber introduces an artificial displacement of 2.7 microns across the field of view (500 microns), we can estimate the actual displacement to be approximately 25 microns, or 5% displacement, across the entire length of the chamber.

2.4 DISCUSSION

The design of the microfluidic device was driven by a desire to observe, at high resolution, how cell motion is impacted by patterned surfaces. The data clearly demonstrated that not only do the average paths of interacting cells differ from those of non-interacting cells, but more importantly, cell motion entering, on, and leaving the patterned stripes bore remarkable similarities to the motions predicted by the Balazs model. The Balazs model predicts an initial downward motion as the cell enters an adhesive stripe. The path of cell #81 (expanded in Figure 2.8) provides a compelling example of such behavior in our microfluidic device. The repetition of this behavior on the same length scale as the stripes further verifies the successful patterning of the surface and the interaction of the cells with that surface.

The Balazs model next predicts a change in direction as the cell becomes localized within the stripe. Because the system was designed at sufficient resolution, we were able to observe this transition experimentally in almost every case where a cell was shown to be interacting with the surface. The final element of the Balazs model predicts the path that a cell would take as it exits an adhesive stripe. As shown in Figure 2.8, the data fit the model.

In addition to demonstrating the existence of a behavior analogous to the one described by the Balazs model, our observations also support the conclusions of a computational model by Chang et al., in which a state diagram was developed to predict the adhesive interactions

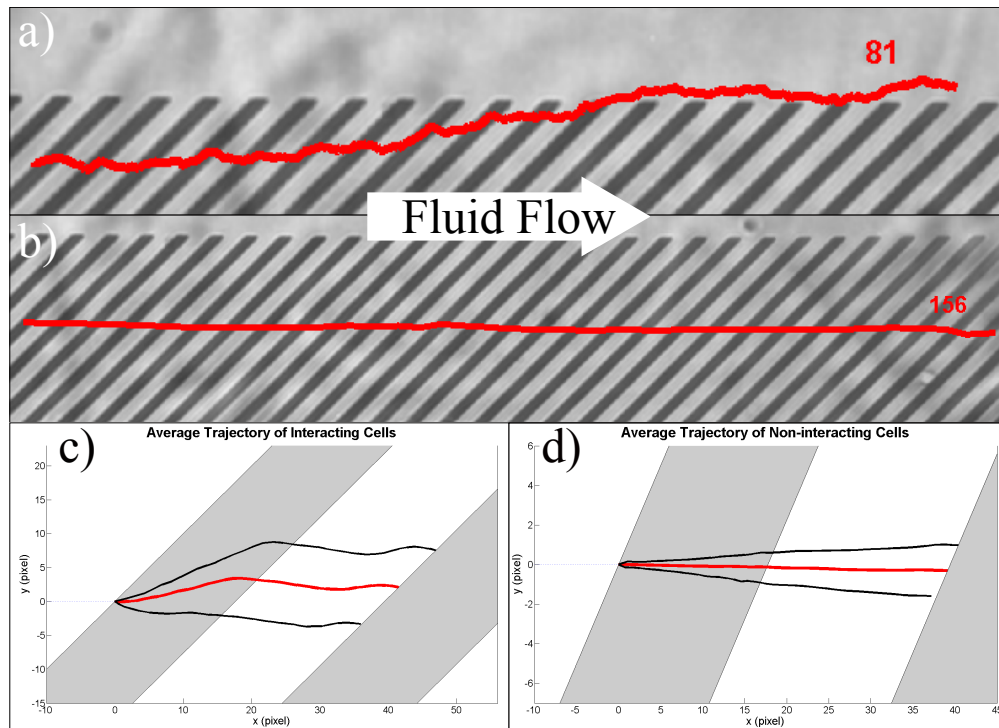


Figure 2.8: Behaviors of interacting and noninteracting cells were visibly different. A representative path of an interacting cell (a) and a noninteracting cell (b) are magnified to demonstrate the rolling behavior and direction of fluid flow (left to right), respectively. By combining the paths of multiple cells from a single video file, the average path they take over a single stripe can be plotted. The mean of this path is shown in red, with black lines representing one standard deviation from the mean. Average paths for interacting (c) and noninteracting (d) cells are shown ((c) $n = 6$ cells, 92 data points; (d) $n = 9$ cells, 96 data points). Reprinted with permission from [9]. Copyright 2011 American Chemical Society.

between leukocytes and surfaces expressing selectin molecules.[11] In the state diagram, the rolling behavior of cells is divided into five distinct states. Each state is characterized by a unique profile of displacement versus time, and is determined by the rate of shear, density of ligand-receptor pairs, dissociation rate, and bond interaction length. In addition to "firm adhesion" and "no adhesion", there exist three unique states of rolling adhesion, termed "fast adhesion", "transient adhesion", and "saltation". Over the range of shear rates tested by Chang et al. ($30\text{--}400\text{ s}^{-1}$), cell rolling only occurred within a particular region of the state diagram, demonstrating that leukocyte rolling requires a delicate balance between ligand density, shear stress, and dissociation rate.

We were able to identify representative paths for each state of adhesion, the profiles of which are shown next to their corresponding graphs from Chang et al. (Figure 2.9). These graphs represent the entire tracked path of a cell, and were not cropped to show only a portion of the path. The existence of all five states indicates that our experiments successfully captured a wide range of potential leukocyte behaviors within our shear stress range ($0.29\text{--}2.2\text{ dynes/cm}^2$). However, we were also able to observe more than one state of adhesion within each set of experimental parameters, indicating a considerable variability in the factors described above. The agreement between our observed data and the model proposed by Chang et al. support the view that our cytotoxic surface promotes leukocyte rolling.

In 2008, Karnik et al. observed the interaction of rolling HL-60 cells with a single patterned edge of P-selectin and a PEG-based blocking agent [130]. They found that rolling HL-60 cells were displaced orthogonal to the direction of flow when P-selectin edges were patterned at appropriate angles. A continuation of the 2008 study by the Karnik group recently suggested that patterned stripes may provide a label-free method of continuous cell separation [131]. The study was conducted under similar shear rates and P-selectin concentrations, but with larger stripe and chamber geometry, and at lower angles ($\leq 20^\circ$). Karnik also used micro-contact printing instead of covalent immobilization for P-selectin patterning. It was found that cell detachment was a random, history independent event, and that the rolling length could be modeled as a Poisson process. Additionally, Karnik found that edge inclination angle had a larger effect on cell displacement than P-selectin

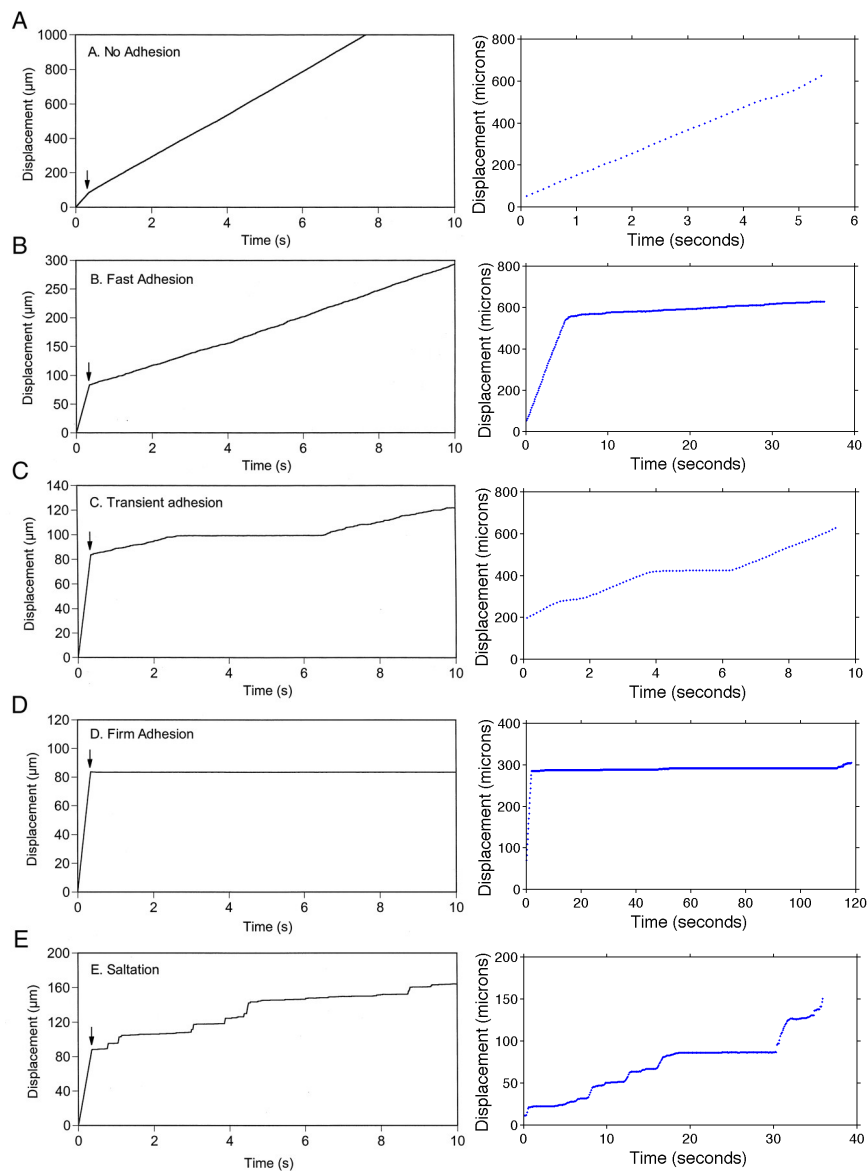


Figure 2.9: Plots of displacement versus time for the five states of adhesion identified by Chang (left) and sample plots of similar behavior identified in our cell tracking videos (right). The five states are no adhesion (a), fast adhesion (b), transient adhesion (c), firm adhesion (d), and saltation (e). These behaviors represent different dynamic states of adhesion mediated by the biophysical and kinetic properties of the system. Left figure copyright (2000) National Academy of Sciences, U.S.A. [11]. Reprinted with permission from [9]. Copyright 2011 American Chemical Society.

concentration (at low shear rates). Based on the displacements achieved, they predicted that a device on the length scale of 1 cm would be sufficient to sort a heterogeneous mixture of cells [131]. The study, however, did not utilize an experimental setup that was capable of sorting cells (GlycoTech parallel flow chambers, with only a single inlet and outlet, were used). Additionally, the fraction of cells interacting with the surface in their system was not reported. The microfluidic device that we describe herein will enable many of the limitations of first generation devices to be overcome. When our data are viewed at low resolution, our results parallel many of the findings from Lee and Karnik that show that patterned cytotoxic surfaces displace the paths of rolling cells.

Following our work, Choi et al. demonstrated sorting of HL-60 cells from K562 cells using a combination of chemical and mechanical patterning. They used indiscriminate P-selectin adsorption in combination with hydrophoresis to improve cell-surface interactions. By patterning large ridges on the channel floor, they altered the axial flow pattern to increase cell-substrate collisions. This approach yielded sorting efficiency up to 95% [136]. Soon thereafter, another publication from the same group showed sorting with a flat substrate that was chemically patterned using our procedure from above [137]. They used very long channel lengths to increase cell interactions by sedimentation. While this method was effective, achieving a 400,000-fold depletion of red blood cells from whole blood, it is also limited in throughput by the slow flow rates necessary to allow sedimentation to be used effectively. Even more recently, Wang and Alexeev et al. confirmed that mechanical patterning can also be used to sort cells by variations in their stiffness [12]. Figure 2.10 shows a schematic of stiffness based sorting, which yielded cell enrichment up to 6.3-fold with a throughput of 250 cells/sec. Choi et al. have also demonstrated that MSC differentiation state is correlated with rolling behavior on E-selectin [138], which may indicate that E-selectin plays a role in the recruitment of undifferentiated MSCs to areas of injury and inflammation. These publications further support the utility of smart surfaces as separation tools in microfluidic devices, but their limited efficiencies and throughputs suffer from the methods used to force cell interaction.

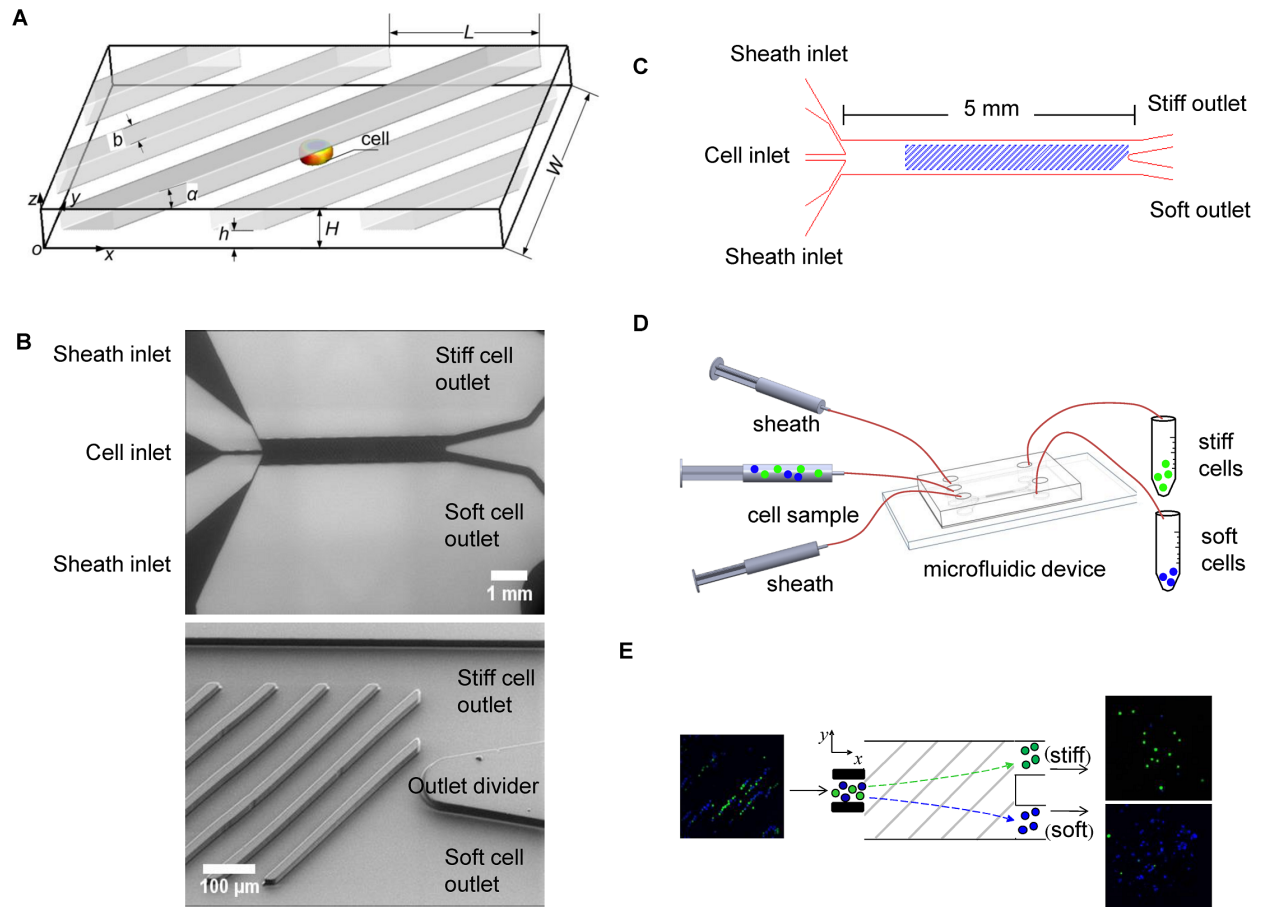


Figure 2.10: Schematic of a channel used for sorting cells based on membrane stiffness. The stripes patterned in the PDMS ceiling of the channel forced cells through a gap of height h that was varied depending on stiffness. SEM images and experimental setup are also shown. (E) shows sorting of untreated K562 cells (green) and $2 \mu\text{M}$ cytochalasin D softened K562 cells (blue). Adapted from [12], open access PLOS ONE.

2.5 CONCLUSION

In conclusion, we have demonstrated the ability of smart surfaces to instruct specific behaviors in cell populations. The behaviors observed under these experimental conditions supported the predictions of two independent models of ligand binding and patterned surface interaction, including the Balazs model, which had not been previously validated with in-vitro experimentation. By validating the predictions of this effect on chemically patterned surfaces, we have demonstrated the validity of the model and thus demonstrated its utility as a predictive tool. Hence, researchers can reliably use these predictions as guidelines for carrying out completely new experiments using chemically and mechanically patterned surfaces.

Because the motion of cells within our device can be predicted computationally, we are also in a position to rationally design improvements to the system, including physical and chemical changes to reduce permanent adhesions and increase the probability of cytotactic interactions. Presently the low rate of cytotactic interactions (<20%) is a limiting factor to the translation of this technique to practical application, but optimization of the channel geometry could yield significant improvements in efficiency. Reducing the channel height, recirculating unsorted cells, or introducing areas of turbulent flow to redistribute cells within the flow profile could all yield dramatic improvements in cell-surface interactions. More active approaches using electrokinetic forces might also be effective at increasing the local concentration of cells near a substrate.

The ability to direct cell motion within a microfluidic device is an important tool for advanced diagnostics and experimental methods. The patterned substrate evaluated herein represents a new addition to those existing methods of cell control and is unique in its advantages and capabilities. The facile, label-free identification of specific cell types could lead to a myriad of advances in laboratory and clinical techniques that require fast, inexpensive cell purification.

3.0 CELL TRACKING AND REGISTRATION

The work presented in this chapter is adapted from a publication currently in press at *IEEE Transactions on Biomedical Engineering* (Edington et al. 2014) [139].

3.1 INTRODUCTION

Fully understanding the interactions between living cells and their surroundings requires more than just a detailed knowledge of their anatomical composition. Direct observation is often necessary for researchers to investigate the cumulative, dynamic output of complex signaling and adhesion pathways. Experiments involving live cell imaging have been invaluable to advancing our understanding of cellular dynamics, but have been hindered by the painstaking nature of collecting and analyzing large sets of visual data.

Live-cell segmentation and tracking dates back to the 1970's when early computer-based methods of cell tracking were developed to automate the tedious process of following cell motion and morphology over extended periods of time [140]. Since then, automated cell tracking has become an important and sophisticated tool for measuring cell motility, building lineage trees, following neurite outgrowth, and a myriad of other applications [141, 142, 143, 144, 145].

The basic approach to cell tracking has not changed considerably over the past 40 years. A digital image is acquired, filtered, and modified to enhance the contrast between the cells and the image background. Based on predefined knowledge of what a cell should look like (shape, color, size, etc.), an algorithm is used to mathematically identify the locations of cells and record them in a data file. This detection routine is repeated for each frame, and

then a second algorithm is used to link the location of individual cells across multiple frames, building a record of their motion over time.

Despite 40 years of research, cell tracking is still a challenging problem that continues to nourish a growing field of study. Accurate, automated cell tracking is complicated by a number of factors, precluding a “one size fits all” solution. Some of these factors include:

- Background and foreground artifacts [146]
- Imaging modalities with a low signal to noise ratio [145]
- Moving frames of reference [147, 148]
- Low or inconsistent frame-rates [149]
- Variable lighting or exposure
- Dense cell crowding [149]
- Inconsistent cell morphology
- Cell mitosis or apoptosis [145]

A large number of new algorithms for detection, tracking, and background elimination have been proposed, each tailored to a particular use, or to overcome a particular weakness of its predecessors. Meijering *et al.* provide an excellent summary of the wide variety of methods being used for cell and particle tracking, and compare the commercial and open source tools currently available to researchers [150, 151]. Over half of these tools run on either the ImageJ or MATLAB platforms, while the other half are written predominantly in a windows-compatible programming language, such as C/C++. This divide is the result of the trade-off between speed and ease of use with compiled and interpreted languages. MATLAB is easier for prototyping new algorithms, as changes to the code are reflected in real-time as the program runs. C++ is much faster and more resource efficient when it comes to executing those algorithms. Further discussion of existing methods illuminates the work described herein.

3.1.1 Segmentation

In the first step of cell tracking, image transformations are applied to a captured frame, with the aim of increasing the signal to noise ratio until cells or particles can be reliably isolated

from the background. Thresholding is the simplest method of segmentation, and is most reliable in cases of high contrast between cells and background. As the experimental noise and variability increases, due to photobleaching, autofluorescence, poor contrast, etc., the methods of segmentation must become more complex to cope with these variations. Template matching is a popular segmentation method which fits predefined models or patches to the image data. This method is much more resilient to background artifacts, but fails when the shape or size of the cells changes dramatically. Watershed transformations and contour delimiting are slightly more intricate, but resistant to the morphology weaknesses of template matching. At the more complex end of the segmentation spectrum, deformable models can rely on both image information and prior shape information [151]. When choosing a segmentation method, researchers must weigh the complexity and reliability of a particular approach to its flexibility. It is generally advisable to identify the simplest algorithm that provides suitable results.

3.1.2 Linking

Knowing the locations of cells in a given frame is of limited value if they cannot be joined with past and future locations. Connecting cells across multiple frames enables the construction of a spatio-temporal pathway, and is crucial for inferring meaningful conclusions about cell behavior. As with segmentation, linking methods fall along a spectrum of complexity that is governed by the experimental needs of each particular study. Nearest-neighbor linking is the most basic approach, and simply assigns new observations to the most proximate locations from the previous frame. Nearest-neighbor linking only works well when cell density is low, and the frame-to-frame displacement (instantaneous velocity) is considerably less than 50% of the average nearest-neighbor distance [152]. When cells or particles split, merge, disappear, or otherwise introduce ambiguities that nearest-neighbor linking cannot resolve, global linking methods yield more consistent results [150]. Global methods such as spatiotemporal tracing [153], graph-based optimization [149], and Bayesian estimation [154, 155] have been explored in recent years, and are often combined with Kalman filtering [156] or more advanced motion models [143] to smooth trajectories and predict locations

during gaps in observation. As with segmentation, more complicated linking strategies are sometimes more difficult to adapt to new situations.

3.1.3 Cell rolling

One of the main driving forces for the development tracking applications has been the study of cell rolling. A number of myeloid cell types, including macrophages and neutrophils, exhibit rolling behavior on the surface of activated endothelium. When an inflammatory response is triggered, endothelial cells will express selectin family adhesion molecules (E-, P-, and L-selectin). Leukocytic cells constitutively display ligands for selectins, and will adhere and roll along selectin coated blood vessels. Rolling slows the cells to a fraction of the hydrodynamic velocity, allowing other adhesion molecules such as ICAM-1, ICAM-2, and VCAM-1 to arrest cell motion and continue the process of extravasation [157, 54].

Cell rolling has been studied with great interest since the identification of the selectin molecules in the late 1980's [158]. Investigating the physical and molecular basis of transient adhesion pathways has provided valuable insight into the inflammatory response. For example, Sawaya *et al.* identified P-selectin as a therapeutic target for reducing damage to transplanted livers during ischemia/reperfusion [159]. P-selectin KO mice, and those treated with blocking antibodies to P-selectin, demonstrated improved survival rates following liver transplantation. P-selectin is also thought to play an important role in tumor growth and metastasis. The production of selectin-binding tumor mucins has been independently correlated with the metastatic progression of epithelial carcinomas, and P-selectin deficient mice show reduced metastatic seeding and growth of subcutaneous implants of human colon carcinoma cells [160].

With the importance of cell rolling in mind, Alexeev *et al.* predicted that micro-scale patterns of transient adhesion molecules could be used to direct cell rolling perpendicular to the direction of flow [8]. Their model was concurrently investigated and independently verified by our group [161] and Lee *et al.* [162]. Some practical applications of patterned substrate microfluidics include leukocyte enrichment, inflammatory drug screening tools, and diagnostic tests for tumor metastatic potential [137, 160]. The model, however, is not lim-

ited to the selectin family of adhesion molecules, and may hold for any transient adhesion molecules with kinetic parameters within a target range [163]. During our studies, we recognized the need for a tracking program tailored to this particular type of flow experiment. With no commercially available product that met our needs, we decided to develop a custom solution. Even though the code was written with a particular set of experimental needs in mind, great effort was made to design the package in such a way that it could be easily modified for new applications.

3.2 METHODS

3.2.1 Microfluidic channel fabrication

The tracking program was used to collect data on cell motion within custom made microfluidic devices, similar to those previously described [161]. Briefly, the device consisted of a glass bottomed chamber with a polydimethylsiloxane (PDMS) top to form the fluid channels. The glass substrate was patterned with gold stripes, which were sputter-deposited using conventional photolithographic techniques. The gold features allowed us to target protein attachment using carboxylate terminated thiols that self-assemble into a dense monolayer on the gold surface. Areas without gold were blocked using a fluorinated silane to reduce protein adsorption. The cell adhesion protein P-selectin was chosen because it is well characterized and frequently used in cell rolling studies [54, 164, 165, 162, 161]. Fc-chimeric P-selectin was covalently linked to the carboxyl end groups of the thiol monolayer using 1-Ethyl-3-(3-dimethylaminopropyl)carbodiimide (EDC) and N-hydroxysuccinimide (NHS). EDC/NHS coupling generated an ester-linked leaving group at the carboxyl group, which was then replaced by covalent attachment to primary amines on the lysine side chains of the protein. The microfluidic chamber was secured in a custom microscope stage and perfused with human promyeloblast leukocytes (HL-60, ATCC) resuspended in PBS containing Ca^{2+} and Mg^{2+} (selectin binding is calcium dependent). Flow rates were controlled using a syringe pump, and shear rates were calculated from flow rate and channel dimensions.

3.2.2 Equipment

All experiments were performed on a desktop computer with an Intel Core i7 2600K processor (3.4 GHz), 16 Gb of DDR3 RAM, and two GeForce GTX 570HD graphics cards. Data could either be analyzed in real-time, or recorded to a solid state drive during experiments, then offloaded to a hard disk drive for storage and offline analysis. A Leica DFC 480 (5.0 megapixels) microscope camera was used to capture images (at a resolution of 1280 x 960 pixels) over a Firewire 400 connection at 10.0 FPS and 20x magnification.

3.2.3 Software overview

Our tracking software was originally written entirely in MATLAB to allow rapid development and easy debugging. The flexibility gained by using an interpreted language such as MATLAB, however, is offset by its lack of speed and efficiency. One of the main goals in developing the software described herein was to enable real-time tracking on the order of 10-30 frames per second. In order to reach this goal using only commercially available PC components, it was necessary to rewrite some portions of the program in C++. Figure 3.1 describes the structure of the tracking software, with major components indicated in bold, and arrows describing the flow of information from one subroutine to another.

3.2.4 Background removal

In order to identify the outlines of cells in each image, static elements of the background must first be identified and subtracted from the incoming information. In offline mode, this is accomplished by averaging the entire image set to generate a mean background image. The OpenCV accumulator() function is used to sum the image set, and is then divided by the total number of frames. In real-time mode, background subtraction is only performed using the first frame, because tracking must begin immediately. While theoretically more prone to errors, this method has provided more than acceptable results in practice.

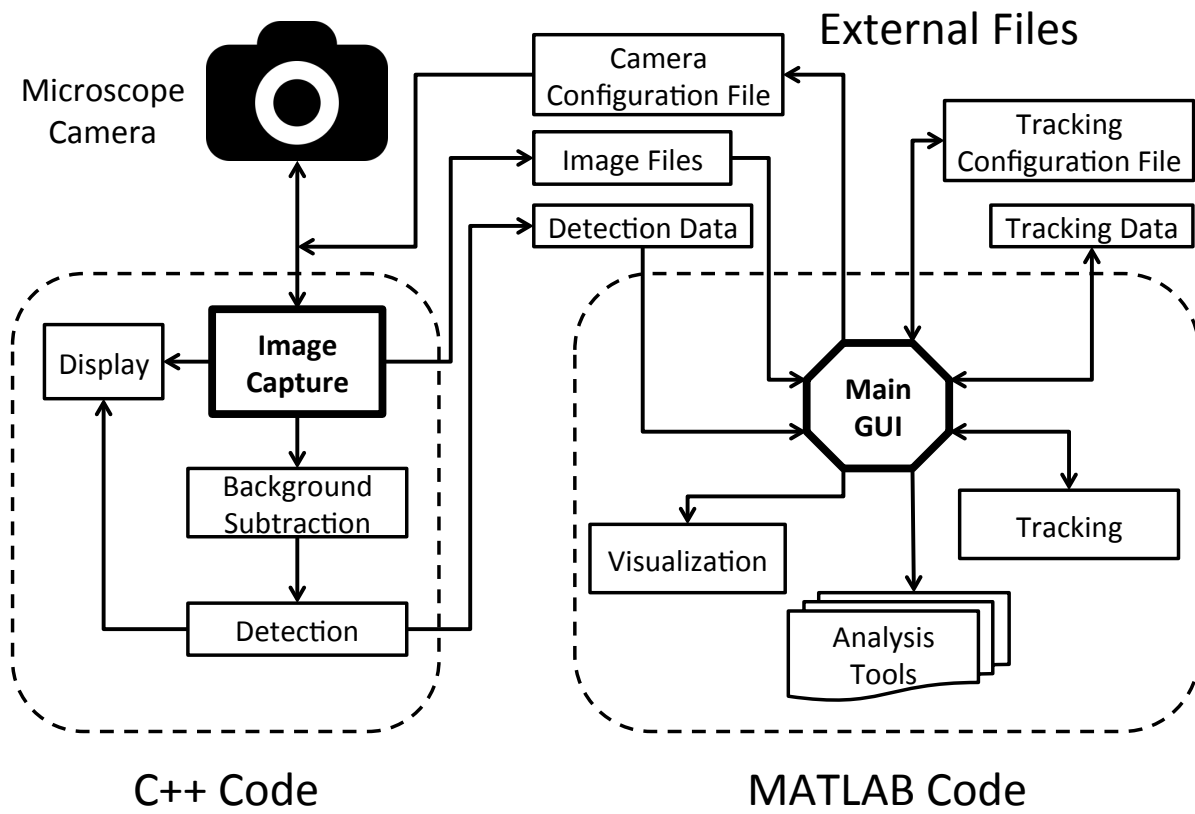


Figure 3.1: Flowchart of the different components of the tracking program, with subroutines grouped by language. Arrows indicate the flow of information, and main processes are bolded.

3.2.5 Cell detection

To rapidly identify all cells in a given image, a series of circular and ring shaped filters are generated from the configuration file, which provides user defined values for minimum and maximum cell radius (in pixels), grayscale thresholds, and acceptable noise levels. The ring filters are generated by creating matrices of appropriate size for all integer values between the minimum and maximum radius. Each matrix undergoes a distance transformation, followed by binary thresholding to create a binary ring with a thickness equal to 30% of its radius. This ring represents an approximation of the dark outline around a cell when viewed with a phase contrast microscope. The matrices containing the ring filters are then loaded into the GPU memory, where they can be quickly accessed for parallel template matching. The detection program takes advantage of the built-in *matchTemplate()* function in OpenCV, and implements the `CV_TM_CCORR_NORMED` method of comparison. This algorithm finds the normalized cross correlation between the template ring filters and a section of the source image.

$$R(x, y) = \frac{\sum_{x',y'} (T(x', y') \cdot I'(x + x', y + y'))}{\sqrt{\sum_{x',y'} T(x', y')^2 \cdot \sum_{x',y'} I(x + x', y + y')^2}} \quad (3.1)$$

Normalization reduces errors caused by variations in lighting or exposure, and is typically more robust than regular cross correlation. In Equation 3.1, R represents the result matrix, which contains a “score” for each point on the image. The score indicates the similarity between the source image I and the template T . Local maxima indicate the most likely locations of template matches. The summation is performed over the width and height of template ($x' = 0 \dots w - 1, y' = 0 \dots h - 1$) as it is translated across the target image. Once a score matrix has been generated for each ring filter, local maxima above the user defined threshold are identified and saved to a data file as an (x,y) location, cell radius, and value (from 0 to 1) of the score at that location.

3.2.6 Cell tracking

Temporal linking of successive cell candidates is performed by a global nearest neighbor association technique, which uses a scoremap to identify the most likely cell candidates to connect to existing cell tracks. During real-time mode, the tracking routine will load data files as they are created by the detection program. After loading the information about the potential cell candidates, the tracking program will then attempt to fit those observations to the list of existing cell tracks. Candidates that are not matched will either initiate new tracks, or be discarded if they are determined to be anomalous.

In order to determine which track each cell belongs to, there must be a quantitative method of scoring how likely each cell is to belong to each track. The region around a given cell that is subject to scoring is determined by a gating size G_s . Gate size is a user defined variable (in pixels) that is multiplied by a weighting factor W from 0.2–1 as a function of the angle θ between the previous location and the current location. This creates a “bubble”, resembling the reflection of a nautilus spiral, around each cell (Figure 3.2). Beyond this region all scores are given a value of $-\infty$. Because the region is non-circular, and is weighted by angle, it gives higher preference to locations immediately in front of the previous track (to the right, positive x-direction), and scales back to a minimum immediately behind the track (to the left, negative x-direction). The angled weighting factor allows us to take advantage of the *a-priori* knowledge of flow direction to reduce tracking errors. For applications in which fluid flow is not left-to-right, this weighting can be adjusted by modifying the MATLAB script that calculates the association matrix.

$$S = \begin{cases} -\infty & \text{if } d^2 > G_s^2 + \Delta G_i \\ & \text{or } d^2 > G_s^2 W \\ G_s^2 + \Delta G_i - d^2 - \alpha R_{ij} & \text{otherwise} \end{cases} \quad (3.2)$$

$$W = 1 - \frac{(1 - 0.2)\theta}{180} \quad (3.3)$$

$$\Delta G_i = 2 \ln((1 - p_d)^{n_u}) \quad (3.4)$$

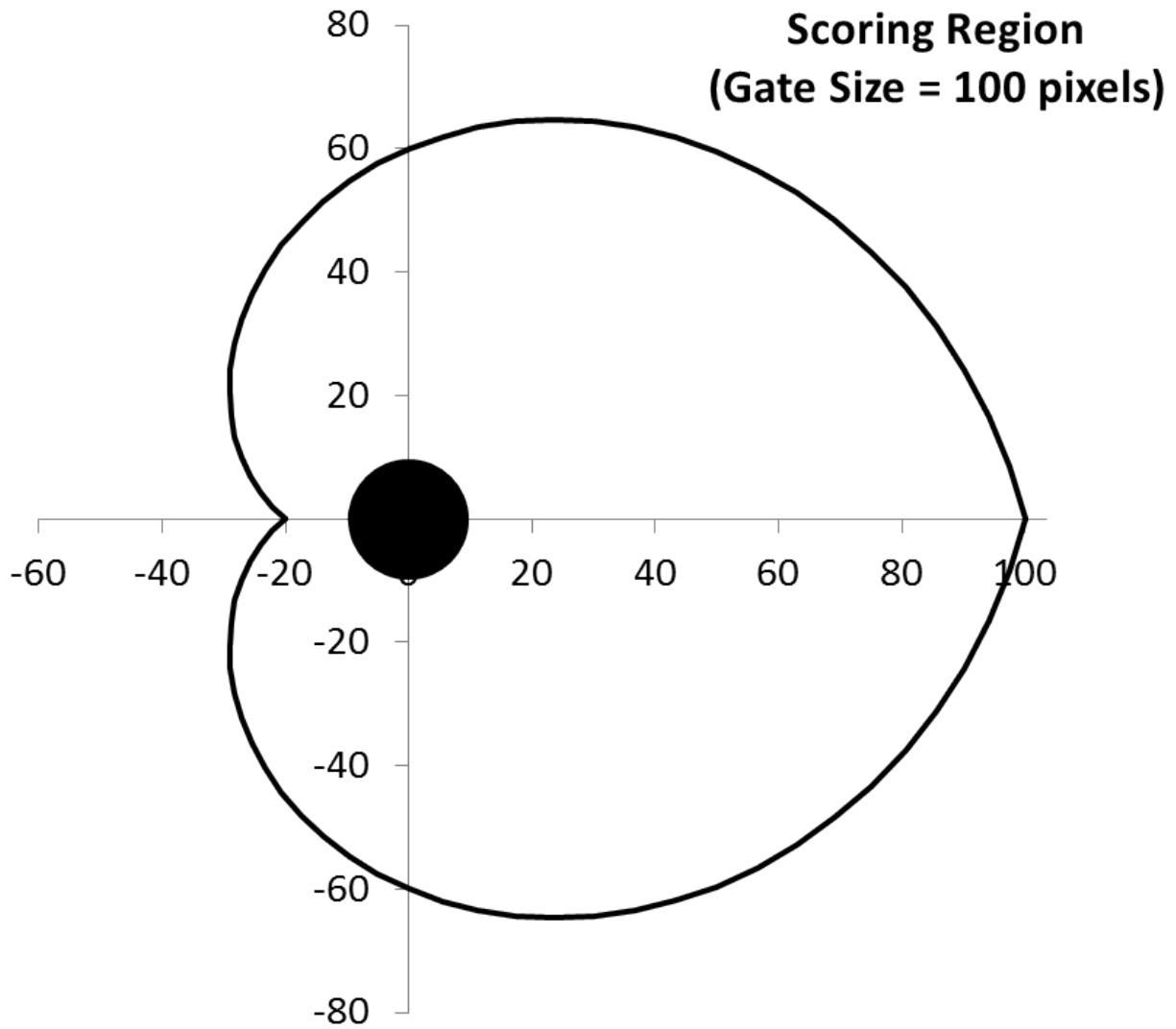


Figure 3.2: Scoring region around a cell located at index $(x, y) = (0, 0)$, giving preference to cells moving from left to right with the direction of fluid flow. Units for both axes are in pixels.

The score (Equation 3.2) is determined based on the gate size, detection probability, distance, radius mismatch, and consecutive missed frames. The gate size, G_s is a user-determined variable, while ΔG_i is a function of the detection probability p_d and the number of consecutive missed frames, n_u , as shown in Equation 3.4. The detection probability can be modified in the code, but is typically set to 0.9 to indicate that we desire a 90% certainty of detection. Increasing p_d or n_u reduces ΔG_i , lowering the overall score and making selection of cell candidates more strict. This means that a cell candidate is more likely to be assigned to a track that has fewer missing frames, all other factors being equal. The score also diminishes with the square of the distance between the current and previous location, as well as with the mismatch in cell radius from one frame to the next. R_{ij} is the square of the difference between the current and previous cell radii, and α is a weighting factor applied to R_{ij} . In summary, the scoring system prioritizes matching new cell candidates with existing tracks that have similar radii, fewer missing data points, and are physically closer. This is similar to the nearest neighbor linking method, but utilizes global attributes such as prior cell radius and number of missed frames to reduce errors (hence ‘Global Nearest-Neighbor Association’).

After the scoremap is computed, the observations from the current frame are assigned to existing tracks using the built in “assignmentOptimal()” function, which is based on the Munkres (aka Hungarian) algorithm for minimal cost assignment [166]. Preference is given to confirmed tracks before assignment to tentative tracks is performed, reducing the likelihood of premature termination of an established track. Once observations in the scoremap have been assigned to confirmed and tentative tracks, any unaccounted observations are used to create a new tentative track. We were able to further reduce any accidental new tracks by limiting the final assignment step to observations with x-values less than 100 pixels, so that only cells entering from the left-hand side of the screen could generate new tracks.

3.2.7 Analysis tools

Once data collection is complete, there are a number of built-in tools that we designed to simplify the process of analyzing large volumes of tracking information. Figure 3.3 shows the

tracking interface with a sample video and tracking file loaded. The home interface displays the video file in the center of the window, with menu options along the top and a selection pane on the right-hand side. The top of the selection pane allows the user to load or delete tracking files, which can be useful for comparing the tracking results obtained from different threshold parameters. The lower half of the selection pane displays a numbered list of all cells in the tracking data file. Here, the user can select or deselect individual cells. Only selected cells have their tracks overlaid on the video file, and any analyses performed by the software will use only the current selection.

By modifying a threshold value under the *Parameters* menu, the user can automatically select subpopulations of cells with a net lateral displacement above, below, or within that parameter. For example, if the parameter is set to 20, the “Lat Disp” buttons above the track list will automatically select cells with a start-to-end lateral displacement above 20 μm , below -20 μm , or within $\pm 20 \mu\text{m}$. Custom selections of cell tracks can be saved as a new tracking file to make it easy for a researcher to return to a list of cells of particular interest.

Under the *Analysis* menu, a number of our custom made analysis tools can be found, including plotting tools, speed and displacement statistics, and a tool to show the average trajectory of one or more cells in relation to the patterned stripes. Detailed descriptions of the analysis tools are found with accompanying figures in the results section.

3.3 RESULTS

3.3.1 Performance evaluation

To evaluate the differences between automatically and manually derived tracking data, 14 cells were tracked for 150 frames, or until each cell was no longer visible. Manual tracking was performed three times, each by a different volunteer. Cell X and Y position was compared to the automatic tracking for each frame, and the root mean squared error (RMSE) for each track was found using Equation 3.5. The RMSE of two data sets, A and B (each of length n), is the standard deviation of the residuals between the two groups. This method has been applied to tracking validation in similar studies [148].

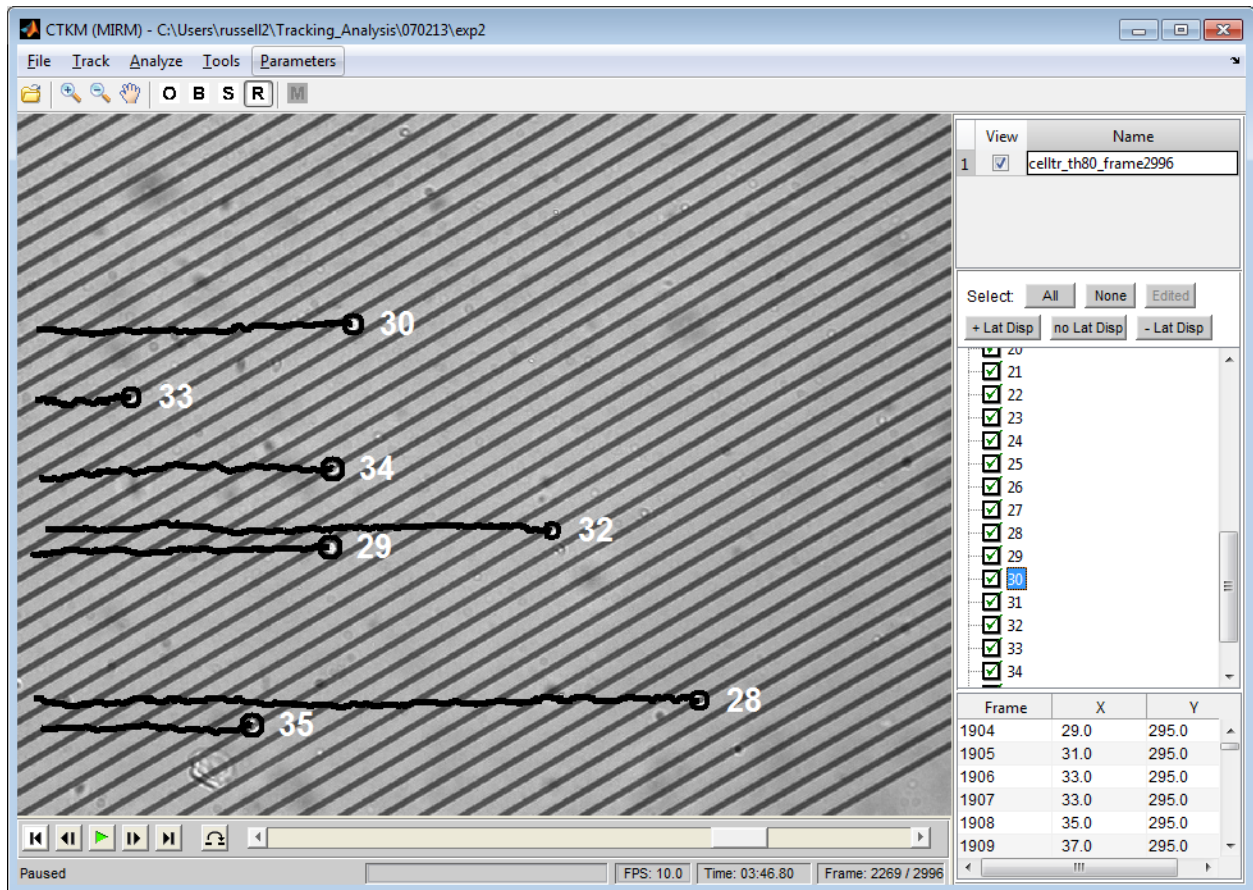


Figure 3.3: Screenshot of the tracking and analysis interface, with cell number and path overlaid onto the video file, selection tools (right-hand column), and analysis tools (top menus). Cell tracks and labels have been enhanced for readability.

$$\sqrt{\frac{\sum_{t=1}^n (A_t - B_t)^2}{n}} \quad (3.5)$$

Automatically tracked data were exported directly from the MATLAB matrices used to store them during analysis, while manual tracking was conducted using the “Manual Tracking” plugin for ImageJ, obtained from the NIH ImageJ website [167]. All data collection and analyses were performed in pixels to avoid cumulative rounding errors, and final values were converted to micrometers using a conversion factor of 1.856 pixels/micrometer. The conversion factor was calculated with ImageJ, using a scale bar image taken at the same objective and resolution as the experimental data.

The validation results shown in Table 3.1 indicate a close agreement between manual and automated tracking data. The X and Y RMSE remained significantly lower than the cell radius across all participants.

3.3.2 Analysis tools

3.3.2.1 Plotting motion All cell paths for a given video can be plotted over the background image, with multi-colored paths for easy visualization (Figure 3.4). We found that this view is the most useful for quickly identifying interesting cell behavior, flow profiles around debris, and areas of high cell concentration. Another visualization method, which we call lateral displacement, plots all cell trajectories from a common starting point to highlight their deviation from the straight-line path that would be expected for non-adherent cells (Figure 3.5).

3.3.2.2 Speed histogram A histogram of cell speeds can be quickly generated from a selection, showing the distribution of instantaneous (frame-to-frame) cell velocity for a given experiment. This particular function was designed to help us estimate the average height of the cells within a channel of known dimensions. Well-mixed cells would be expected to have a normal distribution, with faster cells at the center of the channel, and slower cells near the walls.

Table 3.1: Correlation of automatic and manual position data. Values are the root mean squared error (RMSE), in micrometers, between each participant’s observation and the automated tracking location of the cell. All participants were given the same 150 frame sequence and asked to track all visible cells until they left the field of view. X and Y coordinates were compared separately to demonstrate the isotropy of the RMSE.

Cell	Participant 1		Participant 2		Participant 3	
	X	Y	X	Y	X	Y
1	3.94	0.89	2.84	2.05	0.21	0.84
2	4.39	2.28	1.14	1.94	2.64	4.22
3	4.48	0.87	3.48	0.84	1.94	0.57
4	5.98	2.77	4.71	3.96	1.45	2.38
5	2.63	3.12	1.32	4.00	1.94	0.40
6	2.99	0.92	0.09	0.48	1.14	3.56
7	0.52	1.03	3.54	1.81	0.17	1.12
8	0.74	3.03	0.00	3.43	0.26	1.58
9	4.57	2.77	1.45	2.42	0.75	0.35
10	1.14	3.43	4.05	4.31	0.92	0.62
11	5.41	3.21	0.84	0.18	2.38	1.63
12	2.94	2.28	1.63	5.46	0.70	1.45
13	1.57	1.01	2.13	2.36	1.12	0.11
14	1.16	2.01	2.02	0.30	4.95	0.50
Mean	3.04	2.12	2.09	2.40	1.47	1.38

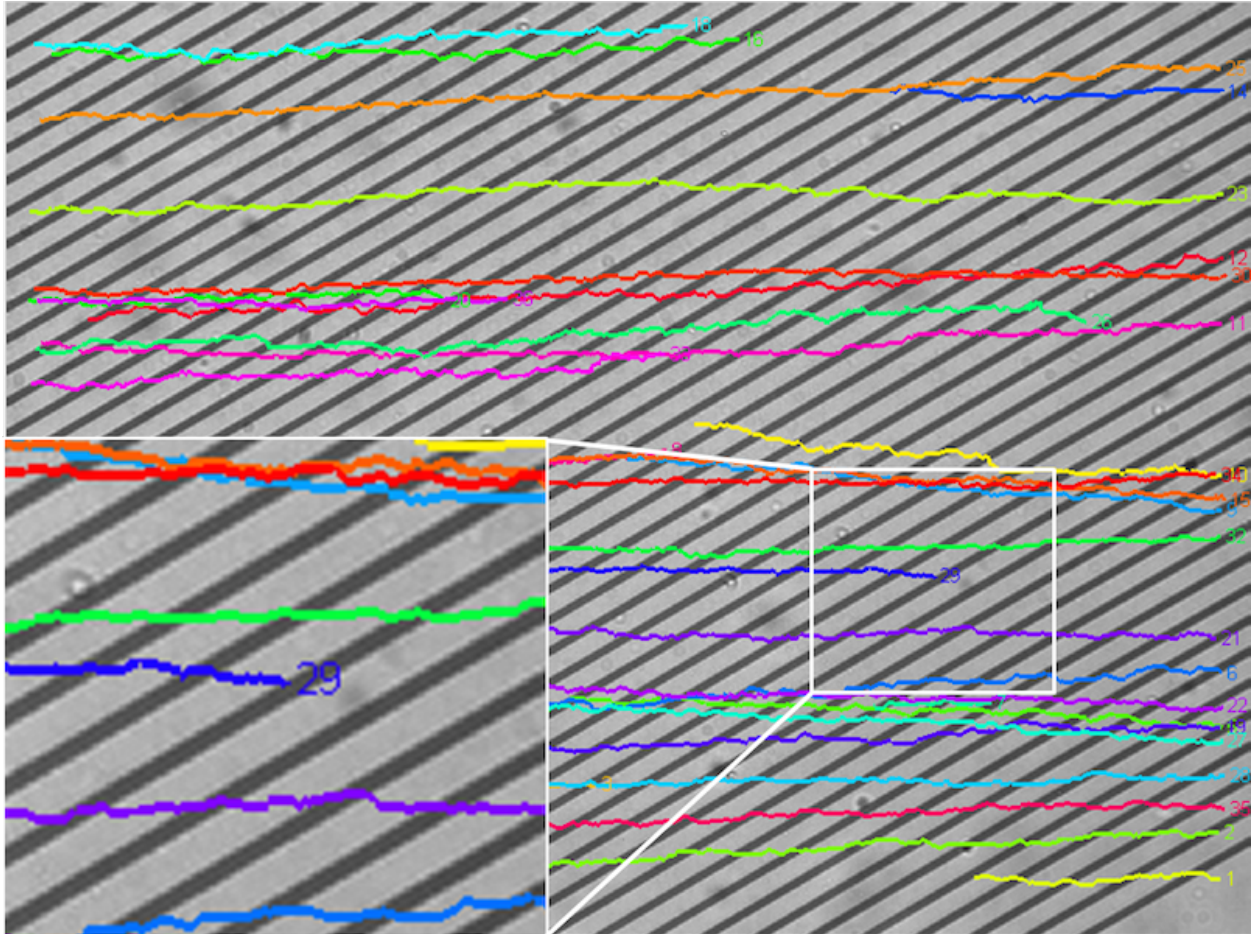


Figure 3.4: Overlay of a selection of cell trajectories on the background image. Inlay shows magnified portion of highlighted paths.

3.3.2.3 Speed analysis A speed analysis function generates a list of properties for each cell in the selection, including start frame, end frame, mean speed, total displacement, min/max lateral displacement, and final lateral displacement. The table can then be easily copied into an Excel document to facilitate further analysis or accumulation of data from multiple experiments.

3.3.2.4 Tracklets and editing All tracking algorithms are prone to occasional error. Most automated tracking programs (especially freeware) lack the ability to manually edit tracks [150]. To correct for observed errors, we created a tracklet editing mode, which can be used to manually override the tracking data. By selecting an individual cell and clicking the “Edit” icon, the user enters the tracklet editing mode. The tracked locations of the cell are presented as individual points, and the user can create new tracklets by designating start and end points using the right mouse button. There is a separate analysis tool for generating a speed report for manual tracklets, so that the original and manual tracking data can be simultaneously preserved.

We found the tracklet editing feature especially useful for cells with unusual or deformed morphologies, such as mitotic and apoptotic cells. In these cases, the automated tracking algorithm would find the location at the center of mass, resulting in oscillating lateral displacement as the oblong cells tumbled forward. The resultant data from these paths would not be representative of the trajectory of the cells, and would often misrepresent the location of cell-substrate adhesion (stripe versus gap adhesion). Tracklet editing allowed for manual correction of these errors.

3.3.2.5 Average trajectory One of the primary goals of our flow study was to understand cell rolling at the interface between low and high densities of adhesion molecules (protein patterns). To easily visualize the transition from gap to stripe (low to high P-selectin density), we developed an analysis tool to find the “average” cell trajectory over many stripes and display it as a single path. Stripes are automatically detected based on an approximate angle and stripe width given by the user. The location of the stripes is displayed in one plot, while a second plot shows the cell trajectories, with data points divided

Lateral Displacement (μm)

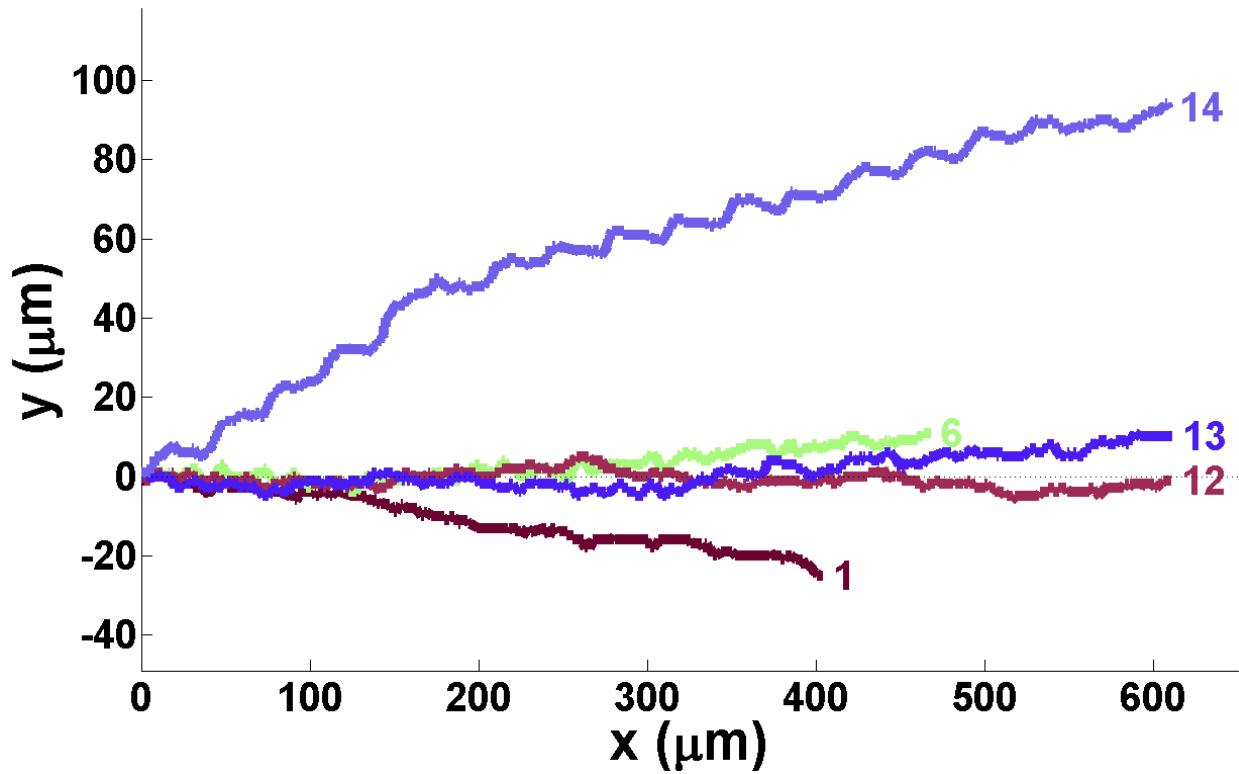


Figure 3.5: Sample data showing cell displacement from initial starting position. Plotting lateral displacement from a common origin makes it easier to rapidly identify unusual behavior (1), interacting (14), and non-interacting cells (6, 12, 13).

into “stripe” and “gap” regions. The motion of the cells in these regions is then averaged to create a mean trajectory, with alternate paths showing the standard error above and below the mean (Figure 3.6).

3.4 DISCUSSION

3.4.1 Real-time tracking in brightfield images

Data collection enabled by the tracking program allowed us to study rolling behavior, optimize our experimental parameters (such as P-selectin concentration and shear rate), and identify gradual behaviors by using large data sets to increase statistical power.

We found that a minimum P-selectin incubation concentration of ~ 2 nM was required to establish stable rolling (defined as speed below 50% of the hydrodynamic velocity). Rolling speed was minimized at ~ 35 nM incubation concentration. Rolling speed did not decrease further with increasing incubation concentrations, indicating that all available sites were saturated or that the density of P-selectin greatly exceeded the density of the PSGL-1 ligand on the cell surface, such that no more bonds could form in a given area.

We also observed that lateral displacement in the direction of the stripes appeared to reach a maximum at shear stresses near 0.5 dynes/cm², however this was not statistically significant from other shear stresses where stable rolling occurs. Cell detachment and a high displacement variability from one stripe to another was most likely responsible for the large standard deviations in lateral displacement.

3.4.2 Triphasic rolling behavior

When cell rolling velocity was examined as a function of wall shear stress, we discovered that it appears to follow a triphasic trend with increasing shear stress (Figure 3.7). Previous literature indicates this may be due to a transition from slip bonds to catch bonds, and then back to slip bonds as shear stress progressively increases. This behavior is similar to the triphasic response observed by Wayman *et al.* [48] on E-selectin, but the rolling velocity of

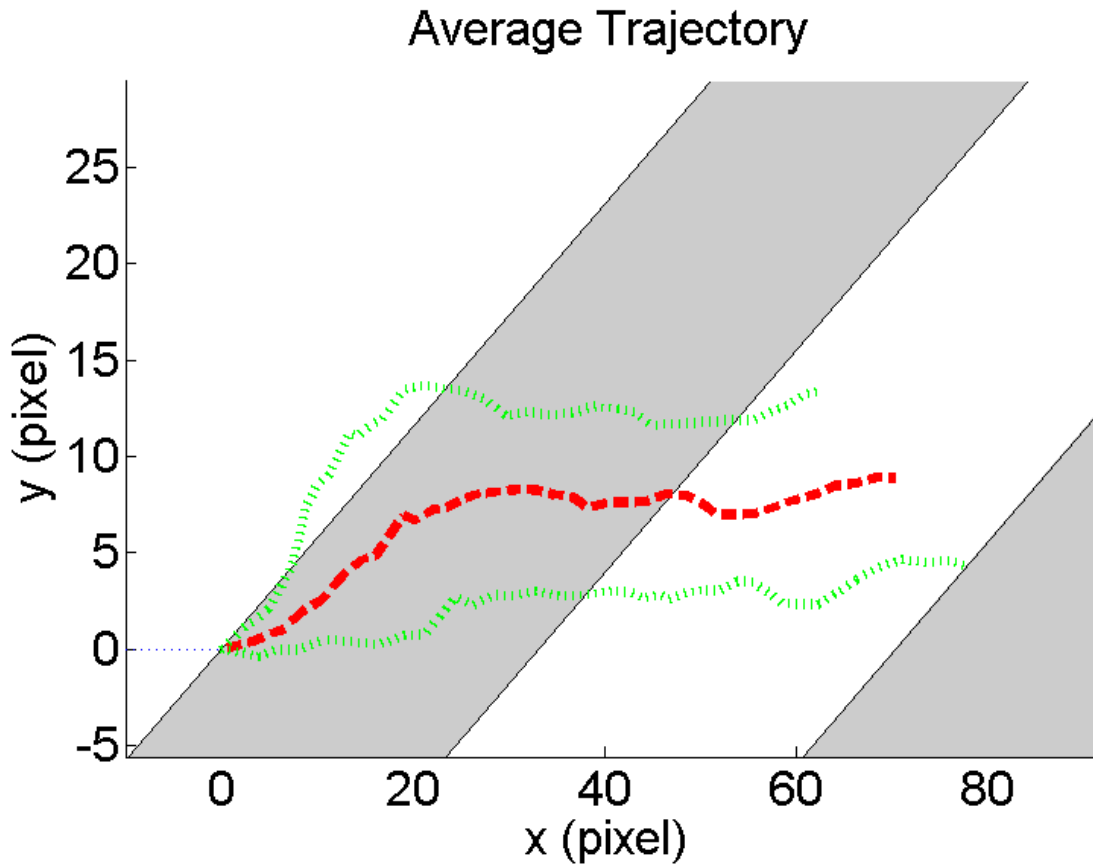


Figure 3.6: Automatic detection of gold/protein stripes is used to generate an averaged trajectory for one or more cells. Path in red shows the mean location of the cell on stripe and gap regions. Green lines show \pm SE.

our HL-60 cells was approximately half that of Wayman *et al.* This may be a result of the differences in site density and ligand kinetics between our experimental setup and Wayman *et al.*

Data was found to be non-normally distributed (failed the Kolmogorov-Smirnov test), as the hydrodynamic velocity generated a hard shoulder on one side of the data distribution. We also found that the data contained a number of outliers in velocity, which appeared to be a result of cells that did not roll for the duration of the time they were tracked. Outliers were removed using the interquartile method, eliminating values above or below 2.2x the interquartile range. While 1.5 is often used as the multiplier, or “g-value”, for determining outliers, the more conservative value of 2.2 is recommended by Hoaglin *et al.* [168], building off the original method from Tukey *et al.* in 1977 [169].

Previously, triphasic behavior has not been observed for P-selectin mediated rolling. Flow chamber experiments with similar shear stresses were conducted for L-selectin and did not seem to exhibit triphasic behavior [170, 171]. Wayman *et al.* hypothesized that prior studies had simply not tested the necessary range and resolution of shear rates to observe the initial, low-stress slip regime for P-selectin. This idea is reinforced by the relative lack of data points at shear stresses below 1 dyne/cm² in existing studies of cell rolling on P-selectin coated substrates [172, 54, 173].

3.4.3 Automated feature detection

The ability to automatically register physical features of the substrate, rather than simply subtracting them as background noise, provides valuable functionality to researchers. In our particular case, it allows us to more easily correlate changes in cell velocity to physical location, allowing us to easily link motion data to substrate properties.

One might envision the use of an active, rather than passive, microfluidic device that reacts to particular cell behaviors. Observed changes in speed or direction could trigger computer controlled actuation of valves, laser tweezers, electrophoretic pads, or other various MEMS components that would act on the cell through a vision-based feedback loop. There are already examples of vision-aided manipulation, such as the automated tracking and laser

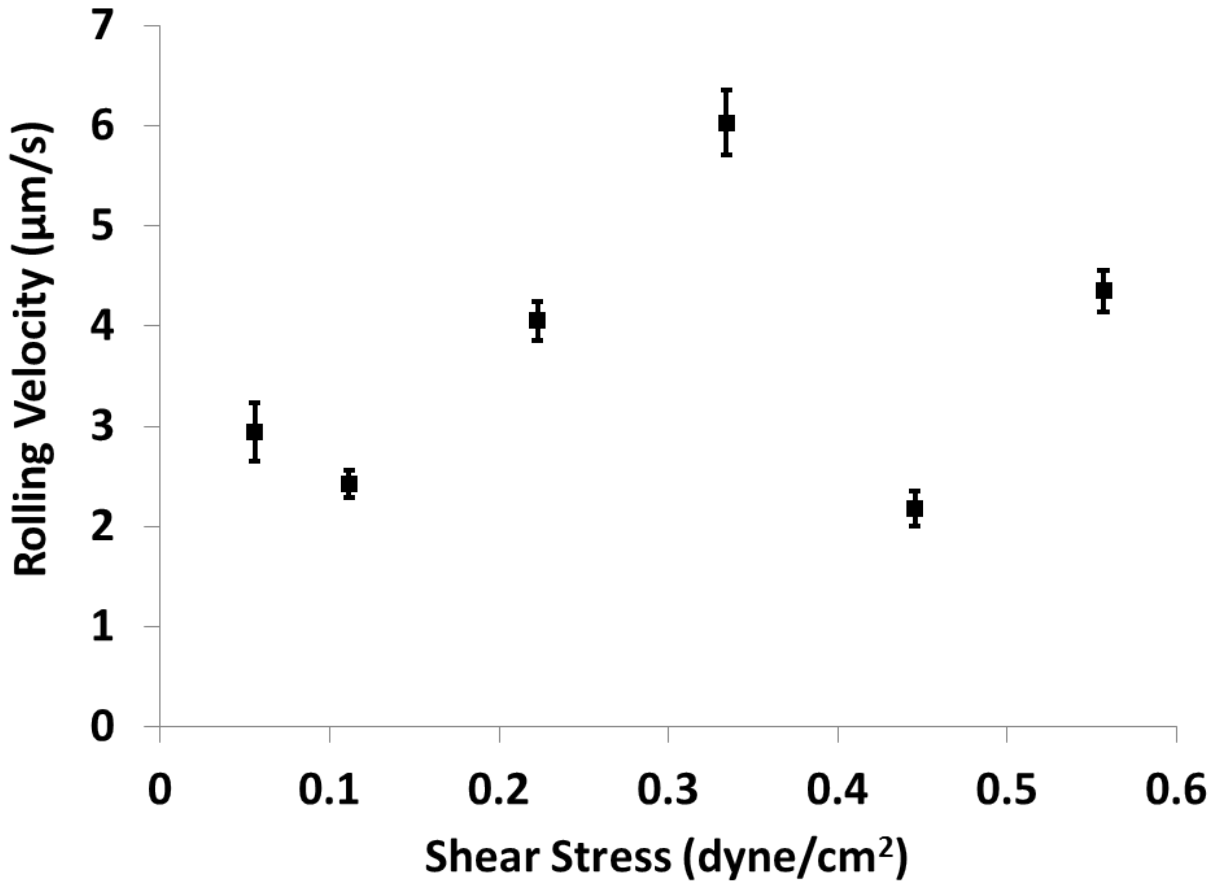


Figure 3.7: Velocity of HL-60 cells rolling on variable density (striped) patterns of P-selectin. Response appears triphasic with increasing shear stress. P-selectin incubation concentration was 70 nM. Data points are mean velocity \pm SE. $N \geq 42$ cells for each data point.

micromanipulation of cells by Stuhmann *et al.*, who used automated tracking to guide neuronal growth [174]. This particular application took place on a timescale of 1 s^{-1} , and did not register to any background features.

Automated identification of these features would negate the tedious registration and alignment steps that would otherwise be required to establish repeatability and precision on such a small scale. In this study we have used the simple example of patterned stripes, which are easily visible to the computer tracking system. In the case of more complicated structures, visual alignment marks could be used instead.

3.4.4 Equipment limitations

The camera firmware was ultimately the limiting factor in our experiments, capping the image capture rate at 10.0 FPS. We periodically compared the timestamps on captured images to ensure that processing overhead was not altering our results. If the time required to capture, write, and analyze each image was longer than 100 milliseconds, the true frame rate would drop below 10. This was never the case during experiments with the final version of the software, therefore we believe that much lower computing power would likely be sufficient to capture and analyze video in real-time.

3.4.5 Target areas for improvement

Even though the tracking program runs effectively in real-time, the speed can be hindered by the specific range of cell radii that are being searched for. The more ring filters that are created (one for each integer between the min and max size), the longer it takes for the algorithm to apply template matching across the whole image. Even with GPU acceleration of the template matching, the effective frame-rate can decrease rapidly as the radius range increases. Fortunately most populations of cells fall within a relatively narrow range of sizes, especially homogeneous cultures. Nevertheless, it is important to have *a priori* knowledge of the mean and standard deviation of cell size in order to maximize segmentation speed.

Using the current method of background subtraction, the software can be very sensitive to background motion in the experiment. Accidental movement of the microscope stage can

result in high numbers of false positives as the background subtraction begins to generate image artifacts. A dynamic background estimation might mitigate or resolve these problems, but the computational costs associated with continuously averaging the background may outweigh the tracking benefits.

Cell density and velocity play a major role in the error rate of the tracking algorithm. As the number of cells in the field of view increases, the resource use rises along with the time required to segment, track, and display cell locations. The selection of an optimal gating parameter depends on the video frame-rate, cell density, and cell velocity. All three affect the average distance between cells from one frame to the next.

3.5 CONCLUSION

In summary, we have developed a hybrid MATLAB/C++ tracking program that can be used for both real-time and offline tracking of fast-moving cells. The program is uniquely suited for analyzing motion in relation to patterned substrates, and provides a combination of automated and manual tracking options not found in existing freeware solutions. Validation has indicated that automated tracking is accurate to within a single cell radius, and can reduce hours or days of manual labor to minutes or seconds.

3.5.1 Software download

The tool described herein is available by download to streamline the study of cell motion against patterned substrates. We hope that it will provide a flexible framework that can be easily adapted to a wide variety of needs, including real-time control of cell manipulation. The source, binary, and script files (including some revision history) are freely available for download from our lab website (<http://dhti.cmu.edu/dhti/russell-lab/>) and is distributed under the GNU General Public License.

4.0 CELLULAR FOCUSING AND LOCALIZATION

4.1 INTRODUCTION

The primary challenge for improving cell rolling, as with many other microfluidic techniques reliant upon cell-surface interactions, is the initiation and maintenance of those adhesive interactions. Generous channel dimensions are required in many cases, because constraining the cells' motion via physical barriers can interfere with their behavior, cause damage, or trap larger cells and obstruct the flow path. Consequently, many cells (over 80%) float above the surface and never interact with the substrate [1, 9]. At long time points, some cell types will settle due to sedimentation forces [137], but these forces are insufficient to establish practical throughput, even in a channel with low to modest flow rates. It is therefore desirable to explore other methods of promoting cell-surface interaction via externally applied forces.

4.1.1 Existing methods of cell focusing

Electrical, optical, acoustic, mechanical, and hydrodynamic methods of manipulating the location of cells within microfluidic devices have been demonstrated [13, 5]. We wanted to explore focusing methods that would be compatible with our existing cell rolling experiments, and would not interfere with the effects of cell rolling on lateral motion. After careful examination of the available literature, we decided to use two different approaches that were readily available to us.

Modern flow cytometry uses a strong electric field between parallel conducting plates to rapidly direct cells into different collection vessels after they have been interrogated. We sought to imitate this effect using transparent, conductive plates of indium tin oxide (ITO)

placed above and below the flow channel, but situated externally from the device to avoid complex fabrication steps and electrochemistry issues commonly associated with integrated electrodes [13].

We also tested an emerging method of nanofabrication, known as two-photon polymerization, to print three dimensional structures for cell focusing. By incorporating the physical structures upstream of the target substrate, we could isolate any flow artifacts to a linear segment of the channel, leaving the downstream flow unaffected.

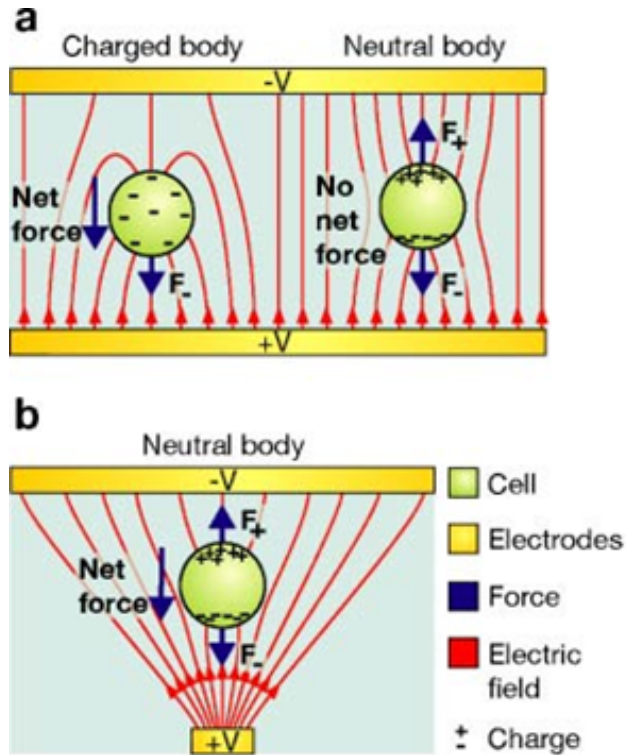
4.1.1.1 Electrophoresis Electrophoresis (EP) and dielectrophoresis (DEP) are electrokinetic phenomena that act on different properties of particles suspended in fluid environments. Electrophoresis is the force exerted by a uniform electric field on a charged particle or cell in an electrolyte solution [175, 13]. The charge on the cell is strongly dependent on its surface adsorbed species, which can give it a positive or negative charge. The force that an electric field applies to a charged particle is given by $F = qE$, where q is the net charge on the particle and E is the magnitude of the electric field. According to the double layer theory, the particle's surface charges will be screened by a diffuse layer of ions in the liquid, which have an equal and opposite charge. When a uniform electric field is applied, it exerts a force on the charged particle and the diffuse layer surrounding it. These forces manifest in opposing directions, and the cell will begin to move toward the electrode with the charge opposite that of its membrane. The opposing force caused by the double layer is known as the electrophoretic retardation force. As velocity increases, the drag force on the cell also increases until the net force becomes zero and a constant velocity is achieved ($F_{tot} = F_{elec} + F_{drag} + F_{ret} = 0$). The mobility of a cell in response to a given field is generally quantified in terms of electrophoretic mobility ($\mu = \epsilon_m \frac{\xi}{\eta}$) where ϵ_m is the permittivity of the liquid, η is the viscosity, and ξ is the zeta potential of the cell. The typical electrophoretic mobility of a biological cell is $\sim 10^{-4} \frac{cm^2}{V \cdot s}$, or $1 \mu m/s$ in a field of $1 V/cm$, but values can vary considerably from one cell type to another [176]. Some experimentally determined properties of HL60 cells are shown in Table 4.1.

Table 4.1: Electric and dielectric properties of HL-60 cells

Parameter	Value	Units	Source
Net Charge (undiff. HL60)	+12	mV	C. J. Park 2009 [177]
Net Charge (diff. HL60-PMN)	-16	mV	C. J. Park 2009 [177]
Membrane Capacitance (live)	15.6 ± 0.9	$\frac{mF}{m^2}$	Huang 2007 [178]
Membrane Capacitance (live)	17.5 ± 0.8	$\frac{mF}{m^2}$	Wang 2002 [179]
Membrane Capacitance (apoptotic)	9.1 ± 0.5	$\frac{mF}{m^2}$	Wang 2002 [179]
DEP Crossover Frequency	$\sim 80 \rightarrow 130$	kHz	Wang 2002 [179]
Membrane Conductance (live)	2.25 ± 1.1	$10^3 \frac{S}{m^2}$	Huang 2007 [178]
Membrane Conductance (live)	2.5 ± 1.1	$10^3 \frac{S}{m^2}$	Wang 2002 [179]
Membrane Conductance (apoptotic)	4.2 ± 1.0	$10^3 \frac{S}{m^2}$	Wang 2002 [179]
Electrophoretic Mobility (non-synched)	$0 \rightarrow -2.75$	$10^{-4} \frac{cm^2}{V \cdot s}$	Akagi 2008 [175]
Electrophoretic Mobility (G1 synched)	$-0.25 \rightarrow -1.5$	$10^{-4} \frac{cm^2}{V \cdot s}$	Akagi 2008 [175]

4.1.1.2 Dielectrophoresis Dielectrophoresis arises from the interaction of a particle’s dipole with the spatial gradient of a non-uniform electric field (see Figure 4.1) [13]. When placed in an electric field, an induced dipole is formed from free charge in the cell, polarization charge in the liquid, or a combination of the two. Even if the cell has no net charge, the gradient of the electric field creates a greater force on one of the dipoles, resulting in cell motion up the field gradient. As a result, DEP has the advantage of being able to separate cells with no charge or the same charge, as long as there is a difference in their dielectric properties, such as membrane capacitance and membrane conductance. Additionally, polarization has been shown to be a more specific indicator of phenotype than net charge [13].

Because DEP relies on a non-uniform field gradient, which generates a force on dipoles that is independent of the direction of the electric field polarity, AC electric fields can be used. Alternating fields have a reduced physiological impact on cells, and greatly reduce any electrochemical reactions at the electrodes (two common problems with EP). AC fields also dampen any EP-induced motion, making the technique more sensitive to differences in cell




 Voldman J. 2006.
Annu. Rev. Biomed. Eng. 8:425–54

Figure 4.1: EP and DEP. (a) Charged and neutral particle in a uniform electric field. The charged particle (left) feels an EP force, whereas the dipole induced in the uncharged particle (right) will not result in a net force ($F=F_+$). (b) A neutral particle in a nonuniform electric field. The particle will experience a net force toward the electric-field maximum because the field magnitude is different at each end of the particle ($F < F_+$). Reprinted with permission from [13]. Copyright 2006 Annual Reviews.

properties other than surface charge. Unfortunately, the equations governing AC-DEP are considerably more complex. The general equation governing DEP is: $F_{dep} = p \cdot \nabla E$ where p is the particles dipole moment, and ∇E is the field gradient. For a uniform sphere placed into a sinusoidal electric field, the overall induced dipole is given by Equation 4.1 [13].

$$p(r) = 4\pi\epsilon_m R^3 \left(\frac{\epsilon_p - \epsilon_m}{\epsilon_p + 2\epsilon_m} \right) E(r) = 4\pi\epsilon_m R^3 \cdot K(\omega) \cdot E(r) \quad (4.1)$$

In this equation, ϵ_m is the permittivity of the medium, ϵ_p is the permittivity of the particle, R is the particle radius, and $E(r)$ is the complex electric field phasor, which gives spatial information on field intensity and polarization. The simplified version combines the permittivity values into a single factor $K(\omega)$, also known as the Clausius-Mossatti (CM) factor. This factor is important because it defines the direction and intensity of the DEP forces. If the relative polarizability of the cell is greater than that of the medium, then the real part of the CM factor, $Re[K(\omega)]$, will be positive, and the cell will be directed up the field gradient (known as positive DEP, or pDEP). If $Re[K(\omega)]$ is negative, then the force will be directed down the field gradient, and the cell will experience negative DEP (nDEP) forces. Because the CM factor is a complex function of the dielectric properties of a cell, different phenotypes can have different CM factors for portions of the frequency spectrum. The point at which the CM factor is zero, as it passes from negative to positive, is known as the “cross-over frequency”. In order to separate two different cell phenotypes, the frequency and solution conductivity can be manipulated to achieve a pDEP force for one phenotype, and an nDEP force for the other, by working in the region between the cross-over frequencies of the two phenotypes (see Figure 4.2). This approach has been used to separate live/dead cells [180], cancer cell lines from dilute whole blood [181], and even to enrich hematopoietic stem cells from whole blood [182].

4.1.2 Two-photon polymerization

Two-photon polymerization (often called TPP or DLW for direct laser writing) is a lithographic fabrication technique that uses a focused, pulsed laser beam to selectively polymerize shapes within small volumes of UV curable photoresist. To limit repetition, please refer to

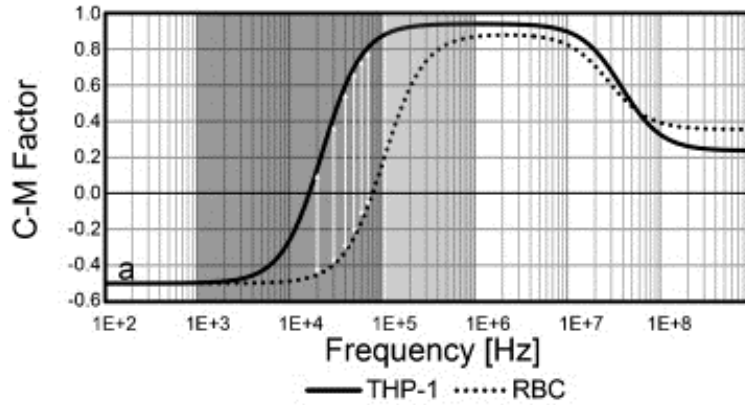


Figure 4.2: Mathematical modeling of the Clausius-Mossatti factor as a function of frequency for THP-1 cells and red blood cells. Unique CM-factor curves allow the two cell types to be separated in regions where the CM-factor is positive for THP-1 cells and negative for RBCs (white arrows). Reprinted from [14], with permission from Elsevier.

Sections 1.2.3, 5.1.2, and 5.4.2 for more in-depth background and discussions about TPP.

4.2 MATERIALS AND METHODS

4.2.1 Microfluidic channels within conductive parallel plates

Microfluidic channels were fabricated in the same manner as previously described. In order to minimize the dielectric capacitance of our microfluidic chambers, the PDMS layer was reduced to a thickness of 1.5 mm (total device thickness 2 mm). Channels were sandwiched between two glass plates coated with indium tin oxide (Aldrich 703176), with the coated layer in contact with the outside surface of the device. The ITO layer was 15-30 nm thick, with a transmittance of 86% and a surface resistivity of 70-100 Ω . The sandwich of materials was gently clamped together in a custom acrylic stage mount to maintain distance and physical contact between the plates and the device. A Mastech HY3003D power supply was used to apply constant potential of up to 30V across the plates during experiments. Copper wire

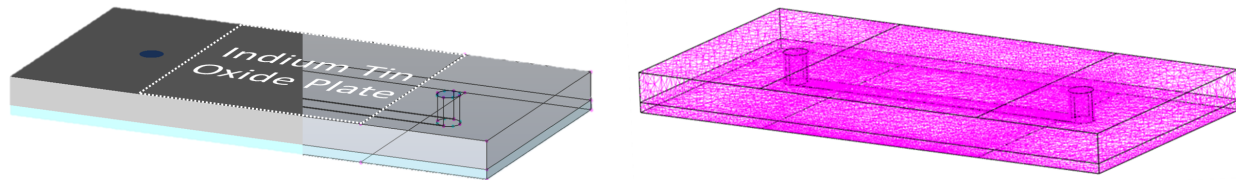


Figure 4.3: Three dimensional model of the simple microfluidic channel being modeled in IES COULOMB (left). Gray area represents PDMS (1.5 mm thick), light blue is pyrex glass (0.5 mm thick), and dark blue is fluid ($30\ \mu\text{m}$ channel height). The internal channel is visible in the translucent wireframe cross-section on the right. Automatic meshing of boundary elements in preparation for modeling (right).

connected the power supply to the backside of the glass plates, which was in turn connected to the ITO by a silver glue bandbus that wrapped around the edges of the plate. Prior to flow experiments, all connections were verified with a digital multimeter.

4.2.2 Modeling

Modeling was conducted using the COULOMB 3D electric field design and analysis software package (Integrated Engineering Software). The software can calculate electric field strength, force, torque, and capacitance using both the Finite Element Method (FEM) and Boundary Element Method (BEM). A true-to-size, 3-dimensional model of the experimental setup was constructed in COULOMB using the integrated drawing tools (Figure 4.3). Material properties (conductivity and relative permittivity) were then assigned to the discrete volumes representing PDMS, pyrex glass, and fluid within the channel (modeling was conducted with both DI water and PBS values).

Modeling was conducted in both BEM and FEM modes to verify the similitude of the predicted field strengths. Global physics settings were adjusted to simulate a static, balanced-charge initial condition in permittivity mode at 20°C . The automatic matrix generator was used to mesh the 3D model, with a minimum 25,000 polygons. The solver was run with an

accuracy/speed factor of 1, with an iterative accuracy of 1×10^{-6} and a material non-linear convergence factor of 0.01. These settings were developed and verified in collaboration with a technical support representative from IES.

4.2.3 Testing the effect of uniform applied DC fields on cell velocity

Experiments were conducted using HL-60 cells resuspended in either standard PBS, or low ionic strength PBS, which was diluted with DI water and made isotonic with the addition of sucrose. Isotonic strength was calculated using Equation 4.2, where c_i is the molar concentration of ion i and z_i is the charge number of i .

$$I = \frac{1}{2} \sum_{i=1}^n c_i z_i^2 \quad (4.2)$$

$$\Pi = iMRT \quad (4.3)$$

Osmotic pressure was determined with Equation 4.3, in which i is the van 't Hoff factor, indicating the dissociation fraction of dissolved species, and M is the molarity of the dissolved species. For example, a 10-fold dilution of PBS results in an ionic strength of 0.019, and requires the addition of 100.63 g/L of sucrose to return to isotonic conditions (~ 330 mOsm).

Flow experiments were conducted at flow rates of 0.25 or 0.5 $\mu\text{L}/\text{min}$, with applied potentials of 30V or 15V applied for either 1 or 3 minutes, with equal intervals without field (all permutations of the parameters were performed). To eliminate residual charge between plates when the field was removed, both plates were shorted to ground after the power supply had been turned off. Videos of cell motion for at least 3 on/off cycles were recorded for each experiment. Cells were tracked using the automated software described in Chapter 3, and speeds were exported to an excel file with corresponding time stamps for analysis.

Analysis was performed by comparing histograms of instantaneous cell speed for groups with and without electric field. Velocity over time was also plotted continuously to determine if cell speed changed within groups over time, which would indicate a considerable lag time between field and response.

4.2.4 3D printed filters

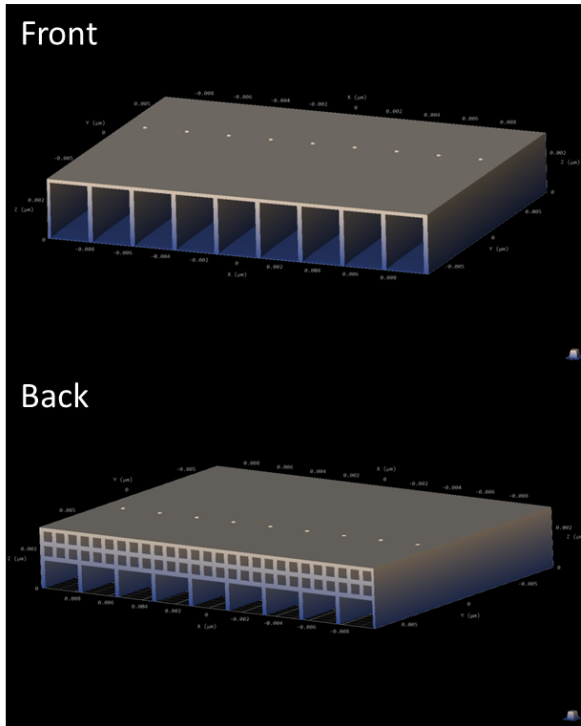
Two different structures were designed in Autodesk Inventor to act as directional filters for cells in laminar flow. Shown in Figure 4.4, the hydrodynamic cross-sections of the directional filters were intended to exclude cells or particles above a $5\ \mu\text{m}$ diameter while still allowing partial fluid flow through the network of channels. The vertical filter blocked 36.95% of the channel cross-section (54.8% in the top half of the channel, 17.3% in the bottom half), while the horizontal filter obstructed 54.4% of the channel uniformly in both top and bottom halves.

Filters were scaled to fit within the maximum writing field of the Nanoscribe Photonic Professional GT, a region of approximately $140\times 140\ \mu\text{m}^2$ in galvo mode. Stage movements were then used to stitch together multiple filters to create a line of four copies across the channel. Three lines of four filters each were patterned in IP-G resist on glass substrates, using a one hour prebake at 100°C and 45 minute development in PGMEA, followed by 20 minute rinse in IPA before drying with N_2 . Total printing time was 14 hours per substrate.

Substrates with printed filters were then bonded to a PDMS channel with a depth of $30\ \mu\text{m}$ using 24 seconds of oxygen plasma at 50 W, 1 Torr O_2 . Filters visually appeared to fill the entire depth of the channel, but no significant deformation of the structures was observed. After bonding, the devices were glued to a microscope slide with clear acrylic glue to reinforce the thin TPP glass substrate against damage.

To test the filters, $5\ \mu\text{m}$ polystyrene beads in ethanol were pumped through the channels at low to moderate flow rates. Videos were recorded and converted to virtual stacks in ImageJ, then overlaid using the z-projection feature to create a single image of the minimum pixel values at each point. This method makes the particle streamlines plainly visible and easy to assess visually.

Vertical Filter



Horizontal Filter

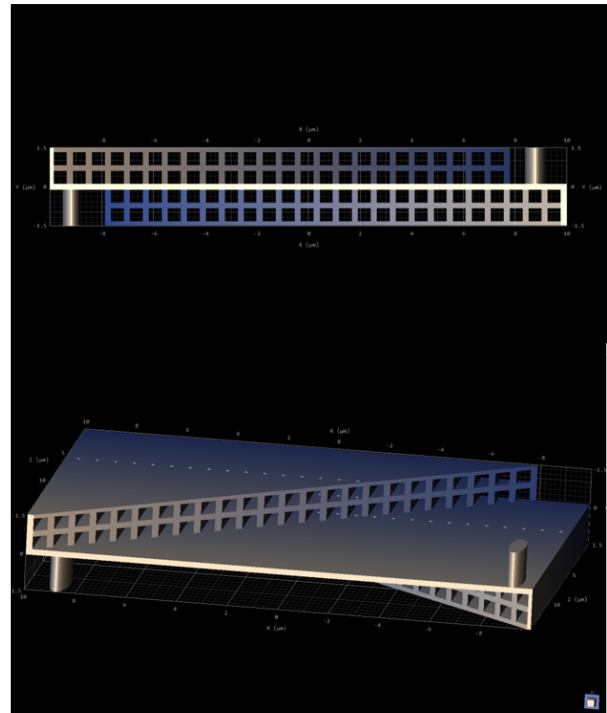


Figure 4.4: Models of 3D printed filters designed to concentrate cells toward the substrate (left, vertical filter) or move cells horizontally in response to their height in the channel (right, horizontal filter). The interior of the vertical filter slopes downward to guide particles too large to fit through the $5 \times 5 \mu\text{m}$ rectangular channels. The horizontal filter makes it easier to query the height of cells when viewing from overhead.

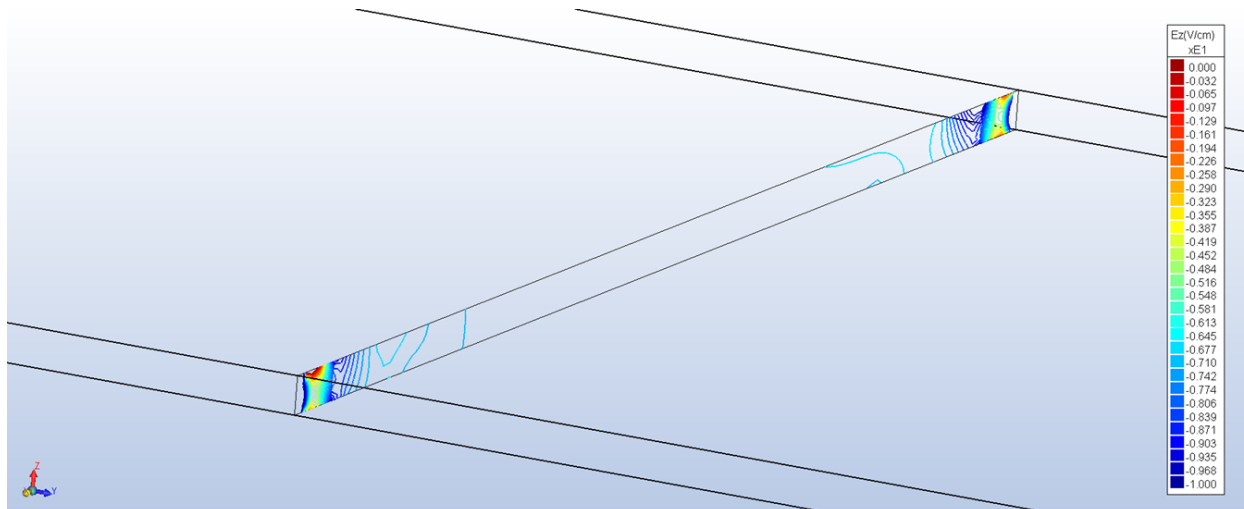


Figure 4.5: Isocontours of the z-component of electric field (V/cm) within the channel. Strong geometric effects occur in the corners of the channel, but the field remains highly uniform across the middle 90%.

4.3 RESULTS

4.3.1 Modeling indicates uniform field generation throughout channel

Modeling results indicated that the electric field strength within the channel was approximately 7 V/cm with an applied potential of 30 V (150 V/cm) across the ITO plates. The field was highly uniform within the volume of the fluid channel, with the exception of $\sim 5\%$ of the channel near the sidewalls (Figure 4.5).

The field was also predominantly oriented in the z-direction, with the z-component of the field comprising 99.998% of the total magnitude (200-fold higher than y-component, 400-fold higher than x-component), as shown in Figure 4.6.

We can easily calculate the anticipated cell velocity from the known electrophoretic mobility of HL-60 cells found in Table 4.1. For a best-case scenario, cells with an EPM of $-2.75 \frac{cm^2}{V \cdot s}$, the velocity would be $19.25 \mu m/s$, requiring only 1 second to move a $10 \mu m$ cell from the top of a $30 \mu m$ channel to the substrate. Field strength within the channel scales

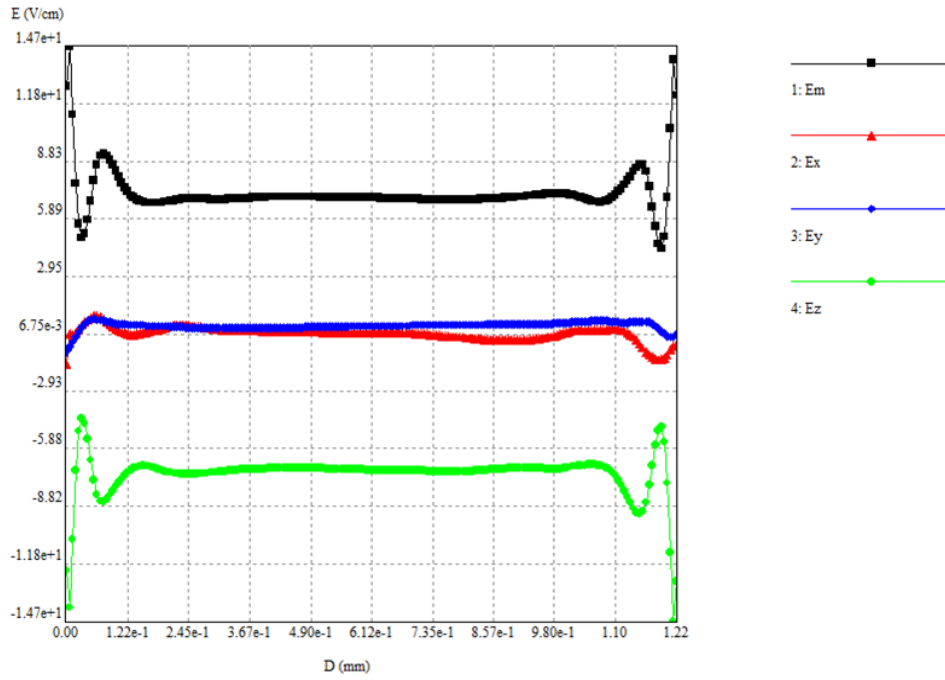


Figure 4.6: The total E-field magnitude (black) and x-, y-, z-components (red, blue, green, respectively) along the length of the channel. Measured along a line equidistant between the channel walls, floor, and ceiling. The z-component is the primary contributor to the total field magnitude, and maintains a consistent strength of ~ 7 V/cm between $D = 2$ mm and $D = 10$ mm, which is the area beneath the plates, and encompasses most of the channel length.

linearly with applied field, as does cell speed, so even with EPM values or field strengths 1/60th of the ideal, we would expect complete localization of cells to the channel bottom within 1 minute. We would also expect minimal motion of cells in the x-y plane due to the low field components in those directions.

4.3.2 Electrophoretic focusing results are inconsistent

Early attempts to focus cells to the microfluidic substrate yielded promising results. In Figure 4.7, the application of electric field appears to reduce the velocity of cells from the predicted hydrodynamic velocity at the center of the channel, to the predicted flow velocity one cell radius from the channel bottom.

Another experiment (data not shown) also yielded significant shifts in cell velocity ($p < 0.001$). Positive results were isolated, however, and over 90% of experiments did not produce a significant change in cell velocity with the application of a field, including attempts to exactly recreate the conditions of the positive results (see Figure 4.8).

The curiously binary nature of these results made troubleshooting extremely difficult. The nature of working with microfluidic devices, their size and closed channels, precludes the direct measurement of electric field within the channels.

4.3.3 3D printed filters

Printed filters were successfully patterned and showed only minor warping due to resist shrinkage after development. Scanning electron microscopy in Figure 4.9 shows the vertical filter entrance. Bonding of channels over the printed structures did not appear to cause damage.

After introduction of liquid to the bonded channels, it became apparent that most of the narrow channels still contained unpolymerized IP-G. Diffusion of the resist during development appeared to be inhibited by the channel dimensions and IP-G viscosity. Longer development times yielded insignificant improvements. The unwanted resist blocked flow through the narrow channels, creating 100% obstruction of flow in most of the filter regions. The resultant flow rates through the unobstructed regions were much higher than desired,

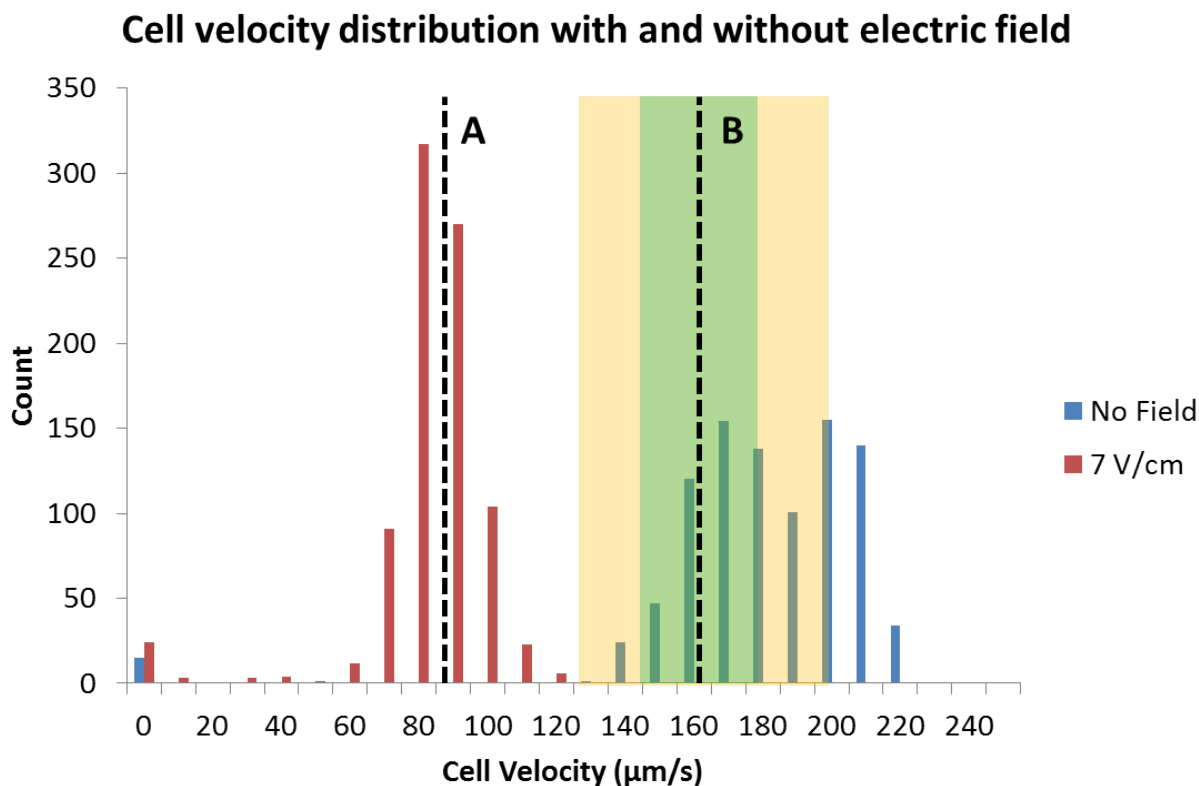


Figure 4.7: Histogram of cell velocity distribution. Cell velocities without an applied field (blue) were distributed around the predicted maximum hydrodynamic velocity (B) that was calculated in [APPENDIX C](#). Green and orange regions show the shift in predicted velocity in the event of $\pm 10\%$ error in flow rate or channel height (respectively). With an applied potential of 30 V, predicted to generate a field of ~ 7 V/cm inside the channel, cell velocities (red) were significantly slower and more tightly grouped, as would be expected for a focused distribution. They also centered nicely around the predicted hydrodynamic velocity $5 \mu\text{m}$ (or 1 cell radius) from the channel floor (A).

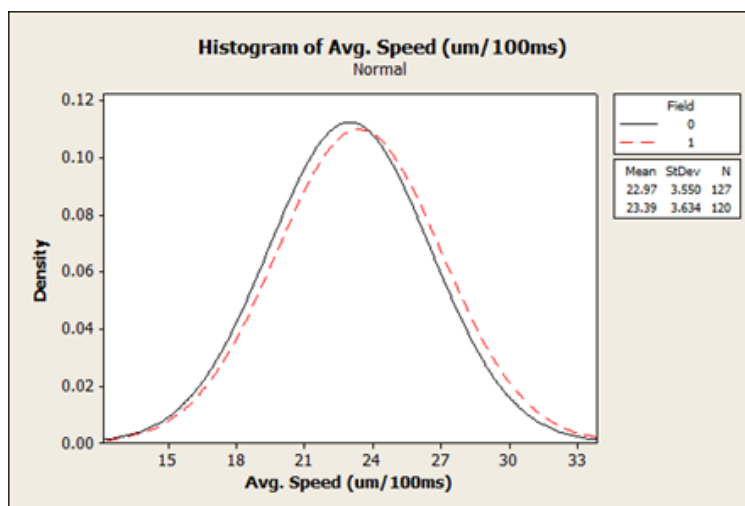


Figure 4.8: Smoothed histogram of average cell speed with (red dashed line) and without (black solid line) an electric field. Experiment was conducted with 10-fold diluted PBS, made isotonic with sucrose. Flow rate is $0.5 \mu\text{L}/\text{min}$, plate potential 30 V. This data is representative of $\sim 90\%$ of results.

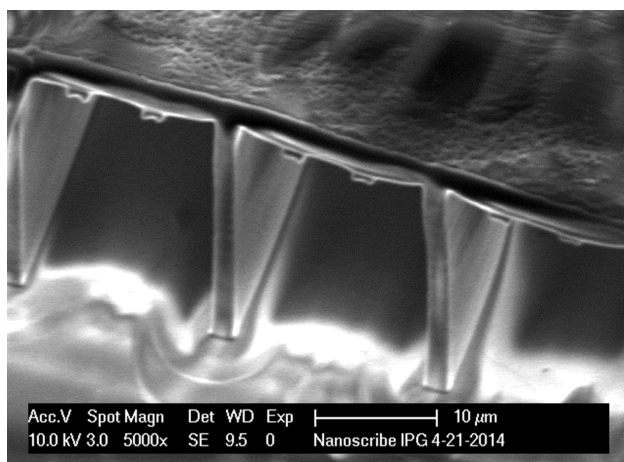


Figure 4.9: SEM image of the entry way of the particle filter designed to force cells closer to the substrate. Entrance is $\sim 28 \mu\text{m}$ in height, and exit is $\sim 12 \mu\text{m}$ tall, the average diameter of an HL-60 cell.

and caused “blooming” of streamlines at the filter outlets, as seen in the highlighted regions A, B, and C in Figure 4.10.

The polystyrene beads in Figure 4.10 have a density of 1.05 g/cm^3 , whereas the ethanol carrier fluid has a density of 0.789 g/cm^3 . We would expect that most of the beads would sediment toward the bottom of the channel. Because the filter is oriented for left-to-right flow, and the image is obtained from an inverted microscope, the upper outlet of the horizontal filter (region C in Figure 4.10) should indicate particles in the top half of the channel, and the lower outlet (region A in Figure 4.10) should indicate particles near the bottom. Counterintuitively, the majority of particles appeared to be in the top half of the channel. When the experiment was repeated with HL-60 cells (Figure 4.11), a similar result was obtained. Some nonspecific adhesion of cells to the filters was observed, but many cells were still able to pass through them unimpeded.

4.4 DISCUSSION

Many attempts were made to improve the consistency and results of the field focusing experiments, but variations in field strength, ionic strength, osmotic pressure, flow rate, and cell passage all yielded results similar to those in Figure 4.8, leading us to believe that the results shown in Figure 4.7 were anomalous.

At the onset of the aforementioned experiments, there was little to no available literature on long range capacitive coupling in microfluidic devices. Retrospective examination of the timeline of electrokinetic literature reveals insights into the physics of our experimental procedure. Starting with the use of hybrid EP/DEP devices, the evolution of DEP practices up to the current day demonstrates that DEP can succeed in situations similar to our setup, which we believe was ultimately unsuitable for EP.

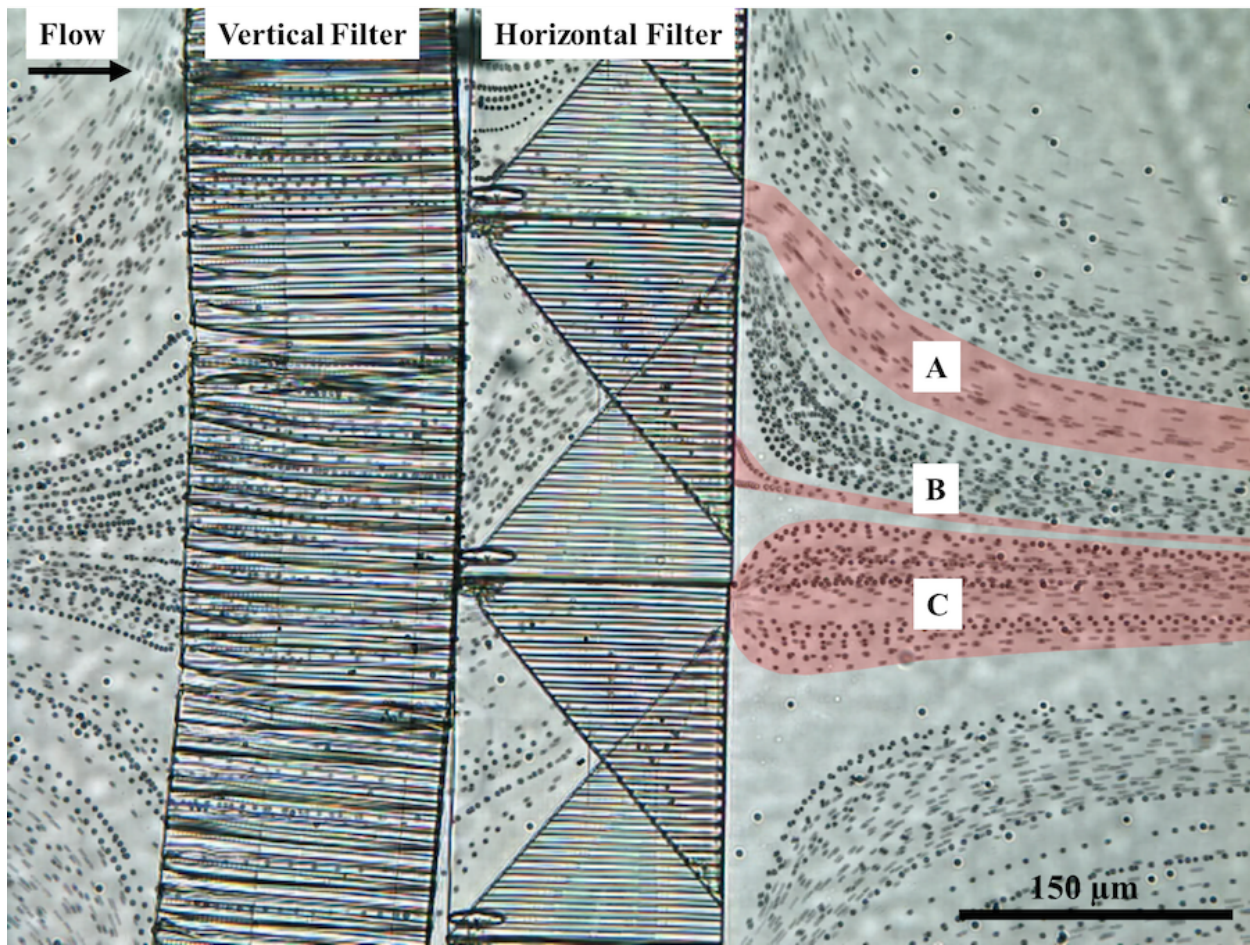


Figure 4.10: Time-lapse projection of $5\ \mu\text{m}$ polystyrene beads flowing through printed filters. Fluid flow is left-to-right. Lower outlets show particles in the upper half of the channel (A). Some particles are small enough to exit prematurely through the printed channels (B). The majority of particles appear to exit through the upper outlets, indicating that they are in the bottom 50% of the channel (C).

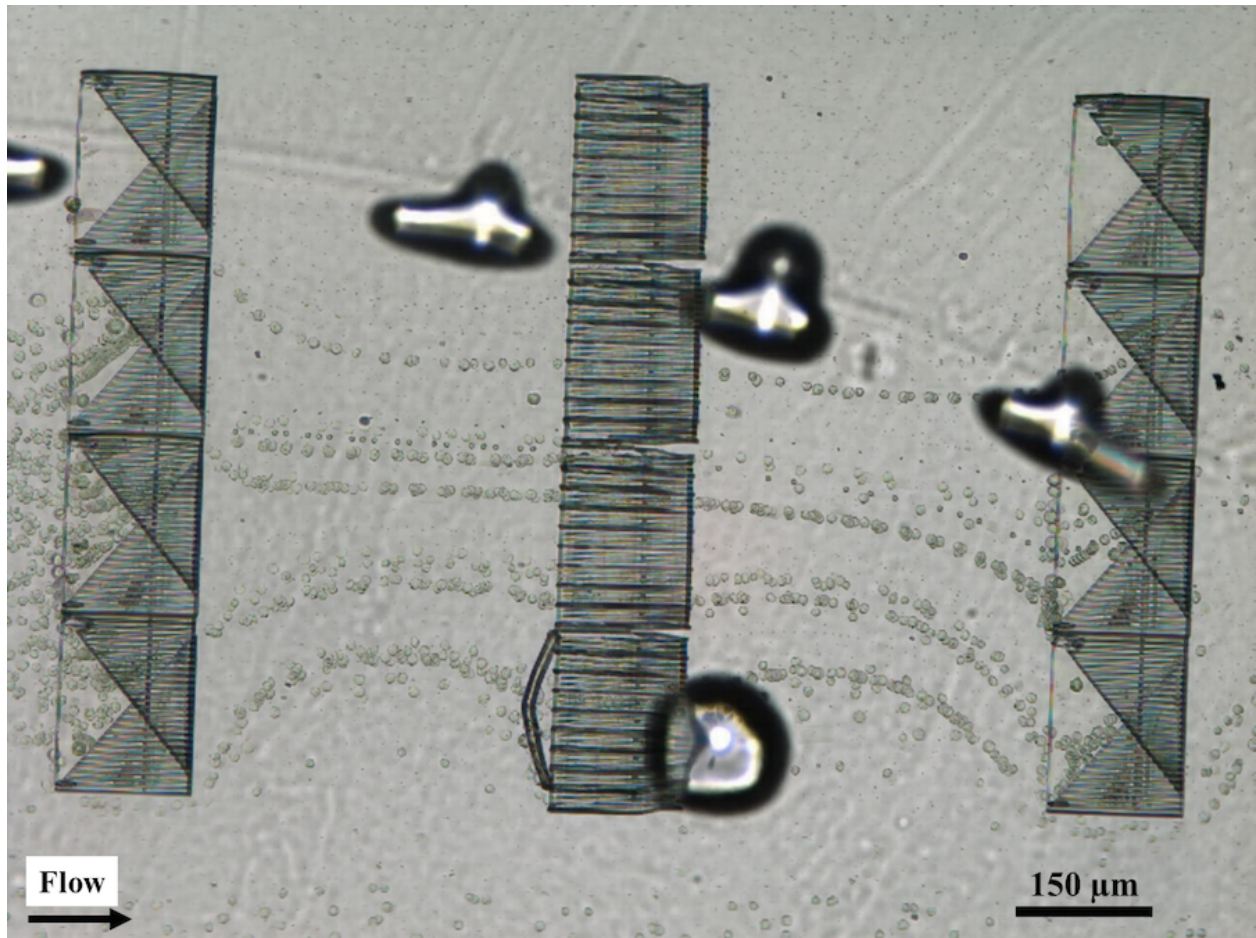


Figure 4.11: Time-lapse projection of HL-60 cells flowing through printed filters. Fluid flow is left to right. The visible bubbles were trapped during gluing of the thin glass substrate to a microscope slide, and are not inside the fluid channel. Cells flowing through the horizontal filter are concentrated into discrete flow lines.

4.4.1 Promising new forms of electrokinetic manipulation

Hybrid devices incorporating both DC and AC fields, known as insulator based DEP (iDEP), started to appear around 2003 [183]. These devices use electrodes at the ends of the channels to produce an electrophoretic flow, while insulating posts along the channel distort the field to create DEP forces. In the past few years, completely contactless dielectrophoresis been experimentally demonstrated for the first time [184]. Contactless DEP (cDEP) mitigates some of the challenges associated with traditional DEP, such as surface fouling, bubble formation, and electrode delamination [185]. Microfluidics for cDEP typically use patterned metal or high conductivity liquid electrodes, isolated from the fluid flow by a thin PDMS membrane as shown in Figure 4.12.

Contactless DEP works through an electrical property known as capacitive coupling, an electrical phenomenon in which energy is transferred between nodes of a circuit through a capacitive element [186]. Coupling is used in electronics to filter out the DC bias from one circuit while passing along the AC signal to the next. The charging time of a capacitor is dictated by its capacitance and the applied voltage, as well as the resistance of the circuit. As the capacitor charges and stores energy in the electric field between plates, the charging current drops as the capacitor becomes charged up to the voltage of the power source. Charge on the plates is dictated by $Q = CV_b[1 - e^{-\frac{t}{RC}}]$, where charge Q asymptotically approaches the charging voltage V_b as time t increases. The time constant, RC , used to describe the charging rate of the capacitor, increases with capacitance. For typical circuits the charging time is very small, meaning that capacitive coupling is severely degraded at low frequencies approaching $\frac{1}{RC}$. In this scenario, capacitive coupling acts as a high band-pass filter, which can be beneficial or detrimental depending on the desired application. Closely spaced traces on a printed circuit board, or parallel buses on a breadboard can often cause accidental coupling that leads to noise in the circuit. Parasitic coupling, as the noise is often referred, is mitigated with appropriate spacing of elements or the inclusion of a grounded plate or trace between the interfering elements, which will preferentially couple with the induced field.

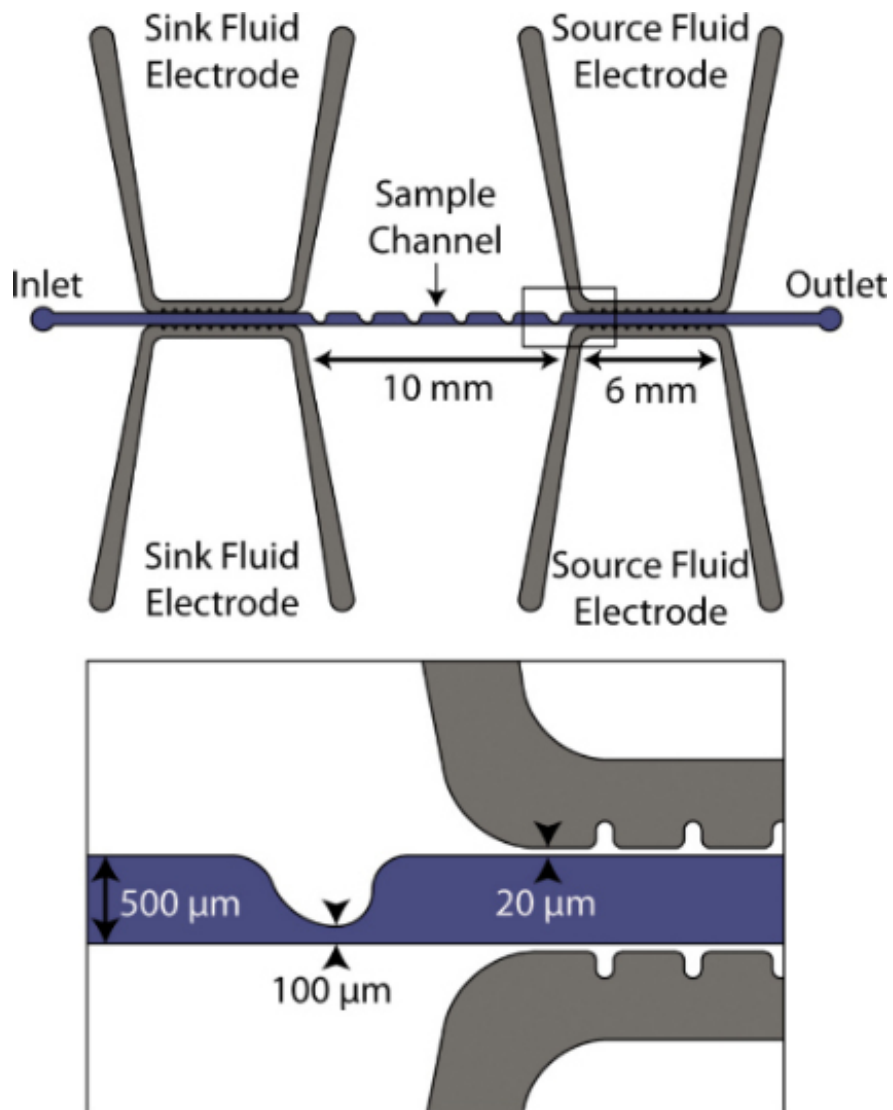


Figure 4.12: Microfluidic channel for contactless dielectrophoretic separation of cells. Fluidic electrodes are isolated from sample flow by $20\ \mu\text{m}$ PDMS walls. Sawtooth geometry increases capacitively coupled electric field, thereby increasing cDEP forces on cells. Reprinted from [15], open access JOVE Creative Commons.

By using frequencies much higher than the capacitive charging time, cDEP can transfer energy into the fluid channel and maintain a non-uniform electric field to induce cell motion. The primary challenge for cDEP is that the crossover frequency of most cells is on the order of 1-100 kHz, where capacitive coupling can weaken the DEP force. Recent work has sought to optimize channel and electrode geometry to improve the low frequency response of these devices [14]. Others have combined cDEP and iDEP, utilizing both external electrodes and internal dielectric geometry to synergistically enhance DEP forces in a technique coined $O\pi$ DEP [187]. By transitioning to long range coupling, in which electrodes are patterned outside the microfluidic device itself, the electrodes can be reused indefinitely, significantly lowering the cost and complexity of the disposable portion of the device.

Less than six months ago, Chen et al. published a cDEP design that exemplifies the properties that will make microfluidics a low cost replacement for laboratory tests [16]. They created a low voltage, long-range cDEP chip that could effectively separate red blood cells from plasma in whole blood (separation quality 89.4%). The electrodes were patterned on the outside surfaces of two glass slides with a polymer channel sandwiched between them, making the electrode separation distance >2 mm (Figure 4.13). Even with such a large separation distance, they were able to achieve separation using applied voltages of just 1-3 V (100 kHz - 1 MHz). The chip also utilized capillary force to drive fluid through the channel, eliminating the need for a flow pump. In this case, high frequency waveform generation is the only remaining barrier to creating a cheap, hand-held, battery powered microfluidic cDEP device.

In the context of the above discussion, the physics preventing a DC, uniform electric field from inducing cell motion can be more easily understood. The modeling prediction of field strengths on the order of 7-10 V/cm would only be applicable for the $t=0$ condition when the voltage is first applied to the ITO plates. Shortly after capacitive coupling, the induced surface charge would reach a maximum and be quickly screened by the formation of an electrical double layer within the channel. The double layer effect occurs as ionic species in the fluid migrate to the channel surface, forming an ordered layer of oppositely charged polarity with a single layer of solvent molecules separating them from the electrode. The solvent layer acts like the dielectric material in a traditional capacitor, allowing extremely high field

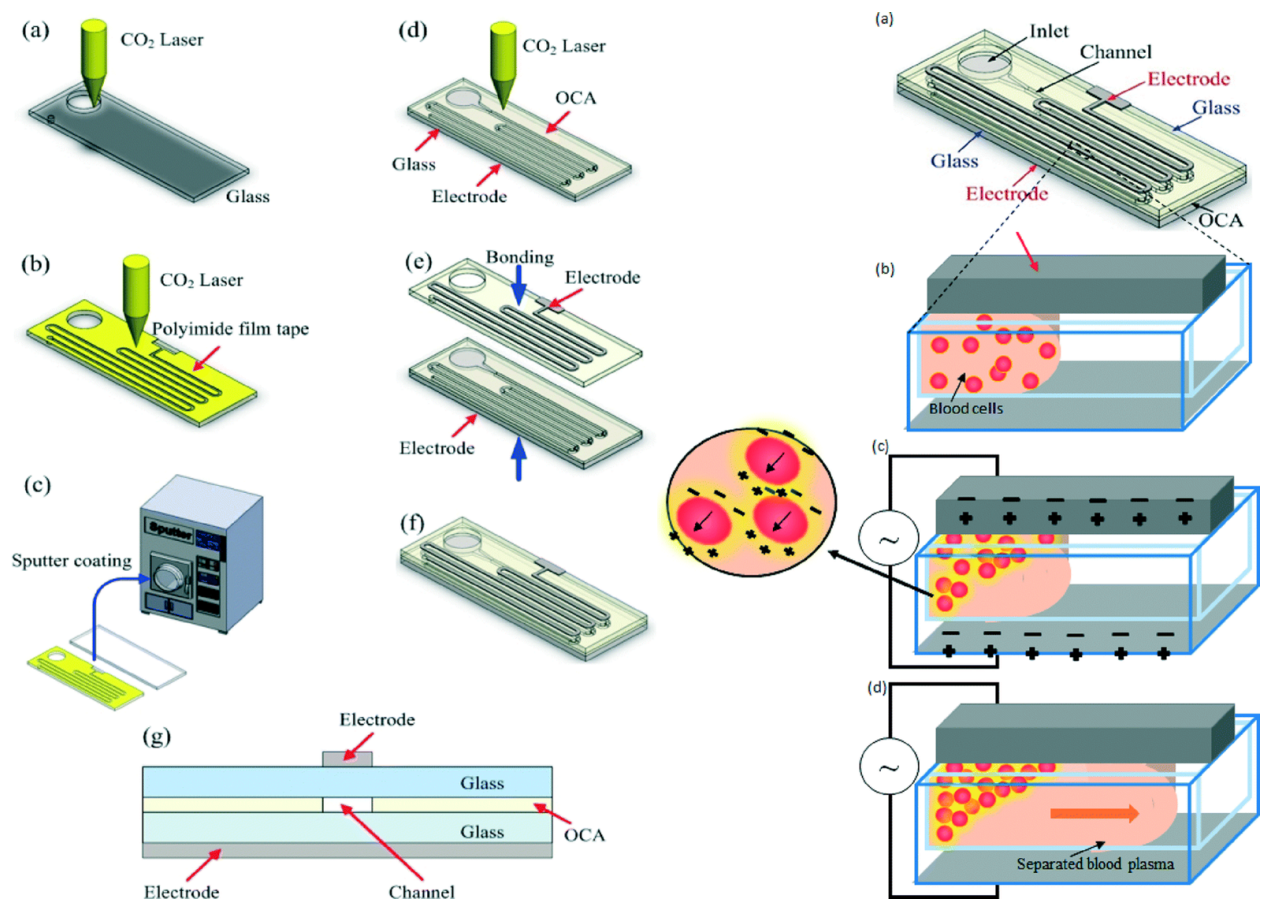


Figure 4.13: Fabrication and operation of the first long-range, low-voltage, contactless DEP device. Electrodes are not integrated into the channel layer, and operate with electrode spacing of more than 2 mm, using 1-3 V. Frequencies of 100 kHz to 1 MHz were used to successfully separate red blood cells from whole blood in a capillary driven flow channel. Adapted from figures 1 and 2 from [16] with permission of the Royal Society of Chemistry.

strengths to exist within the 0.1-10 nm thickness of the charged layer. In their discussion of equilibrium DC electrokinetics, Ben et al. describe the rapid formation of this polarized Debye layer, in which the electrostatic force is much greater than the applied electric field ($E_s \gg E_\infty$), with a layer thickness λ described by Equation 4.4, where C_∞ is electrolyte concentration and $\hat{\epsilon}$ is electrolyte permittivity (R, T, and F are standard constants) [188].

$$\lambda = \sqrt{RT\hat{\epsilon}/F^2C_\infty} \quad (4.4)$$

Outside of this layer, E_s approaches zero as the potential difference drops to zero, typically within a range of 10-100 nm [188]. In this range, the inward electrostatic flux of ions is balanced by the outward diffusive flux, resulting in zero net flux and the formation of an equilibrium Boltzmann distribution of co-ions and counterions [188]. At typical flow rates and electrolyte concentrations, the resultant Péclet number (the ratio of advective transport to diffusive transport) is high enough to effectively guarantee steady state screening of the applied electric field. Extremely low ionic strength buffers or higher fields and flow rates might be able to establish a weak field within a channel, but the necessary parameters are more likely outside the realm of practicality. Therefore, without the benefit of a frequency generator, we would not be able to create a penetrating electric field using our described experimental setup.

We attribute the few, seemingly positive experimental results to human error, such as the clamping pressure of the parallel plates deforming the channels, flow pump inconsistencies due to unseen bubbles, or increasing outlet pressures. It is also possible that moisture on the surface of the PDMS could create a conductive path to the channel inlet, resulting in electro-osmotic flow which, working against the flow pump, would reduce the apparent speed of flowing cells. Ambient humidity might even be a potential factor in this regard, but humidity was not recorded during experiments. We believe this story highlights the importance of establishing experimental repeatability; appropriate skepticism and rigor led to the understanding necessary to explain the results in a productive manner.

4.4.2 Printed filters enable easy interrogation of particle location

Incomplete removal of undeveloped resist inside long filter elements remains an issue with the geometries discussed earlier. Even with increased development times, there appears to be a critical channel length ($>50\text{-}60\ \mu\text{m}$) that inhibits removal of the viscous resist. Incorporation of small through-holes in the channels did not significantly improve diffusion, and caused increased warping and longer print times. Future work will require an improved design that takes this challenge into consideration.

Even with these challenges, the horizontal filters successfully identified particle height within the channel, inducing an easily observable reaction. It does appear, however, that the leading edge of the horizontal filters may have sagged toward the surface due to surface tension during drying. A sloping edge would direct more flow to the top half of the channel, directing a disproportionate amount of particles toward the upper half of the channel. Future designs should include more support structures to prevent collapse of the leading edge, and use a more open geometry to allow full development and removal of bulk resist.

Similar in-channel structures have been created by other groups recently, but not with the intent of locally concentrating particles or cells. Wang et al. used TPP to create size cutoff filters and one-way valves in etched glass channels, using direct in-channel printing (Figure 4.14) [17].

They were able to successfully sieve particles with a $4\ \mu\text{m}$ cutoff diameter, and create unidirectional motion of particles using fish-scale shaped pores that prevent backward motion through the sieve. Amato et al. improved upon this microseive design by using cross-flow washing to remove captured debris from the front of the filter, making it reusable and robust [189].

Lim et al. used a combination of planar lithography and TPP to create an SU-8 channel with incorporated crossing manifold micromixers (CMMs) as shown in Figure 4.15. These manifolds are similar in design to our filters, but do not have size-specific features. As a result, they can only be used for mixing laminar flows to accelerate diffusion of neighboring chemicals [18].

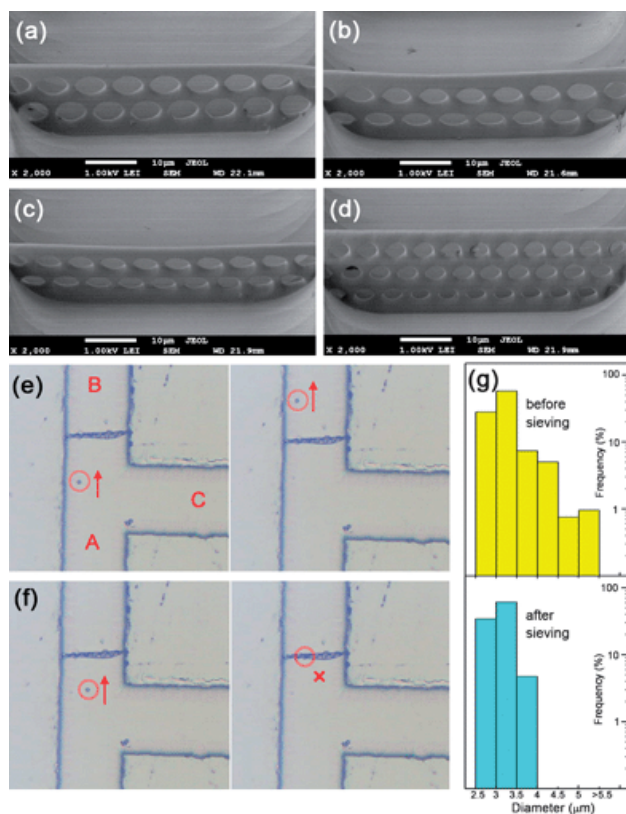


Figure 4.14: Microsieves printed in etched glass channels with pore diameters of 5.5 μm (a), 5 μm (b), 4 μm (c), and 3.5 μm (d) respectively. Results of microparticle sieving with the 4 μm pore size shown in (e), (f), and (g). Adapted from [17] with permission of the Royal Society of Chemistry (RSC).

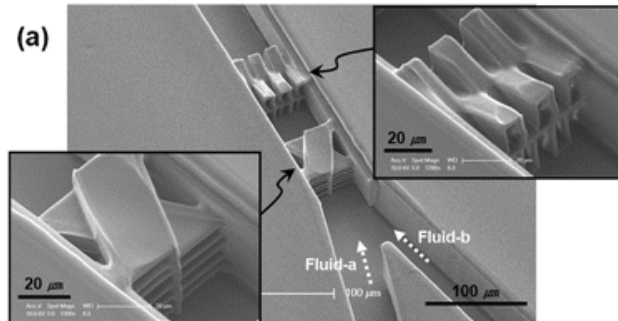


Figure 4.15: Crossing manifold micromixers (CMMs) in microchannels, both fabricated from SU-8 resist. Adapted from [18] with permission of the Royal Society of Chemistry (RSC).

4.5 CONCLUSION

In summary, our modeling results indicated what was most likely an accurate representation of the electric field at $t = 0$, but did not account for the rapid formation of an ionic double layer that completely screened the field on very short time scales. Sporadic false-positives were most likely caused by unintentional electro-osmotic flow or some other human error. The voltage range and electrode separation we chose were later shown to be reasonable in cDEP literature [16], indicating that relevant sorting can be achieved at such ranges, but only with the use of asymmetric electrodes and high frequency fields. The application of cDEP or O π DEP remains a relevant mode of enhancing cell substrate interactions in future work.

The use of two-photon polymerization allowed for easy fabrication of printed microfilters for redirecting cell paths under flow. Cells and particles could be queried for vertical location, and were organized into discrete and overlapping flow paths. This organizational filtering could be valuable for downstream concentration, measurement, or analysis. Future work will incorporate design changes to prevent the horizontal filters from sagging, and to allow the complete development of all features. Coating resist structures with bovine serum albumin should prevent non-specific adhesion. With improved focusing filters, we should be able to

increase cell substrate adhesion and dramatically improve the throughput of devices that rely on cell-surface interactions.

5.0 MAGNETIC MICRO-ROBOTS FOR NON-CONTACT MANIPULATION OF CELLS AND PARTICLES

The work presented in this chapter is the subject of a publication currently in preparation for *Lab on a Chip* (Edington and Ye et al. 2014) [190].

5.1 INTRODUCTION

Manipulation of objects at the micro- and nano-scale is becoming increasingly important in applications for MEMS, microfluidics, microscale assembly of complex systems, and lab-on-a-chip technologies. To this end, existing methods either act upon an intrinsic property of the agent being manipulated (size, charge, density, etc.), or introduce man-made manipulators (end effectors) into the system. Electrophoresis [175, 13], dielectrophoresis [191, 192], flow fractionation [193, 194], and acoustic forces [195, 196] fall into the first category. Methods requiring the introduction of an artificial effector typically include optical tweezers [197, 198], micro-grippers [199, 200, 201], and micro-robots [98, 202, 203, 204, 19].

Magnetic methods of manipulation are particularly attractive because they can be applied at relatively large distances, through insulating, opaque materials, and selectively generate large forces on magnetic materials with no deleterious effects on biological entities. Magnetic forms of control are already widely used in biological science, especially in magnetically activated cell sorting (MACS) [205, 206], purification of DNA, proteins, and peptides [207, 208], and immunoassays [209]. These methods typically attach a magnetic particle to a cell or protein via high specificity ligands or covalent immobilization. While excellent for high-throughput capture of species of interest, these contact-based manipulation methods

are typically an interim step, and must be removed from their targets afterwards. More recently, non-contact magnetic micro-robots have been developed to circumvent some of these issues [19, 202]. These methods use magnetic particles to induce a rotational fluid flow, which can be crafted to redirect particle motion in low Reynolds number (Re) regimes.

Here we report the development of magnetic docking substrates and rotating magnetic microsphere systems at an order of magnitude smaller than previously reported [19]. We also investigate the use of a new method of nanofabrication, two-photon polymerization (TPP), for crafting magnetic micro-robots from UV curable photoresist polymers containing magnetic nanoparticles (MNPs). We discuss the advantages and limitations of both approaches, and demonstrate a microfluidic device capable of generating size gradients of particles under continuous flow.

5.1.1 Magnetic micro-robots for control of micro-object motion

A magnetic micro-robot is capable of generating rotational flows in close vicinity by high-speed rotation. When the micro-robot spins about an axis perpendicular to the underlying substrate, it generates a rotational flow field around the same rotation axis in an otherwise quiescent fluid (Figure 5.1). Such a flow field applies drag forces to other micro-objects in the disturbed fluid, pushing them to follow the local streamlines. Meanwhile, the induced rotational flow also provides centric forces pointing towards the rotation axis, which act to trap the moving objects on stable orbits around the rotating micro-robot. Both the drag force and the centric forces are highly dependent on the size of the objects. The forces experienced by a spherical micro-object inside the induced rotational flow is analyzed in [19].

When such a micro-robot system is placed in laminar flow, the induced rotational flow can be superimposed onto the background flow given the linear nature of the flows at very low Re. When any micro-objects that are originally following the background flow enter the region significantly disturbed by the induced rotational flow, they begin to experience the forces arising from the induced rotational flow. In this region, not only do these forces change the speed of the objects, but they can also cause migration of objects between streamlines.

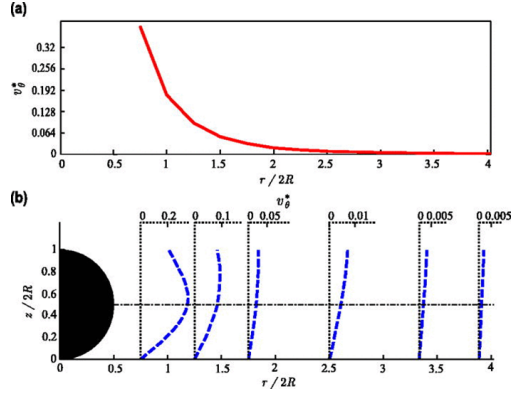


Figure 5.1: Tangential fluid velocity around a rotating microsphere. Adapted with permission from [19]. Copyright 2012, AIP Publishing LLC.

Since these forces are dependent on object’s size, the degree of migration is also associated with object’s size. Therefore, such a system enables the generation of size-gradients of micro-objects at the exit of the disturbed region.

5.1.2 Two photon polymerization for micro-robot fabrication

Two photon polymerization (TPP) is an extension of traditional photolithography, which uses light to selectively excite a photosensitive resist and initiate polymerization [210, 211, 212, 213, 214]. The unusual and defining feature of two photon absorption is the non-linear nature of initiator activation. Rather than polymerization occurring in a linear fashion with increasing power, no polymerization takes place until a critical threshold is exceeded. When a laser is tightly focused into a diffraction-limited spot within a volume of photoresist, photon density exceeds the activation threshold only in that focal region. This restricts polymerization to a small volume typically referred to as a “voxel” [20], without causing partial polymerization in areas just outside the focal region. The voxel can be likened to a three dimensional pixel, which can then be scanned through the photoresist to polymerize structures with resolutions below the diffraction limits normally imposed by one photon lithography [211]. Figure 5.3 shows the typical size and shape of a TPP voxel, and Figure

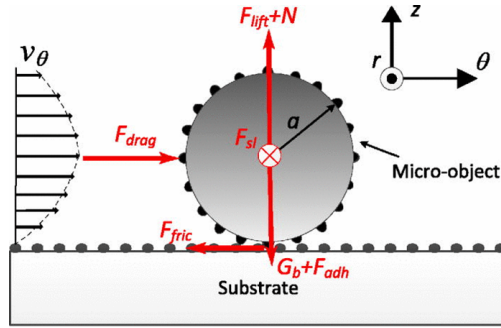


Figure 5.2: Free body diagram of a spherical micro-object in contact with the substrate, within the rotational flows induced by a spinning micro-robot. Viewed along the radial axis, ignoring radial and vertical fluidic drag forces. The microscopic roughness on the object and the substrate is enlarged. Adapted with permission from [19]. Copyright 2012, AIP Publishing LLC.

5.4 shows a schematic and resultant structures of TPP printing.

Two photon lithography presents numerous potential applications, including improved photonics for telecommunications and computing [215], invisibility cloaking meta-materials [216, 217], micro-needles for transdermal drug delivery [218], and 3D printable bioscaffolds and vasculature [219]. Recently, incorporation of magnetic nanoparticles into TPP resists has yielded magnetically controllable structures that could be used to manipulate cells, carry drug payloads, or otherwise allow precise actuation at the micron scale [220, 221].

5.2 MATERIALS AND METHODS

5.2.1 Electromagnetic-coil system

The magnetic micro-robots were driven by a magnetic field that was remotely applied by an electromagnetic-coil system (Figure 5.5). The system consists of three sets of electromagnets for in-plane and out-of-plane fields. Two pairs of iron-core electromagnets arranged

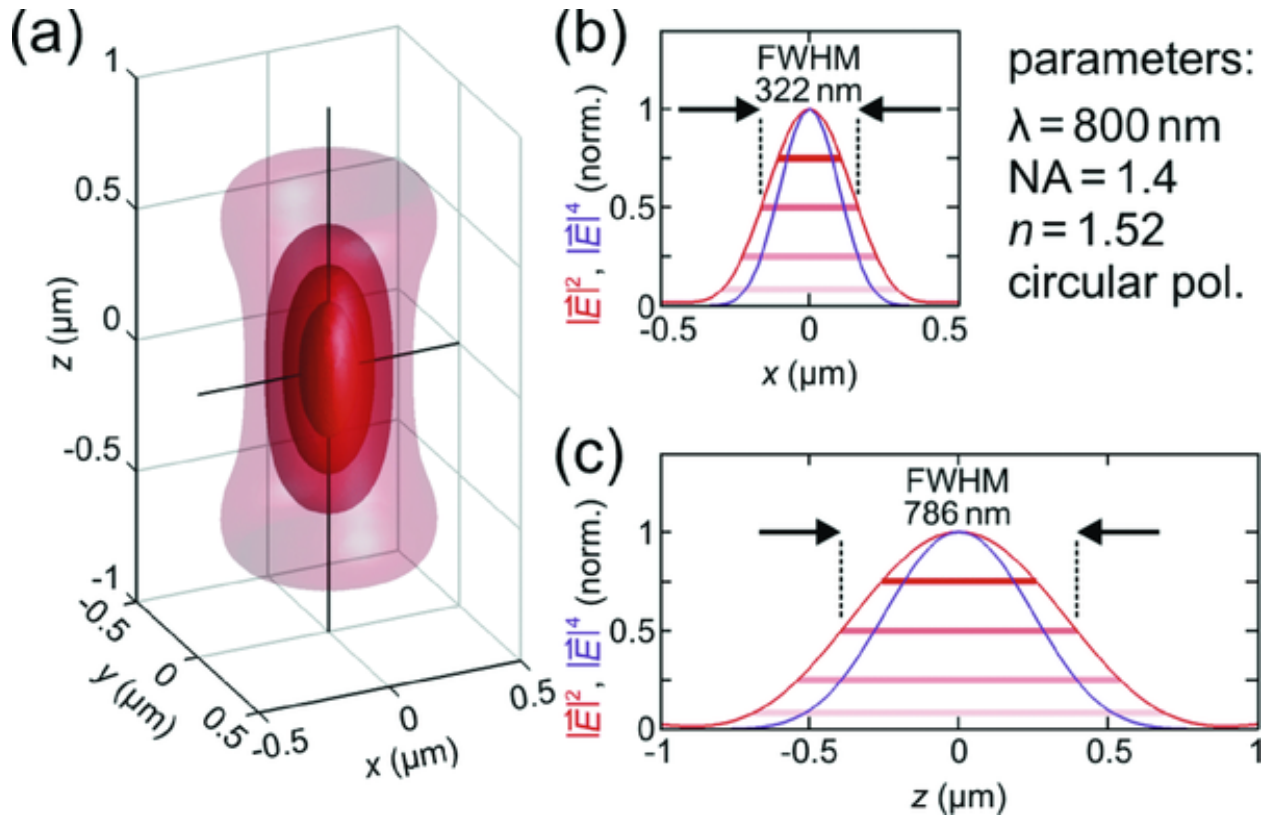


Figure 5.3: Calculated focal intensity distribution of a typical writing spot. (a) Iso-intensity surfaces. The profiles along the two black lines are depicted in b) and c). (b) Lateral profiles of $|\vec{E}|^2$ (red) and $|\vec{E}|^4$ (purple) correspond to one-photon exposure and two-photon exposure, respectively. (c) Axial profiles of $|\vec{E}|^2$ (red) and $|\vec{E}|^4$ (purple). The horizontal lines in b) and c) correspond to the iso-intensity values of the surfaces in a). Adapted with permission from [20]. Copyright 2013, John Wiley and Sons.

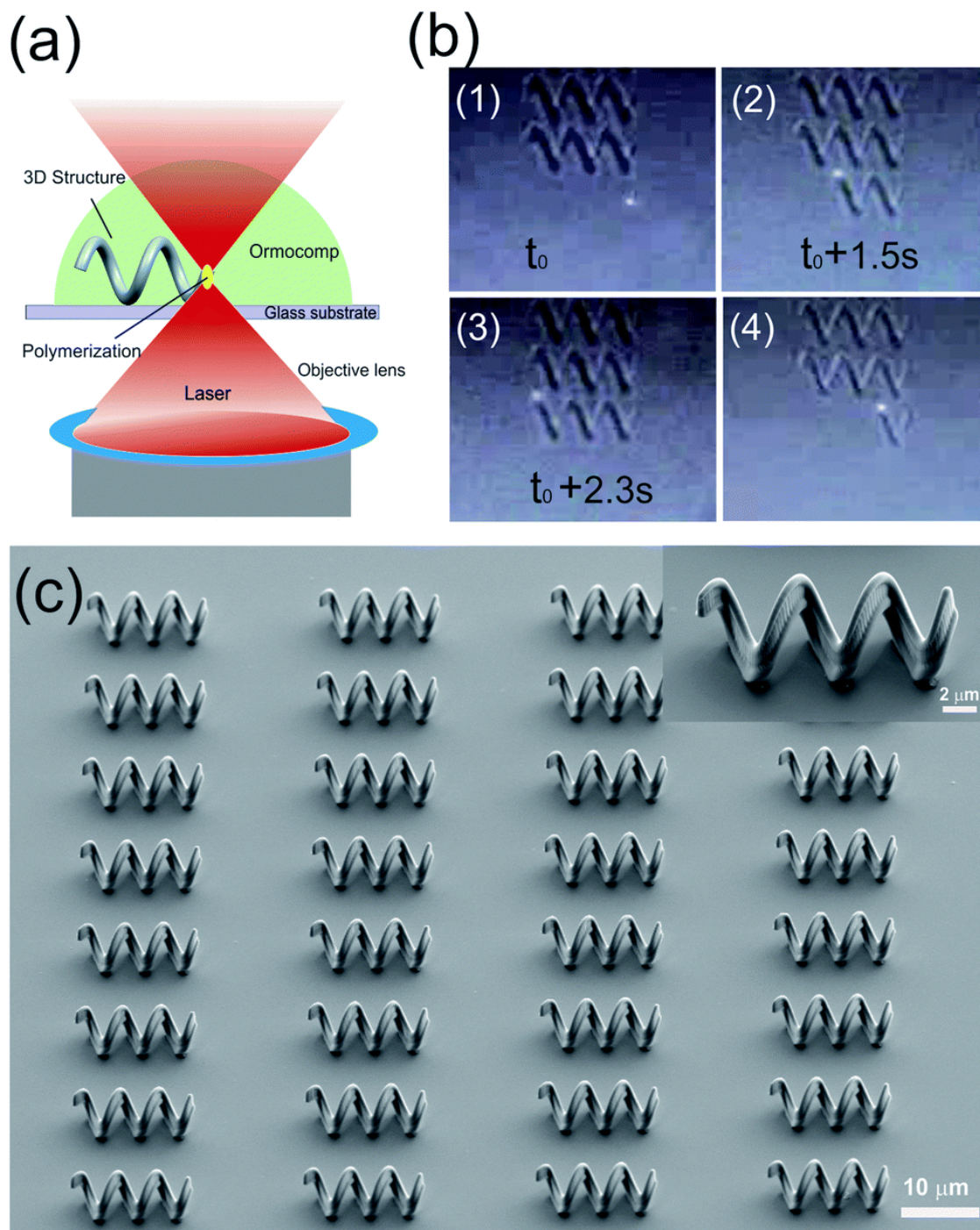


Figure 5.4: Schematic of TPP operation using ORMOCOMP photoresist to fabricate helical microstructures. Adapted from [21] with permission of the Royal Society of Chemistry.

perpendicular to each other were used to generate in-plane fields, while the out-of-plane field was generated by a third, vertically placed solenoid. The coil system was built into a microscope stage insert so that it could be placed into an inverted microscope (Axio Observer, Carl Zeiss). Each pair of the iron-core electromagnets was powered by a Syren 10 motor driver (Dimension Engineering LLC), while the vertically placed solenoid was powered by a third motor driver of the same type. Motor drivers were controlled by an Arduino Uno R3 microcontroller with a customized PC software interface for real-time adjustments of the magnetic field parameters. The magnetic field strength was calibrated using a gauss meter probe (Model 410, Lake Shore Cryotronics, Inc.). A maximum in-plane magnetic field of 3.5 mT could be achieved, with a maximum out-of-plane magnetic field of 8 mT. The in-plane magnetic field was measured to be uniform within 7.5% of the nominal value. The details of the electromagnetic-coil system is listed in Table 5.1.

5.2.2 Magnetic microspheres

Magnetic neodymium alloy microspheres (NdPrFeCoTiZrB alloy) were obtained from Magnequench International Inc. (MQP-S-11-9-20001-070). Properties of these particles can be found in Table 5.2. The microspheres were provided unmagnetized and ranging in size from 2-100 μm in diameter.

We separated the particles by size using a stack of four high precision, stainless steel sieves (H&C Sieving Systems) with cutoff mesh sizes of 63, 45, 32, and 20 μm (U.S. #230, 325, 450, and 625 respectively). During experiments, the unmagnetized microspheres could be easily handled and placed onto the substrates or injected into the microfluidic devices. They could then be manipulated into place using the helmholtz coils described earlier, which can induce weak magnetization and motion without causing the microspheres to agglomerate. Once positioned, the particles were magnetized by placing the substrate or microfluidic device into a stationary field with a strength of 100-200 mT. After magnetization the particles were far more responsive to external magnetic fields, but also tended to irreversibly attach to nearby particles unless held in place using a magnetic dock built into the surface of the substrate.

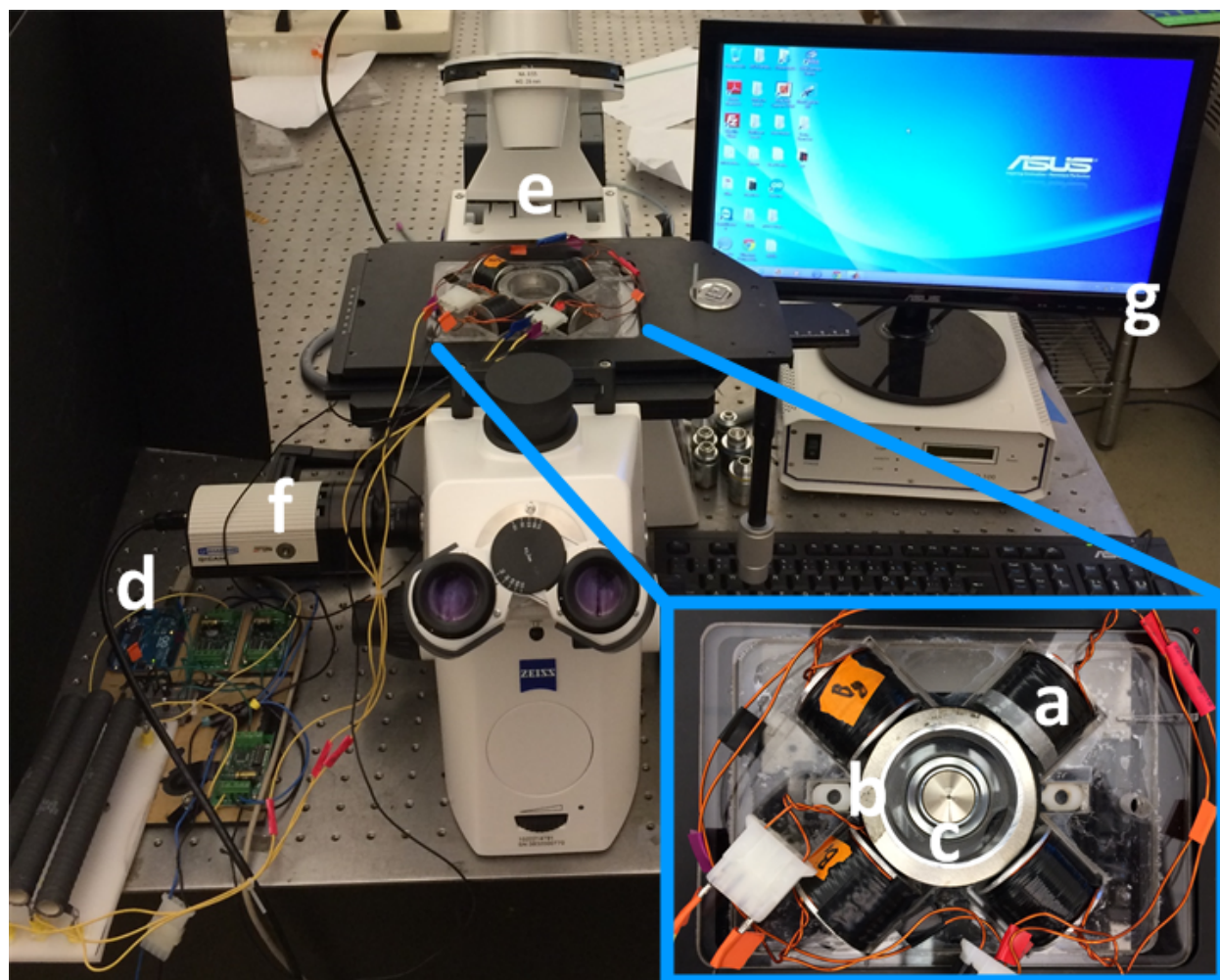


Figure 5.5: (a) Four orthogonally oriented iron-core electromagnets are used to generate an in-plane uniform magnetic field. (b) A vertically placed solenoid is used to generate an out-of-plane uniform magnetic field. (c) The workspace in the center of the solenoid is 40 mm in diameter. (d) The coil current is controlled with an Arduino Uno microcontroller board. (e) The samples are imaged using a 20x or 32x objective in an inverted phase contrast microscope (Axio Observer, Carl Zeiss). (f) Images of the samples were captured at 19 frames per second with a CCD digital camera (QICAM 12-bit, QImaging). (g) A desktop computer with the custom user interface communicates with the microcontroller board for real-time adjustment of magnetic field parameters. Reproduced from [22] with permission of the Royal Society of Chemistry.

Table 5.1: Parameters of the electromagnetic-coil system for actuation of micro-robots.

Property	In-plane Coils	Out-of-plane Coil
Number of turns	120	90
Resistance (Ω)	0.3	0.2
Wire diameter (mm)	1.024	1.024
Coil length (mm)	28	40
Inner diameter (mm)	23	35
Maximum driving current (A)	9	9
Maximum field at the center (mT)	3.5	8.0

Table 5.2: Material properties of NdPrFeCoTiZrB alloy microspheres, adapted from the Magnequench material data sheet available online (MQP-S-11-9-20001-070).

Material Property (NdFeB Microspheres)	Value	Units
Residual Induction, B_r	730-760	mT
Energy Product, $(BH)_{max}$	80-92	kJ/m^3
Intrinsic Coercivity, H_{ci}	670-750	kA/m
Coercive Force, H_c	440	kA/m
Magnetizing Field to >95% Saturation, H_s	≥ 1600	kA/m
Density (theoretical)	7.43	g/cm^3
Apparent Density	3.6-4.2	g/cm^3

Table 5.3: Material properties of magnetite nanoparticles used to create composite resists for two photon polymerization. Adapted from materials specifications sheet from Chemicell.

Material Property (Fe ₃ O ₄ MNPs)	Value	Units
Particle size (metallic core)	110-130	nm
Particle size (hydrodynamic)	150	nm
Concentration	125	mg/mL
Particle number	5.2x10 ¹⁴	g ⁻¹
Ferrofluid density	1.25	g/cm ³

5.2.3 Magnetic nanoparticle composite resist

Magnetite nanoparticles (Fe₃O₄) were obtained from Chemicell GmbH in a pre-made ferrofluid suspension. Particles were coated in a block copolymer dispersant and suspended in γ -butyrolactone. Nanoparticles were added to IP-G resist (Nanoscribe) to make 6x1 mL samples in a range of concentrations (0%, 0.1%, 0.5%, 1%, 2%, and 4% by volume). Compositions were calculated using Equation 5.1 with constants from Table 5.3.

$$\frac{Desired\%}{100} \cdot \frac{1 \text{ mL stock}}{125 \text{ mg MNP}} \cdot \frac{1000 \text{ mg}}{\text{g}} \cdot \frac{1 \text{ g}}{5.2 \times 10^{14} \text{ MNP}} \cdot \frac{1 \text{ MNP}}{1.8 \times 10^{-15} \text{ cm}^3} \cdot \frac{1 \text{ cm}^3}{1 \text{ mL}} = \frac{\text{mL MNP}}{\text{mL Total}} \quad (5.1)$$

Mixtures were created by adding the appropriate volume of stock ferrofluid to photoresist for 1 mL total volume. The composite was mixed for 15 minutes with a handheld sonication probe, pulsed at an on/off rate of 10% to prevent heat buildup. Samples were stored at 2-8°C until use. Visual observation indicated that the composites remained in stable suspension for over 25 days, but for consistency the suspensions were always resonicated for 2 minutes immediately prior to use.

Table 5.4: Laser properties of the Toptica NIR FemtoFiber Pro Erbium fiber laser used for two photon polymerization.

Laser Property	Value	Units
Calibration Power (100%)	50	mW
Wavelength	780	nm
Pulse Duration	80-100	fs
Pulse Frequency	80	MHz
Energy per pulse	0.625	nJ
Photons per pulse	2.45	billion

5.2.4 3D printing of MNP-composite resist

Samples of each composite mixture were drop-cast onto TPP glass substrates (20 μL , 1 cm droplet diam.) and baked on a hotplate. IP-G samples were baked at 100°C for 1.5 hours (ramp rate 20°C/min) to drive out excess solvent and gel the PMMA component (3 vol.%). PMMA gelation provides physical support for printed structures that are not attached to the substrate, or have large horizontal overhangs. Without this gelation step, loose structures would drift through the resist during printing, pushed by the momentum imparted on them by absorbed photons near the focal point of the laser. The same effect is utilized in optical tweezers, but in this case creates undesirable results.

A Photonic Professional GT (Nanoscribe GmbH) with a FemtoFiber Pro NIR laser (Toptica Photonics, Table 5.4) was used for all two-photon polymerization of resists. Printing was performed using a 63x objective (NA=1.4) in oil immersion mode. After TPP, IP-G samples were developed in propylene glycol monomethyl ether acetate (PGMEA 99.5%, Sigma-Aldrich) for 15-20 minutes to remove undeveloped resist. Samples were then submerged in 2-propanol to rinse away the PGMEA. Samples intended for SEM imaging were then dried with gentle N_2 , while samples intended for magnetic field experiments were maintained in propanol until use. Storage in propanol helps to prevent stiction between the

mobile and stationary components of the printed features, which is caused by the surface tension between microstructures during drying. Critical point drying with supercritical CO₂ can also be used to limit stiction from electrostatic forces, hydrogen bonding, and Van der Waals forces [222].

5.2.5 Sputtered nickel docks

Nickel docking substrates were fabricated using traditional lithographic techniques and RF plasma sputtering. Glass wafers (4 in. diameter, 0.5 mm thickness, roughness <20 Å) were cleaned with acetone and 2-propanol prior to oven-based application of an HMDS adhesion promoter. A negative photoresist (AZ-5214E, MicroChemicals GmbH) was spun on the treated wafer at 6000 rpm for 45 seconds to create a 1.1 μm thick film. After a 2 minute, 95°C softbake, the wafer was exposed on a Karl Süss MA6 aligner for 50 seconds in vacuum contact mode, using a chrome photomask of the desired dock geometries (Photosciences Inc.). Immediately after exposure, the wafer was baked at 105°C for 30 seconds and 115°C for 2 minutes to crosslink the exposed regions (bulk field). Following a 150 second flood exposure (no mask), the wafer was developed in a 1:4 solution of AZ-400K developer diluted in DI water, with gentle agitation for 0.8 minutes (48 seconds), then rinsed thoroughly in DI water and dried. Oxygen plasma (100W forward power, 1 minute) was used to descum the exposed regions before sputtering. RF sputtering of metallic nickel was performed in a Perkin Elmer 8L, using an argon pressure of 12.5 mTorr and 100W forward power for 60 minutes (with a 10 minute presputter). The resulting nickel features, after acetone lift-off of the resist layer, were measured with a contact profilometer.

Dock features were fabricated in 3 geometries (circle, square, and donut) with diameters of 10-40 μm (circle and square) or 5:15-30:90 μm (donut, inner:outer diameter). Docks were arranged in regularly spaced arrays with spacing between docks at 1, 3, 5, and 10 times the diameter, such that all permutations of shape, size, and spacing were represented on each substrate fabricated (see Figure 5.18). Additional substrates were fabricated in the same manner with docks positioned appropriately for bonding of a PDMS channel such that microparticle spinning could be evaluated under flow (see Figure 5.6).

5.2.6 Electroplated nickel docks

Using sputtering to create magnetic features imposes some undesirable limitations that we sought to overcome as we further explored the use of docking substrates. Sputtering is expensive and slow, depositing approximately 8 nm/min. Above thicknesses of 500 nm, the stress generated within the deposited film can cause cracking and delamination, making lift-off resists an ineffective approach. We therefore concomitantly fabricated electroplated versions of the magnetic docking arrays to overcome the thickness limitations associated with sputtering.

Glass wafers were cleaned and coated with a 100 nm copper seed layer (CVC Connexion Sputtering System, 250 W forward power). The copper layer was then masked with a thick ($\sim 15 \mu\text{m}$) layer of AZ-4620 photoresist, spun at 1000 rpm for 120 seconds, and softbaked for 5 minutes at 95°C. The wafer was exposed in vacuum contact mode with the chrome photomask for 135 seconds at 5 mW/cm², then developed in 1:4 AZ-400K developer solution for 5 minutes. Prior to electroplating, a 1 minute, 100 W plasma descum was performed to remove any remaining residue and ensure good electrical conduction in the exposed regions.

Electroplating was performed using a commercially available nickel electroplating kit (Caswell #NP3). The prepared wafer was attached to an acrylic holder using copper tape. Tape was applied to the edges of the wafer where the protective resist layer had been removed with an acetone soaked cotton swab. A digital multimeter was used to confirm good electrical contact between the copper seed layer on the wafer and the power supply connector. Before introducing the wafer to the electroplating solution, it was sonicated in DI water for 3 minutes to remove air bubbles trapped in the resist features and ensure uniform plating. After sonication, the wet wafer was transferred to the electroplating bath, which was maintained at 50°C during plating. A sacrificial nickel anode was submerged on the opposite side of the bath, and connected to the positive terminal. The wafer was then connected to the negative terminal of the power supply. Electroplating of the docks was performed at 100 mA forward current and a voltage of 1.52 V for 10 minutes. After plating, the wafer was removed and rinsed thoroughly with DI water, then dried with nitrogen.

The plated wafer was rinsed in acetone to remove the photoresist layer. The copper layer was then removed by etching for 20 seconds in Aluminum A Transene etchant. The etch time was formulated to completely remove the copper seed layer around the nickel docks, but avoid undercutting them and compromising their adhesion. After etching, the wafer was rinsed with DI water, dried, and diced into individual substrates for use in experiments.

5.2.7 Microfluidic channels

Microfluidic channels were molded in polydimethylsiloxane (PDMS) using the same procedures as in previous work [161]. Briefly, a silicon wafer was patterned with a protective photoresist, and reactive ion etching was used to create a negative impression of the channel geometry. After etching, the mold was coated in a fluorinated silane to facilitate release of cured PDMS. Sylgard 184 (Dow Corning) was mixed in a 10:1 ratio, degassed, and poured over the mold. After curing for 24 hours, the mold was baked for 1 hour at 75°C. The cured channels were diced and removed from the mold prior to bonding. Bonding was performed using 24 seconds of oxygen plasma (International Plasma Corporation, IPC Barrel Etcher) with a forward power of 50 W and 1 Torr O₂. After carefully bringing the PDMS channels into contact with the glass substrates, the bonded devices were heated to 75°C for 2 minutes to strengthen the bond.

Channels were secured in a removable, non-magnetic clamping sandwich that fit snugly into the central helmoltz coil on the microscope stage. A 20x objective was used for all flow experiments. Samples were introduced through polyether etherketone (PEEK) tubing inserted into the inlets and outlets of the channel, and flow rates were controlled with two separate syringe pumps (KDS Legato 110, BS-8000 DUAL, Braintree Scientific). Separate pumps allowed us to control the ratio of inlet flow rates and adjust the location of the interface between the particle and buffer streams (see Figure 5.7).

5.2.7.1 Lateral migration of micro-particles between streamlines When a particle is exposed to a unidirectional shear flow, two kinds of forces can act on the object surfaces. The first force is parallel to the direction of the flow, which is the drag force that

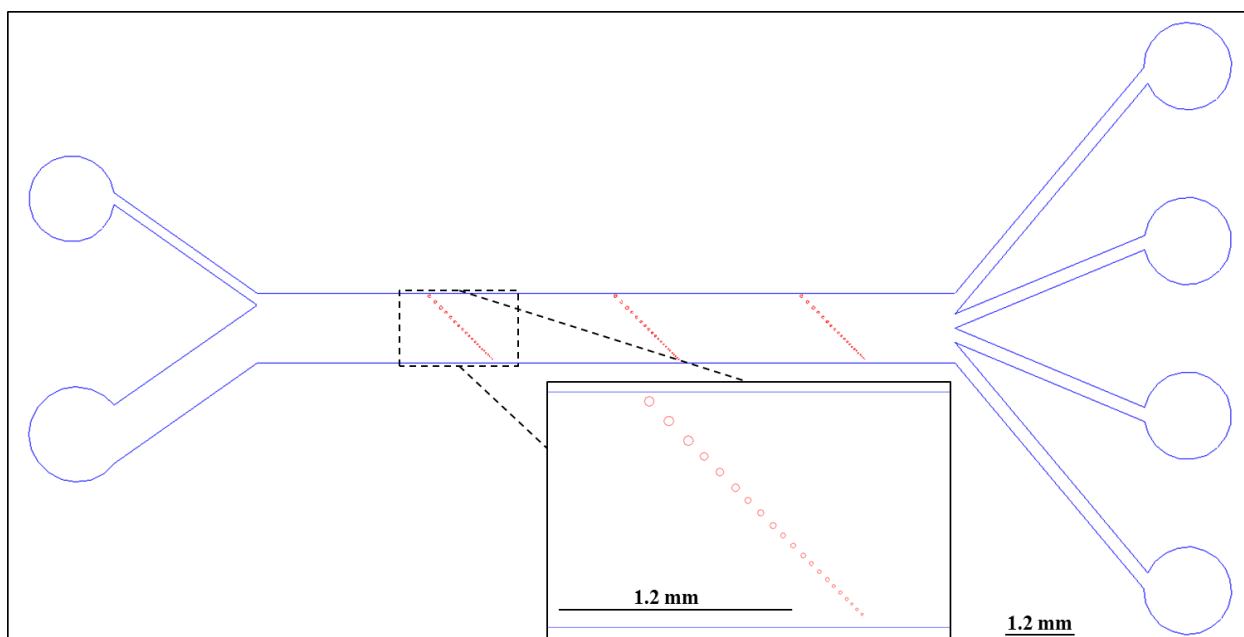


Figure 5.6: AutoCAD design of masks for microfluidic channel (blue outline) and magnetic docks (red circles). The narrow inlet (upper left inlet) concentrates particles along the top of the channel. The docks are arranged to allow spinning microrobots to hand off captured particles, moving them through the buffer flow (lower left inlet) and toward successively lower outlets (right).

Boundary location vs. ratio of inlet flow

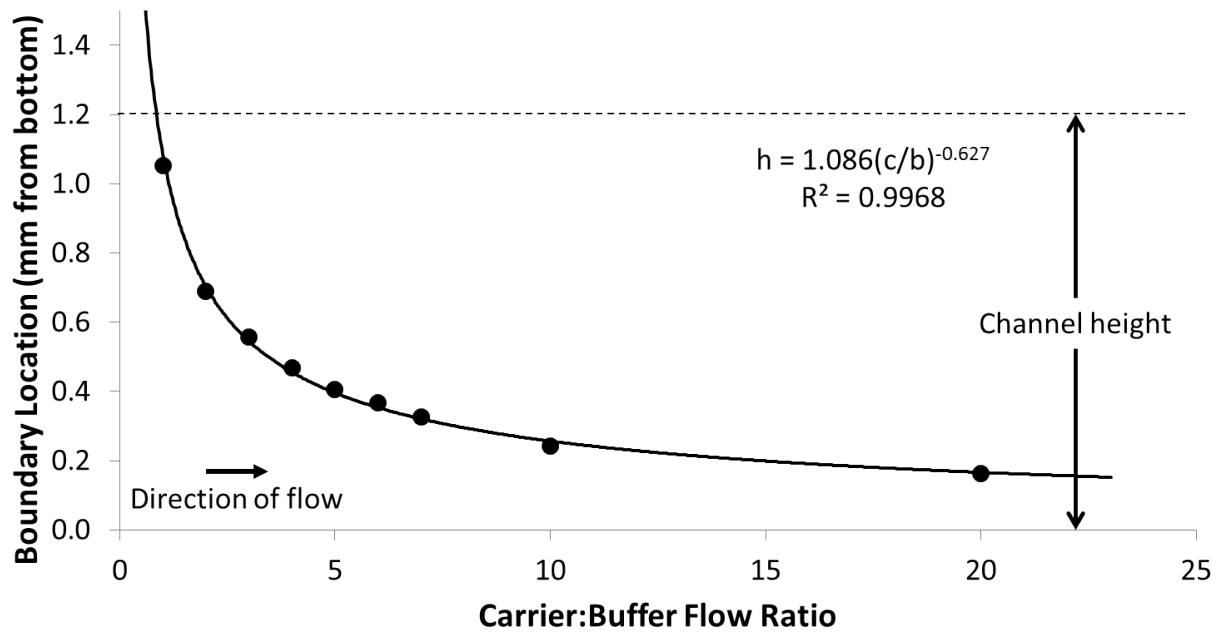


Figure 5.7: Plot of the lateral location of the fluid interface between the wide and narrow inlets. The narrow inlet was designated the “top” of the channel, with the wide, buffer inlet at the “bottom”. A power fit shows good agreement with the experimental data, allowing us to predict the inlet flows needed to locate the interface at any given dock on the substrate.

acts to accelerate the particle inside the flow until it is force-free in the same direction. The other force is perpendicular to the direction of the flow, which is usually referred to as the “lift force”. This force would cause lateral migration of the particle between streamlines. However, such lift forces do not always exist. In fact, a theoretical study has shown that under Stokes flow conditions where inertial effects are completely negligible, no lateral force would exist in any unidirectional flow due to the linearity of the system [223]. Therefore, inertial effects are necessary for inducing lateral migration of particles between streamlines in shear flows.

Many studies have been carried out on the lateral migration of particles inside confined environments such as microfluidic channels. Typically, the inertial lift forces experienced by a particle arises from two sources: wall effects and the interaction between the particle and the shear gradient of the flow. The former always acts to push the particle away from the wall, while the direction of the latter is more complicated. Two effects can contribute to this part of the lift force. The first effect arises from any simple shear component of the flow velocity and follows the observation by Saffman [224, 225] that if the the particle lags behind the local undisturbed flow, such a force acts to push the particle up the shear gradient. The second effect is due to the curvature of the velocity profile and exists only when there is a gradient of shear [226]. Therefore, the lift force ultimately experienced by the particle would be the total balance between these three effects. Figure 5.8 shows how these three effects alter the lateral migration of a particle in the presence of a 2D quadratic flow near a wall. In a simple shear flow, the lift forces arising from the Saffman effect can be calculated by Equation 5.2.

$$F_{lift(saff)} = 6.46\rho a^2\nu^{0.5}v_{pf}\dot{\gamma}^{0.5}, \quad (5.2)$$

where a is the radius of the particle, ρ is the density of the fluid, ν is the viscosity of the fluid, v_{pf} is the particle’s velocity relative to the local velocity of the undisturbed flow at its center, and $\dot{\gamma}$ is the shear rate. The total lift force of a particle immersed in Poiseuille flow in a straight channel has been found to be [227]:

$$F_{lift} = \frac{6a^4\rho U_f^2}{\pi H^2} f(d/H), \quad (5.3)$$

where U_f is the center flow velocity, H is the width of the channel, d is the distance of the particle from bottom wall and $f(d/H)$ is a coefficient associated with particle's lateral position inside the channel. Such a force is hard to observe when Re is very small.

When a micro-robot spins inside a microfluidic channel in the presence of background flow, it still generates a local rotational flow field around it (Figure 5.1). The disturbed flow region can be treated as the linear superposition of the background flow and the induced rotational flow due to the linearity of the system at very small Re . The inertial lift force on particles still exists inside the disturbed flow region, but could be significantly different than anywhere else inside the channel due to the local rotational flow. The presence of the induced rotational field could generate a large shear gradient inside the flow region, which could significantly amplify the inertial effects, and hence the lift force. In addition, if the micro-robot is placed close to the wall, it also concentrates the streamlines in the gap between it and the wall. Therefore, particles could migrate to another streamline inside the gap much more easily. Such migration would be more observable when the particles leave the disturbed flow region, as the flow cross-section widens and returns to normal speeds. When the particles are traveling inside the rotational flow region, they also experience a centrifugal force due to angular acceleration as they orbit around the rotating robot. Such force acts to push the particles away from the rotating robot. Therefore, the net lateral force the particles experience inside the rotational flow region would be the combination of all previously introduced inertial lift effects plus the centrifugal force. The final migration of particles is determined by this net lateral force.

5.2.7.2 Rotational flow induced by spinning spherical micro-robots inside a microfluidic channel Numerical simulations were carried out to understand the flow pattern inside a microfluidic channel in the presence of a spinning spherical micro-robot. A commercial finite-element software COMSOL Multiphysics 4.3 with the laminar flow interface was used for the simulations. The microfluidic channel was modeled as a rectilinear block with dimensions of $1000\ \mu\text{m}$ (length) \times $100\ \mu\text{m}$ (width) \times $60\ \mu\text{m}$ (height) with three spheres each of a diameter of $20\ \mu\text{m}$ located at the center of its length. Figure 5.9 shows the established model. An average flow velocity of $100\ \mu\text{m/s}$ was specified on one end of the block as the

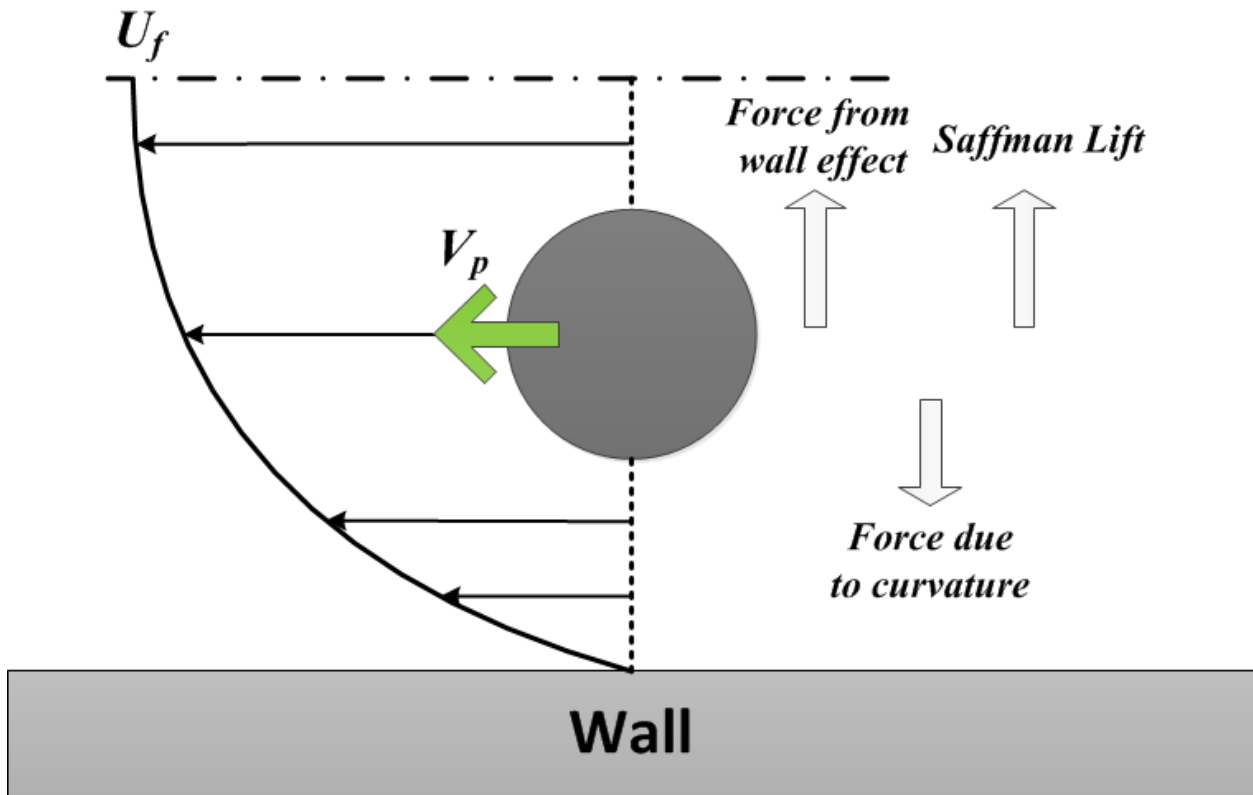


Figure 5.8: Diagram of the different forces influencing the motion of a microparticle under laminar flow (U_f).

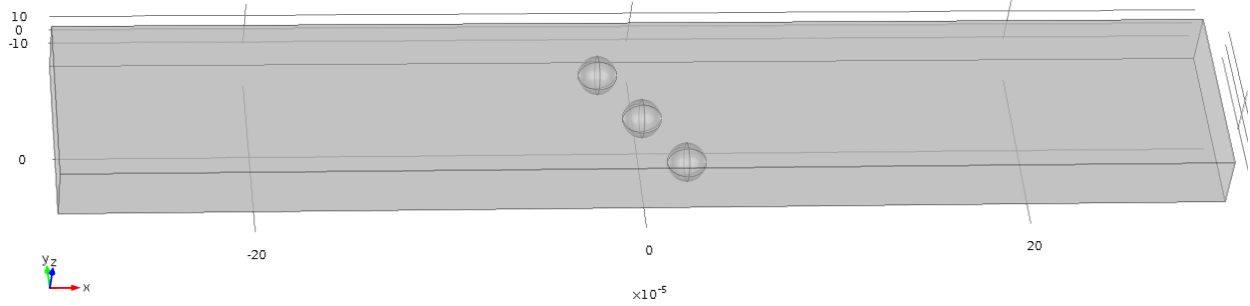


Figure 5.9: The microfluidic channel was modeled as a rectilinear block with dimensions of $1000\ \mu\text{m}$ (length) \times $100\ \mu\text{m}$ (width) \times $60\ \mu\text{m}$ (height) with three spheres each of a diameter of $20\ \mu\text{m}$ located at the center of its length.

inlet, while the other end was specified as the outlet with zero normal stress. Modeling of rotation of the spheres was achieved by specifying the linear velocities on the surfaces of the three spheres according to the desired rotation speed of 15 Hz. A total of 366,957 tetrahedral elements were used in the simulations.

The first set of simulations was to study the influence of gap distance between the sidewall and the nearest robot on the flow pattern. The streamlines of the flow inside the channel for different gap sizes on the equatorial plane of the spheres ($z = 10\ \mu\text{m}$) are shown in Figure 5.10. It was observed that as the gap size increases, the portion of flow that is compressed through the gap increases as well. When the gap is too small, vortices could form in front of the gap, which are undesirable for the purpose of sorting. To further examine the flow velocity profile at the gap, we plotted the velocities at the gap along the width of the channel on $z = 10\ \mu\text{m}$ (Figure 5.11). The velocity profiles indicate that a narrower gap would result in a larger shear gradient at the gap, which could lead to a more significant lateral force for particle migration. Therefore, there exists an optimal range of gap size for the purpose of sorting. Such range is expected to be around 0.7–1 times the radius of the spherical micro-robot according to the simulation results.

The second set of simulations studied the influence of separation between robots. The streamlines of the flow inside the channel for different gap sizes on the equatorial plane of

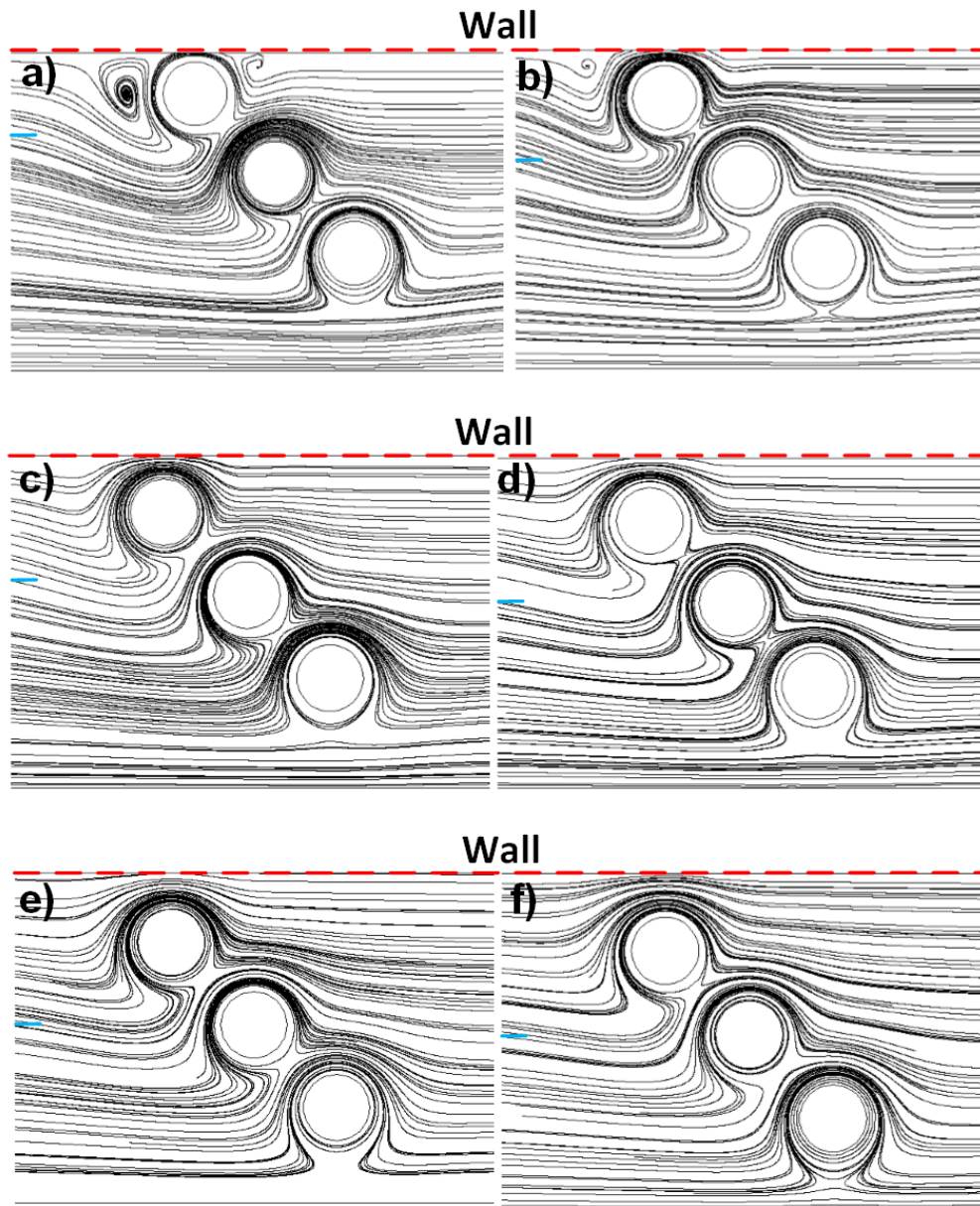


Figure 5.10: Streamlines were taken on the equatorial plane of the spheres at $z = 10 \mu\text{m}$. a) Gap size = 0.3 radius of sphere (R). b) Gap size = $0.5R$. b) Gap size = $0.7R$. b) Gap size = $0.9R$. b) Gap size = $1.1R$. b) Gap size = $1.3R$. The short blue solid dash indicates how much flow is compressed through the gap.

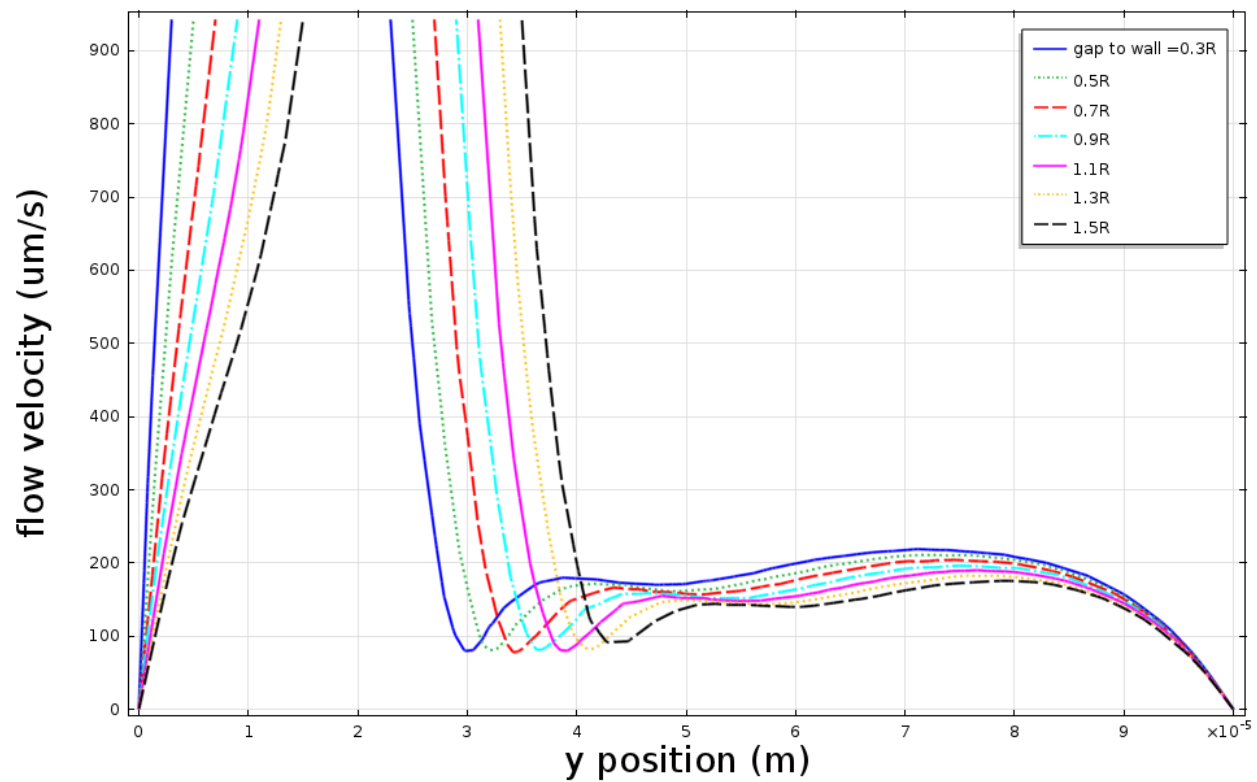


Figure 5.11: Profile of fluid velocity at $z = 10 \mu\text{m}$, with varying gap-to-wall ratios as a function of microsphere radius R .

the spheres ($z = 10 \mu\text{m}$) are shown in Figure 5.12. As the separation decreases, the overlap between individual rotational flow fields induced by each micro-robot increase, which make it easier for micro-particles to be conveyed down the width of the channel with the streamlines once they pass the gap between the first robot and the top wall and get trapped by the rotational flow induced by the first robot. However, since the micro-robots are magnetic, they would attract to each other if the separation was too small. From experimental observation, the minimum separation that could still prevent attraction between robots was about $4R$, depending on how strong the robots were magnetized. A separation of $4.5R$ or above should be used to achieve stable, separate rotation of each micro-robot inside the channel.

5.2.7.3 Magnetic docking Magnetic micro-docks were made of Nickel, which is a soft magnetic material. Such soft magnetic material could only be magnetized when exposed to an external magnetic field, applied by a nearby magnetic micro-robot or by the electromagnetic coil system in this case. To examine whether or not such magnetic docks are capable of holding the magnetic micro-robots in place under a strong background flow when global magnetic field is applied by the coils, numerical simulations were carried out using the same finite-element package COMSOL Multiphysics 4.3 with the AC/DC module. The micro-robot was modeled as a $30 \mu\text{m}$ diameter sphere placed on top of a dock with an outer diameter of $30 \mu\text{m}$ and a thickness of 500 nm . Two types of dock shape were examined: disk-shaped and donut-shape with an inner diameter of $10 \mu\text{m}$. Figure 5.13 shows the established model. A downward magnetic field (B_z) was applied in the whole space filled with non-magnetic material, while the magnetization of the micro-robot was specified in the negative z -direction as the magnetic micro-robot would always tend to align its magnetization with the external field. The relative magnetic permeability of both the Nickel dock and the NdFeB micro-robot was also specified. A total of 1,881,243 tetrahedral elements were used in the simulations.

In the first set of simulations, the influence of three different parameters on the interactive forces on the micro-robot applied by the micro-dock in z -direction (F_z) were examined: field strength of B_z , relative permeability of the docking material, and the strength of magnetization of the micro-robot. The results are plotted in Figure 5.14. It is observed that the disk-shaped docks can generally provide stronger holding force F_z than donut-shaped

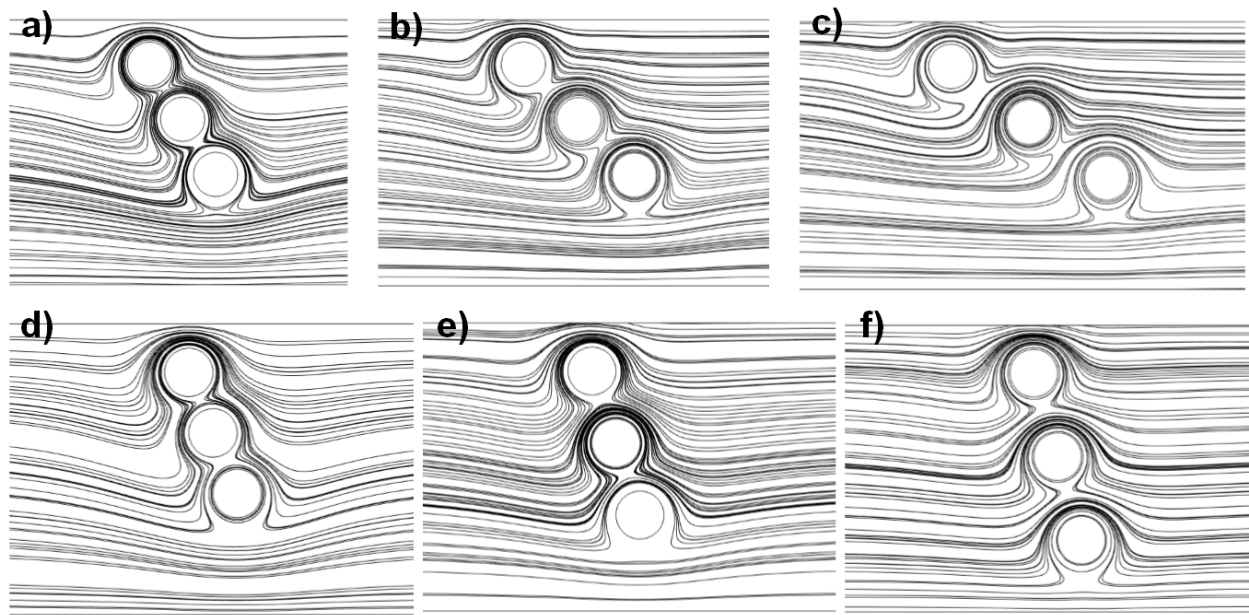


Figure 5.12: Streamlines were taken on the equatorial plane of the spheres at $z = 10 \mu\text{m}$. For a)–c), the vertical separation was fixed at $2.5R$ while horizontal separation varied from $1.5R$ for a), $2R$ for b) to $2.5R$ for c). For d)–f), the horizontal separation was fixed at $1R$ while vertical separation varied from $2.5R$ for d), $3R$ for e) to $3.5R$ for f).

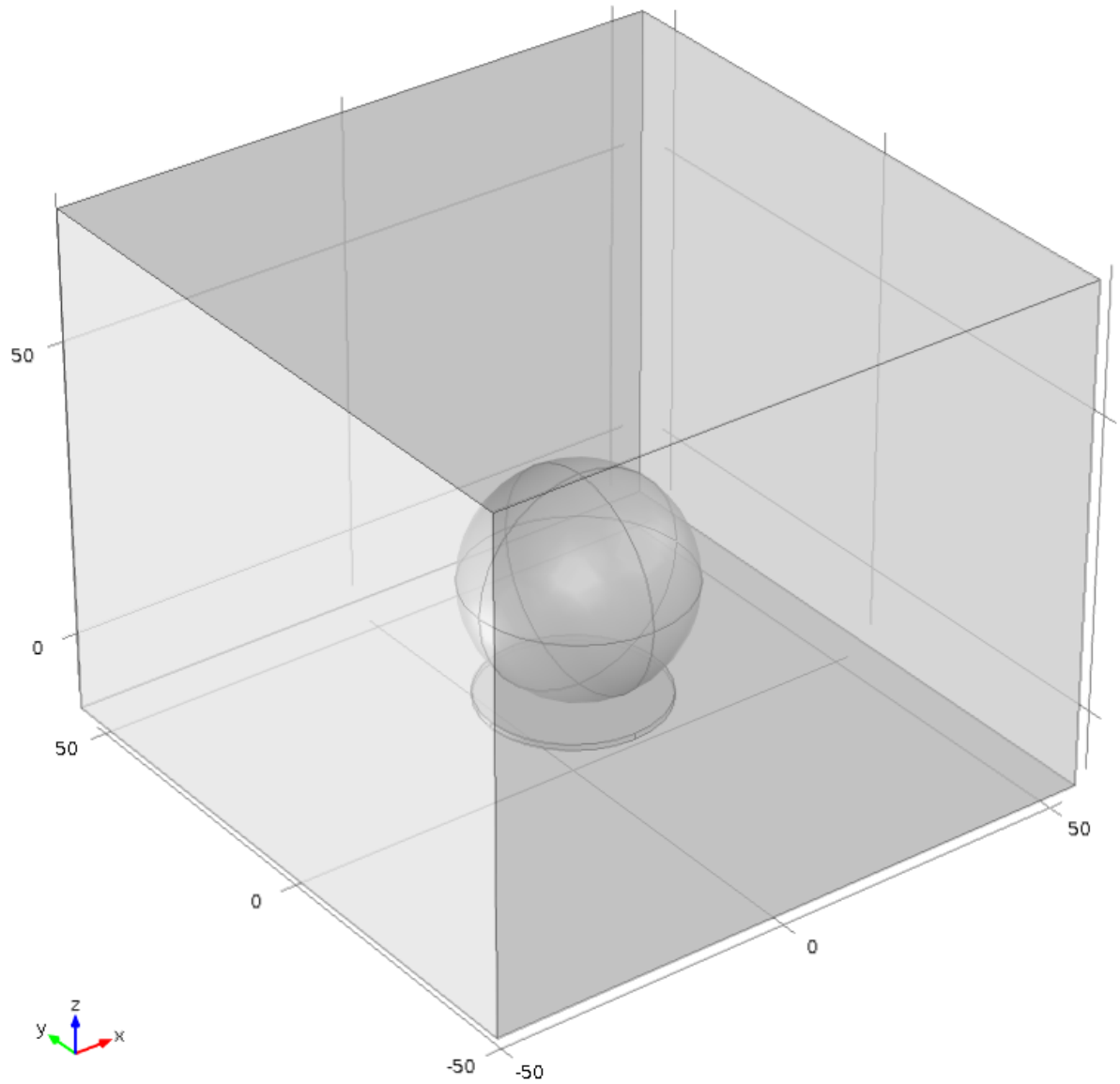


Figure 5.13: The micro-robot was modeled as a $30\ \mu\text{m}$ -in-diameter sphere placed on top of a dock with an outer diameter of $30\ \mu\text{m}$ and a thickness of $500\ \text{nm}$.

dock, because the former has more magnetic material in the same volume. Another general observation is that all three parameters have a positive effect on F_z . While F_z increases linearly with B_z , it first increases rapidly with an increasing relative permeability, and then approaches saturation after a relative permeability of 1000. The magnetization of the micro-robot has a much stronger effect on F_z than the other two parameters.

In the second set of simulations, we examined how the lateral misalignment between the robot and the dock would affect F_z and the lateral interactive force - the centric force (F_{ct}). In these simulations, all the parameters were kept constant except for the lateral position of the micro-robot on the dock. The results are plotted in Figure 5.15. Unlike in the zero-misalignment case where F_z remains attractive, F_z shifts between attractive and repulsive in the non-zero misalignment case. The attractive F_z peaks at a relative misalignment of around $0.6R$, and then drops till it becomes repulsive as misalignment increases for both disk-shaped and donut-shaped dock. For the centric force F_{ct} , it remains repulsive when the relative misalignment is smaller than $0.6R$, and shifts to attractive as misalignment goes above $0.6R$. These results indicate that there could be two possible positions for the micro-robot to stay on the dock in steady state, one is at the center of the dock where the holding force F_z is at its maximum, and the other is at a distance of about $0.6R$ from the dock center. However, the robot cannot stay stably on the first position as any small perturbation would result in a radial force that pushes the robot away from this position.

Now it is possible to compare the drag force experienced by a spherical micro-robot under a strong background flow. Under the Stokes drag assumption, the drag force experienced by a sphere in a unidirectional flow can be calculated by:

$$F_{drag(stokes)} = 6\pi\rho\nu Rv_{pf}. \quad (5.4)$$

For a fixed $30\mu\text{m}$ spherical robot under a very strong flow of 1mm/s flow rate in water, the drag force is estimated by Equation 5.4 to be approximately 0.3nN , which is less than 5% of F_z on a weakly magnetized micro-robot placed at the center of the dock. Therefore, such a robot can stay at the center of the dock as long as the friction coefficient between the robot and the dock is greater than 0.05. In real experiments, the flow rate would not reach the value of 1mm/s , and hence the nickel docking should be functional. Increasing the

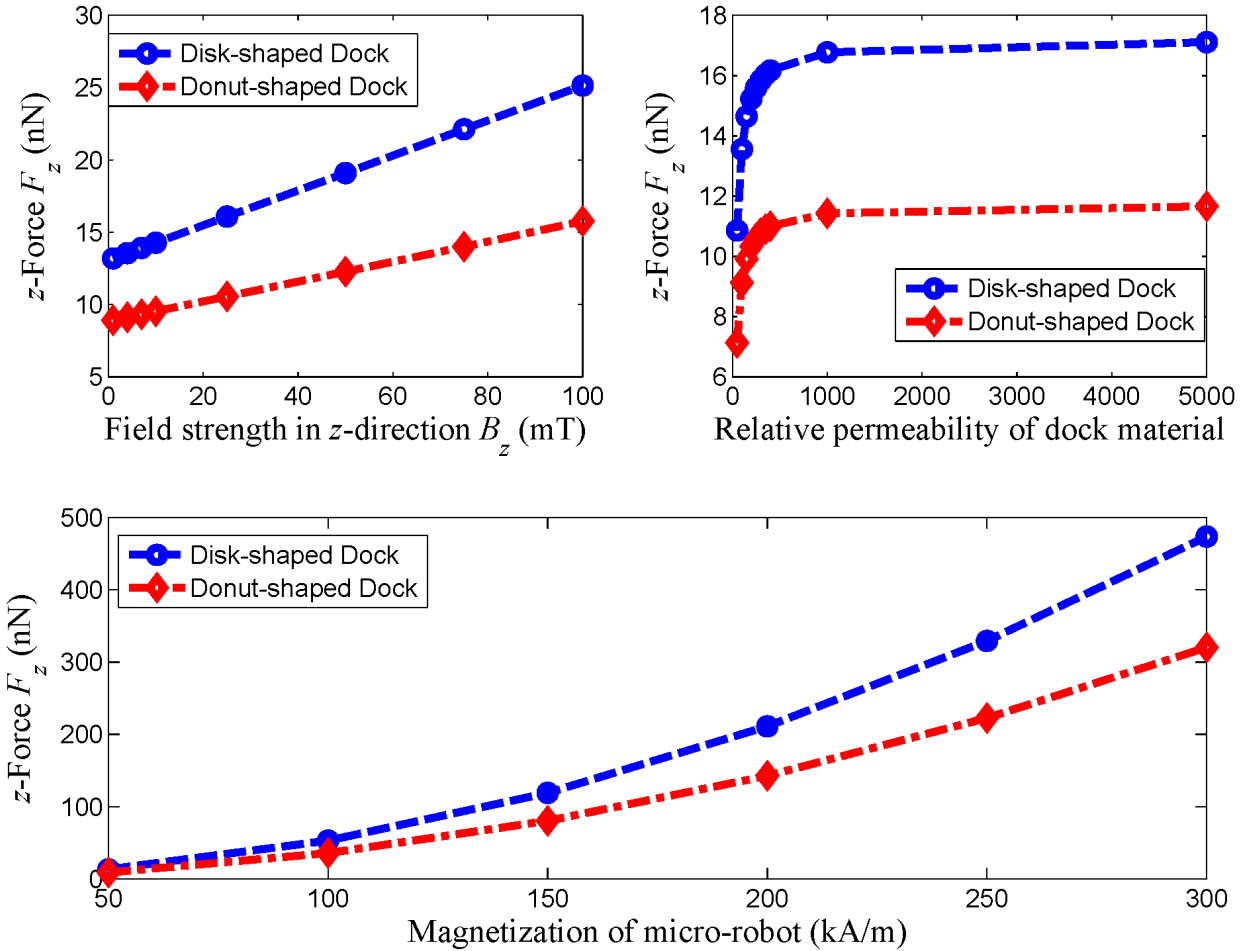


Figure 5.14: a) B_z varied while magnetization of the micro-robot and the relative permeability of dock were kept constant at 50 kA/m and 100, respectively. b) The relative permeability of dock varied while B_z and magnetization of the micro-robot were kept constant at 4 mT and 50 kA/m, respectively. c) Magnetization of the micro-robot varied while B_z and relative permeability of the dock were kept constant at 4 mT and 100, respectively.

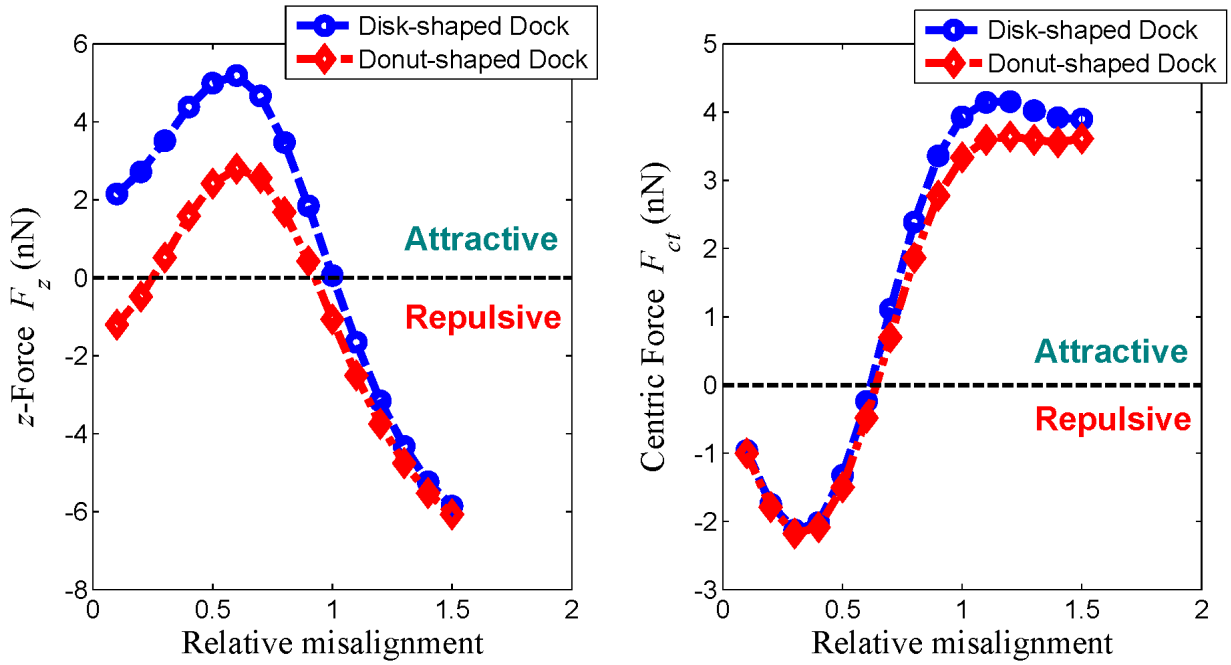


Figure 5.15: B_z , relative permeability of the dock and magnetization of the micro-robot were kept constant at 4 mT, 100 and 50 kA/m, respectively. Lateral misalignments were normalized by radius of the robot. a) Influence on the interactive force in z -direction (F_z) b) Influence on the interactive force in radial direction (F_{ct}).

magnetization of micro-robot would be the most practical way to secure the functionality of the nickel docking.

5.3 RESULTS

5.3.1 Composite resist characterization

Characterization of printing parameters was performed using line tests, as seen in Figure 5.16. The TPP laser is rapidly scanned through a wide range of power and speed parameters, creating narrow lines of polymerized resist on the glass surface that can be imaged via SEM. Line tests for scan speeds from 100-10,000 $\mu\text{m/s}$ and powers from 0-100% were performed for all 6 concentrations of IP-G composite to indicate the range of feasible parameters for printing. We found SU-8 adhesion to glass too weak to reliably perform and image line tests or print 3-dimensional structures. We therefore chose to perform the remaining experiments using IP-G composites.

5.3.2 3D printed microrobots

A variety of magnetic IP-G composite structures were fabricated using TPP. Printed structures were well-formed and structurally sound in resist composites up to 1 vol% (Figure 5.17). At concentrations of 2 and 4 vol%, the viable range of printing parameters narrowed considerably, resolution dropped, and layer-to-layer as well as structure-to-glass adhesion was substantially reduced.

Rotation of 1% structures in applied fields up to 8 mT were limited to ~ 1 Hz, with no rotation observed for 0.5% and 0.1% composites. Stiction occurred in the majority of 3D prints, even when post-development drying was avoided, requiring physical detachment by force applied with a glass needle micromanipulator.

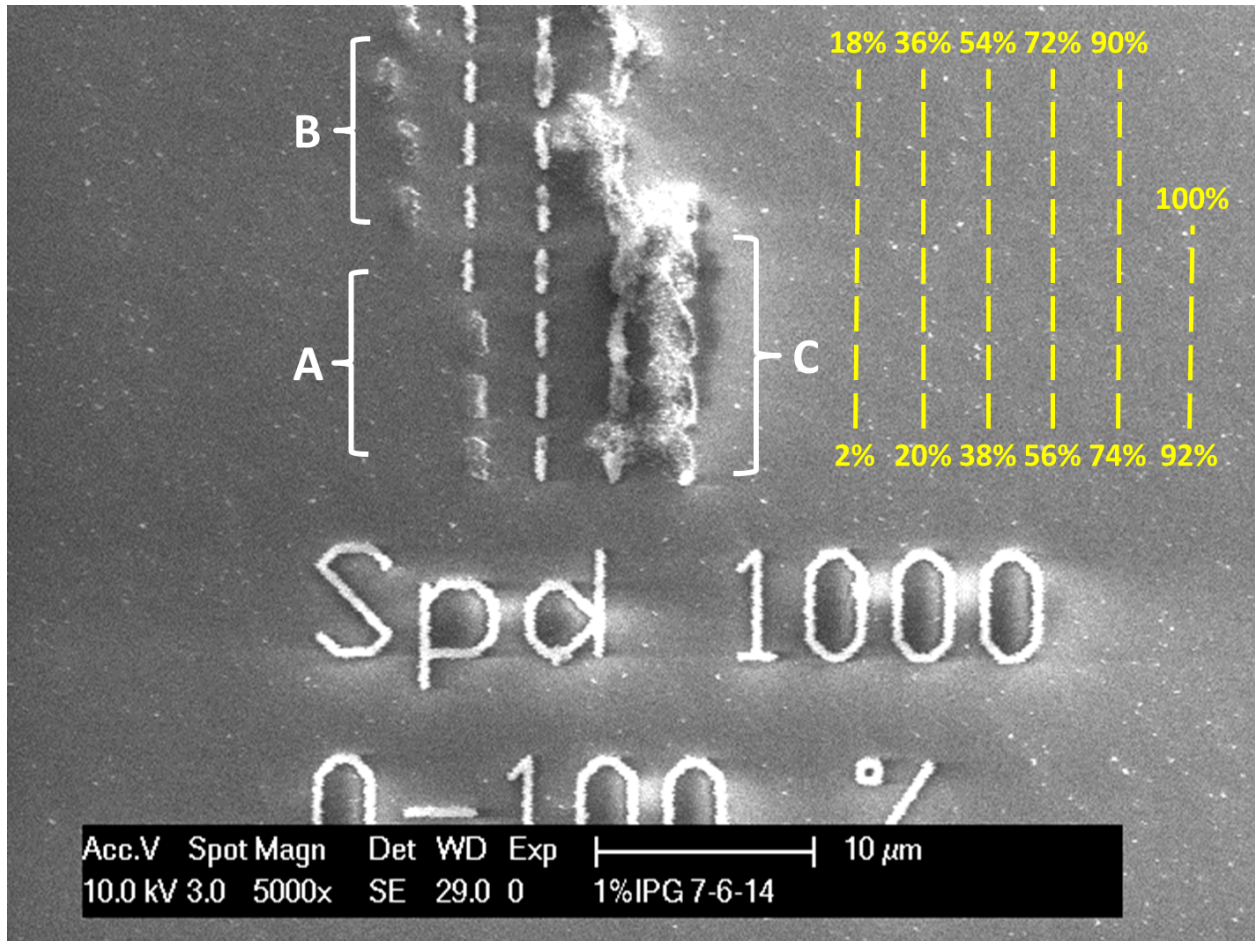


Figure 5.16: Sample SEM image of the line test used to characterize writing parameters. Sample is IP-G resist containing 1 vol.% magnetite MNPs. Lines are written with increasing power from left to right, bottom to top, in a snaking fashion, with power changing in 2% increments from 0-100%. On the left-hand side, lines are missing (A) or poorly polymerized (B) due to insufficient power and poor adhesion. On the right, excessive power caused localized heating, monomer degradation, and gas formation that destroyed the feature resolution (C).

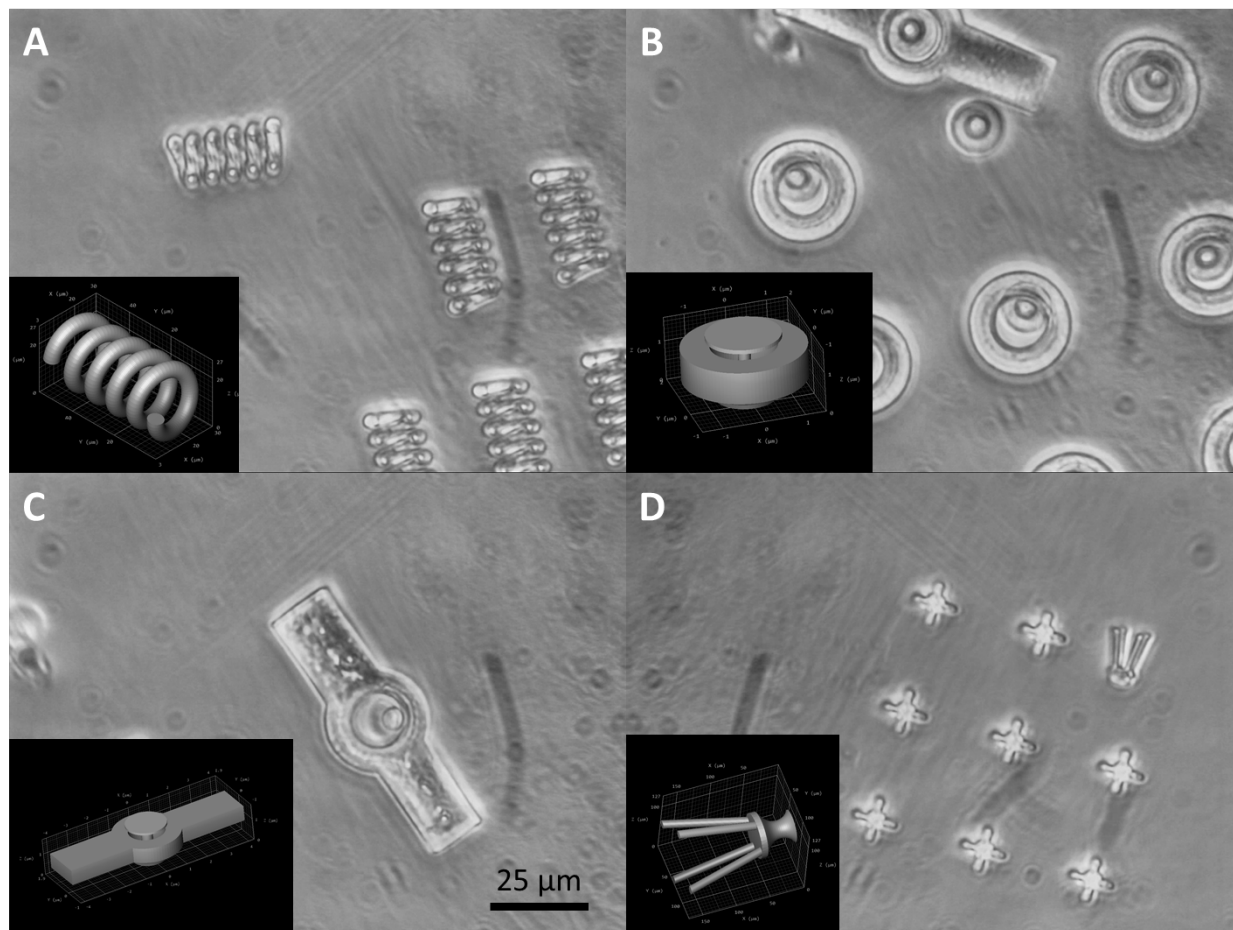


Figure 5.17: Brightfield microscopy of 3D printed microrobots in water. Various structures were designed: (A) corkscrew, (B) spinning disk, (C) spinning bar, and (D) flagella/sputnik. Structures are printed in IP-G resist with 1 vol% Fe_3O_4 MNPs. Structures were well formed but could only spin at ≤ 1 Hz. Structures with 2% MNPs were poorly formed and failed to adhere properly to the substrate.

5.3.3 Magnetic docking substrates

Docking substrates were well formed and consistent in thickness when patterned with RF sputtering. One hour of sputtering time yielded film thicknesses of 490-500 nm, and approached the limitations of lift-off resist patterning with nickel. Longer times often resulted in film cracking or delamination due to internal stress. Electroplated docks were less uniform, and exhibited thicknesses ranging from 1.2 to 3.5 μm within single docks. Thickness was greater at the edges of the features, creating a concave structure that might beneficially “cradle” the microspheres by conforming to a semispherical shape.

In practice, we found little difference between sputtered and electroplated docks. Stable docking appeared to be more dependent on the structure and magnetization of individual microspheres placed on the docks, with some microspheres performing well on all dock sizes and shapes, while others exhibited poor attraction and spinning, even when magnetized in the same field. Microstructural differences are likely responsible for the inconsistent magnetization of the spinners.

Magnetic microspheres could be successfully localized to individual docks by rolling them along the substrate using rotational fields parallel to the substrate. Movements in the x-y plane were mapped to the arrow keys of a computer keyboard for easy manual control. Once positioned, the microsphere exhibited a natural tendency toward the dock. The downward force applied by the dock on the particle (holding force) could be increased using a vertically oriented electromagnetic coil. Stable rotational speeds of ≥ 40 Hz could be obtained in static fluid environments using field strengths of only 1 mT. Higher speeds are likely possible, but could not be visually confirmed due to the frame rate of the camera used. Under fluid flow, higher vertical fields were required to keep the microspheres on the docks. Increased downward force, and therefore surface friction, reduced the maximum rotation to ~ 20 Hz with 1.5-3.0 mT rotational field strength.

5.3.4 Size-dependence of micro-particle trajectory in microfluidic channels

One microsphere was placed on the topmost nickel dock within the microfluidic channel, and polystyrene beads of 5 μm , 10 μm , and 20 μm were injected through the top inlet in

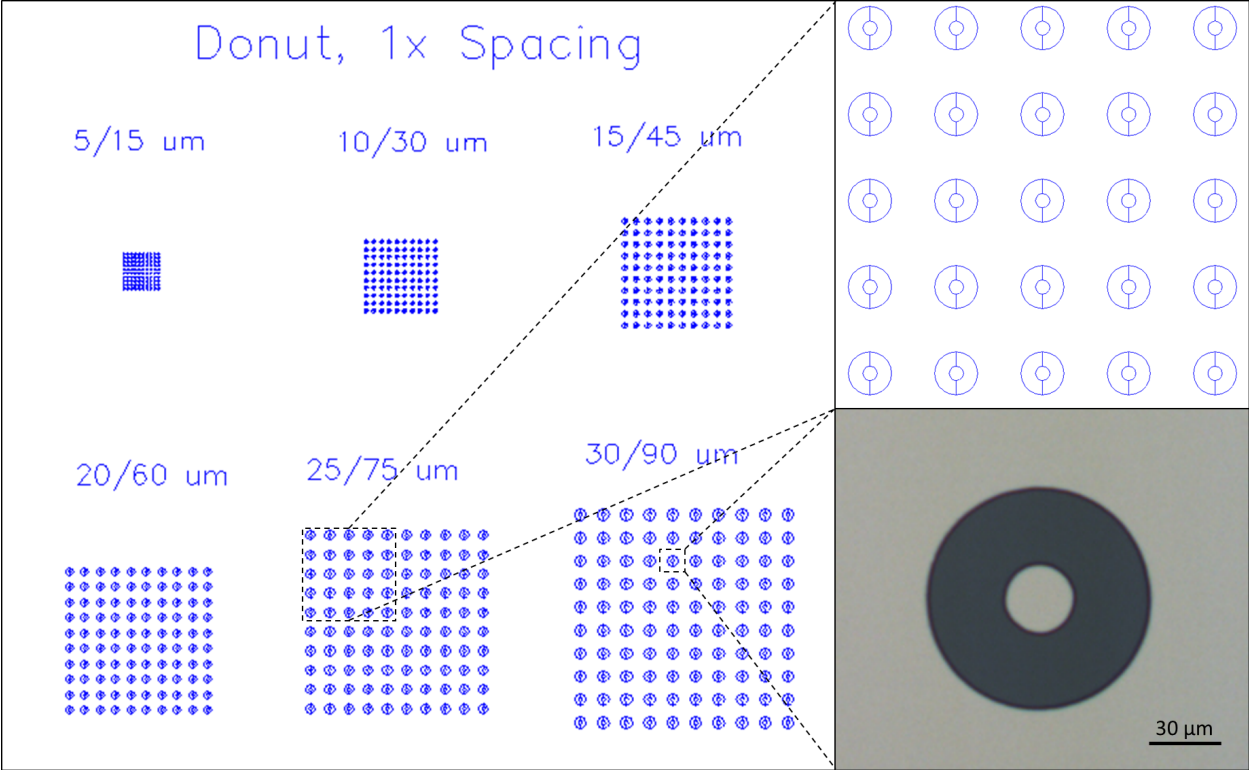


Figure 5.18: AutoCAD model of subsection of magnetic docking arrays, showing donut shaped docks with 1 diameter spacing. Diameters are labeled on the substrate as inner/outer diameter in microns. Brightfield microscope inset of sputtered nickel dock with 30/90 μm dimensions (lower right).

separate experiment runs. Buffer flow through the bottom inlet was adjusted to locate the interface of the two inlet flows just above the midpoint of the micro-robot, ensuring that most particles passed between the micro-robot and the channel wall when no magnetic field was applied. After establishing stable flow, a rotational field was applied and the rotational flow around the microsphere was induced. The polystyrene beads passing through the disturbed flow region displayed different responses to the induced rotational flow based on their sizes and left the flow region with distinguishable differences on their displacements along the width direction of the channel from their original trajectories. Results of analysis of videos taken from experiments are summarized in Figure 5.19 to show the size-dependence of vertical displacement Δy of particles before entering and after leaving the region significantly disturbed by induced rotational flow. Both $5\ \mu\text{m}$ and $10\ \mu\text{m}$ polystyrene beads exhibited positive Δy 's, meaning that they were pulled away from the channel sidewall in the rotational flow region, while the $20\ \mu\text{m}$ beads exhibited a negative Δy , which means they were pushed closer to the sidewall. The size-dependent displacement of particle via induced rotational flows potentially enables separation of particles with different sizes in continuous flow.

5.3.5 Manipulation in microfluidic channels with multiple micro-robots

Microspheres were arranged consecutively onto the nickel docks within microfluidic channels, and polystyrene beads of varying sizes were injected through the top inlet. Buffer flow through the bottom inlet was controlled to adjust the interface of the two inlet flows just above the midpoint of the first micro-robot. By ensuring that most particles passed between the micro-robot and the channel wall when no field was applied, we ensured that the particles would be forced to pass within capture range. After establishing stable flow, a rotational field was applied, and particles were deflected from their normal paths, with some particles exchanging orbits from one micro-robot to the next (hand-off).

Analysis of the flow videos revealed that hand-off occurred more frequently with larger sized particles, and created an overall gradient of particle sizes. Figure 5.20 shows analysis of a 3,654 frame video, with automated particle detection (ImageJ) in the rightmost $40\ \mu\text{m}$

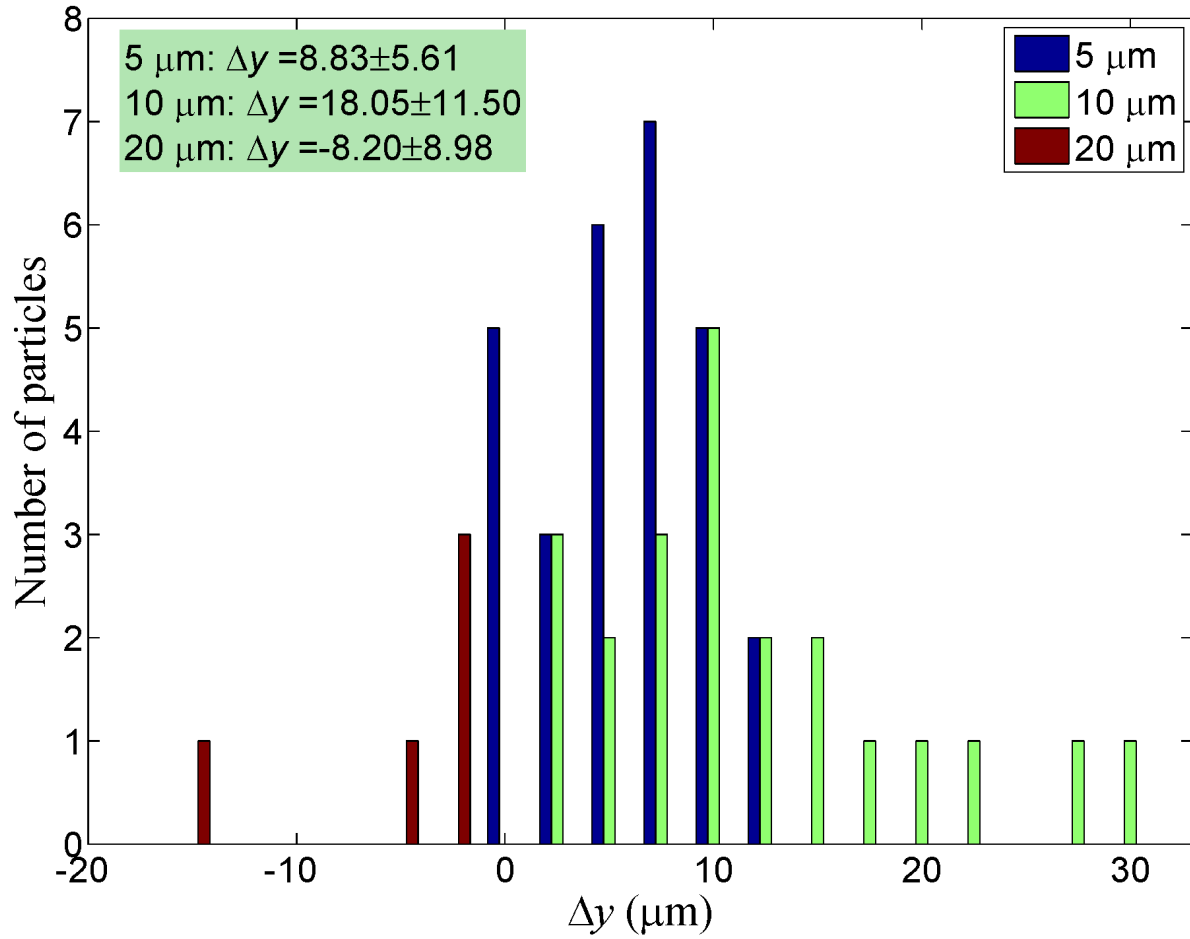


Figure 5.19: Size-dependent vertical migration of particles in induced rotational flow. Flow rate is $4.5 \mu\text{L}/\text{min}$ (channel height $76 \mu\text{m}$). Field strength = 1.5 mT , rotation frequency = 15 Hz . Magnetic micro-robot size was $56 \mu\text{m}$ in diameter.

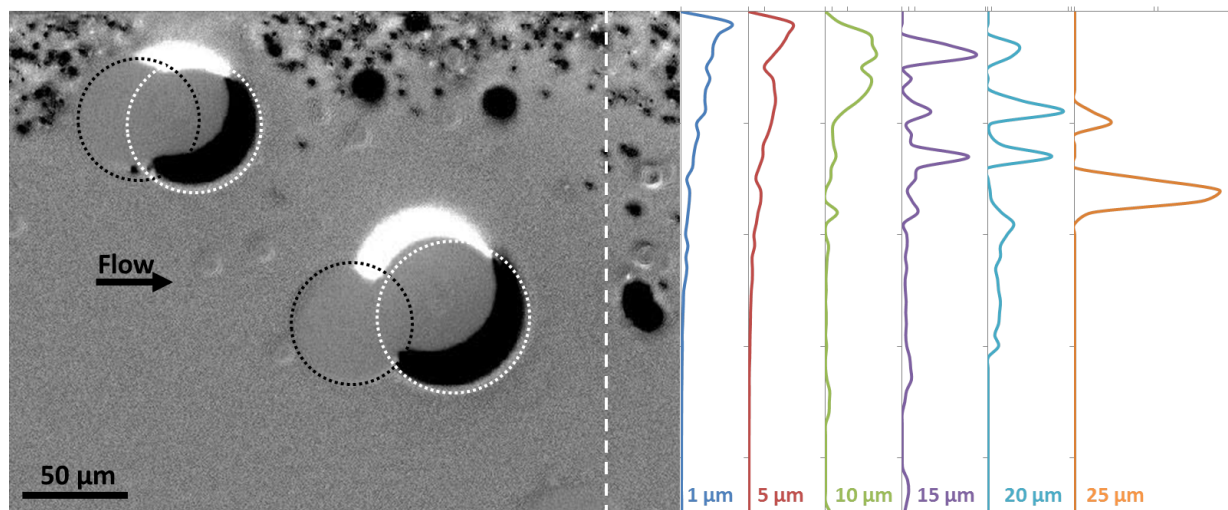


Figure 5.20: Freeze-frame of high-speed footage of spinning microspheres (white dotted outline) on magnetic docks (black dotted outline) with polystyrene beads of various sizes. Vertical distribution (in $5 \mu\text{m}$ increments) of particle sizes are shown for bins around discrete microsphere diameters. Distributions are normalized to the total number of particles in each bin. Flow rate is $3.03 \mu\text{L}/\text{min}$ (channel height $76 \mu\text{m}$), number of frames combined = 3,654. Field strength 1.5 mT, rotation frequency = 20 Hz.

of the images. Median particle distance from the top of the channel increased with particle size in all but the 10 μm group.

5.4 DISCUSSION

5.4.1 IP-G composites exhibit superior patterning, adhesion, and consistency

Much of the existing work involving TPP with and without MNP composites uses SU-8 resist [228, 229, 221, 230, 213], which is widely used in the MEMS field for its many favorable properties, including excellent chemical and thermal stability and good mechanical properties [231, 230]. We began our tests with SU-8 2010 (Microchem), but found the adhesion to glass substrates be poor, and most structures printed in SU-8 were detached during the development process. Weak adhesion to glass is a known issue with SU-8, though other studies had either used structures with large surface footprints [229] or structures that were not designed to detach from the surface [221], so adhesion had not been a limiting factor.

Pretreatment of the glass wafers with HMDS adhesion promoter yielded little improvement in quality. Some successful structures were patterned using a hard-baked adhesion layer of SU-8 spun over the wafer surface, similar to Witzgall et al. [101] (our procedure can be found in APPENDIX D). Bonding SU-8 to PDMS then becomes an additional challenge, as silanol groups do not react with SU-8, so the PDMS must instead be treated with nitrogen plasma, generating amino groups on the PDMS surface. This method, however, can only bond to SU-8 layers that have not been cured above 95°C, leading circularly back to the SU-8/glass adhesion issue [232]. We also found SU-8 to be much more sensitive to laser power than IP-G, with ionization of the resist occurring at approximately 1/2 the power used for IP-G. This difference in sensitivity is most likely due to chemical differences between the initiators and polymerization mechanisms of IP-G (photo-initiated free radical polymerization) and SU-8 (cationic chain growth by photoacid generated ring opening polymerization). Due to these challenges, the majority of tests were performed using IP-G composites.

5.4.2 Limitations imposed by the physics of TPP

We found that degradation of SU-8 seemed to occur independently of scan speed above powers of $\sim 20\%$ (10 mW), indicating that a critical pulse energy (roughly 0.125 nJ/pulse in our case) might have been reached. IP-G exhibited similar behavior at MNP concentrations above 1 vol%, and either adhesion or structural integrity resulted in the loss of features from the glass surface during development. Previous work with MNP composites has only reported scan speeds in the range of 5-100 $\mu\text{m/s}$ [221], which can take hours to print a single structure with dimensions in the 10-20 μm range. Here we investigated scan speeds up to 10,000 $\mu\text{m/s}$; the galvo-driven version of the Photonic Professional GT can reach scan speeds above 40,000 $\mu\text{m/s}$. In some of the earliest demonstrations of TPP, Witzgall et al. reported an exposure threshold of 3.2 TW/cm^2 and a damage threshold of 8.1 TW/cm^2 for SU-8, a 2.5-fold window for exposure [101]. Differences in experimental variables (laser wavelength, focal area, pulse time, SU-8 composition) make for a difficult comparison to Suter et al. [221], but agree generally with the idea that the window of exposure dictates the possible excitation parameters.

Using values from Suter et al. [221], which indicated that a laser power of 2.0 mW and 50 $\mu\text{m/s}$ scan speed resulted in a line width of 295 nm, we find that the average power within the cross-sectional area of the voxel is 0.93 TW/cm^2 . While lower than the predicted threshold of 3.2 TW/cm^2 , the scan speed is much slower than would be expected. The energy carried by the upper limit, 8.1 TW/cm^2 , 120-fs pulse in Witzgall et al. delivers 9.72 nJ/ μm^2 , whereas the 780 nm, 80 fs, 2.0 mW pulse in Suter et al. should deliver 0.35 nJ/ μm^2 . If polymerization were purely dependent on cumulative energy delivered, then ~ 28 pulses would approach the damage limit of a single voxel of SU-8. This, however, would dictate a scan speed over 430,000 $\mu\text{m/s}$ to avoid damage, about 4 orders of magnitude higher than the 50 $\mu\text{m/s}$ used by Suter. This simple calculation highlights the complexity of two-photon polymerization, especially below the single-shot threshold, and the challenges associated with comparing data across publications. Serbin et al. indicated a polymerization threshold of 27 KJ/cm^2 , delivered in 1.5×10^6 pulses, which matches more closely with the estimated 5.94 KJ/cm^2 delivered over 1.68×10^5 pulses by Suter [215, 221]. Liu et al. used a model of TPP

to experimentally fit their experimental setup to a simple exposure equation, $\frac{P^2}{v} \geq 3.6 \frac{mW^2}{\mu m/s}$, defining the exposure threshold for SU-8 wall structures in terms of laser power P and scan speed v [233]. This relation is only applicable for their specific setup, and is a function of peak intensity, pulse duration, repetition rate, exposure time, focal spot radius, focal spot aspect ratio, Rayleigh range, and an experimentally determined constant. The addition of metallic nanoparticles would only further complicate such calculations. While Yasui and Ikuta have proposed a general 3D model for photocurable resins that accounts for scattering and absorption when microparticles are added to the resin, it is unlikely that this model will extend to nanoparticle composites, where the particle diameter is less than the excitation wavelength [234].

While more investigation is needed to elucidate the exact mechanisms controlling TPP, it is clear that differences in optical and chemical properties of the resist play a large part in the limitations of nanoscale 3D printing. New advances in chemistry and optics will be needed to make the technology commercially practical, but many promising applications have already been demonstrated to date. There are a number of excellent reviews detailing the state-of-the art in TPP chemistry, physics, and applications [103, 20, 235, 236].

5.4.3 3D printing magnetic micro-robots

Line tests, when compiled into a contour plot (Figure 5.21), indicate the effects of resist composition on ideal printing parameters. There is a general trend toward a narrowing of parameter space as increased volume fractions of magnetic nanoparticles are used. This is to be expected, as scattering, absorption, and localized heating increase along with particle concentration. Slight inconsistencies of this pattern are likely attributable to high variability when working near the limits of speed and power, as well as run-to-run variability in substrate cleanliness and surface adhesion. Fischer et al. performed similar characterization plots of polymerization and damage thresholds, comparing pulse energy and repetition rates for a number of other photoresists [237].

While line tests provide a good starting point for identifying viable parameter spaces, the printing of large structures requires consideration of additional variables: vertical spacing

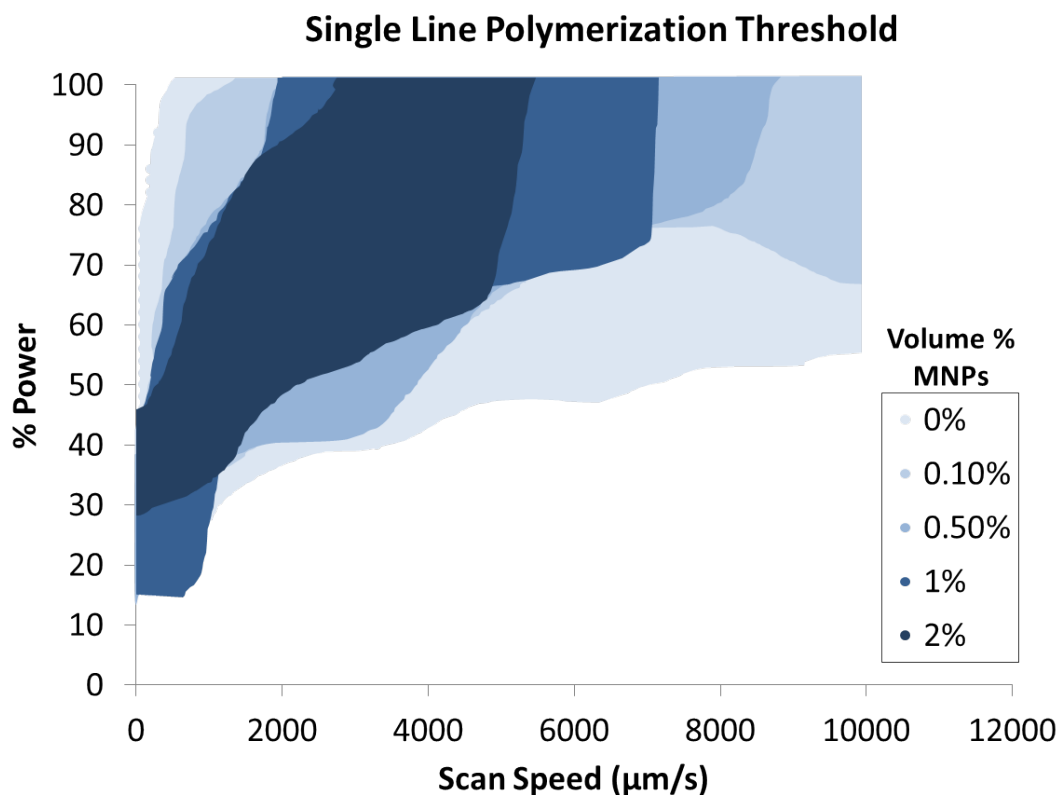


Figure 5.21: Polymerization threshold of IP-G magnetic nanoparticle composite. Colored regions highlight combinations of laser power and scan speed that create well-formed lines on the surface of glass substrates. Parameters above these contours result in localized heating, monomer degradation, and gas evolution. Parameters below the contours result in insufficient polymerization and/or weak adhesion. Increasing concentrations of magnetic nanoparticles (vol.%) are shown in successively darker shades.

between layers (“slicing”), horizontal spacing between lines in the x-y plane (“hatching”), and the physical dimensions of the structure (especially height in the z-direction). The horizontal and vertical spacing determines the amount of overlap between neighboring voxels, and therefore controls the integrity of the printed structure and the aggregate amount of energy absorbed by the resist and nanoparticles. The height of the structure in the z-direction also plays an important role in the selection of speed and power parameters. As the focal point passes deeper into the resist, more photons are absorbed or scattered by MNPs, reducing the apparent energy reaching the voxel until the power falls below the polymerization threshold. Structure height also determines how many times the laser will pass over a given point, increasing the net energy absorbed and contributing to local heating. This is especially problematic in structures with narrow x-y dimensions, as the laser will pass over the same area more frequently when layer writing time is short. In practice, we found the actual parameter space for writing multi-layer structures to be shifted downward in both power and speed, with much narrower ranges than the single line tests suggest.

The application of 3D lithography for MEMS devices, particularly those intended for use in microfluidic devices, is still limited in large part by materials issues. Printed structures are inherently delicate and susceptible to damage during the channel bonding process. The most ideal solution to this problem is to print the structures within an established channel, which we implemented with very limited success. Both IP-G and SU-8 structures were successfully patterned into pre-bonded PDMS channels (data not shown), but complete removal of unpolymerized resist proved to be time consuming and prohibitive. The standard developer for IP-G and SU-8, PGMEA, swells PDMS, leading to high stresses on the glass substrate and channel collapse, both of which contribute to detachment and damage of printed structures. Furthermore, preheating of the resists to remove solvent requires prebaking times over 24 hours. The effect on properties of glass and PDMS surfaces after long-term contact with resists at elevated temperatures has not been investigated to the best of our knowledge. In-channel printing has been reported by Wu et al. earlier this year, but required the use of all-glass microfluidics to avoid swelling issues [238]. They also used laser lithography to pattern their channels, using a photosensitized Foturan glass (Schott Glass Corp.) that could be annealed and selectively etched following lithography. Long bake times were still

necessary due to diffusion-limited solvent removal from within the glass channels, and bake times increased with channel length. Increased adoption of TPP for microfluidics applications, particularly in biomedical fields, would benefit from two-photon compatible resists that require minimal solvent removal and develop in a PDMS-compatible agent.

5.4.4 Spinning microspheres can generate particle size gradients in laminar flow

We observed a gradual increase in mean and median translation with increase in particle size. Two tailed student t-tests assuming equal variances indicated that the mean particle displacement of all groups were statistically different from one another ($p < 0.01$) with the exception of the comparisons between the 15, 20, and 25 μm size groups. This may be the result of lower particle counts for larger polystyrene beads, or binning selection. The improvement in capture with increasing particle size agrees well with earlier predictions that stable vortex capture occurs for objects in the size range $0.5 < \frac{r_{obj}}{r_{manip}} < 1$, where the radius of the object being manipulated (r_{obj}) should be similar to the radius of the manipulator (r_{manip}), which in the case of Figure 5.20 sees particle diameters approaching 1/2 the size of the 45-65 μm spinners [19].

Interestingly, separate experiments with a single micro-robot indicated different size-dependent effects (Figure 5.19). These experiments used higher flow rates, so inertial forces would have a larger impact on particle trajectory, reducing the effective size of the vortex around the robot. More work is needed to definitively characterize the complex effects of manipulator size, gap size, flow rate, and rotation frequency, but they all appear to factor into the resulting displacement of captured particles. It is encouraging to see that although the results are different, we consistently see distinct groupings of displacement with regard to particle size, further confirming the size effect.

5.5 CONCLUSION

In conclusion, we developed microrobots on patterned substrates using two distinct approaches. Two photon polymerization promises flexibility, rapid prototyping, and easy design of any 3D structure, but ultimately proved insufficient due to our specific needs and the physical limitations of the materials. These limitations illuminated valuable information about the nature to two-photon absorption and the effects of opaque particle incorporation.

Traditional lithography allowed us to generate a working system in which to validate the concept of size sorting with microvortex generation in laminar flow. This method was effective, but will be difficult to scale up, as each additional microsphere that must be docked adds setup time and complexity to the system, whereas TPP fabrication would not suffer such limitations.

Future work will involve stable dispersion of magnetic nanoparticles with much smaller core diameters, on the order of 10 nm, to allow TPP at increased vol%^s that will yield stronger magnetic forces. Once this challenge is overcome, we plan to create a size sorting channel containing large numbers of spinners to perform more complex tasks. We also envision a narrow channel with vortex generators arranged in configurations that might allow a single cell to be circulated continuously while moderate flow introduces nutrients and chemical signals, creating a nanobioreactor to study single cell growth in suspension. More aggressive speeds and shapes might also allow on-chip mechanical cell lysis to be incorporated into lab-on-a-chip operations. Magnetic micromanipulation will undoubtedly play an important role in future advances and applications of microfluidics.

6.0 SUMMARY AND FUTURE DIRECTIONS

In summary, this work has advanced microfluidic cell handling in a number of fields, and provided useful information about others. We successfully demonstrated differential adhesion as a method for cell sorting, revealing leukocyte deflection on stripes of P-selectin. Other publications reaffirmed this work and also identified the potential for sorting by mechanical patterning [131, 136, 137, 12, 138]. This technique possesses strong advantages over traditional methods like FACS, such as label free sorting and cost savings. It can also be easily integrated into lab-on-a-chip devices as a sample preparation tool, or used for cancer and disease diagnostics.

We also created a freely available, open-source software tool for tracking cells and particles in relation to patterned substrates. We found it to be a highly accurate and efficient way of tracking cells and condensing large amounts of tracking data into meaningful and understandable formats. We think this tool could be a valuable resource for other researchers that need to analyze large amounts of similar data but may not have the resources available to buy a commercial tracking tool or develop their own.

In efforts to focus cells toward the bottom substrate to enhance rolling, we developed two methods of redirecting cell motion within microfluidic channels. Although our results using electrical fields were not conclusive, publications after the work was performed confirmed our modeling results as reasonable and allowed us to identify the physical limitations preventing success.

Printed filters used to redirect cells and particles proved much more successful. We could definitively query the vertical location of the particles by an imposed horizontal motion, and improvements in geometry should allow us to use them to force cells into contact with the surface of the channel. We think the side-to-side motion of the horizontal filters may prove

valuable in other applications as well, such as compressing streamlines into a smaller local region to promote hydrophoresis and concentrating diffuse cells into discrete flow paths for downstream functions.

Finally, we developed a completely new method of size-based sorting by non-contact manipulation with magnetic micro-robots. We fabricated rotating magnetic structures using both traditional and two-photon lithography. New challenges for TPP fabrication of magnetic structures were identified, along with possible solutions. The relationship between exposure parameters and nanoparticle incorporation was characterized for photoresist composites. We also characterized soft magnetic substrate features for use as docks to localize untethered robots under laminar flow, and modeled the flow effects of particles spinning on those docks. Experimental confirmation of the modeling was ultimately achieved, creating particle size gradients in a continuous fashion under flow.

Figure 6.1 shows this author's qualitative assessment of the benefits and drawbacks of a number of microfluidic methods beyond those studied in this work. A researcher looking to implement one of these techniques into his or her microfluidic device might find such a broad visualization useful for narrowing the selection process.

When comparing the methods listed, the first and most important distinction is that microfluidic methods of discrimination between different cell populations are predominantly label free and operate in a continuous manner, without requiring interruptions in fluid flow. Avoiding labels or tags is useful for downstream applications where extra steps would be required to remove them, for example in cell therapies where the output of the device would eventually be reintroduced to the patient's bloodstream.

Cost is a major factor for many of these techniques, especially those tied to complex external equipment. Optical sorting techniques still require expensive light sources and focusing optics, and dielectrophoresis needs frequency generators that can operate in the kHz and MHz range. Technological advances outside the microfluidic realm may bring these costs down in the near future, but in the mean time, hydrodynamic forces remain the least expensive by far. Unfortunately, the cost benefits of hydrodynamic sorting are offset by the lack of specificity to relevant cell properties.

	Label free	Continuous	Non-contact	Tunable (real-time)	Reliable Fabrication	Specificity	Efficiency	Scalability	Force Strength	Cost
Cytotactic Rolling	✓	✓	✗	✗	✓	✓	✓	✓	✓	✓
3D Printed Filters	✓	✓	✗	✗	✓	✗	✓	✓	✓	✗
Magnetic Micro-robots	✓	✓	✓	✓	✗	✓	✓	✗	✓	✓
3D Printed Micro-robots	✓	✓	✓	✓	✓	✓	✓	✓	✓	✗
Dielectrophoresis	✓	✓	✓	✓	✓	✓	✓	✓	✓	✓
Hydrodynamic Forces	✓	✓	✓	✓	✓	✗	✓	✓	✓	✓
Optical Forces	✓	✓	✓	✓	✓	✗	✓	✗	✓	✗
Acoustic Forces	✓	✓	✓	✓	✓	✓	✓	✓	✓	✓
Traditional FACS	✗	✓	✓	✓	✓	✓	✓	✓	✓	✗
Traditional MACS	✗	✗	✗	✗	✓	✓	✓	✓	✓	✓

Figure 6.1: A comparison of different methods of force application and cell/particle sorting across various metrics. These ratings are the author’s subjective opinion and serve more as a general guide to the relative strengths and weaknesses of each method. Properties such as efficiency, reliability, and cost can vary wildly within each technique, depending on the complexity of the fabrication process and the supporting equipment required.

The challenges associated with scaling up and mass producing microfluidic devices may explain the slower than expected adoption of microfluidic devices in commercial settings. While not insurmountable, more work is clearly needed to develop cost-effective and flexible fabrication methods more varied than the traditional glass/PDMS architectures common today. The Whitesides group, and the corresponding spin-off company *Diagnostics for All*, have been developing paper-based microfluidics for a number of years, which promise to bring the cost of many tests down to a few dollars or even cents.

Cytotactic rolling is the only continuous method of microfluidic cell isolation that provides specificity at the molecular level. Protein recognition is critical in a scientific field that predominantly identifies cell phenotype by surface chemistry. Cytotactic devices (and microfluidics in general) may soon find commercial application as inexpensive alternatives to traditional lab tests in third world countries and consumer products. Recent years have seen an explosion in health and fitness tracking devices that log physical activity, measure heart rate, and track food intake (products from *FitBit*, *Jawbone*, *Samsung*, and *Apple* to name a few). Affordable home testing is on the horizon for measuring more complex health indicators. The *Cue*, for example, is a device available for preorder from a group of UCLA and UCSD entrepreneurs that detects testosterone, the flu, inflammation, fertility, and vitamin D using disposable cartridges. A cytotactic white blood cell counter or circulating tumor cell detector are not outside the realm of possibility, and could even interface directly with a smartphone for control and measurement.

6.1 FUTURE DIRECTIONS

In the years since the start of this work, cell rolling on patterned substrates has advanced from theory to a proven method of cell isolation [131, 136, 137, 138]. It has not, however, been demonstrated for non-selectin adhesion molecules and their ligands, despite indications that such systems should be possible based on the range of adhesion kinetics favorable for rolling [11] and observed physiological rolling behavior of lymphocytes with CD44/hyaluronate [63]. Future work is needed to test new protein/ligand combinations. We would also like to use

dielectrophoretic or mechanical flow focusing to improve the rate of interactions between the cells and the patterned substrates, although some work has already been accomplished in this area by other researchers.

Changes to the tracking program are needed to make it more adaptable to other substrate patterns and easier to integrate with a wider variety of MEMS devices. It is our hope that other researchers will use and build upon this platform.

Cell sorting and focusing using contactless electrokinetic forces will be another area of future work. We would first attempt to reproduce the false-positive results by intentionally creating electro-osmotic flow. We would then want to incorporate asymmetrical electrodes for contactless DEP to achieve the original goal of cell localization to the surface. The use of these forces was only recently introduced, and we have not found evidence of their use in combination with protein coated surfaces. Therefore, it remains unknown if they would viably enhance cell interaction without interfering with the structure and function of bound proteins on the channel surface. Improvements in the 3D printed filters will also be pursued in order to make them easier to fabricate, more robust, and less likely to create streamline blooming at the outlets.

Finally we wish to improve our TPP methodology for easier incorporation of printed microrobots into microfluidic devices. We would then determine size-based sorting efficiency when using tens or hundreds of micro-robots in unison. We believe the stable suspension of smaller magnetite cores in resist should allow higher volume fractions to be printed, which would lead to stronger magnetic manipulation forces. We would also like to test different arrangements of these devices for non-contact manipulation of cells to craft nano-bioreactors, on-chip mechanical shearing chambers, and particle trapping tools. Development of improved substrates for the untethered micro-robots will also be pursued, to allow easier scaling of these devices for larger applications. The dynamic, reconfigurable nature of the magnetic micro-robots will make them versatile tools for future microfluidic technologies.

APPENDIX A

CHAMBER BOTTOM FABRICATION WORKFLOW

Materials

- 4 Glass wafers (as of 6/1, new wafers are Pyrex 0.5mm thick, roughness <20Å, scratch/dig 60/40 double side polished, global flatness <40um)
- AZ5214-E photoresist
- AZ400K developer
- Eye dropper(s)

Procedure for Patterning Gold

1. Wash/dry wafer in washing machine
2. Run 2-minute HMDS vapor prime (instructions on machine)
3. Spin AZ5214-E resist (6000rpm for 45 seconds)
4. Soft bake at 95C for 2 min (program 2)
5. Expose on MA6 aligner for 50 seconds in vacuum contact mode (see MA6 procedure)
6. Bake at 105C for 30 seconds (ensure good contact and uniform heating!)
7. Bake at 115C for 120 seconds (ensure good contact and uniform heating!)
8. Flood expose on MA6 for 150 seconds
9. Develop completely submerged in 1:4 AZ400K developer solution with slight agitation for 0.8 min (800 mL water, 200 mL developer)
10. Rinse immediately with DI water gun, then run through wash/dry cycle
11. Plasma descum with O₂ plasma (100W forward power, 1 minute)

12. Sputter (see sputtering procedure)
 - a. Ti presputter - 200W, 10 minutes
 - b. Ti sputter - 100W, 12 seconds
 - c. Au presputter - 50W, 2 minutes
 - d. Au sputter - 50W, 24 seconds
13. Submerge in acetone in a sealed container
 - a. Leave overnight.
 - b. Remove bulk gold and replace acetone. Sonicate 5 minutes and remove quickly.
 - c. Use an acetone soaked q-tip to gently wipe away any gold residue on back of wafer or near stripes. NEVER wipe over stripes. Ultrasonicate in fresh acetone if necessary.
14. Spin junk photoresist (program 2) to protect from dicing debris
15. Give coated wafer to clean room staff (Chris Bowman) for dicing
16. Clean diced glass bottoms in acetone and store in clean plate

MA6 Aligner Procedure

1. Fill out log sheet and record lamp time
2. Check that micromanipulators are centered at 10 on both sides, and rotation (small black tab) is at zero
3. Turn on all 4 gas lines
4. Flip the lamp power switch on the black box below the machine. Lamp will run diagnostics and then display rdy when finished.
5. Once the lamp is ready, press the start button, and lamp will begin to warm up to 275W
6. Twist the green power switch on the MA6
7. Once startup is complete, press Load to begin
8. When prompted for configuration choose MA6 and press enter
9. Set the program to vacuum contact mode by pressing Edit Program, selecting Vac mode, then pressing Edit Program again
10. Set the time to 50 seconds by pressing Edit Parameter, setting time with the arrow keys (hold Fast when pressing arrows to jump 10 seconds at a time)
11. Place the mask, chrome up, in the mask holder, clipping it into place

12. Press Change Mask and press enter to toggle the vacuum on
13. Carefully slide the mask onto the rails, until it clicks into place
14. Press the Change Mask button again to lock the mask in place
15. Press Load to begin loading procedure
16. When prompted, slide out the tray, align wafer to flat markers, slide into machine, and confirm with Enter
17. Wait for WEC to complete, then, when ready, press Exposure
18. After exposure, slide tray out and bake wafer (see above)
19. Set program to Flood expose and time to 150 seconds using above procedure
20. Press Change Mask and remove the mask for the flood exposure. Enter to confirm.
21. When flood exposing, completing the Load procedure will initiate exposure, so make sure everything is set correctly before loading wafer.
22. After exposure, remove wafer, unload mask, and shutdown machine and lamp
23. Close 3 gas lines, leave Nitrogen on for 5 minutes to cool the lamp.

Perkin-Elmer 6J Sputtering Procedure

1. Turn off the ion gauge to prevent damage as pressure increases during venting
2. Close Hi-Vac valve (red switch), and once closed, open Vent valve
3. Wait for chamber to vent (fill out log sheet)
4. Once green up to air light indicates chamber is vented, use HOIST-UP switch to raise the chamber lid until the stage is accessible
5. Place the wafer face up in the center of the front stage
6. Lower chamber lid, making sure that lid seals evenly around the entire rim. Multiple attempts may be necessary to properly align lid
7. Turn off the vent switch, then open the roughing valve (rough vac to 7.5×10^{-2})
8. Close the roughing valve, open the High-Vac valve, and turn on the ion gauge
9. Wait approximately 1 hour, until the chamber reaches 7.5×10^{-2} on ion gauge (7.5×10^{-5})
10. Turn the ion gauge off.
11. On the left middle panel, toggle the 3-way exhaust valve switch to the closed position.
12. Flip the toggle switch to the center position, then turn the knob to S.S. (Steady State).

13. Turn on gas #1 using the black valve on the chamber lid, then the flow controller toggle switch #1 to on (careful, 3-way toggle)
 - a. The red readout should level out around 5. If not, check the set point knob to see if someone changed the setting.
14. Flip the yellow power switch on the top left panel.
15. Presputter
 - a. Settings for lid: etch / sputter deposit / target #1 / DC
 - b. Watch wall clock for presputter timing (10 min. Ti, 2 min Au)
 - c. Use the power controller on the far right to set the power to about 25W
 - d. Press Start on the power controller, then slowly raise the power to desired wattage (200W for Ti PS, 50W for Au PS)
 - e. Record presputter parameters on log sheet
 - f. Prepare for sputter by setting clock with blue knobs
16. Sputter
 - a. Turn power down to desired sputtering power (100W Ti, 50W Au)
 - b. Turn knob on lid to move sample stage to desired target
 - c. As soon as the movement light goes out, flip the silver toggle switch to start the timer.
 - d. Once the timer ends, the power will automatically be cut. Turn the knob to zero.
 - e. Move the sample back to the front stage, reset the timer, and repeat presputter/sputter if necessary. Make sure power and time settings are changed appropriately
17. When finished, turn off gas toggle (middle position) and gas valve on lid.
18. Turn the exhaust valve controller knob to the toggle setting, then flip the toggle to open
19. Once gas diminishes, power down (yellow switch) and close hi vac valve
20. Open vent valve and remove sample once chamber fully vents.
21. Pump chamber back up using roughing/high-vac procedure from above.

APPENDIX B

PSGL-1 BIOTINYLATED MICROSPHERES

PSGL-1 was conjugated to microspheres using a Pierce EZ-LinkTM Sulfo-NHS-LC Biotinylation kit (Pierce 21435) according to the included instructions. Biotinylation was confirmed by modifying superavidin functionlabeled polystyrene microspheres (Bangs Labs CP01N) with the conjugated protein. Microspheres were then labeled with Anti-human PSGL-1/CD162-Alexa Fluor 488 (R&D Systems FAB9961G) and quantified using flow cytometry.

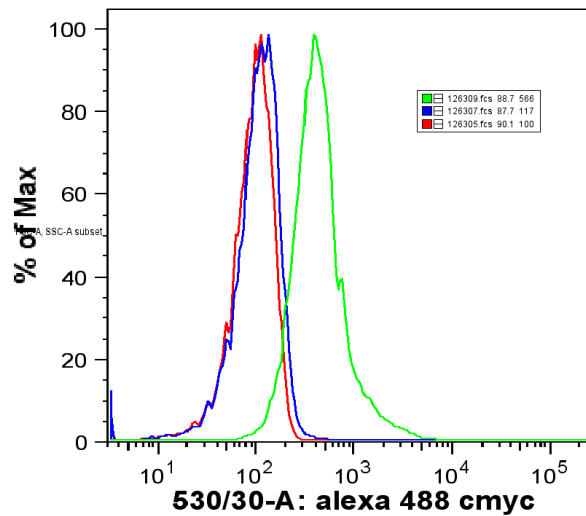


Figure B1: Flow cytometry of Alexa Fluor 488 anti-PSGL-1 labeled microspheres shows strong signal from PSGL-1 modified microspheres, indicating that the ligand is successfully bound to the beads in high concentrations.

Procedure for Conjugation of Biotinylated PSGL-1 to Streptavidin Beads

(C. Edington - 5/1/13)

Biotinylation of Protein (PSGL-1/Fc Chimera - R&D Systems)

1. Refer to the instructions from ThermoScientific for the EZ-LinkTM Sulfo-NHS-LC Biotinylation Kit (#21435) for calculations and warnings. Read this document thoroughly. Refer to Excel Document *Superavidin Microsphere Coverage.xlsx* for calculations.
2. 50 μg of PSGL-1/Fc Chimera can coat:
 - a. 2.63 mL of 10.14 μm beads at complete coverage (6.3M sites/bead)
 - b. 1,650 mL of 10.14 μm beads at 10,000 sites/bead
 - c. 11.6 μL of 0.22 μm beads at complete coverage (14.6K sites/bead)
 - d. 16.9 μL of 0.22 μm beads at 10,000 sites/bead
 - e. The volumes above are for 1%wt solids (original concentration)
3. Remove the vial of Sulfo-NHS-LC-Biotin from freezer and equilibrate it to room temperature before opening in step 5.
4. Remove the vial of PSGL-1/Fc chimera from the freezer and equilibrate to room temperature.
5. Buffer Exchange (small volumes)
 - a. For small volumes (10-150 μL), use a 7k MW cutoff mini Slide-a-lyzer tube, and perform buffer exchange and reactions in the same tube. For larger volumes (0.5-2mL) use Zeba Spin desalting columns included with the biotinylation kit (see Section C for Zeba instructions).
 - b. Presoak the dialysis tube in 1 L of MiliQ water for 15 minutes to remove any glycerol and other contaminants.
 - c. Reconstitute the 50 μg vial of PSGL-1/Fc in 100 μL of sterile filtered PBS (pH 7.2-8.0) to achieve 0.5 mg/mL concentration. Transfer entire volume to the dialysis tube.
 - d. Dialyze for 60 minutes in 250 mL of sterile PBS by suspending the Slide-a-Lyzer above the dialysate with the bottom membrane in contact with the solution. This can be done with a plastic float or by clamping the tube in place with a ring stand. The buffer exchange is needed to remove the Tris and NaCl in the lyophilized protein.

If the volume level of the sample is lower than the level of dialysate, hydrostatic pressure will force dialysate into the unit, diluting the sample.

6. Immediately before use, prepare 10mM Sulfo-NHS-LC-Biotin by dissolving 4.4 mg in 800 μ L ultrapure water.
7. Add the appropriate volume of Sulfo-NHS-LC-Biotin solution
 - a. For 50 μ g of 105.2 kDa MW homodimer PSGL-1/Fc, use 1.5 μ L of Sulfo-NHS solution is required to achieve the recommended 20-fold molar excess.
 - b. Incubate reaction for 60 minutes at room temperature (or 2 hr on ice)
8. Repeat the buffer exchange from step 4 to remove excess biotin reagent. Collect sample from dialysis unit and store at 2-8 degrees until use.
9. Estimation of biotin incorporation can be performed following the instructions from the biotinylation kit, but this will consume at least 20 μ L of biotinylated protein.

Combination with streptavidin coated microspheres

1. Allow microsphere suspension to come to room temperature, then vortex for 20 seconds prior to use.
2. Prepare wash buffer: 0.1M PBS, pH 7.4 (same buffer as used in biotinylation procedure)
3. Wash an aliquot of microspheres (see above) 3 times with a 10x volume of wash buffer each time.
 - a. Centrifuge 10 μ m microspheres at 1,200 x g for 15 minutes
 - b. Remove supernatant and resuspend pellet in appropriate volume of wash buffer
 - c. For 0.2 μ m beads, centrifugation is not possible. These beads should be dialyzed overnight using 100K MWCO dialysis tubing or a Slide-a-lyzer cassette. Wash the membrane thoroughly in ultrapure water prior to use.
4. Resuspend the final pellet in wash buffer to a concentration of 0.05% solids (0.5 mg/mL) which is 20x the original volume.
5. To this solution, add your biotinylated IgG that has been dissolved in the same buffer. See above for appropriate volumes.
6. Incubate at room temperature (22°C) for 60 minutes with gentle mixing.
7. Wash the particles 3 times with another 10X volume of wash buffer (step 3)

8. Resuspend antibody-coated beads in 0.1 M PBS, pH 7.4, to desired storage concentration (often 0.5 mg/mL).
9. Store at 2-8°C

Technical Resources

- ThermoScientific Instructions for EZ-Link Sulfo-NHS-LC-Biotinylation Kit (#21435)
- Bangs Labs Product Data Sheet 721 - *ProActive Streptavidin Coated Microspheres*
- Bangs Labs TechNote 203 - “Washing Microspheres”
- Excel Document - “Superavidin Microsphere Coverage.xlsx”
- Certificates of Analysis for microspheres, PSGL-1/Fc (R&D #3345-PS-050), and biotinylation kit.

APPENDIX C

CALCULATION OF THE VELOCITY PROFILE IN A LAMINAR FLOW MICROFLUIDIC CHANNEL

Calculation of the velocity profile within the microfluidic channel was critical to determining cell height. Overhead brightfield imaging did not allow quantitative determination of cell position, but velocity was easily acquired using automated tracking. By calculating the predicted hydrodynamic velocity for a given height, we could correlate cell speed with vertical position.

Using an online pressure drop calculator (www.pipeflowcalculations.com) we established that the pressure drop in the channel is 174.55 Pa when flow rate $Q = 0.25 \mu\text{L}/\text{min}$. Channels were rectangular in cross-section, with dimensions 12 mm long, 0.03 mm high, and 1.2 mm wide. For laminar, no slip, incompressible flow, the hydrodynamic velocity $v_x(y)$ as a function of height is given by:

$$v_x(y) = \frac{G}{2\mu}y(d - y) \quad (\text{C.1})$$

with $G = \frac{dP}{dx} = \frac{174.55 \text{ Pa}}{12 \text{ mm}}$, viscosity $\mu = 0.001006 \text{ Pa} \cdot \text{s}$ and $d = 0.03 \text{ mm}$. The maximum hydrodynamic velocity, for a flow rate of $0.25 \mu\text{L}/\text{min}$, is thus found to be $162.7 \frac{\mu\text{m}}{\text{s}}$, with a distribution according to Figure C1.

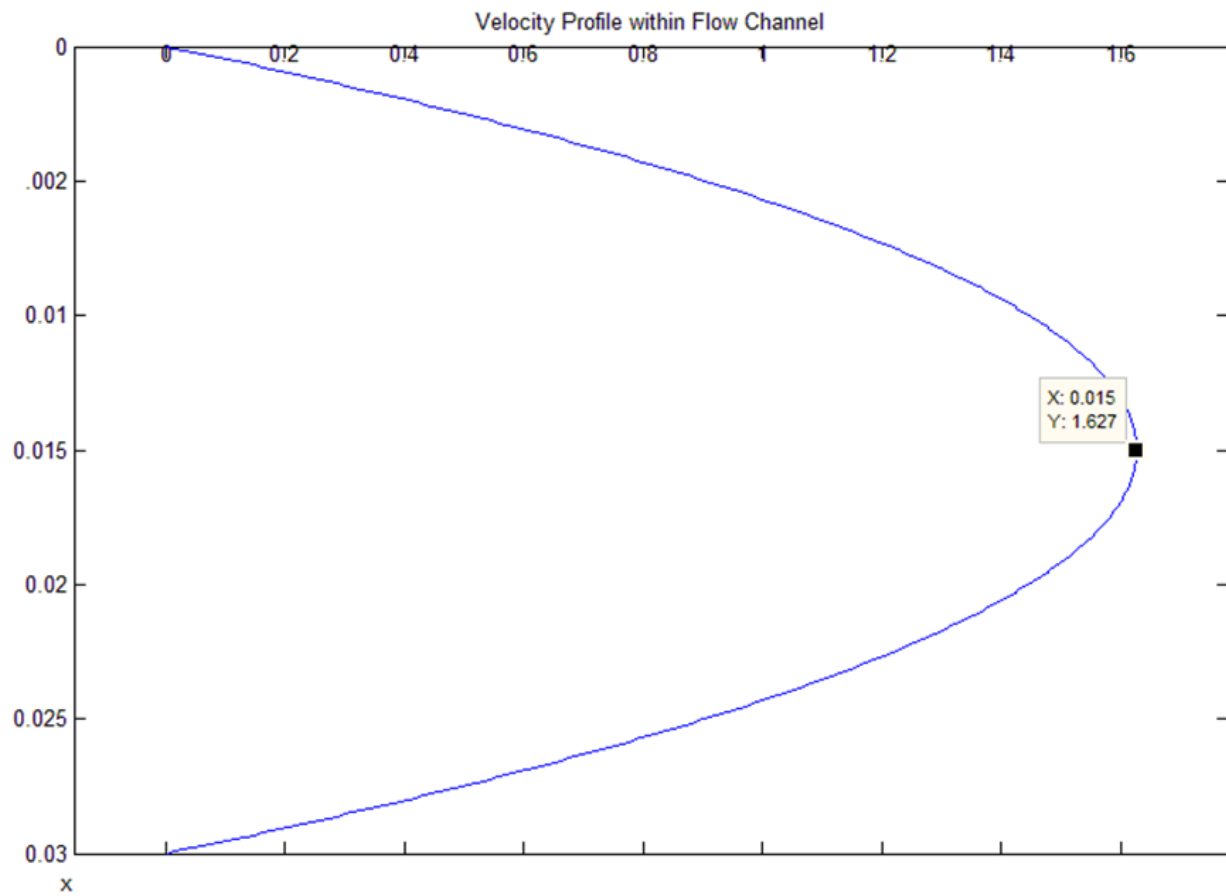


Figure C1: MATLAB plot of velocity profile within a laminar flow channel.

APPENDIX D

TWO PHOTON POLYMERIZATION OF SU-8 MNP COMPOSITES

For SU-8 samples, poor adhesion to the glass substrates posed a serious challenge, and we obtained the best results using an adhesion layer of hard-baked SU-8 2000.5. The adhesion layer was spun at 3000 rpm for 30 seconds, then baked for 10 minutes at 200°C (10°C/min ramp). SU-8 composites were then drop-cast onto the surface and soft-baked for 25 minutes at 95°C. Following TPP they were post-baked for 20 minutes at 95°C and developed for 10 minutes in PGMEA. Developed samples were submerged in 2-propanol for 1 minute to rinse, then dried with N₂.

APPENDIX E

PARTICLE TRACKING AROUND SPINNING MICROSPHERES

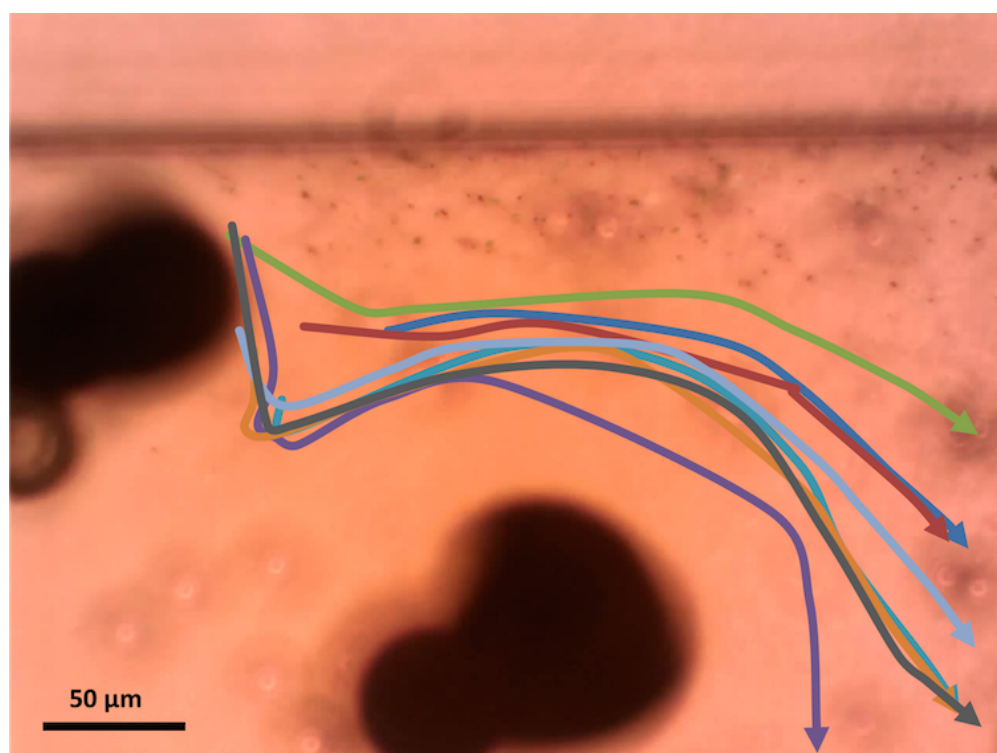


Figure E1: Overlay of manually tracked particle paths on video frame of spinning microspheres under flow.

BIBLIOGRAPHY

- [1] Mehta, P., Cummings, R. D. & McEver, R. P. Affinity and kinetic analysis of p-selectin binding to p-selectin glycoprotein ligand-1. *Journal of Biological Chemistry* **273**, 32506–32513 (1998).
- [2] Dong, C. & Lei, X. X. Biomechanics of cell rolling: shear flow, cell-surface adhesion, and cell deformability. *Journal of biomechanics* **33**, 35–43 (2000).
- [3] Waller, A. Xliv. microscopic examination of some of the principal tissues of the animal frame, as observed in the tongue of the living frog, toad, &c. *The London, Edinburgh, and Dublin Philosophical Magazine and Journal of Science* **29**, 271–287 (1846).
- [4] Whitesides, G. & Stroock, A. Flexible methods for microfluidics. *Phys Today* **54**, 42–48 (2001).
- [5] Gossett, D. R. *et al.* Label-free cell separation and sorting in microfluidic systems. *Analytical and bioanalytical chemistry* **397**, 3249–3267 (2010).
- [6] Jipa, F., Zamfirescu, M., Velea, A., Popescu, M. & Dabu, R. *Femtosecond Laser Lithography in Organic and Non-Organic Materials* (INTECH, 2013).
- [7] GmbH, N. Nanoscribe micro rapid prototyping. <http://www.nanoscribe.de/en/applications/micro-rapid-prototyping/> (2014). Accessed: 2014-08-10.
- [8] Alexeev, A., Verberg, R. & Balazs, A. C. Patterned surfaces segregate compliant microcapsules. *Langmuir* **23**, 983–987 (2007).
- [9] Edington, C. *et al.* Tailoring the trajectory of cell rolling with cytotactic surfaces. *Langmuir* **27**, 1534515351 (2011). URL <http://dx.doi.org/10.1021/la203382k>.
- [10] Patel, N. *et al.* Immobilization of protein molecules onto homogeneous and mixed carboxylate-terminated self-assembled monolayers. *Langmuir* **13**, 64856490 (1997). URL <http://dx.doi.org/10.1021/la970933h>.
- [11] Chang, K.-C., Tees, D. F. J. & Hammer, D. A. The state diagram for cell adhesion under flow: Leukocyte rolling and firm adhesion. *Proceedings of the National Academy of Sciences* **97**, 1126211267 (2000). URL <http://www.pnas.org/content/97/21/11262>.

- [12] Wang, G. *et al.* Stiffness dependent separation of cells in a microfluidic device. *PLoS one* **8**, e75901 (2013).
- [13] Voldman, J. Electrical forces for microscale cell manipulation. *Annu. Rev. Biomed. Eng.* **8**, 425–454 (2006).
- [14] Sano, M. B., Caldwell, J. L. & Davalos, R. V. Modeling and development of a low frequency contactless dielectrophoresis (cdep) platform to sort cancer cells from dilute whole blood samples. *Biosensors and Bioelectronics* **30**, 13–20 (2011).
- [15] Elvington, E. S., Salmanzadeh, A., Stremler, M. A. & Davalos, R. V. Label-free isolation and enrichment of cells through contactless dielectrophoresis. *Journal of visualized experiments: JoVE* (2013).
- [16] Chen, C.-C., Lin, P.-H. & Chung, C.-K. Microfluidic chip for plasma separation from undiluted human whole blood samples using low voltage contactless dielectrophoresis and capillary force. *Lab on a Chip* **14**, 1996–2001 (2014).
- [17] Wang, J. *et al.* Embellishment of microfluidic devices via femtosecond laser micro-nanofabrication for chip functionalization. *Lab Chip* **10**, 1993–1996 (2010).
- [18] Lim, T. W. *et al.* Three-dimensionally crossing manifold micro-mixer for fast mixing in a short channel length. *Lab on a Chip* **11**, 100–103 (2011).
- [19] Ye, Z., Diller, E. & Sitti, M. Micro-manipulation using rotational fluid flows induced by remote magnetic micro-manipulators. *Journal of Applied Physics* **112**, 064912 (2012).
- [20] Fischer, J. & Wegener, M. Three-dimensional optical laser lithography beyond the diffraction limit. *Laser & Photonics Reviews* **7**, 22–44 (2013).
- [21] Qiu, F. *et al.* Noncytotoxic artificial bacterial flagella fabricated from biocompatible ormocomp and iron coating. *Journal of Materials Chemistry B* **2**, 357–362 (2014).
- [22] Ye, Z. & Sitti, M. Dynamic trapping and two-dimensional transport of swimming microorganisms using a rotating magnetic microrobot. *Lab on a Chip* **14**, 2177–2182 (2014).
- [23] Whitesides, G. M. The origins and the future of microfluidics. *Nature* **442**, 368–373 (2006).
- [24] Hong, J. W. & Quake, S. R. Integrated nanoliter systems. *Nature biotechnology* **21**, 1179–1183 (2003).
- [25] Weibel, D. B. *et al.* Torque-actuated valves for microfluidics. *Analytical chemistry* **77**, 4726–4733 (2005).
- [26] Nguyen, N.-T. & Wu, Z. Micromixers - a review. *Journal of Micromechanics and Microengineering* **15**, R1 (2005).

- [27] Günther, A., Jhunjhunwala, M., Thalmann, M., Schmidt, M. A. & Jensen, K. F. Micromixing of miscible liquids in segmented gas-liquid flow. *Langmuir* **21**, 1547–1555 (2005).
- [28] Garstecki, P., Fischbach, M. A. & Whitesides, G. M. Design for mixing using bubbles in branched microfluidic channels. *Applied Physics Letters* **86**, 244108 (2005).
- [29] Laser, D. & Santiago, J. A review of micropumps. *Journal of micromechanics and microengineering* **14**, R35 (2004).
- [30] Erickson, D. & Li, D. Integrated microfluidic devices. *Analytica Chimica Acta* **507**, 11–26 (2004).
- [31] Zheng, B., Roach, L. S. & Ismagilov, R. F. Screening of protein crystallization conditions on a microfluidic chip using nanoliter-size droplets. *Journal of the American Chemical Society* **125**, 11170–11171 (2003).
- [32] Hansen, C. L., Skordalakes, E., Berger, J. M. & Quake, S. R. A robust and scalable microfluidic metering method that allows protein crystal growth by free interface diffusion. *Proceedings of the National Academy of Sciences* **99**, 16531–16536 (2002).
- [33] Wheeler, A. R. *et al.* Microfluidic device for single-cell analysis. *Analytical chemistry* **75**, 3581–3586 (2003).
- [34] Marcus, J. S., Anderson, W. F. & Quake, S. R. Microfluidic single-cell mrna isolation and analysis. *Analytical chemistry* **78**, 3084–3089 (2006).
- [35] Lagally, E., Medintz, I. & Mathies, R. Single-molecule dna amplification and analysis in an integrated microfluidic device. *Analytical chemistry* **73**, 565–570 (2001).
- [36] Dittrich, P. S. & Manz, A. Single-molecule fluorescence detection in microfluidic channels—the holy grail in μ tas? *Analytical and bioanalytical chemistry* **382**, 1771–1782 (2005).
- [37] Cai, L., Friedman, N. & Xie, X. S. Stochastic protein expression in individual cells at the single molecule level. *Nature* **440**, 358–362 (2006).
- [38] Dittrich, P. S. & Manz, A. Lab-on-a-chip: microfluidics in drug discovery. *Nature Reviews Drug Discovery* **5**, 210–218 (2006).
- [39] Pihl, J., Karlsson, M. & Chiu, D. T. Microfluidic technologies in drug discovery. *Drug Discovery Today* **10**, 1377–1383 (2005).
- [40] Stoolman, L. M. Adhesion molecules controlling lymphocyte migration. *Cell* **56**, 907–910 (1989).

- [41] Bevilacqua, M. P., Stengelin, S., Gimbrone, M. A. & Seed, B. Endothelial leukocyte adhesion molecule 1: an inducible receptor for neutrophils related to complement regulatory proteins and lectins. *Science* **243**, 1160–1165 (1989).
- [42] Lasky, L. A. Selectins: interpreters of cell-specific carbohydrate information during inflammation. *Science* **258**, 964–969 (1992).
- [43] Phillips, M. L. *et al.* Elam-1 mediates cell adhesion by recognition of a carbohydrate ligand, sialyl-lex. *Science* **250**, 1130–1132 (1990).
- [44] Varki, A. Selectin ligands. *Proceedings of the National Academy of Sciences* **91**, 7390–7397 (1994).
- [45] Alón, R., Hammer, D. A. & Springer, T. A. Lifetime of the p-selectin-carbohydrate bond and its response to tensile force in hydrodynamic flow. *Nature* **374**, 539–542 (1995).
- [46] Merkel, R., Nassoy, P., Leung, A., Ritchie, K. & Evans, E. Energy landscapes of receptor–ligand bonds explored with dynamic force spectroscopy. *Nature* **397**, 50–53 (1999).
- [47] Marshall, B. T. *et al.* Direct observation of catch bonds involving cell-adhesion molecules. *Nature* **423**, 190–193 (2003).
- [48] Wayman, A. M., Chen, W., McEver, R. P. & Zhu, C. Triphasic force dependence of e-selectin/ligand dissociation governs cell rolling under flow. *Biophysical journal* **99**, 1166–1174 (2010).
- [49] Borsig, L., Wong, R., Hynes, R. O., Varki, N. M. & Varki, A. Synergistic effects of l- and p-selectin in facilitating tumor metastasis can involve non-mucin ligands and implicate leukocytes as enhancers of metastasis. *Proceedings of the National Academy of Sciences* **99**, 2193–2198 (2002).
- [50] Slattery, M. J., Liang, S. & Dong, C. Distinct role of hydrodynamic shear in leukocyte-facilitated tumor cell extravasation. *American Journal of Physiology-Cell Physiology* **288**, C831–C839 (2005).
- [51] Di Wu, Q., Wang, J. H., Condrón, C., Bouchier-Hayes, D. & Redmond, H. P. Human neutrophils facilitate tumor cell transendothelial migration. *American Journal of Physiology-Cell Physiology* **280**, C814–C822 (2001).
- [52] Cheng, H. *et al.* Stem cell membrane engineering for cell rolling using peptide conjugation and tuning of cell–selectin interaction kinetics. *Biomaterials* **33**, 5004–5012 (2012).
- [53] Pouyani, T. & Seed, B. Psgl-1 recognition of p-selectin is controlled by a tyrosine sulfation consensus at the psgl-1 amino terminus. *Cell* **83**, 333–343 (1995).

- [54] Norman, K., Moore, K., McEver, R. & Ley, K. Leukocyte rolling in vivo is mediated by p-selectin glycoprotein ligand-1. *Blood* **86**, 4417–4421 (1995).
- [55] Ley, K. Molecular mechanisms of leukocyte recruitment in the inflammatory process. *Cardiovascular Research* **32**, 733–742 (1996).
- [56] marquis Du Trochet, H. *Recherches anatomiques et physiologiques sur la structure intime des animaux et des végétaux, et sur leur motilité* (JB Baillière, 1824).
- [57] Mulligan, M. *et al.* Protective effects of oligosaccharides in p-selectin-dependent lung injury. *Nature* **364**, 149 (1993).
- [58] Kim, Y. J., Borsig, L., Varki, N. M. & Varki, A. P-selectin deficiency attenuates tumor growth and metastasis. *Proceedings of the National Academy of Sciences* **95**, 9325–9330 (1998).
- [59] Yadav, S. S. *et al.* P-selectin mediates reperfusion injury through neutrophil and platelet sequestration in the warm ischemic mouse liver. *Hepatology* **29**, 1494–1502 (1999).
- [60] Harlan, J. M. Leukocyte-endothelial interactions. *Blood* **65**, 513525 (1985). URL <http://bloodjournal.hematologylibrary.org/content/65/3/513>.
- [61] Takada, M., Nadeau, K. C., Shaw, G. D., Marquette, K. A. & Tilney, N. L. The cytokine-adhesion molecule cascade in ischemia/reperfusion injury of the rat kidney. inhibition by a soluble p-selectin ligand. *Journal of Clinical Investigation* **99**, 2682 (1997).
- [62] Dulkanchainun, T. S. *et al.* Reduction of hepatic ischemia/reperfusion injury by a soluble p-selectin glycoprotein ligand-1. *Annals of surgery* **227**, 832 (1998).
- [63] DeGrendele, H. C., Estess, P., Picker, L. J. & Siegelman, M. H. Cd44 and its ligand hyaluronate mediate rolling under physiologic flow: a novel lymphocyte-endothelial cell primary adhesion pathway. *The Journal of experimental medicine* **183**, 1119–1130 (1996).
- [64] Aigner, S. *et al.* Cd24 mediates rolling of breast carcinoma cells on p-selectin. *The FASEB journal* **12**, 1241–1251 (1998).
- [65] Kristiansen, G. *et al.* Cd24 expression is a new prognostic marker in breast cancer. *Clinical Cancer Research* **9**, 4906–4913 (2003).
- [66] Baumann, P. *et al.* Cd24 expression causes the acquisition of multiple cellular properties associated with tumor growth and metastasis. *Cancer research* **65**, 10783–10793 (2005).
- [67] Tazawa, H. *et al.* Infiltration of neutrophils is required for acquisition of metastatic phenotype of benign murine fibrosarcoma cells: implication of inflammation-associated

- carcinogenesis and tumor progression. *The American journal of pathology* **163**, 2221–2232 (2003).
- [68] Aigner, S. *et al.* Cd24, a mucin-type glycoprotein, is a ligand for p-selectin on human tumor cells. *Blood* **89**, 3385–3395 (1997).
- [69] Kumar, A. & Bhardwaj, A. Methods in cell separation for biomedical application: cryogels as a new tool. *Biomedical materials* **3**, 034008 (2008).
- [70] Lundahl, J., Hallden, G., Hallgren, M., Sköld, C. & Hed, J. Altered expression of cd11b/cd18 and cd62l on human monocytes after cell preparation procedures. *Journal of immunological methods* **180**, 93–100 (1995).
- [71] Fukuda, S. & Schmid-Schönbein, G. W. Centrifugation attenuates the fluid shear response of circulating leukocytes. *Journal of leukocyte biology* **72**, 133–139 (2002).
- [72] SooHoo, J. R. & Walker, G. M. Microfluidic aqueous two phase system for leukocyte concentration from whole blood. *Biomedical microdevices* **11**, 323–329 (2009).
- [73] Takagi, J., Yamada, M., Yasuda, M. & Seki, M. Continuous particle separation in a microchannel having asymmetrically arranged multiple branches. *Lab on a Chip* **5**, 778–784 (2005).
- [74] Yamada, M. *et al.* Microfluidic devices for size-dependent separation of liver cells. *Biomedical microdevices* **9**, 637–645 (2007).
- [75] Di Carlo, D., Edd, J. F., Irimia, D., Tompkins, R. G. & Toner, M. Equilibrium separation and filtration of particles using differential inertial focusing. *Analytical chemistry* **80**, 2204–2211 (2008).
- [76] Kuntaegowdanahalli, S. S., Bhagat, A. A. S., Kumar, G. & Papautsky, I. Inertial microfluidics for continuous particle separation in spiral microchannels. *Lab on a Chip* **9**, 2973–2980 (2009).
- [77] Wu, Z., Willing, B., Bjerketorp, J., Jansson, J. K. & Hjort, K. Soft inertial microfluidics for high throughput separation of bacteria from human blood cells. *Lab on a Chip* **9**, 1193–1199 (2009).
- [78] Choi, S., Song, S., Choi, C. & Park, J.-K. Microfluidic self-sorting of mammalian cells to achieve cell cycle synchrony by hydrophoresis. *Analytical chemistry* **81**, 1964–1968 (2009).
- [79] Choi, S. & Park, J.-K. Continuous hydrophoretic separation and sizing of microparticles using slanted obstacles in a microchannel. *Lab on a Chip* **7**, 890–897 (2007).
- [80] Hsu, C.-H., Di Carlo, D., Chen, C., Irimia, D. & Toner, M. Microvortex for focusing, guiding and sorting of particles. *Lab on a Chip* **8**, 2128–2134 (2008).

- [81] Huang, R. *et al.* A microfluidics approach for the isolation of nucleated red blood cells (nrbc) from the peripheral blood of pregnant women. *Prenatal diagnosis* **28**, 892–899 (2008).
- [82] Kapishnikov, S., Kantsler, V. & Steinberg, V. Continuous particle size separation and size sorting using ultrasound in a microchannel. *Journal of Statistical Mechanics: Theory and Experiment* **2006**, P01012 (2006).
- [83] Lenshof, A. *et al.* Acoustic whole blood plasmapheresis chip for prostate specific antigen microarray diagnostics. *Analytical chemistry* **81**, 6030–6037 (2009).
- [84] Petersson, F., Åberg, L., Swärd-Nilsson, A.-M. & Laurell, T. Free flow acoustophoresis: microfluidic-based mode of particle and cell separation. *Analytical chemistry* **79**, 5117–5123 (2007).
- [85] Haydon, D. The surface charge of cells and some other small particles as indicated by electrophoresis: Ii. the interpretation of the electrophoretic charge. *Biochimica et biophysica acta* **50**, 457–462 (1961).
- [86] Guijt, R. M. *et al.* New approaches for fabrication of microfluidic capillary electrophoresis devices with on-chip conductivity detection. *Electrophoresis* **22**, 235–241 (2001).
- [87] Pethig, R. Dielectrophoresis: using inhomogeneous ac electrical fields to separate and manipulate cells. *Critical Reviews in Biotechnology* **16**, 331–348 (1996).
- [88] Wang, X.-B. *et al.* Cell separation by dielectrophoretic field-flow-fractionation. *Analytical Chemistry* **72**, 832–839 (2000).
- [89] Vahey, M. D. & Voldman, J. An equilibrium method for continuous-flow cell sorting using dielectrophoresis. *Analytical chemistry* **80**, 3135–3143 (2008).
- [90] Cheng, I.-F., Froude, V. E., Zhu, Y., Chang, H.-C. & Chang, H.-C. A continuous high-throughput bioparticle sorter based on 3d traveling-wave dielectrophoresis. *Lab on a Chip* **9**, 3193–3201 (2009).
- [91] Flanagan, L. A. *et al.* Unique dielectric properties distinguish stem cells and their differentiated progeny. *Stem cells* **26**, 656–665 (2008).
- [92] Stott, S. L. *et al.* Isolation of circulating tumor cells using a microvortex-generating herringbone-chip. *Proceedings of the National Academy of Sciences* **107**, 18392–18397 (2010).
- [93] Svoboda, K. & Block, S. M. Biological applications of optical forces. *Annual review of biophysics and biomolecular structure* **23**, 247–285 (1994).
- [94] MacDonald, M., Spalding, G. & Dholakia, K. Microfluidic sorting in an optical lattice. *Nature* **426**, 421–424 (2003).

- [95] Applegate Jr, R. *et al.* Optical trapping, manipulation, and sorting of cells and colloids in microfluidic systems with diode laser bars. *Optics express* **12**, 4390–4398 (2004).
- [96] Milne, G., Rhodes, D., MacDonald, M. & Dholakia, K. Fractionation of polydisperse colloid with acousto-optically generated potential energy landscapes. *Optics letters* **32**, 1144–1146 (2007).
- [97] Saliba, A.-E. *et al.* Microfluidic sorting and multimodal typing of cancer cells in self-assembled magnetic arrays. *Proceedings of the National Academy of Sciences* **107**, 14524–14529 (2010).
- [98] Sitti, M. Miniature devices: Voyage of the microrobots. *Nature* **458**, 1121–1122 (2009).
- [99] Pawashe, C., Floyd, S. & Sitti, M. Modeling and experimental characterization of an untethered magnetic micro-robot. *The International Journal of Robotics Research* **28**, 1077–1094 (2009).
- [100] Diller, E., Pawashe, C., Floyd, S. & Sitti, M. Assembly and disassembly of magnetic mobile micro-robots towards deterministic 2-d reconfigurable micro-systems. *The International Journal of Robotics Research* 0278364911416140 (2011).
- [101] Witzgall, G., Vrijen, R., Yablonovitch, E., Doan, V. & Schwartz, B. J. Single-shot two-photon exposure of commercial photoresist for the production of three-dimensional structures. *Optics letters* **23**, 1745–1747 (1998).
- [102] Sun, H.-B. *et al.* Real three-dimensional microstructures fabricated by photopolymerization of resins through two-photon absorption. *Optics letters* **25**, 1110–1112 (2000).
- [103] Zhang, Y.-L., Chen, Q.-D., Xia, H. & Sun, H.-B. Designable 3d nanofabrication by femtosecond laser direct writing. *Nano Today* **5**, 435–448 (2010).
- [104] Bonner, W. A., Hulett, H. R., Sweet, R. G. & Herzenberg, L. A. Fluorescence activated cell sorting. *Review of Scientific Instruments* **43**, 404409 (1972). URL <http://scitation.aip.org/content/aip/journal/rsi/43/3/10.1063/1.1685647>.
- [105] Herzenberg, L. A. *et al.* The history and future of the fluorescence activated cell sorter and flow cytometry: a view from stanford. *Clinical chemistry* **48**, 18191827 (2002).
- [106] Bauer, J. Advances in cell separation: recent developments in counterflow centrifugal elutriation and continuous flow cell separation. *Journal of Chromatography B: Biomedical Sciences and Applications* **722**, 5569 (1999). URL <http://www.sciencedirect.com/science/article/pii/S0378434798003089>.
- [107] Li, Y., Dalton, C., Crabtree, H. J., Nilsson, G. & Kaler, K. V. I. S. Continuous dielectrophoretic cell separation microfluidic device. *Lab on a Chip* **7**, 239248 (2007). URL <http://pubs.rsc.org/en/content/articlelanding/2007/lc/b613344d>.

- [108] Tsutsui, H. & Ho, C.-M. Cell separation by non-inertial force fields in microfluidic systems. *Mechanics Research Communications* **36**, 92103 (2009). URL <http://www.sciencedirect.com/science/article/pii/S009364130800116X>.
- [109] Petersson, F., berg, L., Swrd-Nilsson, A.-M. & Laurell, T. Free flow acoustophoresis: Microfluidic-based mode of particle and cell separation. *Analytical Chemistry* **79**, 51175123 (2007). URL <http://dx.doi.org/10.1021/ac070444e>.
- [110] MacDonald, M. P., Spalding, G. C. & Dholakia, K. Microfluidic sorting in an optical lattice. *Nature* **426**, 421424 (2003). URL <http://www.nature.com/nature/journal/v426/n6965/full/nature02144.html>.
- [111] Wang, M. M. *et al.* Microfluidic sorting of mammalian cells by optical force switching. *Nature Biotechnology* **23**, 8387 (2005). URL <http://www.nature.com/nbt/journal/v23/n1/full/nbt1050.html>.
- [112] Emmelkamp, J. *et al.* The potential of autofluorescence for the detection of single living cells for label-free cell sorting in microfluidic systems. *ELECTROPHORESIS* **25**, 37403745 (2004). URL <http://onlinelibrary.wiley.com/doi/10.1002/elps.200406070/abstract>.
- [113] Norman, K. E., Moore, K. L., McEver, R. P. & Ley, K. Leukocyte rolling in vivo is mediated by p-selectin glycoprotein ligand-1. *Blood* **86**, 44174421 (1995).
- [114] Lawrence, M. B. & Springer, T. A. Leukocytes roll on a selectin at physiologic flow rates: Distinction from and prerequisite for adhesion through integrins. *Cell* **65**, 859873 (1991). URL <http://www.sciencedirect.com/science/article/pii/S009286749190393D>.
- [115] Lawrence, M. B., Kansas, G. S., Kunkel, E. J. & Ley, K. Threshold levels of fluid shear promote leukocyte adhesion through selectins (CD62l,p,e). *The Journal of Cell Biology* **136**, 717727 (1997). URL <http://jcb.rupress.org/content/136/3/717>.
- [116] Alon, R., Hammer, D. A. & Springer, T. A. Lifetime of the p-selectin-carbohydrate bond and its response to tensile force in hydrodynamic flow. *Nature* **374**, 539542 (1995). URL <http://www.nature.com/nature/journal/v374/n6522/abs/374539a0.html>.
- [117] Burns, A. R. *et al.* P-selectin mediates neutrophil adhesion to endothelial cell borders. *Journal of leukocyte biology* **65**, 299306 (1999).
- [118] Chen, S., Alon, R., Fuhlbrigge, R. C. & Springer, T. A. Rolling and transient tethering of leukocytes on antibodies reveal specializations of selectins. *Proceedings of the National Academy of Sciences* **94**, 31723177 (1997). URL <http://www.pnas.org/content/94/7/3172>.
- [119] Davenpeck, K. L., Brummet, M. E., Hudson, S. A., Mayer, R. J. & Bochner, B. S. Activation of human leukocytes reduces surface p-selectin glycoprotein ligand-1 (PSGL-

- 1, CD162) and adhesion to p-selectin in vitro. *Journal of immunology (Baltimore, Md.: 1950)* **165**, 27642772 (2000).
- [120] Greenberg, A. W., Kerr, W. G. & Hammer, D. A. Relationship between selectin-mediated rolling of hematopoietic stem and progenitor cells and progression in hematopoietic development. *Blood* **95**, 478486 (2000).
- [121] Hicks, A. E. R., Nolan, S. L., Ridger, V. C., Hellewell, P. G. & Norman, K. E. Recombinant p-selectin glycoprotein ligand1 directly inhibits leukocyte rolling by all 3 selectins in vivo: complete inhibition of rolling is not required for anti-inflammatory effect. *Blood* **101**, 32493256 (2003). URL <http://bloodjournal.hematologylibrary.org/content/101/8/3249>.
- [122] Hong, S. *et al.* Covalent immobilization of p-selectin enhances cell rolling. *Langmuir* **23**, 1226112268 (2007). URL <http://dx.doi.org/10.1021/la7014397>.
- [123] Lasky, L. A. Selectin-carbohydrate interactions and the initiation of the inflammatory response. *Annual Review of Biochemistry* **64**, 113140 (1995). URL <http://www.annualreviews.org/doi/abs/10.1146/annurev.bi.64.070195.000553>.
- [124] Lorant, D. E. *et al.* Activation of polymorphonuclear leukocytes reduces their adhesion to p-selectin and causes redistribution of ligands for p-selectin on their surfaces. *Journal of Clinical Investigation* **96**, 171182 (1995). URL <http://www.jci.org/articles/view/118018>.
- [125] Mayadas, T. N., Johnson, R. C., Rayburn, H., Hynes, R. O. & Wagner, D. D. Leukocyte rolling and extravasation are severely compromised in p selectin-deficient mice. *Cell* **74**, 541554 (1993). URL <http://www.sciencedirect.com/science/article/pii/S009286749380055J>.
- [126] Narasipura, S. D., Wojciechowski, J. C., Charles, N., Liesveld, J. L. & King, M. R. P-selectin-coated microtube for enrichment of CD34+ hematopoietic stem and progenitor cells from human bone marrow. *Clinical Chemistry* **54**, 7785 (2008). URL <http://www.clinchem.org/content/54/1/77>.
- [127] Greenberg, A. W. & Hammer, D. A. Cell separation mediated by differential rolling adhesion. *Biotechnology and Bioengineering* **73**, 111124 (2001). URL <http://onlinelibrary.wiley.com/doi/10.1002/bit.1043/abstract>.
- [128] Chang, W. C., Lee, L. P. & Liepmann, D. Biomimetic technique for adhesion-based collection and separation of cells in a microfluidic channel. *Lab on a Chip* **5**, 6473 (2005). URL <http://pubs.rsc.org/en/content/articlelanding/2005/lc/b400455h>.
- [129] Alexeev, A., Verberg, R. & Balazs, A. C. Patterned surfaces segregate compliant microcapsules. *Langmuir* **23**, 983987 (2007). URL <http://dx.doi.org/10.1021/la062914q>.

- [130] Karnik, R. *et al.* Nanomechanical control of cell rolling in two dimensions through surface patterning of receptors. *Nano Letters* **8**, 11531158 (2008). URL <http://dx.doi.org/10.1021/nl073322a>.
- [131] Lee, C.-H., Bose, S., Van Vliet, K. J., Karp, J. M. & Karnik, R. Examining the lateral displacement of HL60 cells rolling on asymmetric p-selectin patterns. *Langmuir* **27**, 240249 (2011). URL <http://dx.doi.org/10.1021/la102871m>.
- [132] Dong, C. & Lei, X. X. Biomechanics of cell rolling: shear flow, cell-surface adhesion, and cell deformability. *Journal of Biomechanics* **33**, 3543 (2000). URL <http://www.sciencedirect.com/science/article/pii/S0021929099001748>.
- [133] Wu, L. *et al.* Impact of carrier stiffness and microtopology on two-dimensional kinetics of p-selectin and p-selectin glycoprotein ligand-1 (PSGL-1) interactions. *Journal of Biological Chemistry* **282**, 98469854 (2007). URL <http://www.jbc.org/content/282/13/9846>.
- [134] Gaver III, D. P. & Kute, S. M. A theoretical model study of the influence of fluid stresses on a cell adhering to a microchannel wall. *Biophysical Journal* **75**, 721733 (1998). URL <http://www.sciencedirect.com/science/article/pii/S0006349598775629>.
- [135] Ushiyama, S., Laue, T. M., Moore, K. L., Erickson, H. & McEver, R. Structural and functional characterization of monomeric soluble p-selectin and comparison with membrane p-selectin. *Journal of Biological Chemistry* **268**, 15229–15237 (1993).
- [136] Choi, S., Karp, J. M. & Karnik, R. Cell sorting by deterministic cell rolling. *Lab on a Chip* **12**, 1427–1430 (2012).
- [137] Bose, S. *et al.* Affinity flow fractionation of cells via transient interactions with asymmetric molecular patterns. *Scientific reports* **3** (2013).
- [138] Choi, S. *et al.* A cell rolling cytometer reveals the correlation between mesenchymal stem cell dynamic adhesion and differentiation state. *Lab on a Chip* **14**, 161–166 (2014).
- [139] Edington, C. *et al.* Real-time tracking and analysis of cell rolling: Registration to patterned substrates and implications for mems-based cell manipulation. *IEEE Trans Biomed Eng* **In press** (2014).
- [140] Garvey, C., Young Jr, J., Coleman, P. & Simon, W. Automated three-dimensional dendrite tracking system. *Electroencephalography and clinical neurophysiology* **35**, 199–204 (1973).
- [141] Coleman, P., Garvey, C., Young, J. & Simon, W. Semiautomatic tracking of neuronal processes. In Lindsay, R. (ed.) *Computer Analysis of Neuronal Structures*, Computers in Biology and Medicine, 91–109 (Springer US, 1977).

- [142] Berns, G. S. & Berns, M. W. Computer-based tracking of living cells. *Exp Cell Res* **142**, 103–9 (1982).
- [143] Li, K. *et al.* Cell population tracking and lineage construction with spatiotemporal context. *Medical image analysis* **12**, 546–566 (2008).
- [144] Ray, N. & Acton, S. T. Data acceptance for automated leukocyte tracking through segmentation of spatiotemporal images. *Biomedical Engineering, IEEE Transactions on* **52**, 1702–1712 (2005).
- [145] Huh, S., Ker, D. F. E., Bise, R., Chen, M. & Kanade, T. Automated mitosis detection of stem cell populations in phase-contrast microscopy images. *Medical Imaging, IEEE Transactions on* **30**, 586–596 (2011).
- [146] Ray, N., Acton, S. T. & Ley, K. Tracking leukocytes in vivo with shape and size constrained active contours. *Medical Imaging, IEEE Transactions on* **21**, 1222–1235 (2002).
- [147] Acton, S. T., Wethmar, K. & Ley, K. Automatic tracking of rolling leukocytes in vivo. *Microvascular Research* **63**, 139–148 (2002).
- [148] Goobic, A. P., Tang, J. & Acton, S. T. Image stabilization and registration for tracking cells in the microvasculature. *Biomedical Engineering, IEEE Transactions on* **52**, 287–299 (2005).
- [149] Jaqaman, K. *et al.* Robust single-particle tracking in live-cell time-lapse sequences. *Nature methods* **5**, 695–702 (2008).
- [150] Meijering, E., Dzyubachyk, O. & Smal, I. Methods for cell and particle tracking. *Methods Enzymol* **504**, 183–200 (2012).
- [151] Meijering, E., Dzyubachyk, O., Smal, I. & van Cappellen, W. A. Tracking in cell and developmental biology. *Seminars in Cell & Developmental Biology* **20**, 894–902 (2009). URL <http://www.sciencedirect.com/science/article/pii/S1084952109001517>. Imaging in Cell and Developmental Biology Planar Cell Polarity.
- [152] Jaqaman, K. & Danuser, G. Computational image analysis of cellular dynamics: A case study based on particle tracking. *Cold Spring Harbor Protocols* **2009**, pdb-top65 (2009).
- [153] Bonneau, S., Dahan, M. & Cohen, L. D. Single quantum dot tracking based on perceptual grouping using minimal paths in a spatiotemporal volume. *Image Processing, IEEE Transactions on* **14**, 1384–1395 (2005).
- [154] Genovesio, A. *et al.* Multiple particle tracking in 3-d+ t microscopy: method and application to the tracking of endocytosed quantum dots. *Image Processing, IEEE Transactions on* **15**, 1062–1070 (2006).

- [155] Smal, I. *et al.* Multiple object tracking in molecular bioimaging by rao-blackwellized marginal particle filtering. *Medical Image Analysis* **12**, 764–777 (2008).
- [156] Kalman, R. E. A new approach to linear filtering and prediction problems. *Journal of basic Engineering* **82**, 35–45 (1960).
- [157] Alon, R. *et al.* The integrin vla-4 supports tethering and rolling in flow on vcam-1. *The Journal of cell biology* **128**, 1243–1253 (1995).
- [158] McEver, R. P., Beckstead, J., Moore, K., Marshall-Carlson, L. & Bainton, D. Gmp-140, a platelet alpha-granule membrane protein, is also synthesized by vascular endothelial cells and is localized in weibel-palade bodies. *Journal of Clinical Investigation* **84**, 92 (1989).
- [159] Sawaya Jr, D. E. *et al.* P-selectin contributes to the initial recruitment of rolling and adherent leukocytes in hepatic venules after ischemia/reperfusion. *Shock* **12**, 227–232 (1999).
- [160] Kim, Y. J., Borsig, L., Varki, N. M. & Varki, A. P-selectin deficiency attenuates tumor growth and metastasis. *Proceedings of the National Academy of Sciences* **95**, 9325–9330 (1998).
- [161] Edington, C. *et al.* Tailoring the trajectory of cell rolling with cytotactic surfaces. *Langmuir* **27**, 15345–15351 (2011). <http://pubs.acs.org/doi/pdf/10.1021/la203382k>.
- [162] Lee, C.-H., Bose, S., Van Vliet, K. J., Karp, J. M. & Karnik, R. Examining the lateral displacement of hl60 cells rolling on asymmetric p-selectin patterns. *Langmuir* **27**, 240–249 (2010).
- [163] Chang, K.-C., Tees, D. F. & Hammer, D. A. The state diagram for cell adhesion under flow: leukocyte rolling and firm adhesion. *Proceedings of the National Academy of Sciences* **97**, 11262–11267 (2000).
- [164] Alón, R., Hammer, D. A. & Springer, T. A. Lifetime of the p-selectin-carbohydrate bond and its response to tensile force in hydrodynamic flow. *Nature* **374**, 539–542 (1995).
- [165] Hong, S. *et al.* Covalent immobilization of p-selectin enhances cell rolling. *Langmuir* **23**, 12261–12268 (2007).
- [166] Kuhn, H. W. The hungarian method for the assignment problem. *Naval research logistics quarterly* **2**, 83–97 (1955).
- [167] Cordeli, F. Manual tracking (2005). URL <http://rsbweb.nih.gov/ij/plugins/track/track.html>.
- [168] Hoaglin, D. C. & Iglewicz, B. Fine-tuning some resistant rules for outlier labeling. *Journal of the American Statistical Association* **82**, 1147–1149 (1987).

- [169] Tukey, J. W. Exploratory data analysis. *Addison-Wesley Series in Behavioral Science: Quantitative Methods* **1** (1977).
- [170] Sarangapani, K. K. *et al.* Low force decelerates l-selectin dissociation from p-selectin glycoprotein ligand-1 and endoglycan. *Journal of Biological Chemistry* **279**, 2291–2298 (2004).
- [171] Yago, T. *et al.* Catch bonds govern adhesion through l-selectin at threshold shear. *The Journal of cell biology* **166**, 913–923 (2004).
- [172] Puri, K. D., Finger, E. B. & Springer, T. A. The faster kinetics of l-selectin than of e-selectin and p-selectin rolling at comparable binding strength. *The Journal of Immunology* **158**, 405–413 (1997).
- [173] Barbaux, S. *et al.* The adhesion mediated by the p-selectin p-selectin glycoprotein ligand-1 (psgl-1) couple is stronger for shorter psgl-1 variants. *Journal of leukocyte biology* **87**, 727–734 (2010).
- [174] Stuhrmann, B. *et al.* Automated tracking and laser micromanipulation of motile cells. *Review of scientific instruments* **76**, 035105 (2005).
- [175] Akagi, T. & Ichiki, T. Cell electrophoresis on a chip: what can we know from the changes in electrophoretic mobility? *Analytical and bioanalytical chemistry* **391**, 2433–2441 (2008).
- [176] Mehrishi, J. N. & Bauer, J. Electrophoresis of cells and the biological relevance of surface charge. *Electrophoresis* **23**, 1984–1994 (2002).
- [177] Park, C. J., Gabrielson, N. P., Pack, D. W., Jamison, R. D. & Wagoner Johnson, A. J. The effect of chitosan on the migration of neutrophil-like hl60 cells, mediated by il-8. *Biomaterials* **30**, 436–444 (2009).
- [178] Huang, C., Chen, A., Wang, L., Guo, M. & Yu, J. Electrokinetic measurements of dielectric properties of membrane for apoptotic hl-60 cells on chip-based device. *Biomedical microdevices* **9**, 335–343 (2007).
- [179] Wang, X., Becker, F. F. & Gascoyne, P. R. Membrane dielectric changes indicate induced apoptosis in hl-60 cells more sensitively than surface phosphatidylserine expression or dna fragmentation. *Biochimica et Biophysica Acta (BBA)-Biomembranes* **1564**, 412–420 (2002).
- [180] Li, H. & Bashir, R. Dielectrophoretic separation and manipulation of live and heat-treated cells of *listeria* on microfabricated devices with interdigitated electrodes. *Sensors and Actuators B: Chemical* **86**, 215–221 (2002).
- [181] Becker, F. F. *et al.* Separation of human breast cancer cells from blood by differential dielectric affinity. *Proceedings of the National Academy of Sciences* **92**, 860–864 (1995).

- [182] Stephens, M., Talary, M., Pethig, R., Burnett, A. & Mills, K. The dielectrophoresis enrichment of cd34+ cells from peripheral blood stem cell harvests. *Bone marrow transplantation* **18**, 777–782 (1996).
- [183] Cummings, E. B. & Singh, A. K. Dielectrophoresis in microchips containing arrays of insulating posts: theoretical and experimental results. *Analytical Chemistry* **75**, 4724–4731 (2003).
- [184] Shafiee, H., Caldwell, J. L., Sano, M. B. & Davalos, R. V. Contactless dielectrophoresis: a new technique for cell manipulation. *Biomedical microdevices* **11**, 997–1006 (2009).
- [185] Hughes, M. P. Strategies for dielectrophoretic separation in laboratory-on-a-chip systems. *Electrophoresis* **23**, 2569–2582 (2002).
- [186] Joffe, E. B. & Lock, K.-S. *Grounds for Grounding: A Circuit to System Handbook* (John Wiley & Sons, 2011).
- [187] Zellner, P., Shake, T., Sahari, A., Behkam, B. & Agah, M. Off-chip passivated-electrode, insulator-based dielectrophoresis ($\sigma\pi\text{dep}$). *Analytical and bioanalytical chemistry* **405**, 6657–6666 (2013).
- [188] Ben, Y., Demekhin, E. A. & Chang, H.-C. Nonlinear electrokinetics and superfast electrophoresis. *Journal of colloid and interface science* **276**, 483–497 (2004).
- [189] Amato, L. *et al.* Integrated three-dimensional filter separates nanoscale from microscale elements in a microfluidic chip. *Lab on a Chip* **12**, 1135–1142 (2012).
- [190] Edington, C., Ye, Z., Sitti, M. & Russell, A. Magnetic micro-robots for non-contact manipulation of cells and particles in microfluidics. *Lab on a Chip* **In preparation** (2014).
- [191] Gascoyne, P. R. & Vykoukal, J. Particle separation by dielectrophoresis. *Electrophoresis* **23**, 1973 (2002).
- [192] Chiou, P. Y., Ohta, A. T. & Wu, M. C. Massively parallel manipulation of single cells and microparticles using optical images. *Nature* **436**, 370–372 (2005).
- [193] Giddings, J., Yang, F. & Myers, M. N. Flow-field-flow fractionation: a versatile new separation method. *Science* **193**, 1244–1245 (1976).
- [194] Huang, L. R., Cox, E. C., Austin, R. H. & Sturm, J. C. Continuous particle separation through deterministic lateral displacement. *Science* **304**, 987–990 (2004).
- [195] Wu, J. Acoustical tweezers. *The Journal of the Acoustical Society of America* **89**, 2140–2143 (1991).
- [196] Kumar, M., Feke, D. L. & Belovich, J. M. Fractionation of cell mixtures using acoustic and laminar flow fields. *Biotechnology and bioengineering* **89**, 129–137 (2005).

- [197] Ashkin, A., Dziedzic, J. & Yamane, T. Optical trapping and manipulation of single cells using infrared laser beams. *Nature* **330**, 769–771 (1987).
- [198] Moffitt, J. R., Chemla, Y. R., Smith, S. B. & Bustamante, C. Recent advances in optical tweezers. *Biochemistry* **77**, 205 (2008).
- [199] Chronis, N. & Lee, L. P. Electrothermally activated su-8 microgripper for single cell manipulation in solution. *Microelectromechanical Systems, Journal of* **14**, 857–863 (2005).
- [200] Leong, T. G. *et al.* Tetherless thermobiochemically actuated microgrippers. *Proceedings of the National Academy of Sciences* **106**, 703–708 (2009).
- [201] Ger, T.-R., Huang, H.-T., Chen, W.-Y. & Lai, M.-F. Magnetically-controllable zigzag structures as cell microgripper. *Lab on a Chip* **13**, 2364–2369 (2013).
- [202] Diller, E., Giltinan, J. & Sitti, M. Independent control of multiple magnetic microrobots in three dimensions. *The International Journal of Robotics Research* **32**, 614–631 (2013).
- [203] Hou, M. T. *et al.* A rolling locomotion method for untethered magnetic microrobots. *Applied Physics Letters* **96**, 024102 (2010).
- [204] Jiang, G.-L. *et al.* Development of rolling magnetic microrobots. *Journal of Micromechanics and Microengineering* **20**, 085042 (2010).
- [205] Miltenyi, S., Müller, W., Weichel, W. & Radbruch, A. High gradient magnetic cell separation with macs. *Cytometry* **11**, 231–238 (1990).
- [206] Molday, R., Yen, S. & Rembaum, A. Application of magnetic microspheres in labelling and separation of cells. *Nature* **268**, 437 (1977).
- [207] Elkin, C. *et al.* Magnetic bead purification of labeled dna fragments for high-throughput capillary electrophoresis sequencing. *Lawrence Berkeley National Laboratory* (2001).
- [208] Safarik, I. & Safarikova, M. Magnetic techniques for the isolation and purification of proteins and peptides. *BioMagnetic Research and Technology* **2**, 7 (2004).
- [209] Kourilov, V. & Steinitz, M. Magnetic-bead enzyme-linked immunosorbent assay verifies adsorption of ligand and epitope accessibility. *Analytical biochemistry* **311**, 166–170 (2002).
- [210] Sun, H.-B., Matsuo, S. & Misawa, H. Three-dimensional photonic crystal structures achieved with two-photon-absorption photopolymerization of resin. *Applied Physics Letters* **74**, 786–788 (1999).
- [211] Kawata, S., Sun, H.-B., Tanaka, T. & Takada, K. Finer features for functional microdevices. *Nature* **412**, 697–698 (2001).

- [212] Straub, M. & Gu, M. Near-infrared photonic crystals with higher-order bandgaps generated by two-photon photopolymerization. *Optics letters* **27**, 1824–1826 (2002).
- [213] Seet, K. K., Juodkazis, S., Jarutis, V. & Misawa, H. Feature-size reduction of photopolymerized structures by femtosecond optical curing of su-8. *Applied physics letters* **89**, 024106 (2006).
- [214] Xing, J.-F. *et al.* Improving spatial resolution of two-photon microfabrication by using photoinitiator with high initiating efficiency. *Applied physics letters* **90**, 131106–131106 (2007).
- [215] Serbin, J. *et al.* Femtosecond laser-induced two-photon polymerization of inorganic organic hybrid materials for applications in photonics. *Optics letters* **28**, 301–303 (2003).
- [216] Wegener, M. & Linden, S. Shaping optical space with metamaterials. *Phys. Today* **63**, 32–36 (2010).
- [217] Fischer, J., Ergin, T. & Wegener, M. Three-dimensional polarization-independent visible-frequency carpet invisibility cloak. *Optics letters* **36**, 2059–2061 (2011).
- [218] Ovsianikov, A. *et al.* Two photon polymerization of polymer–ceramic hybrid materials for transdermal drug delivery. *International journal of applied ceramic technology* **4**, 22–29 (2007).
- [219] Stratakis, E., Ranella, A., Farsari, M. & Fotakis, C. Laser-based micro-nanoengineering for biological applications. *Progress in Quantum Electronics* **33**, 127–163 (2009).
- [220] Xia, H. *et al.* Ferrofluids for fabrication of remotely controllable micro-nanomachines by two-photon polymerization. *Advanced Materials* **22**, 3204–3207 (2010).
- [221] Suter, M. *et al.* Superparamagnetic microrobots: fabrication by two-photon polymerization and biocompatibility. *Biomedical microdevices* **15**, 997–1003 (2013).
- [222] Peele, A., Shew, B., Vora, K. & Li, H. Overcoming su-8 stiction in high aspect ratio structures. *Microsystem technologies* **11**, 221–224 (2005).
- [223] Bretherton, F. P. The motion of rigid particles in a shear flow at low reynolds number. *Journal of Fluid Mechanics* **14**, 284–304 (1962).
- [224] Saffman, P. The lift on a small sphere in a slow shear flow. *Journal of Fluid Mechanics* **22**, 385–400 (1965).
- [225] Saffman, P. Corrigendum to the lift on a small sphere in a slow shear flow. *J. Fluid Mech.* **31**, 624 (1968).

- [226] Feng, J., Hu, H. H. & Joseph, D. D. Direct simulation of initial value problems for the motion of solid bodies in a newtonian fluid. part 2. couette and poiseuille flows. *Journal of Fluid Mechanics* **277**, 271–301 (1994).
- [227] Ho, B. P. & Leal, L. G. Inertial migration of rigid spheres in two-dimensional unidirectional flows. *Journal of Fluid Mechanics* **65**, 365–400 (1974).
- [228] Suter, M. *et al.* A photopatternable superparamagnetic nanocomposite: Material characterization and fabrication of microstructures. *Sensors and Actuators B: Chemical* **156**, 433–443 (2011).
- [229] Suter, M. *et al.* Superparamagnetic photocurable nanocomposite for the fabrication of microcantilevers. *Journal of Micromechanics and Microengineering* **21**, 025023 (2011).
- [230] Teh, W., Dürig, U., Drechsler, U., Smith, C. & Güntherodt, H.-J. Effect of low numerical-aperture femtosecond two-photon absorption on (su-8) resist for ultrahigh-aspect-ratio microstereolithography. *Journal of applied physics* **97**, 054907 (2005).
- [231] Del Campo, A. & Greiner, C. Su-8: a photoresist for high-aspect-ratio and 3d submicron lithography. *Journal of Micromechanics and Microengineering* **17**, R81 (2007).
- [232] Zhang, Z., Zhao, P., Xiao, G., Watts, B. R. & Xu, C. Sealing su-8 microfluidic channels using pdms. *Biomicrofluidics* **5**, 046503 (2011).
- [233] Liu, Y., Nolte, D. D. & Pyrak-Nolte, L. J. Large-format fabrication by two-photon polymerization in su-8. *Applied Physics A* **100**, 181–191 (2010).
- [234] Yasui, M. & Ikuta, K. 3d general photocurable model of resin with various kinds of microparticles. In *Micro Electro Mechanical Systems (MEMS), 2013 IEEE 26th International Conference on*, 453–456 (IEEE, 2013).
- [235] Thiel, M. & Hermatschweiler, M. Three-dimensional laser lithography. *Optik & Photonik* **6**, 36–39 (2011).
- [236] Xu, B.-B. *et al.* Fabrication and multifunction integration of microfluidic chips by femtosecond laser direct writing. *Lab on a chip* **13**, 1677–1690 (2013).
- [237] Fischer, J. *et al.* Three-dimensional multi-photon direct laser writing with variable repetition rate. *Optics express* **21**, 26244–26260 (2013).
- [238] Wu, D. *et al.* Hybrid femtosecond laser microfabrication to achieve true 3d glass/polymer composite biochips with multiscale features and high performance: the concept of ship-in-a-bottle biochip. *Laser & Photonics Reviews* **8**, 458–467 (2014).